UNDERSTANDING OF DEFECT PASSIVATION AND ITS EFFECT ON MULTICRYSTALLINE SILICON SOLAR CELL PERFORMANCE

A Thesis
Presented to
The Academic Faculty

by

Kenta Nakayashiki

In Partial Fulfillment
of the Requirements for the Degree
Doctor of Philosophy in Electrical Engineering

School of Electrical and Computer Engineering
Georgia Institute of Technology
December 2007

UNDERSTANDING OF DEFECT PASSIVATION AND ITS EFFECT ON MULTICRYSTALLINE SILICON SOLAR CELL PERFORMANCE

Approved by:

Dr. Ajeet Rohatgi
School of ECE, Georgia Tech, Adviser

Dr. Miroslav Begović
School of ECE, Georgia Tech

Dr. Bernard Kippelen
School of ECE, Georgia Tech

Dr. Gabriel A. Rincón-Mora
School of ECE, Georgia Tech

Dr. W. Brent Carter
School of MSE, Georgia Tech

Date Approved: 2 October 2007

DEDICATION

To my parents,

Sadao and Minako Nakayashiki,

for their support and patience.

ACKNOWLEDGEMENTS

I would like to express my deepest appreciation to my dissertation advisor, Dr. Ajeet Rohatgi, for providing the infrastructure and motivation for this research. I would also like to thank Dr. Miroslav Begović, Dr. Bernard Kippelen, and Dr. Gabriel A. Rincón-Mora at School of Electrical and Computer Engineering, and Dr. W. Brent Carter at School of Materials Science and Engineering for serving as members of my dissertation committee.

I would like to extend my sincere appreciation to Dr. Dong Seop Kim and Dr. Abasifreke U. Ebong for helpful instructions and discussions on device physics, processing, and characterization and Ms. Denise Taylor for her administrative assistance. I would also like to thank Mr. Bala R. Bathey, Dr. Mark D. Rosenblum, and Dr. Juris P. Kalejs (currently at JPK Consulting) at SCHOTT Solar, Inc. for providing EFG Si wafers and meaningful discussions, Dr. Jack I. Hanoka at Evergreen Solar, Inc. for providing String Ribbon Si wafers, Dr. Sergei Ostapenko and Dr. Igor Tarasov (currently at SDI Tampa) at University of South Florida for performing a scanning photoluminescence analysis, Dr. Bhushan L. Sopori at NREL for his instructions of LBIC system, and members at NREL Characterization and Testing Groups for their help.

Finally, I gratefully acknowledge former and current members of University Center of Excellence for Photovoltaics at Georgia Institute of Technology, Dr. Ji-Weon Jeong at LG Chem, Dr. Vijay Yelundur at Georgia Tech, Dr. Ben Damiani at Intel, Dr. Mohamed M. Hilali at Advent Solar, Alan Ristow, Vichai Meemongkolkiat, Manav Sheoran, Ajay Upadhyaya, Brian Rounsaville, Vijaykumar Upadhyaya, Keith Tate, and Dean C. Sutter for their friendship and creating a great work environment.

This research has been supported in part by the United States Department of Energy under Contract DE-FC36-00GO10600 and in part by the National Renewable Energy Laboratory under Contract AAT-2-31605-02.

TABLE OF CONTENTS

DEDICATION . . . . **iii**

ACKNOWLEDGEMENTS . . . . **iv**

LIST OF TABLES . . . . **x**

LIST OF FIGURES . . . . **xii**

SUMMARY . . . . **xvi**

I INTRODUCTION **1**

1.1 Opportunity and Challenges in PV Energy Conversion 1

1.2 Specific Research Objectives 4

1.2.1 Task 1: Investigation and demonstration of enhanced defect hydrogenation in mc-Si materials using rapid thermal processing 5

1.2.2 Task 2: Fundamental understanding of carrier lifetime enhancement in EFG Si through RTP-assisted reduction of hydrogen-defect dissociation 6

1.2.3 Task 3: Fabrication and characterization of record high-efficiency String Ribbon Si solar cells using photolithography and screen-printed front contacts 6

1.2.4 Task 4: Development of an analytical model to assess the impact of material inhomogeneity on String Ribbon Si solar cell performance 7

1.2.5 Task 5: Application of the analytical model to project the efficiency potential in the presence of inhomogeneous defect distribution . . . 7

II FUNDAMENTALS OF CRYSTALLINE SILICON MATERIALS AND SOLAR CELLS **9**

2.1 Solar Cell Operation and Carrier Recombination Lifetime in Multicrystalline Si 9

2.1.1 Solar cell operation and performance parameters 9

2.1.2 Carrier recombination mechanisms and bulk lifetime 12

2.1.3 Understanding of carrier recombination at the structural defects . . 14

2.1.4 Carrier lifetime measurement techniques 15

2.2 Crystal Growth Technologies of Promising Ribbon Silicon Materials 19

2.2.1 Edge-defined film-fed growth (EFG) Si 21

2.2.2 String Ribbon Si 22

2.2.3 Ribbon growth on substrate (RGS) 23

2.2.4 Dendritic web Si 24

2.3 Impurity Gettering and Defect Passivation Techniques for Minority Carrier Recombination Lifetime Enhancement 25

2.3.1 Phosphorus diffusion-induced impurity gettering 26

2.3.2 Aluminum alloying-induced impurity gettering 27

2.3.3 PECVD SiN_x-induced defect hydrogenation 28

2.3.4 Rapid thermal processing for solar cell fabrication and defect hydrogenation 32

III HISTORY, PROGRESS, AND CURRENT STATUS OF PROMISING PV TECHNOLOGIES 35

3.1 History and Progress of High-Efficiency Crystalline Si Solar Cells 37

3.2 History and Progress of High-Efficiency Solar Cells on Low-Cost mc-Si Materials 40

3.3 Industry-Scale Large-Area Solar Cells 42

IV INVESTIGATION AND DEMONSTRATION OF ENHANCED DEFECT HYDROGENATION IN MULTICRYSTALLINE SILICON MATERIALS USING RAPID THERMAL PROCESSING 49

4.1 Investigation of Contact Firing Time on Carrier Lifetime Enhancement in Multicrystalline Silicon 50

4.2 Characterization, Results and Discussion 51

4.2.1 IQE measurements and SEM analysis of FZ Si solar cells for establishing the process for effective Al-BSF formation 51

4.2.2 Lifetime enhancement by P diffusion-induced gettering and PECVD SiN_x defect hydrogenation in multicrystalline silicon materials . . . 52

4.3 Investigation of PECVD SiN_x-Induced Defect Hydrogenation in EFG Si as a Function of Contact Firing Temperature 56

4.4 Development of Manufacturable Belt Co-Firing Process for Maximum Hydrogenation in EFG Silicon 59

4.5 Conclusions 60

V FUNDAMENTAL UNDERSTANDING OF MINORITY CARRIER LIFETIME ENHANCEMENT IN EFG SILICON THROUGH CHARACTERIZATION OF PECVD SILICON NITRIDE FILMS AND RAPID THERMAL PROCESSING-ASSISTED REDUCTION OF HYDROGEN-DEFECT DISSOCIATION 62

5.1 Characterization of PECVD SiN_x Films as a Source of Hydrogen Atoms for Defect Passivation 62

5.1.1 FTIR measurements to detect the change in N-H and Si-H concentrations in PECVD SiN_x films upon annealing 62

5.1.2 SIMS analysis of hydrogen at the PECVD SiN_x/Si interface 64

5.2 Understanding of Kinetics of Hydrogen-Defect Dissociation Process in EFG Silicon 65

5.3 Room-Temperature Scanning Photoluminescence Mapping to Study the Hydrogen Passivation and Reactivation of Defects in EFG Silicon 71

5.4 Conclusions 76

VI FABRICATION AND ANALYSIS OF RECORD HIGH-EFFICIENCY STRING RIBBON SILICON SOLAR CELLS 77

6.1 Device Fabrication 78

6.2 Device Characterization and Analysis 79

6.2.1 Solar cell results 79

6.2.2 Carrier lifetime measurements using quasi-steady-state photoconductance technique 83

6.2.3 Light beam-induced current scans and internal quantum efficiency measurements 85

6.2.4 Effect of defect hydrogenation on cell performance 89

6.2.5 Analysis of performance limiting factors in 18.3% String Ribbon Si cell 90

6.3 Conclusions 92

VII UNDERSTANDING OF THE EFFECT OF MATERIAL INHOMOGENEITY ON STRING RIBBON SILICON SOLAR CELL PERFORMANCE 93

7.1 Experiment 95

7.2 Results and Discussion 95

7.2.1 Light beam-induced current scans and internal quantum efficiency measurements 95

7.2.2 Extraction of effective diffusion length L_{eff} from the IQE response . 98

7.3 Theoretical and Experimental Assessment of Impact of Electrically Active Defects on Solar Cell Performance 101

7.3.1 Development of the analytical model to assess the loss in V_{OC} resulting from inhomogeneity 101

7.3.2 Model calculations to assess the loss in V_{OC} of a cell with two regions of different recombination intensity 104

7.3.3 Model calculations to assess the loss in V_{OC} of a cell with three regions of different recombination intensity 106

7.3.4 Application of the analytical model to defective cells 107

7.3.5 Analysis of the record high-efficiency and average String Ribbon Si cells using an analytical model 109

7.4 Conclusions 111

VIII APPLICATION OF AN ANALYTICAL MODEL TO DETERMINE THE IMPACT OF MATERIAL INHOMOGENEITY ON SMALL- AND LARGE-AREA MULTICRYSTALLINE SILICON SOLAR CELL PERFORMANCE 113

8.1 Device Modeling and Analysis 114

8.1.1 Application and validation of the inhomogeneity model 114

8.1.2 Inhomogeneity-induced loss in open-circuit voltage of large-area EFG Si cells 124

8.2 Guidelines for Achieving High-Efficiency Ribbon Silicon Solar Cells 129

8.2.1 Variations in ΔV_{OC} values as a function of material and device parameters 129

8.2.2 Effect of improving carrier lifetime in the good region and BSRV in the presence of defects 131

8.2.3 Design of 17%-efficient planar ribbon mc-Si cells in the presence of defects 133

8.3 Conclusions 136

IX ATTEMPTS TO MINIMIZE AREA FRACTION AND RECOMBINATION INTENSITY OF LOW DIFFUSION LENGTH REGIONS BY HIGH-TEMPERATURE THERMAL CYCLES AND DOUBLE-SIDED PECVD SILICON NITRIDE-INDUCED DEFECT HYDROGENATION 138

9.1 Effect of P Diffusion-Induced Impurity Gettering 139

9.2 Effect of Intense PECVD SiN_x-Induced Defect Hydrogenation 142

X GUIDELINES FOR FUTURE WORK 147

10.1 Surface Texturing for Effective Light Trapping 147

APPENDIX A — DETAILED PROCESS SEQUENCE: SCREEN-PRINTED CONTACTS 149

APPENDIX B — DETAILED PROCESS SEQUENCE: PHOTOLITHOGRAPHY-DEFINED CONTACTS . . . 153

APPENDIX C — SAMPLE PREPARATION FOR CARRIER LIFETIME MEASUREMENTS . . . 156

REFERENCES . . . 158

PUBLICATIONS . . . 171

LIST OF TABLES

Table 1 Performance of ribbon Si growth technologies. 20

Table 2 Material quality of ribbon Si materials. 20

Table 3 Progress of laboratory-scale mc-Si solar cell performance. All efficiencies were confirmed independently. 43

Table 4 Progress of large-area solar cell performance on low-cost mc-Si materials. 48

Table 5 Average cell parameters on FZ Si fabricated by three different scheme of firing step ♯1. Peak firing temperature was 750°C. 51

Table 6 Average cell parameters on HEM, EFG, and String Ribbon Si. Peak firing temperature was 750°C. 55

Table 7 Average cell parameters for each firing scheme. Firing time was 1 s for all cases. 58

Table 8 Average values of PL intensities for I_{bb}, I_{def}, and R-parameter in each annealing step. 73

Table 9 Average and best solar cell performance parameters. (*) denotes the efficiency measured and verified at NREL. 80

Table 10 Suns-$\mathrm{V_{OC}}$ measurements on selected solar cells. The second-diode ideality factor ($\mathrm{n_2}$) was assumed to be 2.0. 86

Table 11 PC1D inputs for FZ and String Ribbon Si solar cells. 88

Table 12 Solar cell performance parameters using PC1D simulations with carrier lifetime of 2 μs for photolithography and screen-printed contacts. 89

Table 13 Measured and simulated characteristics on FZ and String Ribbon Si cells using the input parameters listed in Table **??**. 90

Table 14 Analysis of performance limiting factors on 18.3% String Ribbon Si cell. 91

Table 15 Measured String Ribbon Si solar cell parameters and LBIC responses . 97

Table 16 PC1D input parameters for String Ribbon Si solar cell simulation. . . . 100

Table 17 Measured and simulated solar cell parameters on String Ribbon Si using an extracted L_{eff} of 870 μm. 101

Table 18 Summary of model calculations for loss in V_{OC}. 117

Table 19 Cell performance of large-area EFG Si cells used in this study. 124

Table 20 Calculated and measured loss in V_{OC} for large-area EFG Si cells. 127

Table 21 Material and device baseline parameters for model calculations. 130

Table 22 Initial input parameters used for device modeling in PC1D. 134

Table 23 Average cell results of standard (A) and intense gettering (B) processes. 141

Table 24 Average cell results of standard (C) and intense hydrogenation (D) processes. 144

Table 25 Average values of PL intensities for I_{bb} in each process step. 146

LIST OF FIGURES

Figure 1 PV module shipment from 1982 to 2006. 2

Figure 2 US energy consumption by source in 2005. 2

Figure 3 US renewable energy consumption by source in 2005. 3

Figure 4 World cell/module production by substrate in 2006. 4

Figure 5 A schematic of a solar cell with $p-n$ junction. 10

Figure 6 $I-V$ characteristic of a solar cell in the dark and under illumination. . 10

Figure 7 An equivalent circuit of a $p-n$ junction solar cell. 11

Figure 8 Three recombination mechanisms: (a) SRH, (b) radiative, and (c) Auger. 13

Figure 9 A schematic illustration of carrier recombination on dislocation. 15

Figure 10 Configuration of the carrier lifetime measurement system (WCT-100) used in this study. 16

Figure 11 EFG Si ribbon growth: a schematic of EFG Si growth. 21

Figure 12 Pictures of EFG Si growth system: (a) octagonal EFG Si wafers and (b) EFG Si growth in production line. 22

Figure 13 String Ribbon Si growth: a schematic of String Ribbon Si growth. . . . 23

Figure 14 A picture of String Ribbon Si growth. Two ribbons are grown simultaneously. 24

Figure 15 RGS Si ribbon growth: a schematic of RGS Si growth. 25

Figure 16 Dendritic web Si ribbon growth: a schematic of web Si growth. 26

Figure 17 Concept of impurity gettering process. 27

Figure 18 Selected data of hydrogen diffusivity in Si. 32

Figure 19 Schematics and evolution of high-efficiency monocrystalline Si solar cells: (a) First modern crystalline Si cell, (b) Black Cell, (c) PESC, (d) Back-Contact Cell (e) PERC, and (f) PERL Cell. 38

Figure 20 High-efficiency laboratory-scale mc-Si solar cells: (a) UNSW honeycomb textured PERL-type cell and (b) Fraunhofer ISE 20.3% cell. 41

Figure 21 Schematics of high-efficiency industry-scale monocrystalline Si solar cells: (a) Sanyo HIT cell and (b) SunPower back-contact cell 44

Figure 22 Schematics high-efficiency industry-scale mc-Si solar cells: (a) Kyocera RIE textured cell and (b) UKN mechanical grooved buried contact cell. 46

Figure 23 Long-wavelength IQE response of FZ Si cells. 52

Figure 24 SEM micrograph of Al-BSF region in FZ Si: (a) 750°C/1 s and (b) 750°C/120 s firing. 53

Figure 25 Carrier lifetime measurements on HEM, EFG, and String Ribbon Si. Error bar indicates a standard deviation. 54

Figure 26 Efficiencies of EFG Si cells as a function of a firing temperature. Error bar indicates a standard deviation. 58

Figure 27 Average carrier lifetime achieved for each firing scheme. Error bar indicates a standard deviation. 59

Figure 28 (a) Process sequence of belt-line co-firing used in this experiment and (b) efficiency distribution of EFG Si solar cells. Cell size is 4 cm^2. 60

Figure 29 FTIR spectra in the range of 2000 to 3500 cm^{-1}. 63

Figure 30 Change of the total bonded hydrogen concentration after high temperature process. 64

Figure 31 SIMS depth profile of deuterium at Si surface after SiN$_x$ deposition and anneal in an RTP unit at 750°C for 1, 60, and 120 s 66

Figure 32 Normalized lifetime (τ_f/τ_i) of a hydrogenated bare EFG Si sample as a function of annealing temperature for 1 s. 67

Figure 33 Normalized lifetime (τ_f/τ_i) of a hydrogenated bare EFG Si sample as a function of annealing time at 550°C. 68

Figure 34 A comparison of simulation and experimental data showing a fraction of passivated defect as a function of annealing temperature for 1 s annealing of a hydrogenated bare EFG Si sample (ν=1.0×10^{14} s^{-1}). 70

Figure 35 A comparison of simulation and experimental data showing a fraction of passivated defect in a hydrogenated EFG Si sample as a function of annealing time at 550°C (ν=1.0×10^{14} s^{-1}). 70

Figure 36 Room-temperature PL spectra on EFG Si after RTP dehydrogenation at 600°C/1 s. 72

Figure 37 Room-temperature PL mappings of (a) band-to-band (I_{bb}), (b) defect band (I_{def}), and (c) point-by-point ratio of I_{bb}(hydrogenated)/I_{bb}(initial) representing the increase in lifetime. The mapping size is 50×22 mm^2, step=0.5 mm. 74

Figure 38 Line scan through a PL map to quantify the loss in carrier lifetime [I_{bb}(hydrogenated)/I_{bb}(dehydrogenated)] and R-parameters ($I_{\mathrm{def}}/I_{\mathrm{bb}}$) changes after hydrogenation and 700°C dehydrogenation. 75

Figure 39 Progress of laboratory-scale ribbon (EFG and String Ribbon) Si solar cells. 78

Figure 40 Distribution of cell efficiency on String Ribbon Si fabricated by (a) photolithography and (b) screen-printed front contacts. Cell size is 4 cm^2. Units are % in efficiency, mV in V$_{\mathrm{OC}}$, and mA/cm^2 in J$_{\mathrm{SC}}$. 81

Figure 41 $I-V$ curves of record high-efficiency String Ribbon Si cells fabricated with photolithography (18.3%) and screen-printed (16.8%) contacts. Both cells were tested and confirmed by National Renewable Energy Laboratory. 81

Figure 42 Histogram of solar cell efficiencies fabricated by photolithography and screen-printing front contacts. 82

Figure 43 $I-V$ curves of high-efficiency EFG Si cells fabricated with photolithography (18.2%) and screen-printed (16.6%) contacts. Both cells were tested and confirmed by National Renewable Energy Laboratory. 83

Figure 44 Average lifetime in 2.0–3.0 Ωcm String Ribbon Si after each process step. Measurements were performed on several wafers and points (5 wafers and total 40 points) to account for the inhomogeneous material quality. QSSPC technique was used at an injection level of 1.0×10^{15} cm^{-3}. Error bar in the graph represents the standard deviation. 84

Figure 45 LBIC maps of (a) 18.3% (SR1-4) and (b) 17.1% (SR1-3) String Ribbon Si cells. PVScan 5000 system with 980 nm laser was used. 86

Figure 46 IQE response of 2.5 Ωcm FZ and 2.0-3.0 Ωcm String Ribbon Si cells. Simulated IQE response, corresponding to $\mathrm{L_{eff}}$ value of 1590 and 1060 μm, was obtained by PC1D. 87

Figure 47 LBIC scans of String Ribbon Si solar cells. High, moderate, and low V_{OC} cells are shown in left, center, and right sides, respectively. 96

Figure 48 Light-biased IQE response of selected regions (A1, A2, A3, C2, and C3) in String Ribbon Si solar cells and simulated (PC1D) IQE response corresponding to L_{eff} values of 870 μs, 95 μm, and 90 μm. 98

Figure 49 Calculated loss in V_{OC} as a function of defective region with different L_{eff} ratio or recombination intensity. Cell was divided into two regions (high and low L_{eff}s). 105

Figure 50 Calculated loss in V_{OC} for each area fraction of defective regions as a function of moderate region. 106

Figure 51 Histograms of LBIC response shown in Fig. **??**. Maximum LBIC response was 0.62 A/W for all three cells. 108

Figure 52 Methodology developed in this model. 109

Figure 53 IQE response of 17.1% String Ribbon Si cell (SR1-3) in high (A) and low (B) LBIC response regions. Simulated IQE response, corresponding to $\mathrm{L_{eff}}$ value of 1060 and 85 μm, was obtained by PC1D. 110

Figure 54 LBIC scans of 4 cm^2 String Ribbon Si solar cells. 115

Figure 55 Measured IQE response on String Ribbon Si solar cells. 116

Figure 56 LBIC scans of 4 cm^2 HEM and EFG Si solar cells. 118

Figure 57 Measured and simulated IQE response on HEM mc-Si solar cells. 119

Figure 58 Measured and simulated IQE response on EFG Si solar cells. 120

Figure 59 PC1D simulations of cell efficiency as a function of bulk carrier lifetime. 121

Figure 60 Procedure to obtain τ_{bu} from τ_A, τ_B, area fraction of regions A and B. . 122

Figure 61 Relationship between τ_B, area fraction, ΔV_{OC}, and τ_{bu}. The cell SR6 ($\tau_{\text{bu}} = 9$ μs, $\Delta V_{\text{OC}} = 40$ mV, $\tau_B = 2.0$ μs, and $A_B = 40\%$) is also shown in the figure. 123

Figure 62 LBIC scans of 100 cm^2 EFG solar cells. 125

Figure 63 Measured and simulated IQE response in specified locations in Fig. **??**. 126

Figure 64 Linear approximation of L_{eff} in μm from LBIC response in A/W. The best and worst points of LBIC response are indicated in the plot. 128

Figure 65 Model calculations for ΔV_{OC} as a function of (a) base resistivity, (b) cell thickness, (c) τ_B, and (d) τ_{avg}. 130

Figure 66 Model calculations of V_{OC} as a function of carrier lifetime in region A (τ_A). Device thickness is 300 μm. 132

Figure 67 Contour plot of (a) current and (b) future ribbon Si solar cell efficiencies as a function of area fraction of region B and τ_B. 135

Figure 68 Process sequence for standard and intense gettering processes. 140

Figure 69 Cell configuration used in this study. 140

Figure 70 Cell efficiency distribution of standard (A) and intense gettering (B) processes. 142

Figure 71 Process sequence for standard and intense hydrogenation processes. . . 143

Figure 72 Cell efficiency distribution of standard (C) and intense hydrogenation (D) processes. 144

Figure 73 Front and rear PL scans (I_{bb}) of four EFG Si samples: 1) unprocessed or as-grown, 2) P diffused and PECVD SiN$_x$ on the front, 3) P diffused, PECVD SiN$_x$ on the front and Al-BSF on the rear, and 4) P diffused and PECVD SiN$_x$ on the front and rear. 145

Figure 74 Results of PC1D simulations with and without surface texturing as a function of carrier lifetime. 148

Figure 75 Surface texturing using an acidic etch (H_2SO_4/HF/HNO_3) solution on String Ribbon Si. 148

SUMMARY

The cost of photovoltaic (PV) systems needs to be reduced by a factor of three to four to make PV cost-effective with conventional energy sources. This can be accomplished by fabricating high-efficiency cells on low-cost materials using simple and high-throughput cell fabrication technologies. Currently, more than 90% of PV modules are produced from crystalline Si, and most of it is grown in the form of ingot and then sliced into wafers accounting for ∼50% of the PV module manufacturing cost. This cost can be significantly reduced by using the ribbon-type crystalline Si materials, which can be grown directly from the Si melt. This eliminates the need for ingot slicing and deep chemical etch required for surface damage removal. However, the growth of the ribbon Si materials leads to relatively high concentration of metallic impurities and structural defects, resulting in very low as-grown carrier lifetime, typically 1–5 μs. These lifetime values are not sufficient to produce high-efficiency cells. Edge-defined film-fed grown (EFG) and String Ribbon Si materials are two promising ribbon Si candidates for the cost-effective PV and are the main focus of the work described in this thesis. The overall goal of this research is to produce high-efficiency cells on EFG and String Ribbon Si by enhancing the carrier lifetime during the cell processing through characterization and understanding of electrically active defects and technology development to passivate them. Extensive device modeling has been performed to quantitatively assess the impact of defect inhomogeneity on cell performance. The research in this thesis was divided into five major tasks discussed below.

The objective of the first task (Chap. IV) was to demonstrate that the rapid thermal processing (RTP) can enhance the defect hydrogenation and provide a high-quality Al-doped back surface field (Al-BSF) simultaneously. Firing of screen-printed contacts influences the degree of defect hydrogenation as well as the quality of Al-BSF. The RTP provides a better opportunity to tune the firing cycle for the best results. Both monocrystalline float-zone

(FZ) Si and mc-Si (cast, EFG, and String Ribbon) cells were fabricated simultaneously using an RTP firing of screen-printed contacts to accomplish this task. The FZ Si cells were analyzed to investigate the RTP firing time dependence of Al-BSF quality, which was quantified in terms of the uniformity of Al-BSF and open-circuit voltage (V_{OC}) using a scanning electron microscopy (SEM), current-voltage measurements, and long-wavelength internal quantum efficiency (IQE) measurements. It was found that a short RTP firing cycle (1 s) is sufficient to provide the Al-BSF quality as good as 60 and 120 s firing cycle. The mc-Si cells were used to study the effectiveness of the rapid firing on defect hydrogenation, which was assessed through the carrier lifetime measurements using a photoconductance tool. The lifetime measurements revealed that a short firing cycle enhanced the carrier lifetime in ribbon Si materials from 8–12 μs, after the P diffusion gettering, to $\sim$100 μs. In addition, cell efficiency as high as 16.1% was achieved on EFG Si using the optimized contact firing process developed in this task. An attempt was made to transfer the fabrication process established in the RTP system to a more manufacturable continuous belt-line furnace. The rapid co-firing of the front and back contacts in a belt-line furnace also produced $\sim$16%-efficient ribbon Si cells.

The second task (Chap. V) deals with the fundamental understanding of rapid firing-induced effective defect hydrogenation. In this task, it was found that there are two sources for hydrogenation: plasma-enhanced chemical vapor deposited (PECVD) SiN_x film itself contains $\sim 10^{22}$ cm^{-3} atomic hydrogen and the SiN_x/Si interface directly underneath the PECVD SiN_x also traps $\sim 10^{20}$ cm^{-3} atomic hydrogen. Characterization and analysis of the two primary hydrogen sources, PECVD SiN_x film and SiN_x/Si interface, were performed using Fourier Transform Infrared and Secondary Ion Mass Spectrometry techniques in order to explain why short firing cycle can enhance the carrier lifetime effectively. It was found that, upon contact firing, the release of hydrogen atoms from SiN_x films and SiN_x/Si interface slows down with annealing time, indicating that the two sources are not an infinite source of hydrogen for defect passivation. Degree of defect hydrogenation was assessed by carrier lifetime enahncement, which raised the lifetime in ribbon Si materials close to 100 μs. In selected cases, the hydrogenated bare EFG Si samples were re-annealed

systematically to study the dehydrogenation kinetics by monitoring the rate of decrease in carrier lifetimes and determine the activation energy of hydrogenated defects. Activation energy for hydrogen-defect dissociation was found to be 2.4–2.6 eV, which falls between the published activation energies for the dissociation of hydrogen-impurity and hydrogen-dislocation complexes. This suggested that the hydrogenation in ribbon Si materials may involve the passivation of impurity-decorated dislocations. This was also supported by a scanning photoluminescence (PL) study, which showed a defect band at 0.8 eV below the conduction band, which is attributed to dislocations or impurity-dislocation complexes in the literature. Scanning PL spectroscopy maps clearly demonstrated that defective or low carrier lifetime regions were effectively passivated during the rapid hydrogenation anneal and the same regions were reactivated rapidly during the dehydrogenation anneals, which were performed in the range of 400–700°C in a few seconds after removing the PECVD SiN_x film. It was concluded that the rapid hydrogenation was the result of the competition between injection of hydrogen atoms from the SiN_x film and the dissociation from hydrogenated defects during the contact firing cycle. Since the injection or supply of hydrogen slows down with time but its dissociation from defects continues at the same rate, rapid or short firing cycle gives a better passivation.

In the third task (Chap. VI), understanding of defect passivation and technology development in tasks 1 and 2 were used to construct an appropriate process sequence for achieving the record high-efficiency String Ribbon Si solar cells (4 cm^2) using both photolithography-defined (18.3%) and screen-printed (16.8%) front grid contacts. A combination of device fabrication, characterization, and analysis was used to explain the benefit of the process technologies developed in this research and the potential of ribbon Si solar cells.

In the fourth task (Chap. VII), an effort was made to improve the understanding of the impact of spatial distribution of defect inhomogeneities on fully processed high-efficiency String Ribbon Si solar cells with screen-printed contacts. Since ribbon Si materials generally have as-grown carrier lifetimes less than 5 μs, first, an attempt was made to enhance the gettering and defect hydrogenation techniques to raise the area-average lifetime above 90 μs in order to increase the sensitivity and the impact of low diffusion length regions on cell performance. Then, a simplified analytical model was developed to estimate the loss in V_{OC} of String Ribbon Si cells based on the area fraction and recombination intensity of the defective regions in the cells. Model calculations were compared with the experimental data to demonstrate the accuracy of the model developed in this task.

In the fifth task (Chap. VIII), the analytical model developed in task 4 was utilized to assess the performance loss in cast, EFG, and String Ribbon Si solar cells. The model calculations were also extended to large-area industry-type EFG Si cells in order to verify the acceptability of the analytical model for device characterization. A roadmap was established for achieving high-efficiency ribbon Si solar cells in the presence of distributed active defects using a combination of the analytical model and PC1D simulations. Advanced design features were incorporated to develop cell designs that can lead to high-efficiencies (>17%) in the presence of defects. Contour plots were generated to establish the relationship between cell efficiency and the combination of area fraction and carrier lifetime in the defective regions.

In Chap. IV, attempts were made to improve the material homogeneity and cell performance by applying high-temperature thermal cycles and double-sided hydrogenation process into cell fabrication to mitigate the defective regions in mc-Si cells. It was found that it is quite difficult to eliminate the defective regions using conventional process technologies, and further investigation is necessary to understand the nature of unpassivated defects for achieving high-efficiency cells.

Finally, PC1D simulations revealed that the successful implementation of the surface texturing can raise the ribbon Si cell efficiency to >18%.

CHAPTER I

INTRODUCTION

1.1 Opportunity and Challenges in PV Energy Conversion

The demand for energy is growing rapidly because of the rapid increase in the worlds' population and the rise in the standard of living. The majority of this demand has been supplied by fossil fuels (oil, coal, and natural gas). However, the use of fossil fuels for power generation causes pollution and a significant release of greenhouse effect gases, such as CO_2 and NO_x. In addition, fossil fuels, especially oil, are depleting at a rapid pace. Photovoltaic (PV) is one of the most promising sustainable energy technologies that can solve the energy and environmental problems simultaneously because the solar energy is essentially free, unlimited, and not localized in any part of the world and solar cells convert it into electrical energy with zero emission. In the last ten years, the average annual growth of PV module shipment has been greater than 35%/yr, as shown in Fig. 1 [1]. According to the United States PV Industry Roadmap, by the year 2020, PV could supply 15% of the new generating capacity needed in the United States each year and may become 10% of the United States energy portfolio by the year 2030. In spite of its attractiveness and advantages, PV accounted for less than 0.06% of the energy consumed in US in 2005 (Figs. 2 and 3 [2]), because the cost of PV electricity is roughly three to four times higher than the electricity produced from conventional fossil fuels. Currently, the cost of a PV module is about \$3–4/W, which needs to decrease to about \$1/W to be able to compete with conventional fossil fuels. This target can be achieved by fabricating high-efficiency cells on low-cost materials using high-throughput processes. The problem today is that high-efficiency cells are too expensive, and the low-cost cells are not stable or efficient enough to meet the \$1/W target. This provided the motivation for achieving high-efficiency solar cells on low-cost crystalline Si materials in this research.

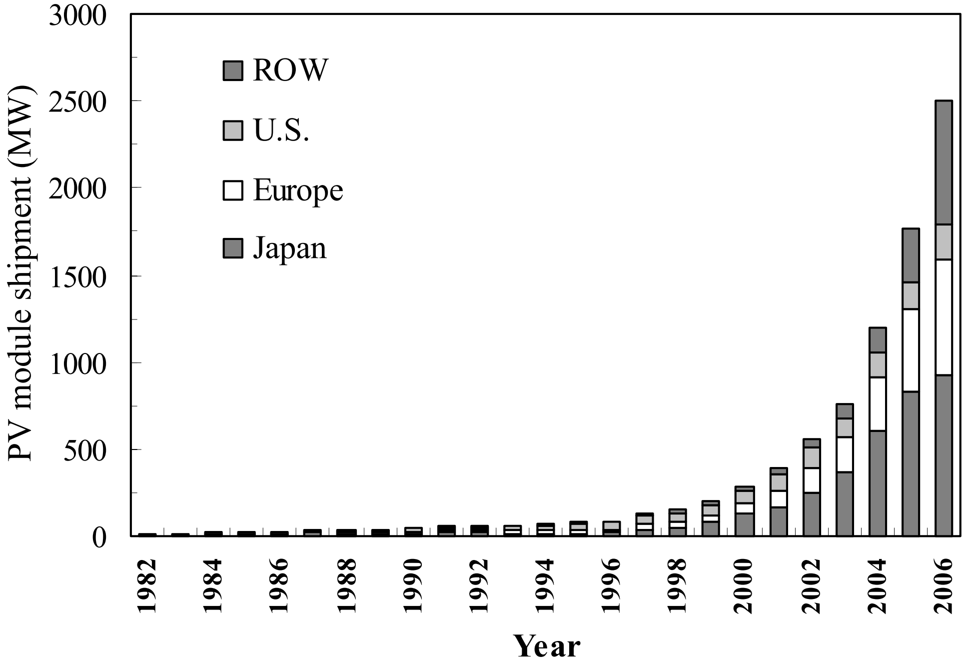

Figure 1: PV module shipment from 1982 to 2006.

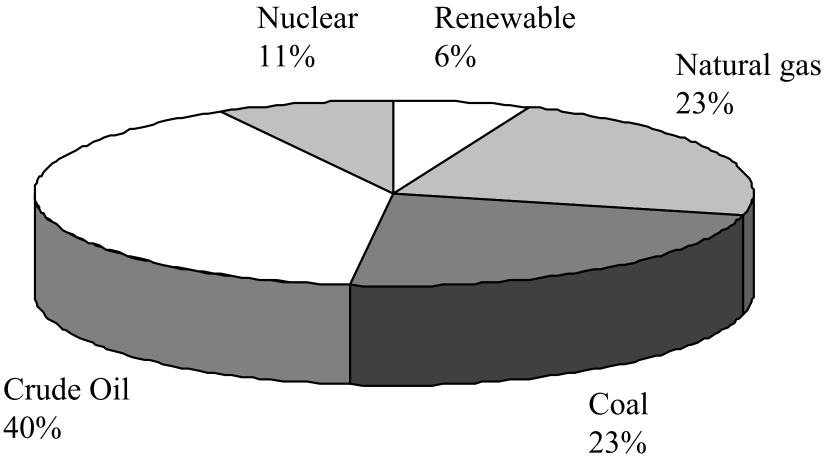

Figure 2: US energy consumption by source in 2005.

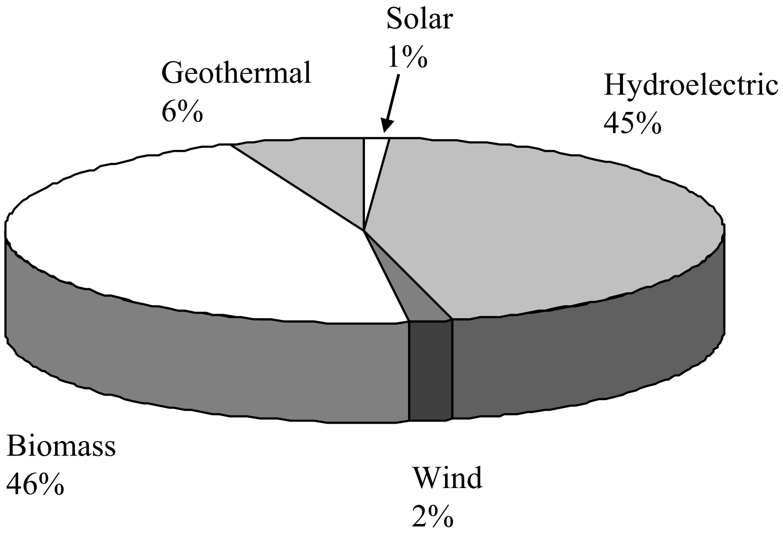

Figure 3: US renewable energy consumption by source in 2005.

Most of the PV modules today (>90%) are produced from crystalline silicon [1]. Unfortunately, the crystalline silicon substrates alone account for 44% of the cost of a PV module [3]. Therefore, the use of a low-cost silicon substrate and cell fabrication technologies without appreciably compromising the cell efficiency should help in achieving the goal of cost-effective PV system. Cast and ribbon mc-Si materials involve relatively simpler and cheaper crystal growth technologies than the monocrystalline Si, such as float zone (FZ) and Czochralski (Cz) silicon. The ribbon silicon materials, which is the focus of this research, offer an additional advantage in cost reduction by eliminating the kerf loss associated with the wafer slicing and deep chemical etching associated with slicing damage [4]. However, the ribbon Si materials suffer from a relatively high concentration of metallic impurities and structural defects. This limits the as-grown carrier lifetime in the range of 1.0 to 5.0 μs, which is not sufficient to produce high-efficiency cells. The challenge is to take advantage of the low-cost silicon mateiral and to develop fabrication technologies that can enhance the carrier lifetime during the cell processing, without any additional steps, to achieve high-efficiency and cost-effective ribbon Si solar cells. If all the active defects

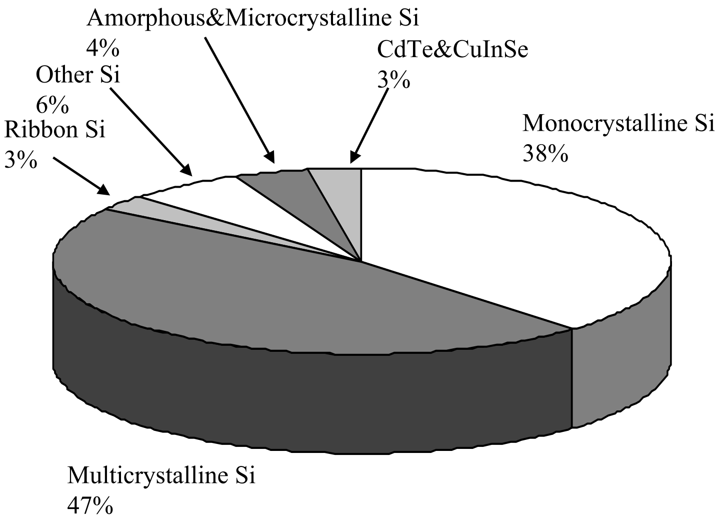

Figure 4: World cell/module production by substrate in 2006.

cannot be passivated during cell processing, then it is also critical to understand and assess the impact of remaining defects on cell performance and establish cell designs that can produce high-efficiency cells in the presence of defects. High-efficiency is critical for cost effectiveness because 1.0% increase in absolute cell efficiency in a 1.0 GW production line, which produces 14% efficient cells, could result in ~70 MW increase in annual production capacity. This amounts to \$280M increase in annual revenue using a current PV module cost of \$4.0/W. This provided the motivation for improving the efficiency of ribbon Si cells in this research through fundamental understanding of defects, material inhomogeneity, technology development, device modeling, and cell fabrication.

1.2 Specific Research Objectives

The overall goal of this study is to fabricate high-efficiency ribbon Si solar cells through enhanced defect passivation, technology development, and fundamental understanding of the impact of active defects on ribbon Si solar cell performance. A systematic approach to meet this objective is outlined in the following five tasks. Task 1 involves the investigation and optimization of the defect hydrogenation process using an appropriate combination of plasma-enhanced chemical vapor deposited (PECVD) SiN_x and screen-printed contact firing in a rapid thermal processing (RTP) system to inject atomic hydrogen from PECVD SiN_x film into the bulk silicon. Since the firing cycle also influences the quality of Al-doped back surface field (Al-BSF), the firing cycle is optimized to achieve an effective defect passivation as well as back surface passivation simultaneously. Task 2 deals with the fundamental understanding of hydrogenation-induced carrier lifetime enhancement in defective materials. In this task, a model is developed to explain and quantify the lifetime enhancement resulting from the rapid firing of cells, which utilizes the kinetics of hydrogen-defect dissociation. Based on the fundamental understanding from this model, a contact firing cycle during the RTP is established to maximize the retention of hydrogen at the defect sites for maximum lifetime enhancement. In task 3, cell fabrication processes developed in this research are integrated in proper sequence to achieve record high-efficiency String Ribbon Si solar cells using photolithography-defined as well as screen-printed front grid contacts. Cell analysis is also performed in this task to quantify and explain the loss mechanisms in the record high-efficiency ribbon Si cells. In task 4, a simplified analytical model is developed to quantify the effect of material inhomogeneity on the open-circuit voltage of String Ribbon Si solar cells resulting from the remaining unpassivated defects. In task 5, the analytical model developed in task 4 is applied to cast, EFG, and String Ribbon Si solar cells to assess the performance loss resulting from the distributed active defects. In addition, the defect inhomogeneity model is used in conjunction with solar cell modeling to predict the cell performance in the presence of distributed active defects and provide guidelines for achieving high-efficiency cells via defect engineering and cell design. The specific tasks proposed in this research are described in more detail below.

1.2.1 Task 1: Investigation and demonstration of enhanced defect hydrogenation in mc-Si materials using rapid thermal processing

The lifetime in as-grown ribbon Si is too low to achieve high-efficiency cells. Therefore, it is important to enhance the carrier lifetime during the cell processing. Phosphorus diffusion-induced impurity gettering and PECVD SiN_x-induced defect hydrogenation are routinely used as a part of solar cell fabrication processes to enhance the carrier lifetime in defective Si materials. The objective of this task is to demonstrate that the rapid thermal processing can enhance the defect hydrogenation and also provide a good Al-BSF simultaneously. Both monocrystalline (FZ) and mc-Si (cast, EFG, and String Ribbon) cells are fabricated simultaneously using RTP to accomplish this task. FZ Si cells are analyzed to investigate the RTP firing time dependence of Al-BSF quality, and the mc-Si cells are used to study the effectiveness of RTP on defect hydrogenation. The Al-BSF quality is quantified in terms of back surface recombination velocity (BSRV) using scanning electron microscopy (SEM) and long-wavelength internal quantum efficiency (IQE) measurements on FZ Si cells. Defect passivation is assessed through carrier lifetime measurements.

1.2.2 Task 2: Fundamental understanding of carrier lifetime enhancement in EFG Si through RTP-assisted reduction of hydrogen-defect dissociation

It is known that PECVD SiN_x-induced defect hydrogenation plays an important role in enhancing the carrier recombination lifetime in ribbon Si solar cells. Atomic hydrogen released from the PECVD SiN_x film during the contact firing cycle penetrates the bulk Si and attaches itself to defects to passivate them. However, the degree of passivation is a strong function of firing cycle. In this task, an RTP system is used to optimize the defect hydrogenation process through basic understanding of the passivation mechanism. In selected cases, hydrogenated bare EFG Si samples are reannealed systematically to study the dehydrogenation kinetics by monitoring the rate of change in minority carrier lifetimes to determine the activation energy of hydrogenated defects. Scanning photoluminescence spectroscopy is performed to identify the nature of passivated defects and understand the process of hydrogen dissociation from the active defects in EFG Si. In addition, the understanding gained from the RTP and photoluminescence study is used to develop a co-firing process for front and rear screen-printed contacts in a continuous belt furnace to achieve high carrier lifetime and high-efficiency EFG Si solar cells.

1.2.3 Task 3: Fabrication and characterization of record high-efficiency String Ribbon Si solar cells using photolithography and screen-printed front contacts

In this task, understanding of defect passivation and technology development in tasks 1 and 2 are combined to construct appropriate process sequence to achieve record high-efficiency

String Ribbon Si solar cells using both photolithography-defined and screen-printed front grid contacts. A combination of device fabrication, characterization, and analysis is used to explain the benefit of the process technologies developed in this research and the potential of ribbon Si solar cells.

1.2.4 Task 4: Development of an analytical model to assess the impact of material inhomogeneity on String Ribbon Si solar cell performance

Inhomogeneously distributed electrically active defects are frequently found to be present in mc-Si materials, even after effective P diffusion gettering and defect passivation. Their distribution and recombination activity can significantly degrade the cell performance. Therefore, understanding and assessment of the impact of the inhomogeneous distribution of defects on solar cell performance has become an area of active investigation. In this task, an effort is made to improve the understanding of the impact of spatial distribution of defect inhomogeneities on fully processed high-performance screen-printed String Ribbon Si solar cells. Since ribbon Si materials generally have as-grown carrier lifetimes of less than 5 μs, first, an attempt is made to enhance the gettering and defect hydrogenation techniques to raise the area-average lifetime to above 90 μs in order to increase the sensitivity and the impact of low diffusion length regions. Then, a simplified analytical model is developed to approximately determine the loss in open-circuit voltage (V_{OC}) of String Ribbon Si cells based on the area fraction of low diffusion length regions mixed with high diffusion length regions. Model calculations are compared with the experimental data to demonstrate that the loss in V_{OC} resulting from material inhomogeneity can be predicted with reasonable accuracy for most cells by dividing the cell into two regions using the simple analytical model.

1.2.5 Task 5: Application of the analytical model to project the efficiency potential in the presence of inhomogeneous defect distribution

The analytical model developed in task 3 is utilized to assess the performance loss in cast, EFG, and String Ribbon Si solar cells. A roadmap is established for achieving high-efficiency ribbon Si solar cells in the presence of distributed active defects using a combination of analytical model and PC1D device simulations. Advanced design features are incorporated to develop cell designs that can lead to high efficiencies in the presence of defects. Contour plots are generated to establish the relationship between cell efficiency and the combination of area fraction and carrier lifetime of defective regions.

CHAPTER II

FUNDAMENTALS OF CRYSTALLINE SILICON MATERIALS AND SOLAR CELLS

2.1 Solar Cell Operation and Carrier Recombination Lifetime in Multicrystalline Si

A solar cell is a semiconductor device that converts sunlight directly into electricity via photovoltaic effect. The photovoltaic effect is a physical phenomena that generates voltage across the junction from the absorption of photons. When the sunlight is incident on the surface of a semiconductor with $p-n$ junction, the built-in field at the junction separates the carriers (electrons and holes) generated by photons in the bulk. Electrons are collected in n-type region, and holes in p-type region, resulting in the carrier separation and voltage generation across the junction. A schematic of a basic crystalline Si solar cell with $p-n$ junction is shown in Fig. 5 . In this section, basic theory and physics of solar cell operation and carrier recombination mechanisms are reviewed.

2.1.1 Solar cell operation and performance parameters

The solar cell efficiency is defined as the product of its short-circuit current density (J_{SC}), open-circuit voltage (V_{OC}), and fill factor (FF).

$$\begin{aligned}\eta &= \frac{J_{\mathrm{SC}} \cdot V_{\mathrm{OC}} \cdot FF}{P_{\mathrm{in}}} \\ &= \frac{J_{\mathrm{mp}} \cdot V_{\mathrm{mp}}}{P_{\mathrm{in}}},\end{aligned} \tag{1}$$

where P_{in} is the incident power on the cell, and FF is the measure of squareness of the current-voltage ($I-V$) curve and can be expressed as [5]:

$$FF = \frac{J_{\mathrm{mp}} \cdot V_{\mathrm{mp}}}{J_{\mathrm{SC}} \cdot V_{\mathrm{OC}}}. \tag{2}$$

J_{mp} and V_{mp} are the current density and voltage at the maximum power point, indicated in Fig. 6, which contains the dark and illuminated $I-V$ curves of a solar cell.

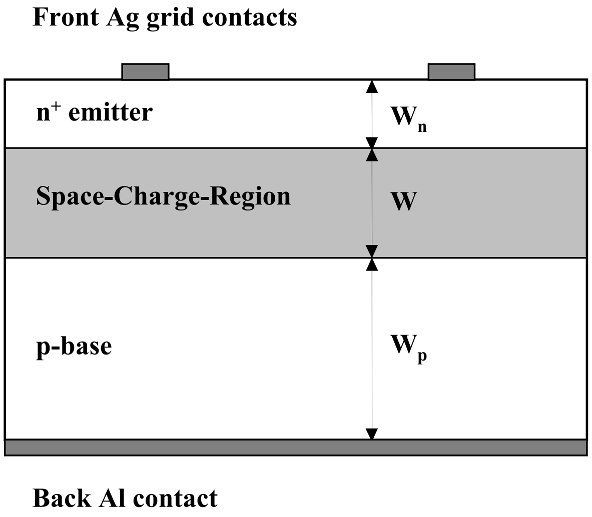

Figure 5: A schematic of a solar cell with $p-n$ junction.

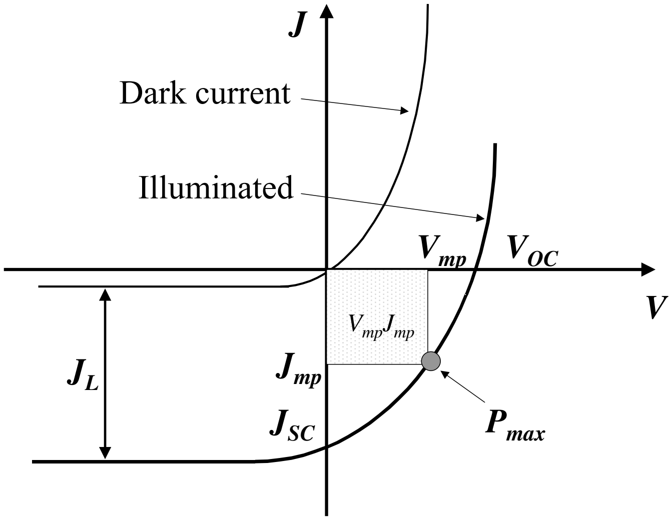

Figure 6: $I-V$ characteristic of a solar cell in the dark and under illumination.

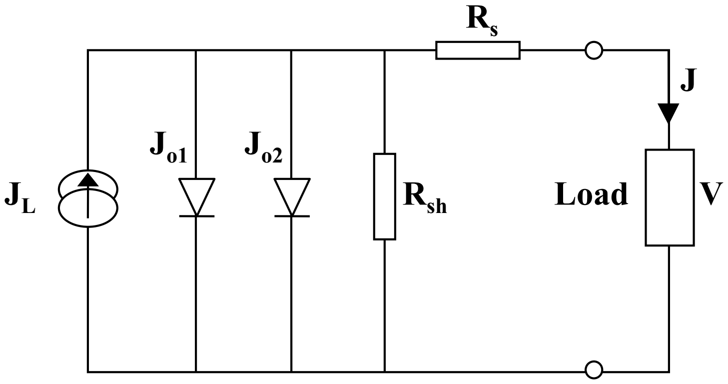

Figure 7: An equivalent circuit of a $p-n$ junction solar cell.

The illuminated $I-V$ characteristic of the solar cell is expressed as [5]:

$$J = J_L - J_{o1}\left[\exp\frac{q(V+JR_s)}{kT} - 1\right] - J_{o2}\left[\exp\frac{q(V+JR_s)}{n_2 kT} - 1\right] - \frac{(V+JR_s)}{R_{sh}}, \quad (3)$$

where J_{o1} represents the diode saturation current density that results from the thermal generation of minority carriers in the base and emitter regions. The J_{o2} corresponds to the junction leakage current density, which represents the carrier generation-recombination in the space-charge region. An equivalent circuit of a $p-n$ junction solar cell is illustrated in Fig. 7. The n_2 is the ideality factors for second-diode and normally 2.0 [6,7]. However, n_2 may vary depending on the energy level of the recombination center in the space-charge region. R_s is the series resistance, and R_{sh} is the shunt resistance.

The open-circuit voltage, V_{OC}, can be expressed as [5]:

$$V_{OC} = \frac{nkT}{q}\ln\left(\frac{J_{SC}}{J_{o1}} + 1\right), \quad (4)$$

where n is the diode ideality factor of single-diode model, k is the Boltzmann's constant, T is the temperature, q is the electron charge, and J_{o1} is the saturation current density. The

J_{o1} can be expressed as [5]:

$$\begin{aligned} J_{\mathrm{o1}} &= J_{\mathrm{oe}} + J_{\mathrm{ob}} \\ &= \frac{qn_i^2 D_p}{N_D L_p}\left[\frac{S_f L_p/D_p + \tanh(W_n/L_p)}{1 + (S_f L_p/D_p)\tanh(W_n/L_p)}\right] + \frac{qn_i^2 D_n}{N_A L_n}\left[\frac{S_b L_n/D_n + \tanh(W_p/L_n)}{1 + (S_b L_n/D_n)\tanh(W_p/L_n)}\right], \end{aligned} \tag{5}$$

where J_{oe} and J_{ob} are the emitter and base components of saturation current density, D_p and D_n are the diffusion coefficient of hole and electron, N_D and N_A are the doping concentrations of emitter and base, S_f and S_b are the front and back surface recombination velocities, W_n and W_p are the thickness of emitter and base regions, and L_p and L_n are the minority carrier diffusion lengths in the emitter and base, respectively. The minority carrier diffusion length in a p-type bulk material, L_b, can be expressed as [5]:

$$\begin{aligned} L_b &= L_n \\ &= \sqrt{D_n \tau_b}, \end{aligned} \tag{6}$$

where τ_b is the minority carrier lifetime in the bulk. Clearly, J_{o1} and V_{OC} are a strong function of carrier lifetime (τ_b).

2.1.2 Carrier recombination mechanisms and bulk lifetime

It has been shown in the previous section that the cell performance is a strong function of total carrier recombination in the cell. There are multiple ways in which a minority carrier can recombine in a cell. Net result of all carrier recombination mechanism is characterized by a recombination lifetime. Three main recombination mechanisms determine the carrier recombination lifetime: 1) radiative recombination τ_{rad}, 2) Auger recombination τ_{Auger}, and 3) Shockley-Read-Hall (SRH) recombination τ_{SRH}. These recombination mechanisms are illustrated in Fig. 8. The net carrier recombination lifetime in the bulk (τ_b) can be expressed as [8]:

$$\frac{1}{\tau_b} = \frac{1}{\tau_{\mathrm{rad}}} + \frac{1}{\tau_{\mathrm{Auger}}} + \frac{1}{\tau_{\mathrm{SRH}}}. \tag{7}$$

The radiative recombination is less important in Si, because it is an indirect bandgap material and its radiative lifetime is extremely high. The radiative recombination lifetime

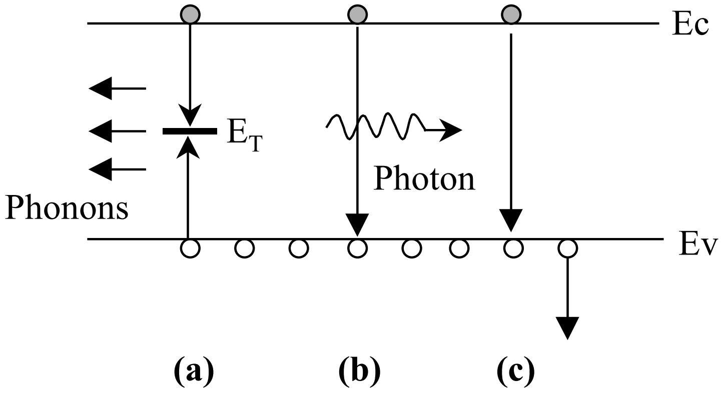

Figure 8: Three recombination mechanisms: (a) SRH, (b) radiative, and (c) Auger.

is expressed as [8]:

$$\tau_{\text{rad}} = \frac{1}{B(p_o + n_o + \Delta n)}, \tag{8}$$

where B is the radiative recombination coefficient (2.0×10^{-15} cm^3/s at 300K in Si [9]), p_o is the equilibrium hole concentration, n_o is the equilibrium electron concentration, and Δn is the injected or excess electron concentration. The Auger recombination is important in the heavily doped emitter region. The Auger lifetime is expressed as [8]:

$$\tau_{\text{Auger}} = \frac{1}{C_p(p_o^2 + 2p_o\Delta n + \Delta n^2)}, \tag{9}$$

where C_p is the Auger recombination coefficient (10^{-31}–10^{-30} cm^6/s at 300K in Si). The SRH recombination is generally the most important process in Si (especially in low-cost Si materials) because of the presence of impurities and structural defects in the bulk, which can introduce deep energy levels or traps within the bandgap. During the SRH recombination process, electron-hole pairs recombine through the deep-level traps, characterized by the density (N_T), energy level (E_T) in the bandgap, and capture cross section (σ_n and σ_p for electrons and holes, respectively). The SRH recombination lifetime is expressed as [8]:

$$\tau_{\text{SRH}} = \frac{\tau_{\text{po}}(n_o + n_1 + \Delta n) + \tau_{\text{no}}(p_o + p_1 + \Delta p)}{p_o + n_o + \Delta n}, \tag{10}$$

where Δp is the excess hole concentration, and n_1, p_1, τ_{no}, and τ_{po} can be defined as:

$$n_1 = n_i \exp \frac{(E_T - E_i)}{kT}, \tag{11}$$

$$p_1 = n_i \exp \frac{-(E_T - E_i)}{kT}, \tag{12}$$

$$\tau_{\text{no}} = \frac{1}{\sigma_n \nu_{\text{th}} N_T}, \tag{13}$$

$$\tau_{\text{po}} = \frac{1}{\sigma_p \nu_{\text{th}} N_T}, \tag{14}$$

where n_i is the intrinsic carrier concentration, and ν_{th} is the thermal velocity of the carriers (1.1×10^7 cm/s at 300K in Si [10]). Under low-injection level, the concentration of excess minority carrier (electron) is small compared to the concentration of majority carrier at equilibrium ($\Delta n = \Delta p \ll p_o$) and Eq. (10) reduces to:

$$\tau_{\text{SRH}} \simeq \tau_{\text{no}}(1 + p_1/p_o). \tag{15}$$

For a midgap trap, $p_1 \ll p_o$ and Eq. (15) can further be simplified to [8]:

$$\begin{aligned} \tau_{\text{SRH}} &\simeq \tau_{\text{no}} \\ &= \frac{1}{\sigma_n \nu_{\text{th}} N_T}, \end{aligned} \tag{16}$$

which again shows that the SRH recombination lifetime is primarily a function of the active defect density in the bulk.

2.1.3 Understanding of carrier recombination at the structural defects

It is well known that the structural defects in mc-Si materials cause a decrease in the carrier lifetime. Carrier recombination at the structural defects is complex and can be understood through the illustration of energy band diagram. The band structure of impurity-decorated dislocation is shown in Fig. 9 [11], where E_{De} and E_{Dh} are the shallow dislocation bands, and E_M is the deep level trap induced by the presence of impurity. For clean dislocations, the recombination between E_{De} and E_{Dh} takes place through the direct channel of $R_{\text{De-Dh}}$. The decoration of dislocation by impurity, which has an energy level of E_M, gives rise to additional recombination channels, $R_{\text{C-M}}$, $R_{\text{V-M}}$, $R_{\text{De-M}}$, and $R_{\text{Dh-M}}$, and hence, enhances the carrier recombination activity. In general, impurities and structural defects are non-uniformly distributed over the mc-Si wafer. Therefore, the recombination activity of these

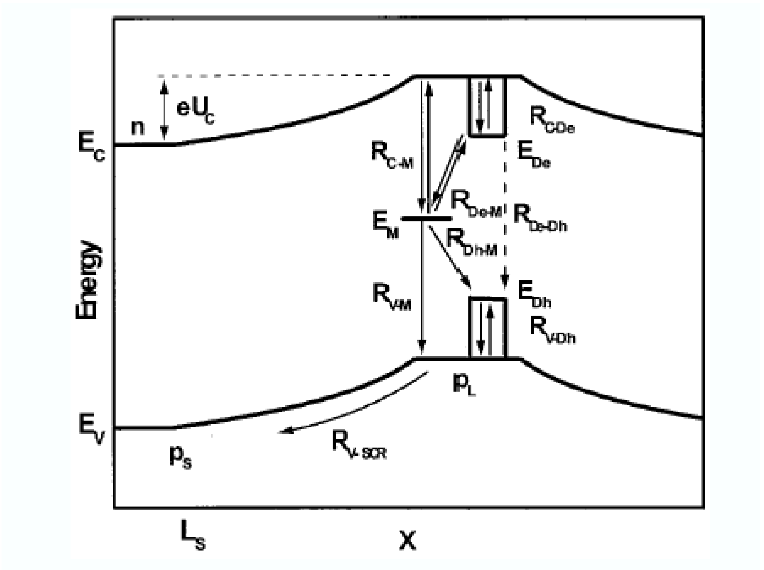

Figure 9: A schematic illustration of carrier recombination on dislocation.

defects varies significantly from one wafer to another and within a wafer depending on the distribution and concentration of impurities in the bulk. Once impurities are trapped at dislocation sites, it is difficult to remove them from the bulk using conventional gettering techniques. It has been reported in the literature [12] that many structural defects in ribbon Si materials become decorated with impurities during the crystal growth, which makes it very challenging to achieve high-efficiency cells on low-cost defective materials.

2.1.4 Carrier lifetime measurement techniques

High carrier lfetime is the key to achieving high-efficiency cells. There are many techniques to measure the carrier lifetime in Si [13]. The photoconductance tool (WCT-100) used in this study was developed by Sinton [14]. The illustration of lifetime measurement system is shown in Fig. 10. A flash lamp is used to generate excess carriers in the wafer and conductance, σ, is measured with the help of an rf bridge from which the carrier concentration can be estimated. An effective lifetime is them obtained from the slope of the decay curve.

The measured lifetimes are always effective lifetime (τ_{eff}), which is composed of bulk

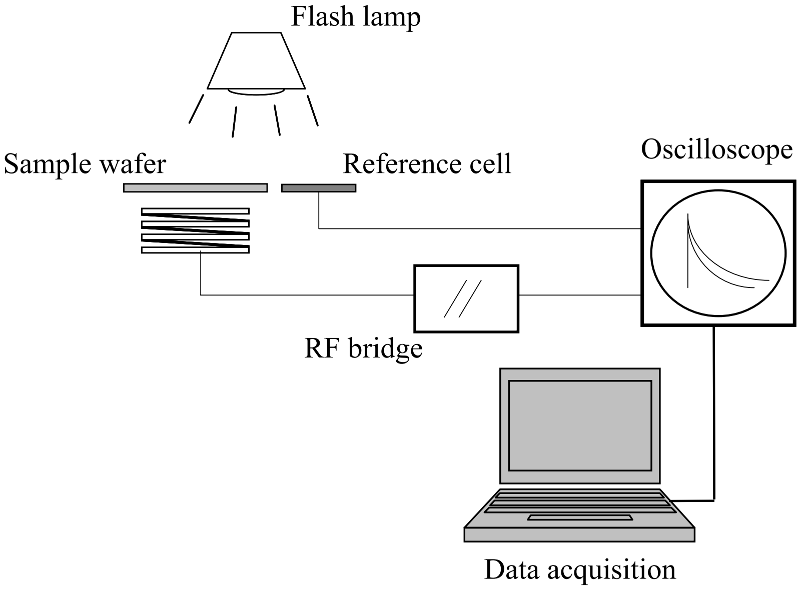

Figure 10: Configuration of the carrier lifetime measurement system (WCT-100) used in this study.

and surface recombination effects [13].

$$\begin{aligned}\frac{1}{\tau_{\text{eff}}} &= \frac{1}{\tau_b} + \frac{1}{\tau_s} \\ &\simeq \frac{1}{\tau_b} + \frac{2S}{W},\end{aligned} \tag{17}$$

where τ_b and τ_s are the bulk and surface recombination lifetime, respectively, S is the surface recombination velocity, and W is the substrate thickness. The τ_b approaches τ_{eff} when S is low. The S can be reduced to less than 10 cm/s on monocrystalline Si material using a I_2/methanol solution for surface passivation during the measurements [15].

The transient photoconductance decay (PCD) and quasi-steady-state photoconductance (QSSPC) measurements have been utilized in this study to extract the carrier lifetime in Si wafers. The effective carrier lifetime can be expressed as a generalized equation [16].

$$\begin{aligned}\tau_{\text{eff}} &= \frac{\Delta n}{U} \\ &= \frac{\Delta n}{G - R} \\ &= \frac{\Delta n}{G - \frac{d\Delta n}{dt}},\end{aligned} \tag{18}$$

where Δn is the excess carrier density, U is the net recombination rate, G is the carrier generation rate, R is the carrier recombination rate, and $d\Delta n/dt$ is the carrier recombination rate. There are two modes of measuring carrier lifetime. In mode 1, which is referred to as photoconductance decay (PCD), short pulses are applied to generate carriers and the decay of carrier concentration is measured in between the pulses. In mode 2, which is referred to quasi-steady-state photoconductance (QSSPC), pulse duration is large relative to decay sampling. Since there is no carrier generation between the light pulse during the transient PCD measurements when carriers recombine and photoconductance decreases (G=0), Eq. (18) can be written as:

$$\tau_{\mathrm{eff,PCD}} = -\frac{\Delta n}{\frac{d\Delta n}{dt}}. \tag{19}$$

In the quasi steady-state mode, when the pulse interval is larger than sampling interval, $d\Delta n/dt$=0, and hence Eq. (18) can be written as:

$$\tau_{\mathrm{eff,QSSPC}} = \frac{\Delta n}{G}. \tag{20}$$

The transient PCD mode is capable of measuring the carrier lifetime greater than 50 μs, while QSSPC set-up enables us to accurately measure the carrier lifetime less than 60 μs [17]. Since most of mc-Si materials have as-grown carrier lifetime less than 50 μs, the QSSPC technique has been employed extensively for carrier lifetime measurements in this research.

The QSSPC technique has been developed by Sinton and Cuevas [17] to determine the carrier lifetime from the steady-state photoconductance. Under the steady-state illumination, the rates of electron-hole pair generation and recombination are equal. The generation and recombination rates can be expressed as current densities, and total recombination within the wafer can be expressed in terms of an effective carrier lifetime [18]. In steady-state,

$$\begin{aligned} J_{\mathrm{ph}} &= J_{\mathrm{rec}} \\ &= \frac{q\Delta n W}{\tau_{\mathrm{eff}}}. \end{aligned} \tag{21}$$

Equation (21) assumes an uniform distribution of excess carriers (Δn) across the wafer. The increase in conductance due to the photogenerated excess carriers can be expressed as [18]:

$$\begin{aligned}\sigma_L &= q(\Delta n\mu_n + \Delta p\mu_p)W \\ &= q(\mu_n + \mu_p)\Delta n W,\end{aligned} \tag{22}$$

where σ_L is the increase in conductance, q is the electron charge, and μ_n and μ_p are the mobilities of electron and hole. Substituting Eq. (22) into Eq. (21) gives:

$$\tau_{\text{eff}} = \frac{\sigma_L}{J_{\text{ph}}(\mu_n + \mu_p)} \tag{23}$$

The J_{ph} can be expressed as [14]:

$$J_{\text{ph}} = J_{\text{ph,1 sun}} \cdot X \cdot T, \tag{24}$$

where $J_{\text{ph,1 sun}}$ is the photogenerated current density at one sun illumination (38 mA/cm^2, pre-set), X is the illumination intensity in suns, and T is the wafer transmission coefficient, which is typically 0.60–0.65 for bare Si wafer [19] because >35% of light is reflected from a bare Si wafer.

In this research, the processed cells are etched down to bare Si using a sequence of chemical solutions of 2:1:1 H_2O:H_2O_2:HCl for Al removal, 1:1 HNO_3:H_2O for Ag removal, 10:1 H_2O:HF for SiN_x removal, and 15:5:2 HNO_3:CH_3COOH:HF for P-doped n$^+$ emitter and Al-BSF removal. The bare Si wafers are then immersed into an I_2/methanol solution for surface passivation, which makes $\tau_{\text{eff}} \simeq \tau_b$ during the measurements. The recombination lifetime is determined at an injection level of 1.0×10^{15} cm^{-3} to avoid the effect of shallow traps on carrier lifetime [20].

The photoconductance tool used in this study offers a fast and an accurate extraction of carrier lifetime. However, the drawback of this measurement is that it can only measure an average lifetime over the region of ~10 cm^2 [21] because of the size of the rf coil used to sense the conductance. In addition, the sensitivity is not completely uniform across the active area of measurement [22]. Since the grain size of mc-Si materials is typically mm^2 to cm^2, it might be difficult to correlate the area-averaged carrier lifetime with cell performance [23]. Recently, microwave-detected photoconductance decay (μW-PCD) measurements have been utilized by some research institutes for characterization of mc-Si materials and cells (e.g. Fraunhofer ISE [24], ISFH [25], and University of Konstanz [26]). A potential advantage of using μW-PCD system is its ability to map the carrier lifetime over the active area with high resolution [27]. The mapping of carrier lifetime enables point-by-point comparisons of the carrier lifetime before and after impurity gettering and defect hydrogenation processes.

2.2 Crystal Growth Technologies of Promising Ribbon Silicon Materials

The cast mc-Si grown by heat exchanger method (HEM) is currently the most popular material for PV accounting for more than 55% of PV modules [28]. However, cast mc-Si technology requires ingot growth and slicing to obtain wafers. Ribbon Si growth technology reduces the material cost further by eliminating the slicing process. The ribbon Si materials are pulled directly from the Si melt, which is ideal for maximizing the use of Si. The use of ribbon Si as a substrate should help in decreasing the cost of PV modules because the growth technology is simpler, and equipment is less expensive compared to monocrystalline Si, such as FZ, Cz, and cast mc-Si materials.

While ribbon Si materials offer the advantages for cost reduction, they usually suffer from lower material quality and throughput. The single-furnace performance for ribbon Si growth is shown in Table 1 [29]. Most of the ribbon Si materials are multicrystalline, except for dendritic web, which is essentially monocrystalline with central twin plains. Ribbon Si experiences high thermal stress during the crystal growth. Therefore, it contains high density of structural defects, such as dislocations and twin boundaries, in addition to impurities, such as Fe and C. The material quality, including the dislocation density and some of the impurity concentrations, of the selected ribbon Si materials is shown in Table 2 [29].

The ribbon Si crystal growth techniques are reviewed in the following section. In addition, impurity gettering and defect hydrogenation techniques are introduced.

Table 1: Performance of ribbon Si growth technologies.

Method	Pull speed (cm/min)	Width (cm)	Throughput (cm^2/min)	Furnaces/ 100 MW
EFG octagon	1.65	8-12.5	165	100
String Ribbon	1-2	5-8	5-16	1175
RGS	600-1000	12.5	7500-12500	2-3
Dendritic web	1-2	5-8	5-16	2000

Table 2: Material quality of ribbon Si materials.

Material	Resistivity (Ωcm)	Carbon (cm^{-3})	Oxygen (cm^{-3})	Dislocation (cm^{-2})
EFG	2-4, p	10^{18}	$<5x10^{16}$	10^5-10^6
String Ribbon	1-3, p	$4x10^{17}$	$<5x10^{16}$	$5x10^5$
RGS	2, p	10^{18}	$2x10^{18}$	10^5-10^7
Dendritic web	5-30, n	N.D.	10^{18}	10^4-10^5

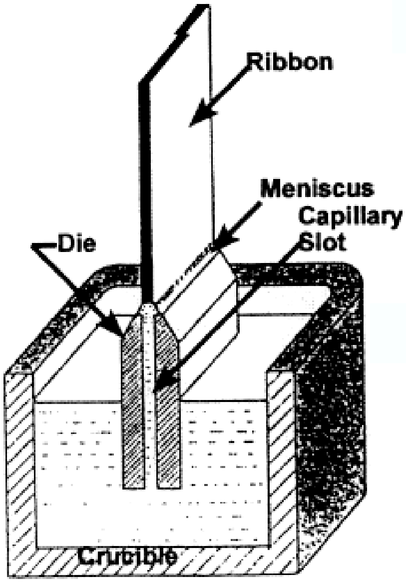

Figure 11: EFG Si ribbon growth: a schematic of EFG Si growth.

2.2.1 Edge-defined film-fed growth (EFG) Si

Edge-defined film-fed growth (EFG) Si is extensively used and studied in this research. The EFG ribbon Si technology was first introduced for sapphire growth using molybdenum dies by LaBelle in 1972 [30] and was first applied to Si ribbons using graphite shape-defining dies and later to silicon tubes in 1975 by Ciszek [31]. In this growth technique, liquid Si rises by capillarity up a narrow channel in the shaping die and spreads across the die's top surface, which defines the base of the meniscus from which the shaped crystal solidifies. The schematic of EFG Si growth is shown in Fig. 11. EFG is the first non-conventional crystal growth technique that was transferred to the large scale production in the PV industry. Octagonal tubes (Fig. 12) with 10.0−12.5 cm wide flat faces are now used for production of PV substrates [32]. Pulling rates are about 2.0 cm/min, but the 80 cm effective width increases the throughput up to 160 cm^2/min or ∼20 m^2/day, which is about 20 times higher than single ribbon pull technologies, such as Web and String Ribbon Si growth. A graphite crucible and a graphite shaping die are used with induction heating. After the growth, rectangular 10.0–12.5 cm wide wafers are cut by a Nd:YAG laser from the tube faces (Fig.

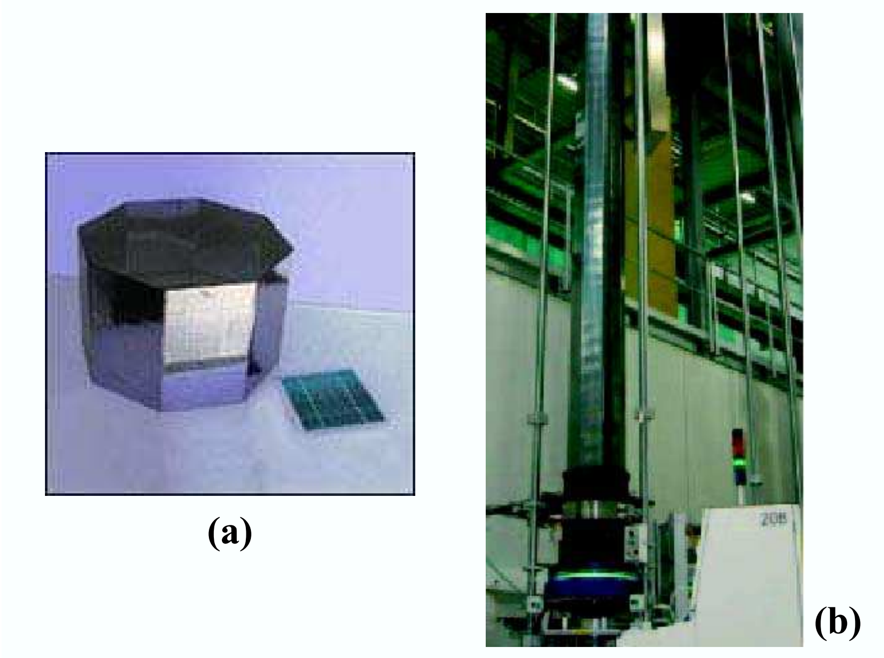

Figure 12: Pictures of EFG Si growth system: (a) octagonal EFG Si wafers and (b) EFG Si growth in production line.

12 [33, 34]). The EFG Si is not a monocrystalline material but is made of elongated grains and twins in the range of mm to cm wide and many cm long. Efficiencies of 18.2% [35] and 16.4% [36] have been reported recently by Georgia Tech and SCHOTT Solar on this material using laboratory and manufacturable cell process technologies, respectively. EFG Si cells are in full commercial production at SCHOTT Solar, Inc. with an annual production of >40 MW [37].

2.2.2 String Ribbon Si

String Ribbon Si is also extensively used in this research and represents a promising candidate for cost-effective PV. String Ribbon Si growth technique was introduced in 1980. This technique uses foreign filaments or strings to support the ribbon Si in betwee the dendrites. The growth takes place directly from a pool of molten Si without a die. The position of the edges is maintained by two strings fed through the bottom of the crucible, which pass through the melt to support the meniscus and the ribbon. The thickness of the ribbon is controlled by surface tension, heat loss from the ribbon, and the pull rate. The schematic of

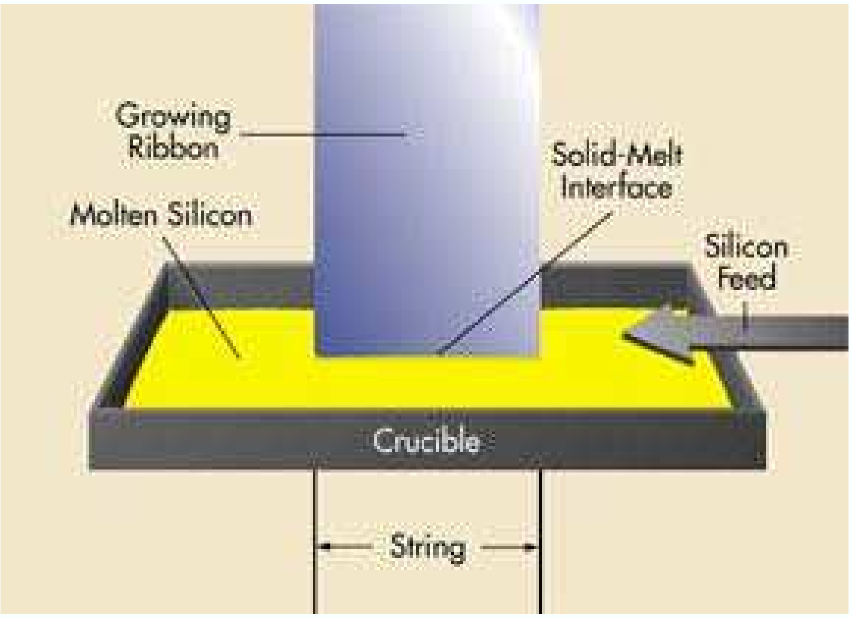

Figure 13: String Ribbon Si growth: a schematic of String Ribbon Si growth.

String Ribbon growth is shown in Fig. 13 [38]. String Ribbons have been grown as wide as 8 cm, with the standard commercial cell size of 8×15 cm^2 and ∼300 μm thick (Fig. 14 [38]). The ribbons are pulled at a rate of about 1−2 cm/min, giving a throughput of about ∼10 cm^2/min. Efficiencies of 17.9% [39] and 15.4% [40] have been reported recently by Georgia Tech and University of Konstanz on this material using laboratory and manufacturable cell process technologies, respectively. String Ribbon Si cells are currently in full commercial production at Evergreen Solar, Inc. with an annual production of >15 MW [41]. Evergreen Solar has recently developed a way to pull two ribbons simultaneously and is currently working on four ribbon growth technology to enhance the throughput.

2.2.3 Ribbon growth on substrate (RGS)

Ribbon growth on substrate (RGS) is another promising ribbon Si technology. however, RGS is not investigated in this research. In the RGS growth technique, the Si melt reservoir and die are placed in close proximity to the top surface of a substrate on which the ribbon is grown (Fig. 15 [42]). The principle is to have a large wedge-shaped crystallization front. The die contains the melt and acts to fix the width of the ribbon. The thickness

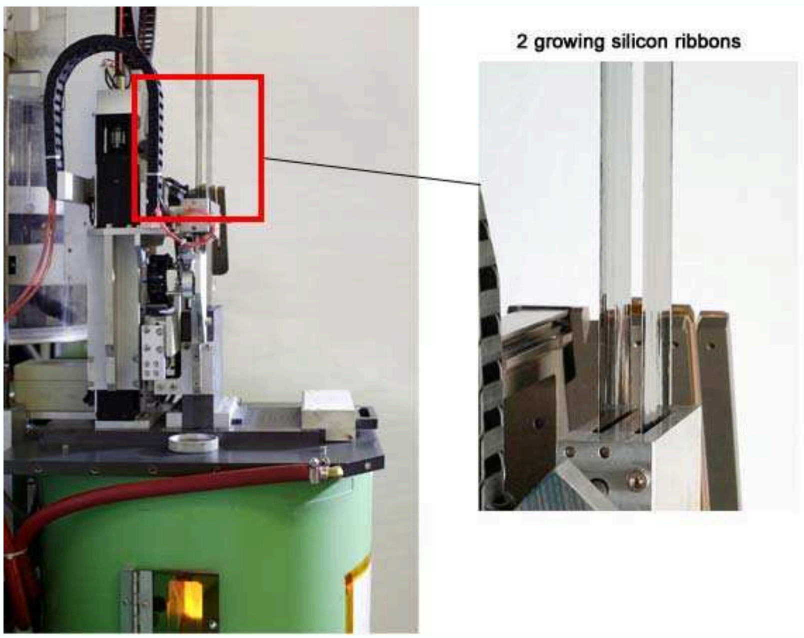

Figure 14: A picture of String Ribbon Si growth. Two ribbons are grown simultaneously.

of the ribbon is controlled by the shape of the die, pulling rate, and surface tension. The directions of crystallization and growth are nearly perpendicular, in contrast to dendritic web and String Ribbon, where they are parallel. The area of the growth interface is now very large compared to the ribbon thickness. Columnar grains penetrate the ribbon thickness. Impurity segregation across the thickness of the ribbon occurs. The grain size is comparable to the ribbon thickness. After cooling, the Si sheet is separated from the coated substrate [4]. The R&D on RGS solar cells has been conducted at ECN in The Netherlands and at University of Konstanz in Germany [43] and efficiencies as high as 12.3% (25 cm^2) have been reported using screen-printing technology [44].

2.2.4 Dendritic web Si

Dendritic web is one of the oldest ribbon Si technologies, which produces essentially monocrystalline ribbon Si. The dendritic web Si is grown directly from molten Si in a crucible without any shaping devices. Development of dendritic web was first initiated at Westinghouse in 1970s [45]. A seed is dipped into molten Si and spreads laterally to form a button. When the seed is withdrawn from the melt, two secondary dendrites propagate from the ends of

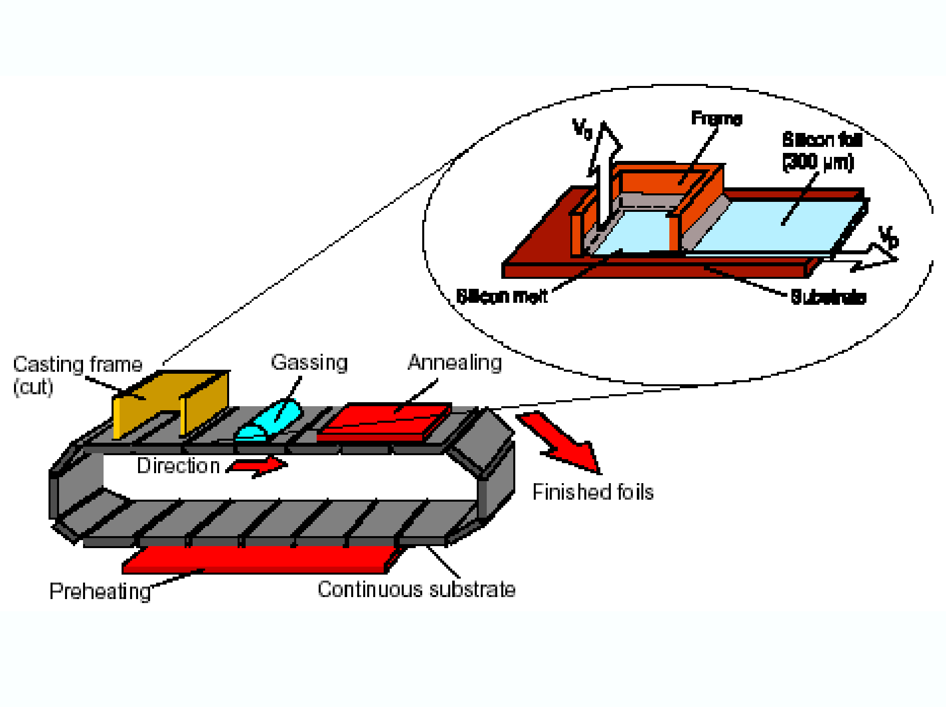

Figure 15: RGS Si ribbon growth: a schematic of RGS Si growth.

the button into the silicon melt, forming a frame to support the freezing ribbon. The width of the ribbon is controlled by the position of the two dendrites that support the liquid film, and typical growth rates are 1−3 cm/min [4]. A schematic of dendritic web growth system is shown in Fig. 16. Dendritic web typically has no grain boundaries, but it does have multiple twin boundaries running parallel to the external surfaces. An efficiency of 17.3% has been reported using a laboratory-scale process [46]. Dendritic web is also not used in this research.

2.3 *Impurity Gettering and Defect Passivation Techniques for Minority Carrier Recombination Lifetime Enhancement*

The as-grown mc-Si materials suffer from relatively low carrier lifetime because of impurities and defects. However, optimized cell processing can significantly enhance the carrier lifetime in finished devices. Fortunately, P diffusion for emitter formation and Al alloying on the rear for Al-BSF formation can getter or extract impurities from the bulk, and annealing

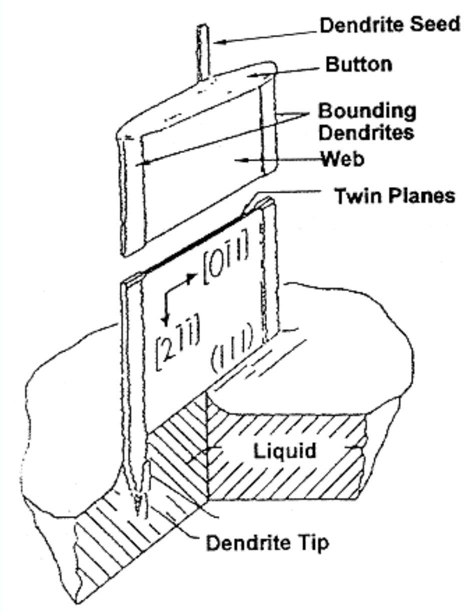

Figure 16: Dendritic web Si ribbon growth: a schematic of web Si growth.

of PECVD SiN_x can inject hydrogen to passivate defects. These techniques are critical for achieving high-efficiency ribbon Si cells and discussed in the following sections.

2.3.1 Phosphorus diffusion-induced impurity gettering

Transition metal impurities give rise to deep levels in silicon and can degrade the bulk lifetime if present in 10^{11}–10^{16} cm^{-3} range [47]. The P diffusion-induced impurity gettering technique has been studied extensively and implemented to improve the material quality by gettering the metal impurities [48, 49]. It has been shown in the literature that fast diffusers like Fe and Cr in the bulk are easier to getter than the slow diffusers like Ti and Mo [50]. In the crystalline Si solar cell fabrication process, the purpose of P diffusion is not only to form the n^+ emitter but also enhance simultaneously the minority carrier diffusion length by removing the impurities in the bulk Si by the well-known gettering effect called *kick-out* mechanism [51]. A gettering process, illustrated in Fig. 17 [52], involves three physical steps induced by heat treatment: (1) release of impurities from active region, (2) diffusion of impurities through the bulk, and (3) capture of impurities in the gettering site [52]. During the P diffusion, silicon interstitials are injected into bulk while kicking

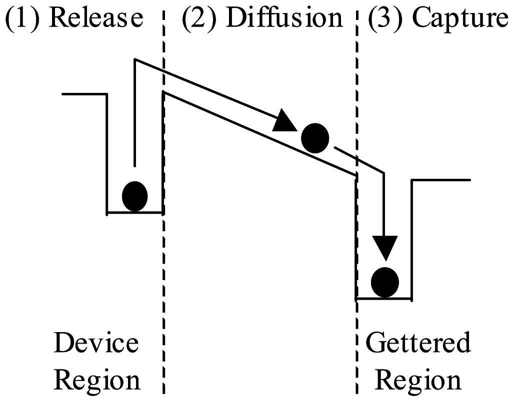

Figure 17: Concept of impurity gettering process.

out the substitutinal harmful impurities into the interstitial sites where they can move rapidly to the sink formed by misfit dislocations generated near the surface being diffused. Although the P diffusion gettering has been implemented successfully in PV industry, it has also been reported in the literature that the effectiveness of P diffusion gettering is quite poor in regions of high dislocation density [12, 53]. It was found in [12] that some low diffusion length regions in EFG Si are highly resistant to diffusion length improvement by P gettering. The experimental results in [12] suggested that some of the structural defects in EFG Si become decorated with precipitated metallic impurities during the crystal growth, and such clusters of precipitated metal impurities are highly stable and cannot be gettered by conventional techniques. There is a need to improve the understanding of the effect of defect clusters on mc-Si solar cells and develop technologies to mitigate their effect. In addition, it was reported in [53] that carrier lifetime in cast mc-Si wafers from bottom (low dislocation density) region of ingots improves significantly after gettering, as opposed to the wafers from the top region of ingot, which contains high dislocation density.

2.3.2 Aluminum alloying-induced impurity gettering

Annealing of Al layer on Si at high temperature (>577°C) can provide impurity getteing sites during the formation of Al-BSF. Al is usually deposited on the rear side of wafers by evaporation (laboratory-scale) or screen-printing (industry-scale) technique. Upon annealing of Al on Si, molten Al/Si layer is formed, which serves as sink for impurities because of much higher solubility of impurities in the molten Al/Si layer than solid Si [54]. A high segregation coefficient between the solid and the liquid layers provides the driving force for impurity gettering into the rear surface.

McHugo *et al.* [48] attempted to improve minority carrier diffusion length by annealing an evaporated Al layer (2.5 μm) on the rear surface of the mc-Si wafers at 800–950°C for 3 hours and found that the very low quality regions showed no appreciable response to gettering process. Joshi *et al.* [55] also made an effort to getter impurities by annealing of evaporated Al (1.0 μm) on commercial cast mc-Si materials. Carrier lifetime did improve, however, it was found that even after the Al gettering at 1100°C for 4 hours, there was a wide range of diffusion length distribution.

Screen-printed Al has been employed by manufacturers because it provides low-cost and high-throughput process compared to the evaporated Al. However, unlike the high purity Al used for the vacuum evaporation process, the screen-printable Al conductor paste contains impurities, such as Fe. Narasimha *et al.* [56] observed the degradation of cell performance when Al-BSF was formed at elevated temperatures (>850°C). This degradation was the result of injection of impurities from the screen-printed Al layer into the bulk Si, which degraded the carrier lifetime throughout the device.

2.3.3 PECVD SiN$_x$-induced defect hydrogenation

2.3.3.1 Hydrogen passivation of metallic impurities

Another technique that is known to enhance the carrier lifetime in defective Si is hydrogen passivation of defects. The advantages of defect hydrogenation are that it can be performed at low-temperature for a short time, which is consistent with the contact firing cycle. In this technique, hydrogen is incorporated during the PECVD SiN$_x$ deposition, which is done to form the anti-reflection coating. PECVD SiN$_x$ film undergoes rapid thermal treatment during the firing of screen-printed contacts. Upon firing, hydrogen atoms are released from SiN$_x$ film and diffuses into the bulk Si and interacts with metallic impurities and structural defects. The interaction of hydrogen with transition metal impurities has been extensively studied by many researchers. It is well known that exposure of Si to a source of atomic hydrogen leads to the passivation of both acceptor [57] and donor [58] impurities. Deep-level transient spectroscopy (DLTS) has been used to identify hydrogen passivation of deep-level impurities in monocrystalline Si [59]. There are two proposed mechanisms for the hydrogen passivation of acceptors. One was qualitatively proposed by Sah et al. [57], which involves the compensation of the acceptor by the donor state introduced by hydrogen in p-type Si. The mobile H^+ is attracted to the negatively charged acceptor ion, where it becomes covalently bonded forming a neutral acceptor-hydrogen complex. The other mechanism was suggested based on observation of IR spectra of hydrogenated p-type Si samples [60], which showed silicon-hydrogen vibrational absorption band at $\sim$1870 cm^{-1}. The proposed mechanism in [60] involves atomic hydrogen tied to one of the four Si atoms surrounding the substitutional B atom, leaving all the valence bonds satisfied. The hydrogen atom is inserted between the B atom and one of its four Si atom neighbors, forming a bond to the Si atom (Si-H). The B atom then relaxes toward the plane of its three Si neighbors. The hydrogen passivation of n-type dopants in Si was first demonstrated by Johnson et al. [61], who showed that the sheet carrier density decreased for thin n-type layers were exposed to a hydrogen plasma at 150°C while the carrier mobility increased. One suggested mechanism involves compensation of the donor ions by the deep acceptor state introduced by hydrogen (H^-) in n-type Si. The H^- is attracted to the positively charged donor (D^+), where it becomes covalently bonded, forming a neutral donor-hydrogen complex. Bergman et al. [62], based on observation of IR absorption bands, suggested that hydrogen is bonded to Si rather than to the donor directly.

It has been demonstrated that substitutional Pt in Si behaves as a model impurity to study the hydrogen passivation because H-Pt complex is thermally stable, and H-Pt bonds in Si are readily identified by IR vibrations [63]. Recently, Stavola et al. [64, 65] combined IR spectroscopy with introduction of Pt as trace impurities to trap and detect hydrogen in Si to determine the concentration and depth of hydrogen introduced into Si during the firing of SiN_x film. In [64], hydrogen incorporation into Si by post-deposition anneal of a

SiN_x film was investigated for different deposition technologies [PECVD and hot-wire CVD (HWCVD)] and annealing treatments [rapid thermal processing (RTP) and tube furnace]. The results in [64] indicated that HWCVD provided the most effective hydrogenation of Pt impurities in Si. The SiN_x film deposited in a low-frequency (50 kHz) PECVD reactor at 425°C was also effective in introducing hydrogen into Si. On the other hand, the SiN_x film deposited in high-frequency (13.56 MHz) PECVD reactor at 300°C introduced significantly less hydrogen into Si than the films deposited in HWCVD or low-frequency PECVD reactors. This is consistent with the results of carrier recombination lifetime measurements reported in [66], which showed that the area-average lifetime of processed String Ribbon Si wafers increased from 5–6 μs to 106 μs by the post-deposition anneal of low-frequency PECVD SiN_x, as opposed to only 29 μs for high-frequency PECVD SiN_x. In addition, RTP was found to be more effective than furnace anneal for hydrogen injection. This demonstrates that PECVD SiN_x is an effective source of hydrogen and an appropriate post-deposition anneal can be very effective in passivating lifetime-limiting defects.

2.3.3.2 Hydrogen passivation of structural defects

It is well known that the structural defects such as dislocations and grain boundaries in mc-Si act as recombination centers for carriers, causing lifetime degradation in mc-Si materials. It has been shown that the dangling bonds in grain boundaries can be passivated by deuterium diffusion [67] and plasma hydrogenation [68,69], where the density of dangling bonds at grain boundary in polycrystalline Si film was significantly reduced by hydrogenation. Johnson et al. [67] found that a factor of approximately 103 more deuterium should be incorporated in the polycrystalline Si film than the density of dangling bonds for effective passivation. In [69], the hydrogen passivation depth along the grain boundary in EFG Si was reported using plasma hydrogenation process, which showed that surface recombination velocity S of the grain boundary tends to decrease as the depth of hydrogen diffusion increases. The EBIC micrographs revealed that the passivation depth was in the range of $5-200$ μm.

Even though there is sufficient evidence in the literature that atomic hydrogen provides a passivation of electrically active impurities and structural defects, there is limited information about how to utilize its potential for maximizing defect hydrogenation, especially during the cell fabrication process without introducing additional processing steps. Most mc-Si materials should benefit from hydrogenation because they contain significant number of lifetime-limiting defects that become electrically inactive by interacting with hydrogen.

2.3.3.3 Diffusion of hydrogen in crystalline Si

For hydrogen to fully passivate the defects in crystalline Si, it needs to diffuse through the entire bulk. The diffusion coefficient of an impurity in a semiconductor follows Arrhenius behavior, $D = D_o \exp(-E_a/kT)$, where E_a is the activation energy, and the prefactor D_o includes entropy effects. The motion of hydrogen in semiconductors is known to be influenced by interactions with impurities. The most straightforward situation occurs at high temperatures (T>1000K), where hydrogen diffuses as an isolated particle (i.e., atomic hydrogen in either neutral or positively charged state). The first determination of the hydrogen diffusion coefficient in Si was performed by Van Wieringen and Warmoltz [70], who obtained the following relationship in the temperature range of 1090–1200°C:

$$D_H = 9.4 \times 10^{-3} \exp\left(\frac{-0.48 \text{ eV}}{kT}\right) \tag{25}$$

Extrapolation of the above equation gives D_H of $\sim 10^{-6}$ cm^2/s at 350°C. However, other researchers reported much lower values at the similar temperatures. Figure 18 shows the selected data of hydrogen diffusivity in crystalline Si [71–73]. The huge difference in diffusion coefficient values at low temperatures (350–400°C) from Eq. (25) and the experimental results (Fig. 18) suggests that diffusion of hydrogen at low temperatures may be hindered by some physical effects, which are not taken into account in Eq. (25). The diffusion of hydrogen in multicrystalline Si is more complex than that in monocrystalline Si because of the interaction of defects with hydrogen. The experimental results described above are based primarily on monocrystalline Si. Sopori *et al.* [74] have reported the observation of a higher bulk diffusivity of hydrogen in cast multicrystalline and silicon sheet. The hydrogenation was performed with a low-energy Kaufman ion source in an energy range of

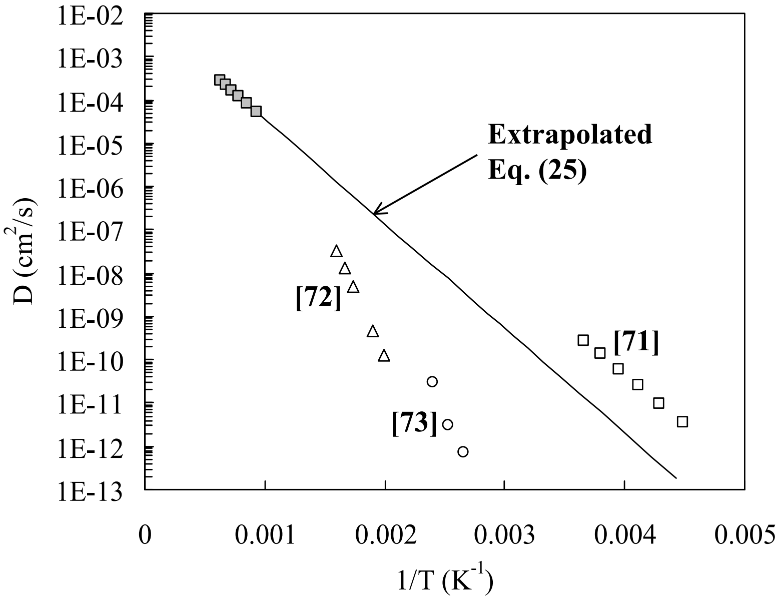

Figure 18: Selected data of hydrogen diffusivity in Si.

500–2000 eV. The implanted samples were analyzed by cross-sectional transmission electron microscopy, secondary ion mass spectroscopy (SIMS), electron beam-induced current (EBIC), and infrared (IR) spectroscopy, and hydrogen diffusivity was expressed as:

$$D = 1.0 \times 10^{-4} \exp\left(\frac{-\Phi}{kT}\right), \tag{26}$$

where Φ_{FZ}=0.56 eV, Φ_{Cz}=0.58 eV, and Φ_{multi}=0.50 eV. It was suggested in [74] that the diffusivity of hydrogen in Si depends on the processes that the wafer has undergone prior to hydrogenation. Thus, diffusion and migration of hydrogen in defective Si is still not fully understood and could be material or process dependent.

2.3.4 Rapid thermal processing for solar cell fabrication and defect hydrogenation

Most PV manufacturers have been employing the conventional belt furnace for contact firing because of its high-throughput. However, an RTP system is an attractive tool for solar cell fabrication because it allows excellent control of temperature ramp-up and cooling rates as well as peak-holding interval. RTP systems have been used successfully in the laboratory for many crystalline Si solar cell fabrication steps, such as oxidation for surface passivation [75], diffusion for shallow emitter formation [76], and firing for screen-printed contacts [77, 78]. In this research, an RTP system is used extensively for screen-printed contact firing. This section provides an overview of the RTP along with the motivation for applying it to low-cost Si solar cells.

The crystalline Si wafers are subjected to many high-temperature treatments during the fabrication of microelectronic devices or integrated circuits (ICs). The high-temperature processing is mostly done by a conventional furnace process (CFP), where the Si wafers are heated and cooled down slowly. In PV industry, the belt furnace is frequently employed for diffusion and contact firing process to increase the throughput.

The motivation for using RTP is that most low-cost defective materials used for PV applications show lifetime degradation upon prolonged exposure to high temperatures (>950°C). The RTP offers several advantages over CFP. CFP involves separate and lengthy furnace diffusions and oxidations at high temperatures. This requires extensive wafer cleaning, prolongs cell processing, uses more chemicals and gases, and consumes a large thermal budget (i.e. greater power consumption). RTP allows fast ramp-up and cooling rates, which reduce the cell processing time. In addition, high-energy photons can accelerate semiconductor processing. All these advantages translate into reduced cell processing cost. Lower thermal budget may prevent defect interactions that often reduce bulk lifetime in low-cost defective materials. The challenge is to incorporate these advantages of RTP into an optimized process sequence that leads to cost reduction without sacrificing cell efficiency.

Even though investigators have been trying to use RTP for solar cell fabrication, not much attention has been focused on exploiting the use of RTP for maximizing defect hydrogenation in mc-Si solar cells. Shorter process times along with rapid ramp-up and cooling rates may enhance the retention of hydrogen at defects to improve defect passivation and reduce the interaction between screen-printed pastes and defects to reduce the possibility of junction shunting, which can lead to lower fill factor and performance of solar cells. This provided the motivation in this research to investigate and optimize the rapid thermal firing, which in a single short step can enhance PECVD SiN_x-induced defect hydrogenation, improve contact quality, and provide high-quality uniform Al-BSF to produce high-efficiency ribbon Si solar cells.

CHAPTER III

HISTORY, PROGRESS, AND CURRENT STATUS OF PROMISING PV TECHNOLOGIES

Besides crystalline Si, several other promising PV technologies are being investigated over the years, such as thin-film cells, III-V-based compound semiconductor cells, dye-sensitized cells, and organic/polymer cells. Currently, crystalline Si accounts for more than 90% of the PV module shipment [1]. Thin-film semiconductors, such as a-Si, CdTe, and CI(G)S, have about 6–7% of the market share. The concentrator cells using III-V materials accounts only for ∼0.04%, and dye-sensitized and organic cells have negligible market share at this time.

The multijunction solar cells based on III-V compound semiconductors are fabricated by depositing multiple thin films using Molecular Beam Epitaxy or Metal-Oxide Chemical Vapor Deposition technique for space [79] and concentrator [80] applications. Recently, Spectrolab achieved 40.7% efficient GaInP/Ga(In)As/Ge multijunction concentrator cell under an illumination of 240 suns. In spite of its high efficiency, the III-V compound solar cells are the most expensive cells on a per-unit-area basis because of the cost of materials and processing.

The dye-sensitized solar cells have a simple structure that consists of two electrodes and an iodide-containing electrolyte. One electrode is composed of dye-coated highly porous nanocrystalline titanium dioxide deposited onto a transparent conducting substrate. The other electrode is a transparent conducting substrate or a tin oxide coated glass. An efficiency of 10.6% has been reported (cell area: 0.16 cm^2) from Swiss Federal Institute of Technology [81]. However, the stability issue still remains [82]. Significant R&D activities are going on in companies, such as Konarka Technologies, Inc. [83] and Peccell Technologies, Inc. [84], to commercialize this technology.

Organic solar cells are fabricated in the form of thin films (typically 100 nm) of organic semiconductors, such as polymers or small-molecule compounds (e.g. polyphenylene vinylene, copper phthalocyanine and carbon fullerenes). Cell efficiencies are typically in the range of 1–5%. However, like dye-sensitized solar cells, organic solar cells also suffer from a performance degradation over time due to the exposure to oxygen, humidity, and temperature [85]. The organic solar cells are still in R&D phase awaiting commercialization [86].

Thin-film technologies, including amorphous Si, polycrystalline CdTe, and $CuInGaSe_2$, are among the promising candidates because they have the potential of reducing the material and manufacturing cost. The absorbing material is only 1–3 μm thick and the cell technology provides the opportunity for monolithic integration. These technologies currently have issues with efficiency, reliability, and scalability. The efficiencies are generally less than 10% and production capacities are below 100 MW.

Crystalline Si provides an intermediate path between the high-cost, high-performance multijunction cells and low-cost, low-performance thin-film cells. Crystalline Si materials offer stable and high-efficiency PV modules using established processing technologies. However, Si materials grown by ingot methods requires a slicing to obtain wafers. In the case of cast mc-Si wafers, which currently dominates the material for producing PV modules, more than 65% of Si is lost as a form of kerf loss during the wafer slicing and subsequent deep chemical surface etching processes [87]. This makes the wafer cost high. Further cost reduction is possible by reducing the material cost. The ribbon Si materials, which are the focus of this study, offer an unique opportunity to reduce the material cost by eliminating the wafer slicing process because ribbon Si can be grown directly from the Si melt, as discussed in Chap. II. In addition, thin (<200 μm) ribbon growth is possible and makes it attractive to cost-effective PV material.

In this chapter, history, progress, and current status of commercialized crystalline Si PV technologies are discussed.

3.1 History and Progress of High-Efficiency Crystalline Si Solar Cells

The crystalline Si solar cell was first invented at Bell Laboratories in 1954 by Chapin, Fuller, and Pearson [88]. The $p - n$ junction cell is shown in Fig. 19(a) in which the thin layer of p-type (B-doped) Si was formed over an n-type monocrystalline Si. The efficiency of this device was about 6.0%.

A significant improvement in cell efficiency was achieved in 1972 at COMSAT Laboratories by applying the grid contacts on the front of the cells using photolithography technique [89, 90]. This allowed much shallower diffused layers for junction formation, reducing the effect of dead layers and increasing the short-wavelength response. The improved solar cell was called “Violet Cell”, and efficiency was reported to be about 14% [89]. In 1974, COMSAT Laboratories announced another improvement on cell performance by employing the surface texturing technique and back surface field formation [91]. The random pyramid texturing was developed in microelectronics and applied to cell fabrication by COMSAT Laboratories, helping in the reduction of reflection loss. The back surface field was developed at NASA Lewis Research Center [92] by driving impurities, such as Al or B, into the backside of a p-type wafer. The resulting impurity concentration gradient or step ($p - p^+$) repelled the electrons generated in the base region towards the front junction, improving the long-wavelength response. The solar cell, shown in Fig. 19(b), was called “Black Cell”, and efficiency was reported to be about 17% [90].

In 1984 and 1986, University of New South Wales (UNSW) achieved 19.1% and 20.9% efficient cells, known as passivated emitter solar cell (PESC), on planar and microgrooved FZ Si wafers, respectively [93, 94]. The PESC technology involved the P diffusion for emitter formation at 800–950°C, thin (10 nm) passivating thermal oxide growth at 800–850°C, photolithography-defined front grid contacts, Ti/Pd evaporation, Ag plating, and ZnS/MgF_2 double-layer antireflection (DLAR) coating. The microgrooved surface texturing, shown in Fig. 19(c), was formed by NaOH anisotropic etching using photolithography and masking oxide growth.

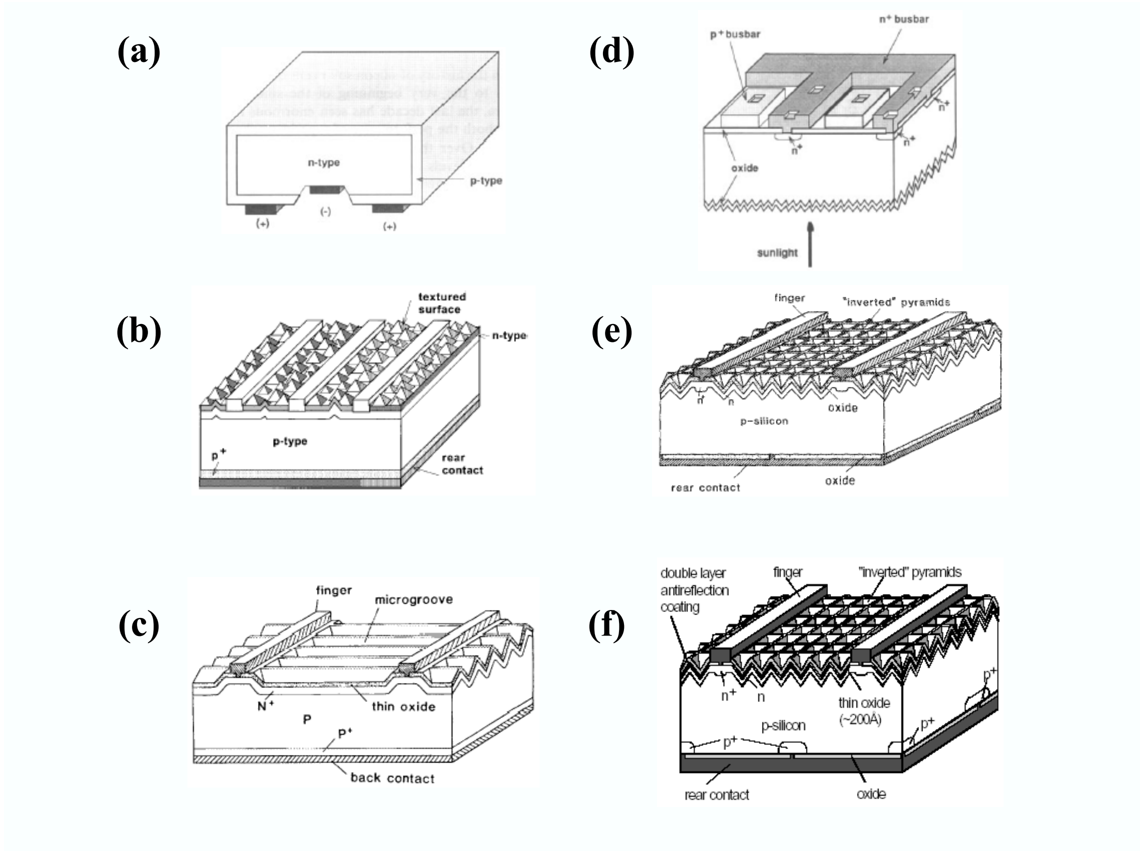

Figure 19: Schematics and evolution of high-efficiency monocrystalline Si solar cells: (a) First modern crystalline Si cell, (b) Black Cell, (c) PESC, (d) Back-Contact Cell (e) PERC, and (f) PERL Cell.

The next major achievement was announced by Stanford University in 1988, first successful implementation of point-contact formation [95, 96]. The device structure is shown in Fig. 19(d). In this design, the effect of shading loss associated with grid contact formation can be eliminated since the metal contacts are placed on the rear side of the cell. However, the performance of the rear contact cells depends strongly on the quality of the base material and surface passivation, because the photo-generated carriers have to travel a long distance from the point of generation near the illuminated surface. King et al. [95, 96] achieved an efficiency of 22.3% using thermal oxide for surface passivation and lightly doped (100 Ωcm) monocrystalline FZ Si (n-type) substrate. The rear point-contact cells have been commercialized by SunPower Corporation.

In 1989, UNSW reported a passivated emitter and rear cell (PERC) with an efficiency of 22.8% [97] on 0.2 Ωcm monocrystalline FZ Si materials. The schematic of PERC cell is shown in Fig. 19(e). In this design, an inverted pyramid texturing technique was employed to reduce the reflection loss from the front surface. The front and rear passivation layers were formed by thermally grown oxide. The passivating and masking oxides for inverted pyramid texturing formation were grown in an O_2 with 2% trichloroethane ambient at 1000°C. The use of chlorine-based processing is to maintain high minority carrier lifetime during the cell processing and to improve the passivation quality. The rear Al layer, in conjunction with thermally grown oxide, acts as an effective reflector.

The highest conversion efficiency confirmed to date has been achieved by the passivated emitter, rear locally diffused (PERL) cell, shown in Fig. 19(f) [98]. The difference between PERC and PERL designs is the presence of the locally diffused regions on the rear side. These locally diffused regions enable good electrical contacts to base regions and reduce surface recombination velocity. This structure has resulted in 24.7% PERL cell on higher resistivity (1.0 Ωcm) FZ Si materials.

3.2 History and Progress of High-Efficiency Solar Cells on Low-Cost mc-Si Materials

Since Si substrate accounts for ~45% cost of a PV module, an extensive research is being conducted on low-cost Si materials, such as cast mc-Si and ribbon Si, which tend to be multicrystalline in nature and contain higher concentration of metallic impurities and structural defects.

In 1996, Georgia Tech reported 1.0 cm^2 18.6% cell on 0.65 Ωcm cast mc-Si material [99]. Cell fabrication process involved a 900°C/30 min P gettering diffusion followed by a second high-temperature step, which produced an excellent SiO_2 emitter surface passivation and an Al-BSF. Defect hydrogenation process was performed by a forming gas anneal at 400°C. Front grid contacts were formed by a combination of lift-off photolithography, metal evaporation, and electroplating.

In 1998, 1.0 cm^2 19.8% mc-Si solar cell was reported by UNSW [100] using the well-known PERL-type processing [98] and honeycomb surface texturing technique, shown in Fig. 20(a). The 1.5 Ωcm, 260 μm thick mc-Si substrate was provided by Eurosolare. Photolithography was used to form the honeycomb textured surface. An acid solution (HNO_3:HF = 50:1) was used to isotropically etch into the substrate to form hemispherical wells. After the surface texturing, a standard PERL-cell process (described in previous section) with a double-layer (ZnS/MgF_2) AR coating was implemented to complete the cell fabrication.

In 2004, Fraunhofer ISE announced the highest efficiency 1.0 cm^2 solar cell with an efficiency of 20.3% on 0.6 Ωcm, 99 μm thick cast mc-Si material provided by Kawasaki Steel [101]. The device structure of this 20.3% mc-Si cell is shown in Fig. 20(b). The fabrication process involved plasma surface texturing, 3.5 hours rear surface wet oxidation, photolithography-defined front grid contacts, thin thermal oxide for front surface passivation, laser-fired rear point contacts, and a double-layer (TiO_2/MgF_2) antireflection (DLAR) coating. The unique feature of this device is the formation of local BSF and point-contacts using a laser.

Significant progress in ribbon Si cell efficiencies has also been reported by many research

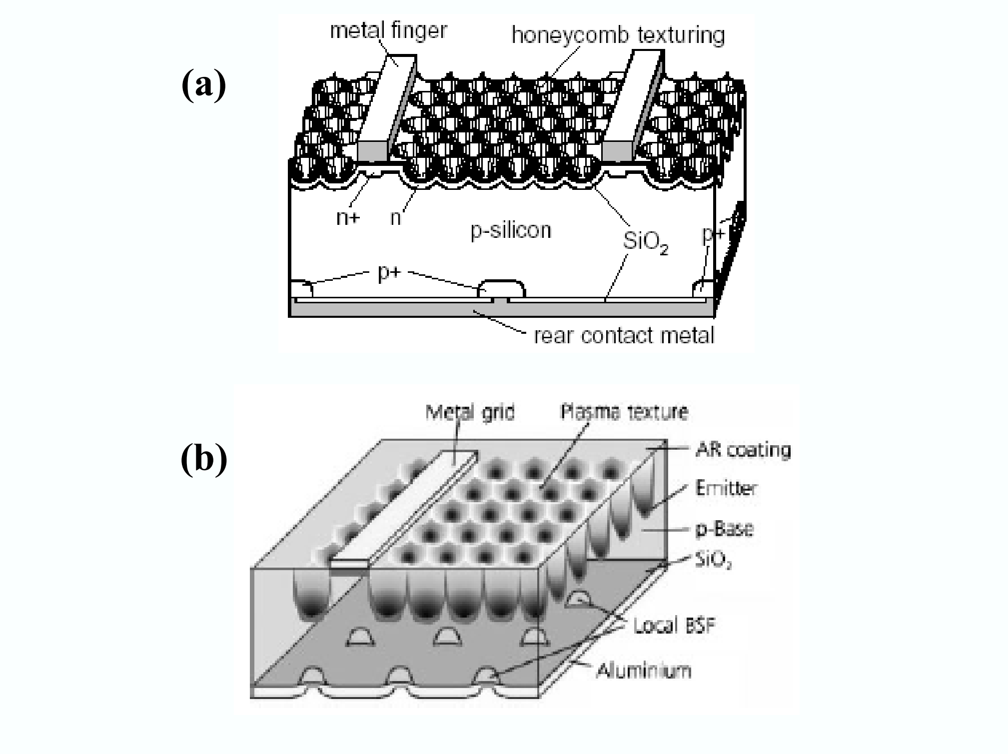

Figure 20: High-efficiency laboratory-scale mc-Si solar cells: (a) UNSW honeycomb textured PERL-type cell and (b) Fraunhofer ISE 20.3% cell.

groups. In 1994, Sana *et al.* [102] reported 14.1% 1.0 cm^2 EFG Si cell using laboratory-scale processing. The fabrication process involved impurity gettering by annealing of evaporated Al, thermal oxide for emitter surface passivation, lift-off photolithography front grid contacts, a forming gas anneal at 400°C for 3.5 h for defect hydrogenation, and ZnS/MgF$_2$ DLAR coating.

In 2003, Hahn and Geiger [103] reported 16.7% (EFG) and 17.7% (String Ribbon) 4.0 cm^2 ribbon Si cells using laboratory-scale processing. The fabrication process involved an Al-gettering step at 800°C for 30 min, a POCl$_3$ diffusion for n$^+$ emitter formation, thermal oxidation for emitter surface passivation, firing of screen-printed Al for Al-BSF formation, photolithography-defined front grid contacts, Al evaporation for rear contact, microwave-induced remote hydrogen plasma defect passivation at 320°C for 60 min, and deposition of ZnS/MgF$_2$ DLAR coating.

The highest ribbon mc-Si solar cell efficiencies of 18.2% on EFG Si and 17.9% on String Ribbon Si (both 4.0 cm^2) have been reported by Georgia Institute of Technology [35, 39]. The fabrication process involved photolithography-defined front grid contacts, rapid thermal processing of SiN$_x$-induced defect hydrogenation and Al-BSF formation, and SiN$_x$/MgF$_2$ DLAR coating. These high-efficiency cells have clearly demonstrated the potential of low-cost Si materials. However, the expensive and time-consuming processes to realize the advanced cell designs, such as thermal oxide surface passivation, photolithography-defined contacts with metal evaporation, and elaborate surface texturing for effective light trapping, make them non-manufacturable. Table 3 [35, 39, 46, 99–105] summarizes the efficiency progress along with the key process technologies used in achieving high-efficiency laboratory-scale mc-Si cells.

3.3 Industry-Scale Large-Area Solar Cells

Production-scale cells fabricated with manufacturable processing technologies have also made a significant progress in recent years.

Table 3: Progress of laboratory-scale mc-Si solar cell performance. All efficiencies were confirmed independently.

Year	Institute	Size (cm^2)	Material	Efficiency (%)	Process	Ref.
1996	GIT	1	Cast	18.2	$POCl_3$, Al-BSF, FGA, ZnS/MgF_2 DLAR	104
1997	GIT	1	Cast	18.6	$POCl_3$, Al-BSF, FGA, ZnS/MgF_2 DLAR	99
1998	UNSW	1	Cast	19.8	honeycomb texturing, thermal oxide, rear locally B diffused BSF, ZnS/MgF_2 DLAR	100
2004	Fraunhofer ISE	1	Cast	20.3	Plasma texturing, 3.5 h wet oxidation, rear laser-fired contact, front thermal oxide, TiO_2/MgF_2 DLAR	101
1997	GIT	4	Web (n)	17.3	B emitter P BSF in RTP, thermal oxide, ZnS/MgF_2 DLAR	46
1994	GIT	1	EFG	14.1	$POCl_3$, Evaporated Al, FGA	102
2003	UKN	4	EFG	16.7	$POCl_3$, Thermal oxide, ZnS/MgF_2 DLAR	103
2004	GIT	4	EFG	18.2	$POCl_3$, RTP Al-BSF, SiN_x/MgF_2 DLAR	35
2001	Evergreen	4	SR	16.2	Lab Process	105
2003	UKN	4	SR	17.7	$POCl_3$, Thermal oxide, ZnS/MgF_2 DLAR	103
2004	GIT	4	SR	17.8	$POCl_3$, RTP Al-BSF, SiN_x/MgF_2 DLAR	35
2004	GIT	4	SR	17.9	$POCl_3$, RTP Al-BSF, SiN_x/MgF_2 DLAR	39

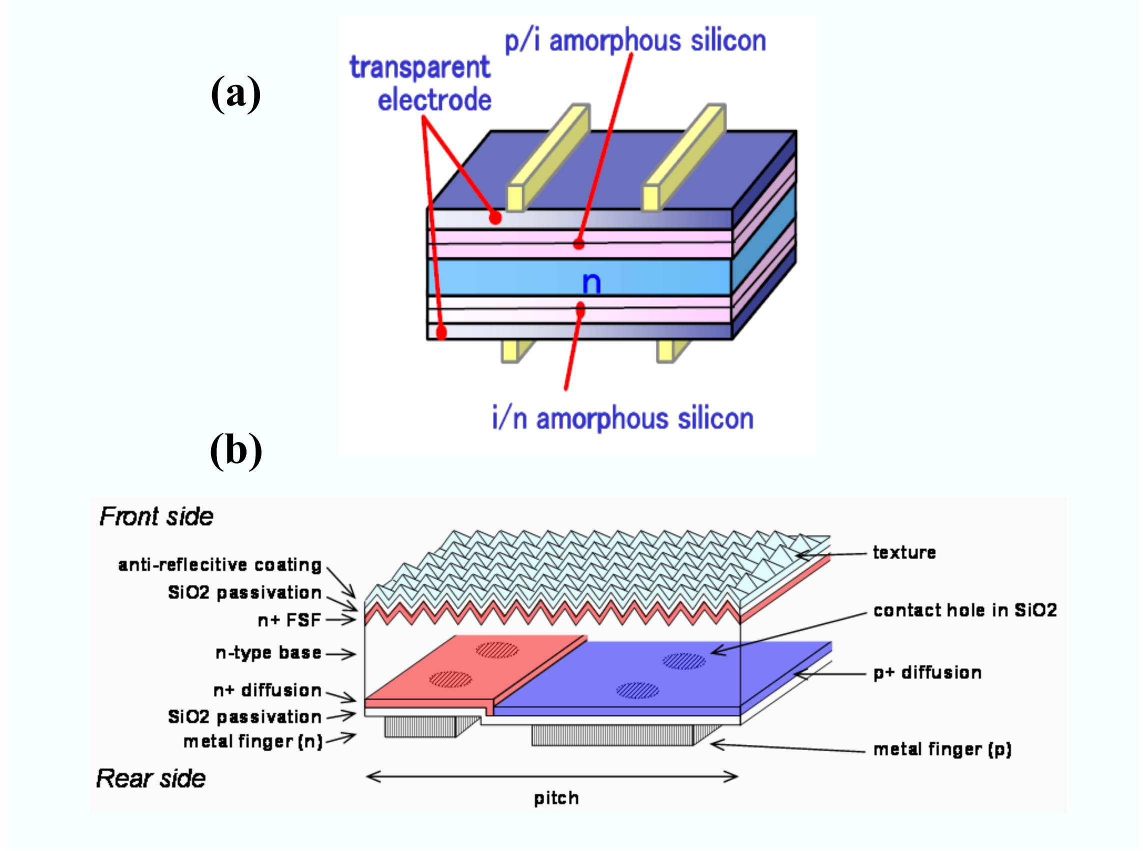

Figure 21: Schematics of high-efficiency industry-scale monocrystalline Si solar cells: (a) Sanyo HIT cell and (b) SunPower back-contact cell

Sanyo Electric achieved high-efficiency cells using hetero-junction with intrinsic thin-layer (HIT) technology, which features a very thin intrinsic amorphous Si (a-Si) layer inserted between p-type a-Si and n-type crystalline Si. The novel HIT cell structure, shown in Fig. 21(a) [106], is attractive because (i) intrinsic a-Si layer provides an excellent surface passivation and high-quality $p-n$ junction formation, (ii) low-temperature processes (<200°C) prevents any thermal degradation of material quality, and (iii) lower temperature coefficient for efficiency degradation ($-0.25\%/^{\circ}$C for HIT as opposed to $-0.45\%/^{\circ}$C for conventional cells [106]) increases the energy production. Sanyo has achieved HIT cells (100 cm^2) with an efficiency of 21.5% (confirmed by AIST) in the laboratory and 19.5% on the production line. The annual production of HIT cells/modules was about 155 MW in 2006 [107].

SunPower Corp. is commercializing novel high-efficiency back-contact cells [108]. In back-contact cell design, interdigitated n^+ and p^+ diffused regions as well as grid lines are located on the rear-side of the wafers, as shown in Fig. 21(b). Key design features that contribute to high-efficiency include localized back contacts, which reduce contact recombination losses, zero contact shading, which permits an optimization of light trapping and passivation, and a backside metallization, which provides better internal reflection from the backside and low series resistance. SunPower Corp. has achieved 21.5% (confirmed by NREL) cell on a 1.0 MW/yr pilot line [108]. The annual production of SunPower's back-contact cells was about 63 MW in 2006 [107].

In 2004, Kyocera Corp. reported 17.7% (confirmed by JET) production-scale cast mc-Si solar cells on 255 cm^2, 1.5 Ωcm resistivity, and 280 μm thick substrate, as shown in Fig. 22(a) [109]. The process sequence involved reactive ion etching for front surface texturing, $POCl_3$ n^+ emitter formation (90 Ω/sq), PECVD SiN_x deposition, screen-printed metallization, and full-area Al-BSF and Ag grid contacts formation in a beltline furnace. The average efficiency was 17.4%. Kyocera's annual production was about 180 MW in 2006 [107].

In 2006, University of Konstanz reported 18.1% (confirmed by Fraunhofer ISE) large-area (138 cm^2) cast mc-Si cell using mechanical V-texturing, LPCVD SiN_x deposition, buried front contacts by mechanical grooving, electroless plating of Ni and Cu, Al screen-printing for Al-BSF formation, and Al evaporation for rear contact formation [110]. The device structure is shown in Fig. 22(b).

ECN reported 17% mc-Si solar cells on 156 cm^2, 1.5 Ωcm resistivity, and 270 μm thick materials using all in-line process [111]. IMEC reported 16.1% mc-Si cells on 156 cm^2, 1.5 Ωcm resistivity, and 150 μm thick materials using *i*-PERC process. They also achieved 16.6% mc-Si cells on 100 cm^2 and 180 μm thick materials and 17.3% 100 cm^2 cells on 105 μm thick monocrystalline Cz Si [112].

The best reported efficiencies for large-area ribbon Si cells have been somewhat lower than cast mc-Si cells probably because of the higher concentration of impurities and structural defects. University of Konstanz reported over 15% efficient 80 cm^2 String Ribbon Si

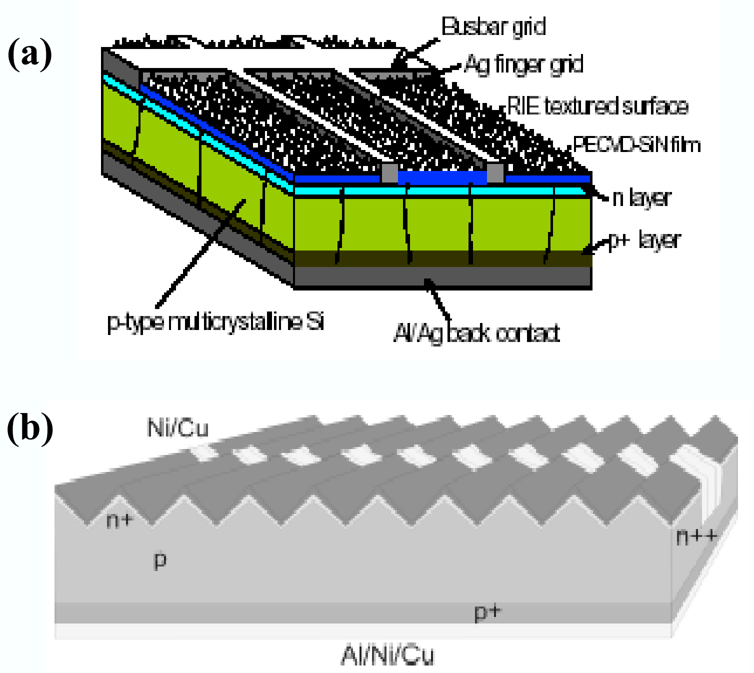

Figure 22: Schematics high-efficiency industry-scale mc-Si solar cells: (a) Kyocera RIE textured cell and (b) UKN mechanical grooved buried contact cell.

solar cells [40] using industry-type fabrication process. Recently, 92.3 cm^2 16.4% EFG Si cell was reported by RWE [36] (currently SCHOTT Solar), involving the emitter formation using $POCl_3$ liquid source, SiN_x AR coating deposition in a PECVD reactor, full-area Al-BSF and Ag grid contact formation in a beltline furnace, and SiN_x/MgF_2 DLAR coating.

A summary of large-area mc-Si solar cell results along with the key process technologies is shown in Table 4 [36, 40, 109–111, 113–124].

Table 4: Progress of large-area solar cell performance on low-cost mc-Si materials.

Year	Institute	Size (cm^2)	Material	Efficiency (%)	Process	Ref.
2000	Mitsubishi	225	Cast	16.8*	Na_2CO_3 texturing, SiN_x SLAR, SP metals, belt process	113
2003	UKN	156	Cast	17.6*	Buried front contact, V-groove acid texturing	114
2004	IMEC	100	Cast	16.7*	200 µm thick, $POCl_3$, PECVD, SP metals, SiN_x/MgF_2 DLAR	115
2004	ECN	156	Cast	16.5* (16.2)	All in-line process, RHFPECVD, 65 Ω/sq emitter, SP metals	116
2005	Kyocera	255	Cast	17.7* (17.4)	$POCl_3$, RIE texturing, SiN_x/MgF_2 DLAR, SP metals, belt co-firing	109
2005	ECN	156	Cast	17.0* (16.5)	All in-line process, RHFPECVD, 70 Ω/sq emitter, SP metals	111
2006	UKN	138	Cast	18.1*	Buried front contact, V-groove acid texturing	110
2006	Kyocera	233	Cast	18.5	RIE surface texture, shallow emitter	117
2007	Mitsubishi	225	Cast	18.0*	Improved RIE texture, narrow grid lines	118
1985	Mobile Solar	44.4	EFG	14.3	Hydrogen passivation	119
1996	ASE	100	EFG	14.5	ASE production line	120
2000	ASE	100	EFG	15.3	Belt emitter, SiN_x SLAR, SP belt co-firing	121
2004	RWE	156	EFG	14.7*	State-of-the-art EFG, RWE Production line	122
2004	RWE	100	EFG	15.3	Advanced EFG, RWE Production line	122
2005	RWE	92.27	EFG	16.4*	200 µm thick, SiN_x/ MgF_2 DLAR, SP metals, belt co-firing	36
2001	UKN	80	SR	14.3*	$POCl_3$, SiN SLAR, SP belt co-firing	123
2002	UKN	80	SR	15.4*	$POCl_3$, SiN SLAR, SP belt co-firing	124
2003	UKN	80	SR	15.4* {16.0*}	$POCl_3$, SiN SLAR, SP belt co-firing {encapsulation}	40

* Independently confirmed

( ) Average value

CHAPTER IV

INVESTIGATION AND DEMONSTRATION OF ENHANCED DEFECT HYDROGENATION IN MULTICRYSTALLINE SILICON MATERIALS USING RAPID THERMAL PROCESSING

As discussed in Chapter II, the ribbon Si has very low as-grown minority carrier lifetimes in the range of 1–5 μs, which is not sufficient for achieving high-efficiency cells (>15%) with screen-printed contacts. Solar cell fabrication usually involves P diffusion for n^+ emitter formation and PECVD SiN_x deposition for anti-reflection coating. Both P diffusion-induced gettering and PECVD SiN_x-induced defect hydrogenation have been shown to improve the minority carrier lifetime in bulk Si [125]. This chapter demonstrates how the use of rapid thermal processing can enhance the defect hydrogenation without sacrificing the Al-doped back surface field (Al-BSF) quality. This is accomplished by fabricating both monocrystalline Si (FZ) and mc-Si (cast mc-Si, EFG, and String Ribbon) cells. The FZ Si cells are analyzed to investigate the firing time-dependence of Al-BSF quality, and the mc-Si cells are analyzed to study the defect hydrogenation, bulk lifetime, and efficiency enhancement due to rapid contact firing. An optimization process is further performed in order to investigate the effectiveness of PECVD SiN_x-induced defect hydrogenation as a function of the contact firing temperature using EFG Si. The understanding gained from the RTP study is used to develop a co-firing process for front and back screen-printed contacts in a continuous belt furnace to achieve high-efficiency EFG Si solar cells.

4.1 Investigation of Contact Firing Time on Carrier Lifetime Enhancement in Multicrystalline Silicon

In this study, 1.6 Ωcm cast mc-Si grown by heat exchanger method (HEM), 3–4 Ωcm EFG, and 3–4 Ωcm String Ribbon Si are used. These materials are p-type and have a thickness of ∼300 μm. HEM, EFG, and String Ribbon Si are provided by GT Solar Technologies (Merrimack, NH), SCHOTT Solar (Billerica, MA), and Evergreen Solar (Marlboro, MA), respectively. FZ Si wafers (2.5 Ωcm, 300 μm thick) are also processed to assess the effect of contact firing time on Al-BSF quality. After the initial cleaning process, the wafers were P diffused in a $POCl_3$ furnace at a set temperature of 877°C for 20 min to form n^+ emitter with a sheet-resistance of $40-50$ Ω/sq. A SiN_x AR layer with a thickness of ∼800 Å and a refractive index of 2.0 was deposited in a low-frequency (50 kHz) PECVD reactor at 425°C. A commercial Al paste was screen printed on the entire back surface followed by an anneal in a rapid thermal processing (RTP) system (AG Associates Heatpulse 610) at 750°C for 1, 60, and 120 s in conjunction with the temperature ramp-up rate of 100°C/s and cooling rate of -40°C/s to form Al-BSF and promote PECVD SiN_x-induced defect hydrogenation (firing step ♯1). The temperature of the sample during the heat treatment in an RTP system was monitored by a thermocouple mounted on the front surface. A commercial Ag paste was also screen printed on the front and annealed in an RTP system with similar ramp-up and cooling rates for grid contact formation (firing step ♯2). Samples were finally isolated by dicing saw and forming gas annealed at 400°C for 10 min. Several 4 cm^2 solar cells were fabricated on each large-area wafer. The solar cell parameters were extracted by illuminated and dark current-voltage ($I-V$) measurements. After the solar cell characterization, samples were stripped down to bare Si by chemical etch and lifetime was measured at several locations at an injection level of 1.0×10^{15} cm^{-3} by quasi steady-state photoconductance (QSSPC) technique [20] using photoconductance tool (Sinton Consulting WCT-100). The I_2/methanol solution was used for surface passivation during the lifetime measurement. Cross-sectional Scanning Electron Microscopy (SEM) (Hitachi 3500H) was also used to investigate the uniformity of Al-BSF region. Prior to the SEM measurements, samples were broken along the crystal direction followed by etching in

Table 5: Average cell parameters on FZ Si fabricated by three different scheme of firing step ♯1. Peak firing temperature was 750°C.

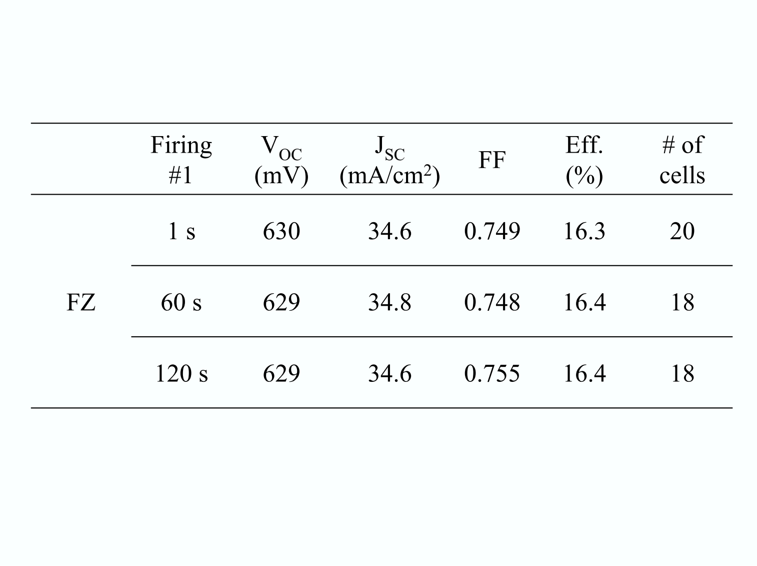

	Firing #1	V_{OC} (mV)	J_{SC} (mA/cm^2)	FF	Eff. (%)	# of cells
FZ	1 s	630	34.6	0.749	16.3	20
	60 s	629	34.8	0.748	16.4	18
	120 s	629	34.6	0.755	16.4	18

1:3:6 HF:HNO_3:CH_3COOH for 10 s. The purpose of this etching is to delineate the Al-BSF (heavily p-doped) from the bulk (lightly p-doped) region.

4.2 Characterization, Results and Discussion

4.2.1 IQE measurements and SEM analysis of FZ Si solar cells for establishing the process for effective Al-BSF formation

The open-circuit voltage (V_{OC}) of a solar cell is a strong function of the minority carrier lifetime as well as the quality of the Al-BSF region. Table 5 shows the average parameters of FZ Si cells fabricated by contact firing at 750°C for 1, 60, and 120 s. The idea was to alter the Al-BSF structures by selecting the firing conditions compatible with defect hydrogenation.

The long-wavelength IQE analysis was performed on the FZ Si cells to assess the quality of Al-BSF region for each scheme. Since the monocrystalline FZ Si used in this study has very high carrier lifetime (>300 μs), the IQE response in the long-wavelength region is related directly to the Al-BSF quality. The IQE response in the long-wavelength region (800−1100 nm), shown in Fig. 23, was essentially independent of SiN_x/Al firing time in the range of 1–120 s at 750°C (firing step #1), indicating that the Al-BSF quality was essentially

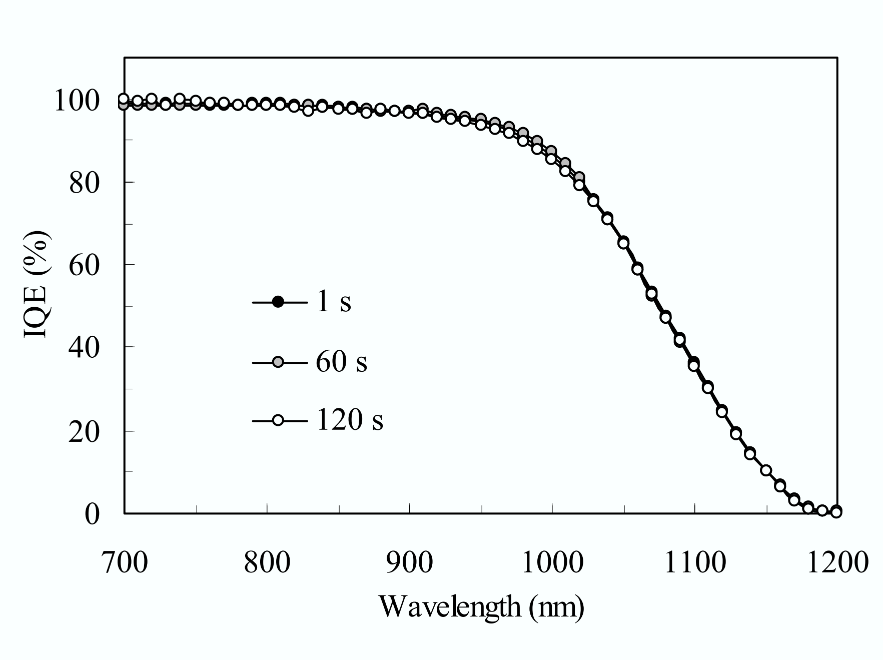

Figure 23: Long-wavelength IQE response of FZ Si cells.

identical for 1 and 120 s firings. In order to verify this, the cross-sectional SEM analysis was performed for each scheme to investigate the uniformity and thickness of the Al-BSF region. Figure 24 shows the SEM pictures of the Al-BSF regions in the FZ samples subjected to 1 and 120 s firing at 750°C. In both cases, the Al-BSF region was quite uniform with an approximate thickness of ~7.8 μm. The Al-BSF pictures, V_{OC}, and the IQE demonstrate that the thickness, uniformity, and quality of Al-BSF region are not a strong function of RTP firing time in the range of 1–120 s. This is important because, as shown below, a very short firing provides more effective defect hydrogenation.

4.2.2 Lifetime enhancement by P diffusion-induced gettering and PECVD SiN$_x$ defect hydrogenation in multicrystalline silicon materials

P diffusion-induced impurity gettering technique has been studied and implemented by many researchers to improve the material quality. In solar cell fabrication process, the purpose of P diffusion is not only to form n$^+$ emitter but also to improve the material quality by removing the impurities from Si bulk by gettering effect. The effect of P diffusion gettering on carrier lifetime is shown in Fig. 25. The lifetime increased from 32 to 88 μs, 3

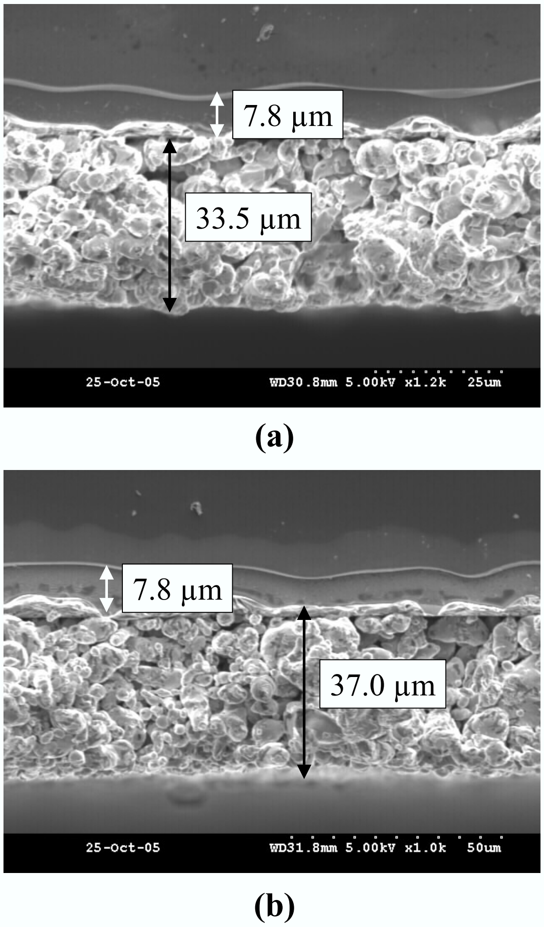

Figure 24: SEM micrograph of Al-BSF region in FZ Si: (a) 750°C/1 s and (b) 750°C/120 s firing.

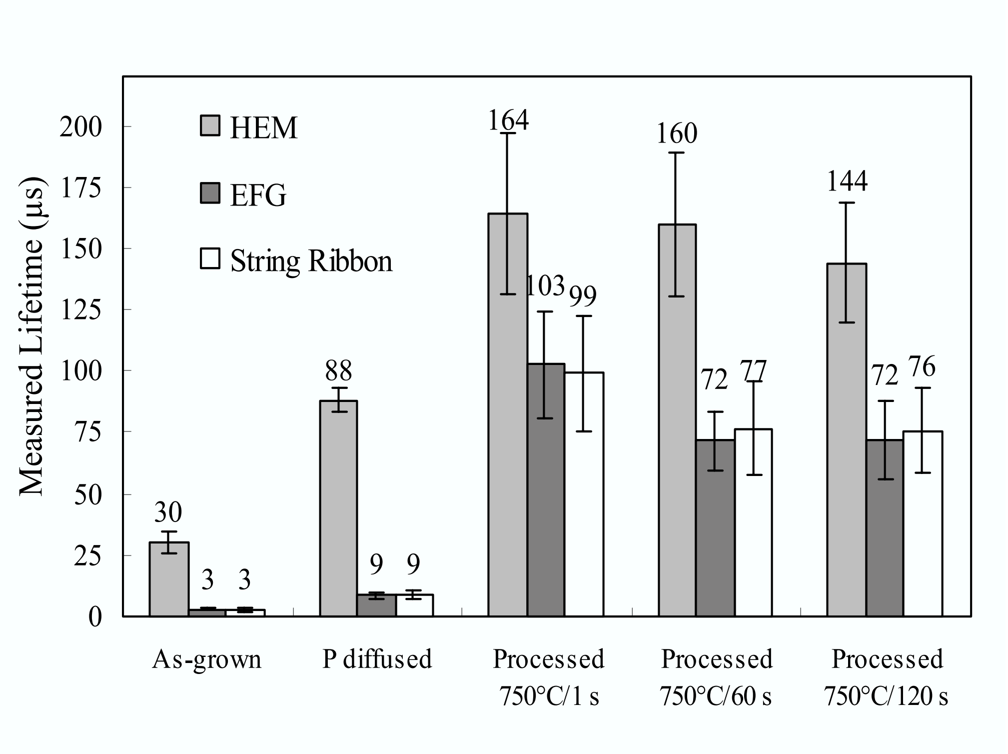

Figure 25: Carrier lifetime measurements on HEM, EFG, and String Ribbon Si. Error bar indicates a standard deviation.

to 9 μs, and 2 to 9 μs in HEM, EFG, and String Ribbon Si, respectively. HEM mc-Si wafers were chosen in the consecutive positions from ingot to minimize the effect of non-uniform distribution of defects. A significant lifetime enhancement, about a factor of three, was observed by P diffusion gettering, indicating that metal impurities were effectively gettered from the Si bulk during the P diffusion. However, in ribbon Si materials, the carrier lifetime was only 9 μs after P diffusion gettering. This corresponds to minority carrier diffusion length ($L_b = \sqrt{D_n \tau_b}$) of 167 μm in 3.0 Ωcm material, where D_n is the diffusion coefficient of electron and τ_b is the bulk carrier lifetime. This is not sufficient to produce high-efficiency cells with screen-printed contacts because the L_b of 167 μm is still much less than the wafer thickness of 300 μm. Note that these lifetime measurements were performed on several wafers (>10 wafers) and locations for statistical purpose at an injection level of 1.0×10^{15} cm^{-3} using QSSPC technique.

Since P diffusion gettering alone is not sufficient to enhance the carrier lifetime to a

Table 6: Average cell parameters on HEM, EFG, and String Ribbon Si. Peak firing temperature was 750°C.

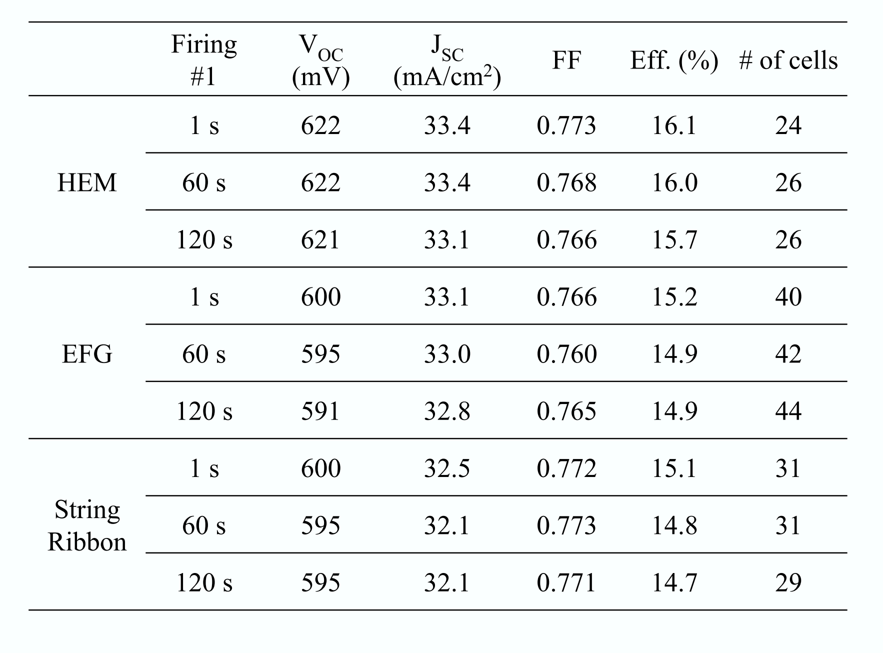

	Firing #1	V_{OC} (mV)	J_{SC} (mA/cm^2)	FF	Eff. (%)	# of cells
HEM	1 s	622	33.4	0.773	16.1	24
	60 s	622	33.4	0.768	16.0	26
	120 s	621	33.1	0.766	15.7	26
EFG	1 s	600	33.1	0.766	15.2	40
	60 s	595	33.0	0.760	14.9	42
	120 s	591	32.8	0.765	14.9	44
String Ribbon	1 s	600	32.5	0.772	15.1	31
	60 s	595	32.1	0.773	14.8	31
	120 s	595	32.1	0.771	14.7	29

satisfactory level, the next step was to investigate the contact firing conditions to passivate defects via hydrogenation without degrading Al-BSF quality. Multiple 4 cm^2 solar cells were fabricated on large-area cast and ribbon mc-Si. The average solar cell performance parameters obtained in this experiment are summarized in Table 6. It is notable that the highest average solar cell performance was achieved for the 1 s firing case. The highest average V_{OC} in EFG Si was 600 mV for 1 s firing. It decreased to 595 mV for 60 s and 591 mV for 120 s firing. The maximum EFG Si cell efficiency achieved by 1 s firing scheme was 16.1% ($V_{OC} = 614$ mV, $J_{SC} = 33.7$ mA/cm^2, $FF = 0.779$), which was measured at National Renewable Energy Laboratory (Golden, CO). In the case of String Ribbon Si, the V_{OC} and J_{SC} showed a similar trend with EFG Si cells, indicating that the short firing cycle provides very effective defect hydrogenation in ribbon Si materials. The solar cells fabricated on HEM mc-Si showed little difference in V_{OC}. This is probably because the carrier lifetime after P diffusion (88 μs) is sufficient to produce solar cells with reasonable performance in HEM mc-Si. The carrier lifetime of 88 μs is nearly equivalent to the L_b of 500 μm in 1.6 Ωcm material, which is much greater than the substrate thickness of 300 μm.

It is clear, based on the results shown in Table 6, that the effective defect hydrogenation occurs rapidly during the contact firing. To verify that the short annealing process enhances the lifetime effectively, processed solar cells were stripped down to bare Si, and lifetime measurements were performed on each material. A large number of processed wafers (>10 wafers) were subjected to the lifetime measurements to satisfy the statistical requirements since the mc-Si materials have an inhomogeneous distribution of electrically active defects. The results of lifetime measurements on these three kinds of processed wafers used in this study are shown in Fig. 25. Note that the error bar in Fig. 25 indicates a standard derivation. A significant enhancement in carrier lifetime was observed after the SiN_x-induced defect hydrogenation during the contact firing process. Consistent with solar cell data in Table 6, it was found that the lifetime for 1 s firing gave the highest average value compared to other two firing schemes (60 s and 120 s) in all three materials, supporting the higher solar cell performance on mc-Si materials in Table 6 for 1 s firing scheme.

4.3 Investigation of PECVD SiN_x-Induced Defect Hydrogenation in EFG Si as a Function of Contact Firing Temperature

In the previous section, it was found that a rapid contact firing cycle enhances bulk carrier lifetime as well as cell efficiency because of the effective defect hydrogenation. In this section, a process optimization was further performed in order to investigate the effect of contact firing temperature on bulk carrier lifetime and cell efficiency.

EFG Si solar cells were again fabricated by the two-step RTP firing process. After P diffusion process, the SiN_x AR coating was deposited in a PECVD reactor. Commercial Al paste (Ferro FX53-038) was screen printed on the entire rear surface and the EFG Si wafers were annealed in an RTP unit at 725, 750, 775, 800, and 825°C for 1 s with a fast temperature ramp-up rate of 100°C/s and cooling rate of −40°C/s (firing step ♯1). The Ag front grid (Ferro 3349) was then screen printed and fired at 700°C in an RTP unit with similar ramp-up and cooling rates (firing step ♯2). A forming gas contact anneal was performed at 400°C for 10 min at the end of the process. Thirty-six 4 cm^2 cells were fabricated for each process scheme in this study to account for the inhomogeneity in the material quality of the EFG Si. The illuminated and shaded $I - V$ measurements were performed to extract the cell performance parameters. The first step involved 1 s hydrogenation at different temperatures, during which PECVD SiN_x on the front and Al on the back were fired simultaneously. The second RTP step involved firing the Ag grid after screen-printing the Ag paste. The average values of the open-circuit voltage (V_{OC}), short-circuit current density (J_{SC}), fill factor (FF), and efficiency for each firing scheme are shown in Table 7. Table 7 indicates that firing at 775°C for 1 s gave maximum average V_{OC} (600 mV). Average FF decreased from 0.748 to 0.720 when the firing temperature was raised from 775°C to 825°C for the Ag paste used in this study. The average cell efficiency for each scheme as a function of peak hydrogenation temperature is shown in Fig. 26. The hydrogenation at 775°C for 1 s gave the average efficiency of 15.3% with a maximum of 15.9% (V_{OC}=605 mV, J_{SC}=34.1 mA/cm^2, FF=0.769), which was confirmed by National Renewable Energy Laboratory (Golden, CO). Figure 26 also reveals that hydrogenation at a higher firing temperature ($\geq$800°C) produces less efficient EFG Si solar cells. The average cell efficiency for 825°C/1 s hydrogenation was only 13.5%, indicating a 1.8% loss in absolute efficiency compared to the 775°C/1 s hydrogenation. Such a huge loss in efficiency cannot be explained by the observed decrease in FF. This loss is largely attributed to the carrier lifetime degradation because of the enhanced dissociation of atomic hydrogen from the hydrogenated defect sites at higher temperature.

To support the above hypothesis, QSSPC lifetime measurements were performed after stripping the cell down to bare Si. An average minority carrier lifetime of 93 μs was achieved with a maximum of 169 μs for the peak hydrogenation temperature of 775°C, as shown in Fig. 27. It should be noted that the lifetimes were measured by the QSSPC technique and averaged over thirty-two different locations (four wafers and eight different locations per wafer) on EFG Si for each firing scheme. The average carrier lifetime decreased to 74 μs for the 800°C/1 s hydrogenation and to 50 μs for the 825°C/1 s hydrogenation. This decreasing trend in carrier lifetime at higher temperature is consistent with the trend in cell performance in Table 7. It is proposed that this decreasing trend in carrier lifetime is the

Table 7: Average cell parameters for each firing scheme. Firing time was 1 s for all cases.

	V_{OC} (mV)	J_{SC} (mA/cm^2)	FF	Eff. (%)
725°C	587	33.8	0.737	14.6
750°C	589	33.8	0.738	14.7
775°C	600	33.9	0.748	15.3
800°C	596	34.0	0.724	14.6
825°C	579	32.4	0.720	13.5

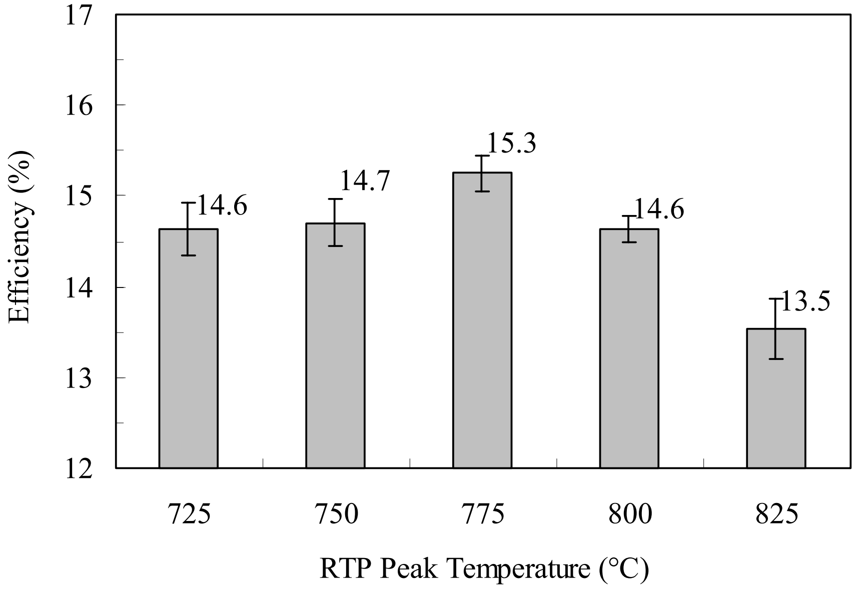

Figure 26: Efficiencies of EFG Si cells as a function of a firing temperature. Error bar indicates a standard deviation.

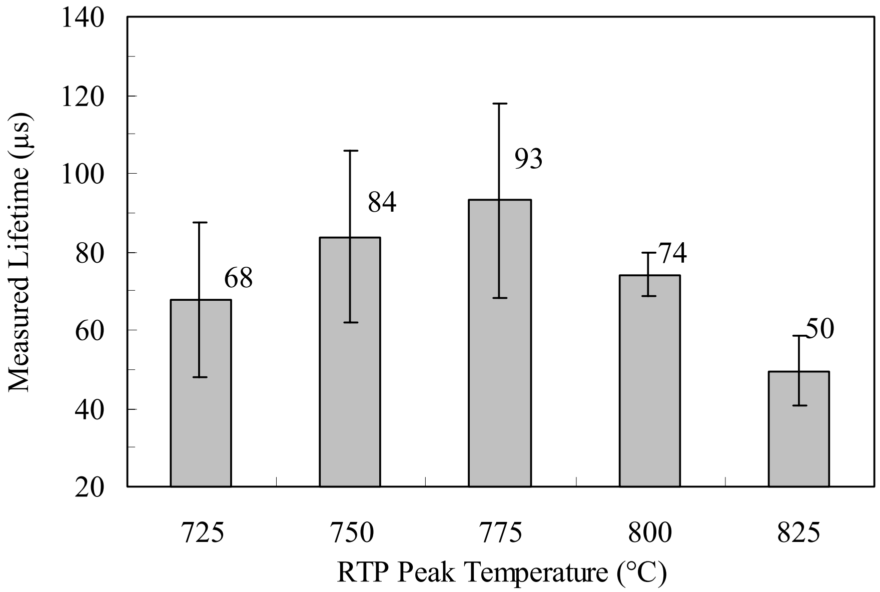

Figure 27: Average carrier lifetime achieved for each firing scheme. Error bar indicates a standard deviation.

result of reactivation of hydrogenated defects at higher annealing temperature. The degree of hydrogenation is dictated by the competition between the supply of hydrogen atoms to the defects from the SiN_x layer and the dissociation of hydrogen from the defects. These two processes happen simultaneously during the hydrogenation or firing cycle. More characterizations and modeling are performed in the next chapter to explain this phenomenon.

4.4 Development of Manufacturable Belt Co-Firing Process for Maximum Hydrogenation in EFG Silicon

The optimum hydrogenation cycle of 775°C/1 s gave an average EFG Si cell efficiency of 15.3% with a maximum of 15.9%, as shown in Fig. 26. However, this process involved two-step RTP contact firing where hydrogen passivation of defects was performed at 775°C for 1 s and the Ag grid contacts were fired at 700°C for 1 s to avoid contact shunting. Since conventional belt furnace firing is preferred in the PV industry because of high-throughput and continuous processing, attempts were made to tailor the temperature profile in a belt

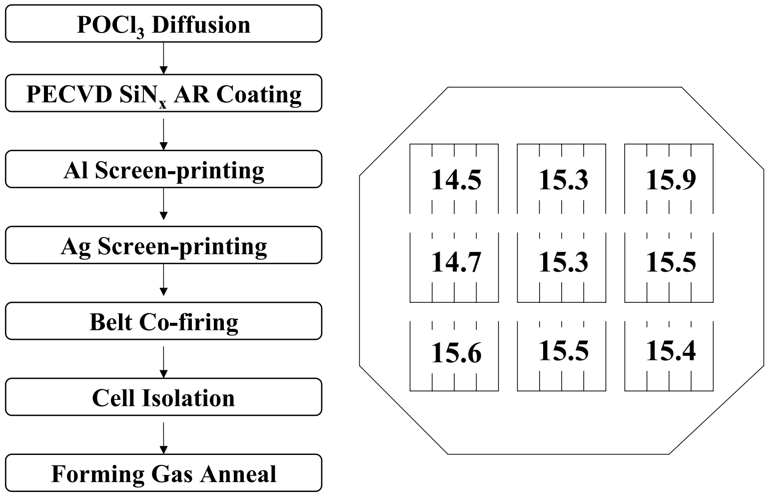

(a) (b)

Figure 28: (a) Process sequence of belt-line co-firing used in this experiment and (b) efficiency distribution of EFG Si solar cells. Cell size is 4 cm^2.

furnace to come close to the RTP hydrogenation temperature profile, which can provide effective hydrogenation along with effective Al-BSF formation and good quality Ag grid contacts in a single firing step. This co-firing process scheme is shown in Fig. 28(a). To avoid contact shunting in the single-step firing scheme, without sacrificing significant hydrogenation, the hydrogenation temperature had to be lowered slightly, and an appropriate Ag paste (DuPont 4948) was selected, which could be fired up to 750°C without contact shunting. This allowed us to hydrogenate the defects effectively by rapid co-firing of contacts in a belt-line furnace, where peak temperature reached ∼750°C for a very short time. This co-firing process produced a maximum efficiency of 15.9% with an average of 15.1% based on 103 EFG Si cells (4 cm^2) with screen-printed contacts. The efficiency distribution of nine 4 cm^2 EFG Si cells on a large-area EFG Si wafer is shown in Fig. 28(b).

4.5 Conclusions

It was found that the PECVD SiN$_x$-induced defect hydrogenation occurs rapidly during the screen-printed contact firing process. The effective defect hydrogenation anneal produced 4 cm^2 EFG Si solar cells with an average efficiency of 15.4% and a maximum efficiency of

16.1%. It was also demonstrated that the simultaneous firing of PECVD SiN_x on the front and Al on the back of an EFG Si wafer at an optimum temperature of 750–775°C for only 1 s raised its carrier lifetime from 3 to >90 μs. This is the result of very rapid SiN_x-induced hydrogenation of defects in EFG Si. A manufacturable single-step belt furnace firing process was also developed in this chapter, which produced a maximum cell efficiency of 15.9% with an average of 15.1% out of 103 EFG Si cells with screen-printed contacts.

CHAPTER V

FUNDAMENTAL UNDERSTANDING OF MINORITY CARRIER LIFETIME ENHANCEMENT IN EFG SILICON THROUGH CHARACTERIZATION OF PECVD SILICON NITRIDE FILMS AND RAPID THERMAL PROCESSING-ASSISTED REDUCTION OF HYDROGEN-DEFECT DISSOCIATION

To realize maximum benefit from a hydrogenation source, it is critical to optimize the firing process to achieve high retention of atomic hydrogen at the defect sites. In the previous chapter, the implementation of a rapid contact firing at an optimum temperature in an RTP system gave a maximum enhancement in carrier lifetime (~3 to ~100 μs) and cell efficiency (~16%). In this chapter, characterization of two primary hydrogen sources, bulk of PECVD SiN_x film and SiN_x/Si interface, is performed using Fourier Transform Infrared (FTIR) and Secondary Ion Mass Spectrometry (SIMS) techniques in order to assess the concentration of hydrogen-related bonds upon contact firing. In addition, a physical model is developed in this chapter to explain how and why the proper use of the rapid contact firing cycle can improve the defect hydrogenation in defective EFG Si, resulting in a significant enhancement in carrier recombination lifetime and cell performance.

5.1 Characterization of PECVD SiN_x Films as a Source of Hydrogen Atoms for Defect Passivation

5.1.1 FTIR measurements to detect the change in N-H and Si-H concentrations in PECVD SiN_x films upon annealing

In the solar cell fabrication process, the SiN_x films are commonly deposited on the front surface of the wafers in a PECVD reactor to reduce the reflectance. Moreover, the deposited

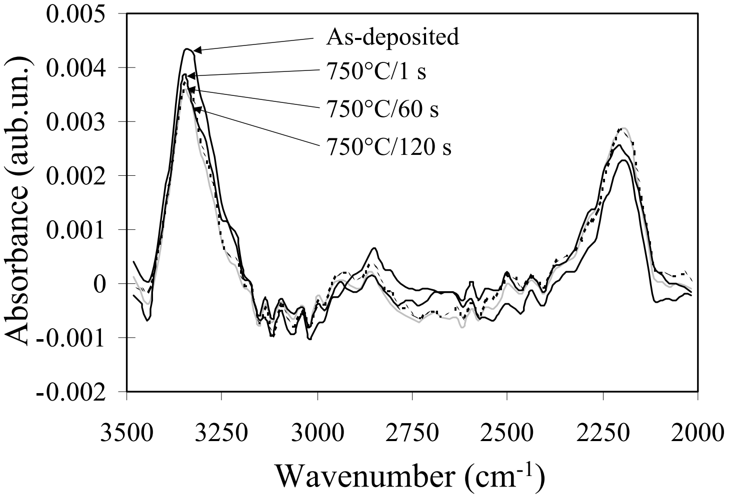

Figure 29: FTIR spectra in the range of 2000 to 3500 cm^{-1}.

SiN$_x$ film serves not only as the antireflection coating but also as the source of hydrogen for reducing the carrier recombination via passivation of defects at the surface and in the bulk. In the SiN$_x$ film, hydrogen is present in the form of nitrogen-hydrogen (N-H) and silicon-hydrogen (Si-H) bonds. The dissociation of bonded hydrogen in the SiN$_x$ film is generally considered as a source of hydrogen atoms for defect hydrogenation.

FTIR measurements (Lester Lefkowitz/PIX04822) were performed on low-frequency (50 kHz) PECVD SiN$_x$ films deposited in this study on 300 μm thick, high-resistivity (500-1000 Ωcm), n-type FZ Si wafers to determine the change in concentration of N-H and Si-H bonds in the deposited SiN$_x$ film as a function of annealing temperature and time. Prior to the SiN$_x$ deposition, FZ Si wafers were etched and cleaned in chemical solutions. The SiN$_x$ film with a refractive index of 2.0 was deposited on both sides of the substrate.

FTIR measurements on the SiN$_x$ film usually show two distinct peaks (Fig. 29) at 3340 cm^{-1} and 2180 cm^{-1}, corresponding to N-H and Si-H bonds, respectively [126]. The absolute concentrations of N-H and Si-H bonds were determined from the area of their respective peaks, using the correlation coefficients in [127], after converting transmittance into absorbance. Consistent with reported data in [128], the concentration of N-H bonds decreased significantly after high temperature anneal. This is probably because the bonding

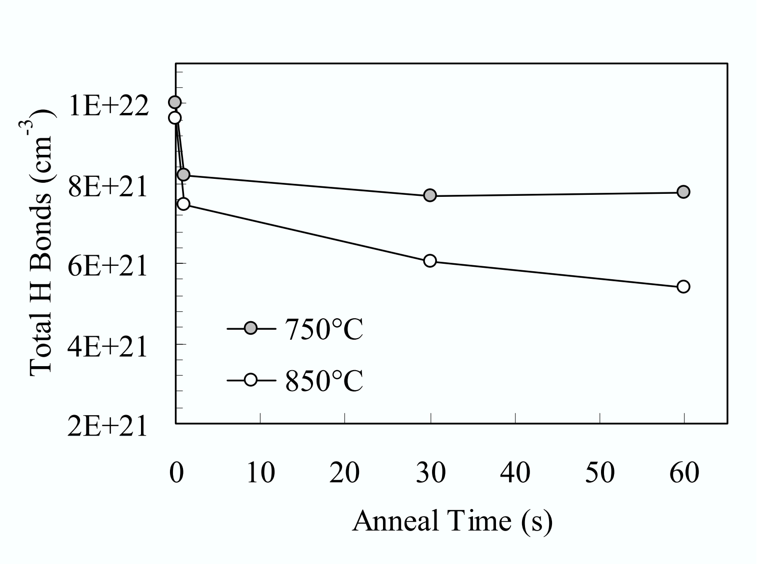

Figure 30: Change of the total bonded hydrogen concentration after high temperature process.

energy of N-H complex is weaker than that of Si-H complex. The concentrations of total bonded hydrogen in the SiN$_x$ film after various heat treatments in an RTP unit are shown in Fig. 30. A rapid decrease in bonded hydrogen content was observed when SiN$_x$ film was annealed at high temperature (>750°C). Equally important is the fact that this decrease is rapid initially (after 1 s anneal) and then slows down. A decrease in concentration of bonded hydrogen in SiN$_x$ film due to high temperature anneal was also observed in [129]. This suggests that the SiN$_x$ film provides a limited source of hydrogen and its supply decreases rapidly with the annealing time.

5.1.2 SIMS analysis of hydrogen at the PECVD SiN$_x$/Si interface

In this section, the hydrogen incorporation at or near the Si surface was quantified by SIMS analysis (Cameca IMS). In order to detect the hydrogen incorporation by SIMS, ND$_3$ was substituted for NH$_3$ during the SiN$_x$ deposition in the low-frequency PECVD reactor. The SiN$_x$ with a thickness of 725 Å was deposited on surface-polished and B-doped Czchralski Si substrates with a resistivity of 50 Ωcm and a thickness of 525 μm. The thickness of SiN$_x$ film was measured by using Ellipsometer (Plasmos SD2300) equipped with a 632.8 nm laser. Prior to the SiN$_x$ deposition, the samples were cleaned in chemical solutions and P diffused in a $POCl_3$ furnace. A 10 cm diameter Cz wafer was cut into four pieces, and Al paste was screen printed on the back. The samples were then annealed in an RTP unit at 750°C for 1, 60, and 120 s in conjunction with a temperature ramp-up rate of 100°C/s and cooling rate of -40°C/s, which are identical to the process used in solar cell fabrication. Prior to the SIMS measurements, Al and SiN_x layers were removed in chemical solutions.

Figure 31 shows the SIMS depth profiles of deuterium (D) in Si after SiN_x deposition in a PECVD reactor and anneal in an RTP unit at 750°C for 1, 60, and 120 s. The detection limit for deuterium is approximately 3.0×10^{15} cm^{-3}. The SIMS depth profile revealed that after the low-frequency PECVD SiN_x deposition, the surface concentration of deuterium had 6.0×10^{19} cm^{-3}, which can be considered as trapped deuterium at the Si surface during the SiN_x deposition. This trapping is the result of PECVD SiN_x deposition-induced surface damage, which could provide a second source for defect hydrogenation. The surface concentration of deuterium dropped from 6.0×10^{19} cm^{-3} to 2.0×10^{18} cm^{-3} after 750°C for 1 s anneal in an RTP. This indicates that the trapped deuterium at or near the Si surface diffused into bulk Si or the SiN_x layer after a 750°C/1 s anneal. It is also important to note that no appreciable difference in deuterium concentration at the surface was observed after 1, 60, and 120 s anneal, indicating that the trapped deuterium diffuses rapidly initially but its supply slows down rapidly during the high temperature (750°C) anneal. This is consistent with the observations in [130] and [131]. This could explain why longer anneal times are not as effective and can even be detrimental if the rate of defect dehydrogenation is fast at the firing temperature. This aspect is modeled and explained in the next section.

5.2 Understanding of Kinetics of Hydrogen-Defect Dissociation Process in EFG Silicon

The FTIR and SIMS data in the previous sections revealed that the release of hydrogen atoms from the low-frequency PECVD SiN_x films and PECVD SiN_x/Si interface is very rapid initially and then slows down. This implies that the hydrogen supply may decrease rapidly with time, while hydrogen dissociation from the passivated defects continues during

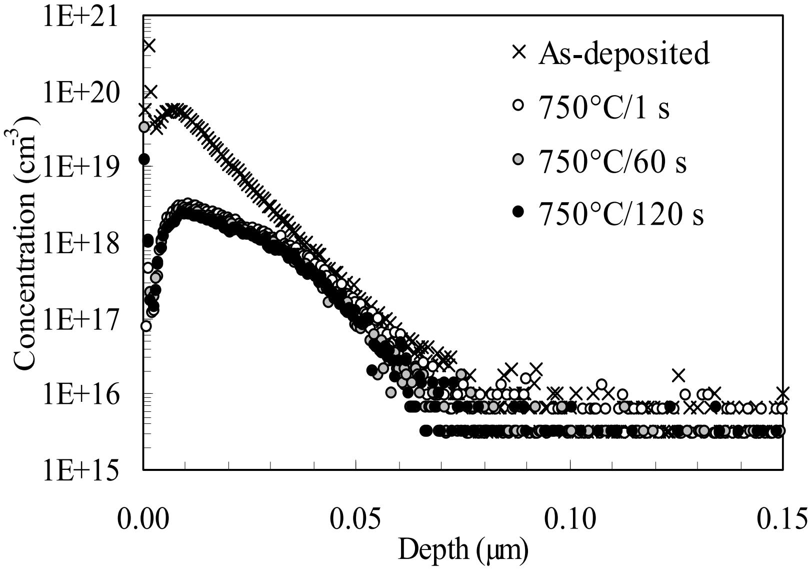

Figure 31: SIMS depth profile of deuterium at Si surface after SiN_x deposition and anneal in an RTP unit at 750°C for 1, 60, and 120 s

the holding interval. As a result, a rapid firing should be able to retain more hydrogen atoms at the defect sites and produce a higher minority carrier lifetime. To understand and quantify the hydrogen-defect dissociation process, hydrogenated samples (750°C/1 s firing in RTP) were first etched down to bare Si to remove the hydrogen supply (SiN_x film) and were then reannealed in an RTP unit in the temperature range of 400−700°C for 1 s. Some samples were also reannealed at 550°C for 5−60 s to study the reactivation of hydrogenated defects as a function of time at lower temperature. Float-zone (FZ) Si with resistivity of 1.3 Ωcm was used as a control to ensure that the change in carrier lifetime is primarily due to the hydrogen out-diffusion and not because of any contamination during the heat treatment. Figure 32 shows a rapid decrease in carrier lifetime above 550°C for 1 s anneal, while no appreciable change in carrier lifetime was observed in FZ Si, which remained at 270−300 μs after 700°C/1 s and 550°C/60 s RTP annealing. Figure 32 also shows that the normalized lifetime, τ_f/τ_i, where τ_i and τ_f are the carrier lifetimes before and after annealing of hydrogenated samples, respectively, was not affected below 500°C for the 1 s anneal. However, carrier lifetime dropped from 99 μs to 8.3 μs ($\tau_f/\tau_i \simeq 0.08$) after

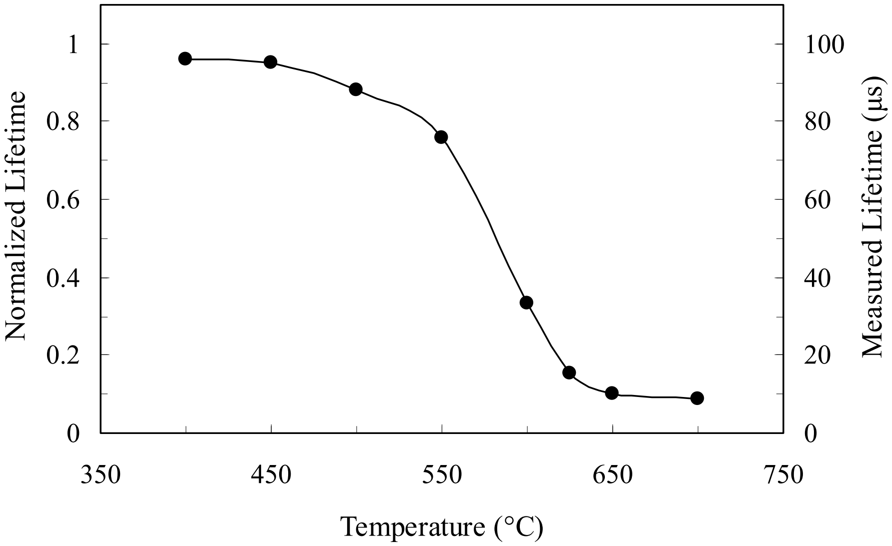

Figure 32: Normalized lifetime (τ_f/τ_i) of a hydrogenated bare EFG Si sample as a function of annealing temperature for 1 s.

700°C/1 s annealing. The carrier lifetime decreases with the increased firing time even at 550°C, as shown in Fig. 33. Figures 32 and 33 clearly indicate that the hydrogen-defect dissociation starts to occur even below the conventional contact firing temperatures in the range of 700−800°C and its effect could become very significant for longer-holding times if the hydrogen supply is cut off or becomes limited.

The hydrogen-defect dissociation can be expressed by the following reaction:

$$XH \xrightarrow{\text{dissociation}} X + H, \tag{27}$$

where H represents hydrogen and X represents a defect or impurity. Assuming that a hydrogen-defect complex (XH) dissociates in accordance with the first-order reaction kinetics, the rate of change in the density of hydrogen-defect complexes can be expressed

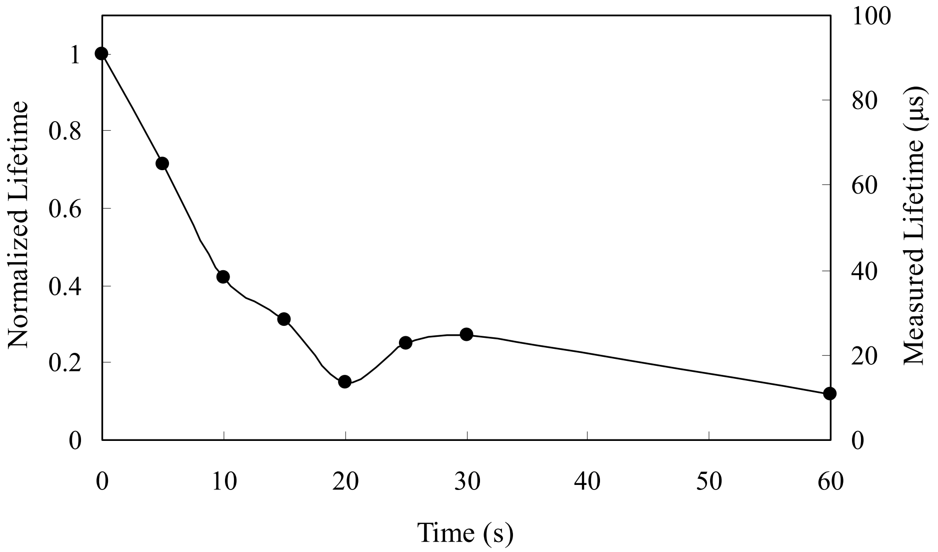

Figure 33: Normalized lifetime (τ_f/τ_i) of a hydrogenated bare EFG Si sample as a function of annealing time at 550°C.

as [132]:

$$\frac{d[XH]}{dt} = -k[XH] \tag{28}$$

$$\int_{N_O}^{N} \frac{d[XH]}{[XH]} = \int_0^t -k dt \tag{29}$$

$$\ln\frac{N}{N_O} = -kt, \tag{30}$$

where k is the reaction rate constant, N_O is the density of hydrogen-defect complexes prior to annealing the hydrogenated sample, and N is the density of hydrogen-defect complexes after the heat treatment for time, t. Most first-order reactions are characterized by an activation energy, and their rate is often expressed by the Arrhenius equation [132]:

$$k = \nu \exp\left(\frac{-E_D}{k_B T}\right), \tag{31}$$

where ν is the frequency factor (frequency of dissociation attempts), E_D is the activation energy, k_B is the Boltzmann constant, and T is the temperature. Substituting Eq. (31) into Eq. (30) gives:

$$\ln\frac{N}{N_O} = -t\nu \exp\left(\frac{-E_D}{k_B T}\right), \tag{32}$$

or

$$\frac{N}{N_O} = \exp\left[-t\nu \exp\left(\frac{-E_D}{k_B T}\right)\right], \tag{33}$$

where N/N_O is the fraction of passivated defects (hydrogen-defect complexes) remaining after a dehydrogenation anneal [133–136].

Since it is difficult to measure N_O and N directly, Eq. (33) was transformed in terms of measured lifetimes τ_i and τ_f, assuming that τ at any stage is inversely proportional to the concentration of unpassivated active defects. The fraction of passivated defects (hydrogen-defect complexes), N/N_O, can now be written as:

$$\begin{aligned}\frac{N}{N_O} &= \frac{\text{concentration of passivated defects after annealing}}{\text{concentration of passivated defects before annealing}} \\ &= \frac{N_T - N'}{N_T - N'_O},\end{aligned} \tag{34}$$

where N'_O and N' are the concentrations of unpassivated defects before and after annealing, respectively, which dictate the carrier lifetime. Note that N'_O and N' are inversely proportional to τ_i and τ_f, respectively. N_T is the total concentration of lifetime-limiting defects that can be passivated, which is also equal to the unpassivated defect concentration when all the hydrogenated defects are reactivated and the lifetime does not decrease with further annealing. The fraction of passivated defects can now be expressed in terms of measured carrier lifetimes:

$$\frac{N}{N_O} = \frac{1/\tau_s - 1/\tau_f}{1/\tau_s - 1/\tau_i}, \tag{35}$$

where τ_s is the saturated lifetime when all the hydrogenated defects are reactivated and the lifetime does not decrease with further annealing. In this study, the fully dehydrogenated carrier lifetime, τ_s, is 8 μs, which is obtained after annealing the samples at 700°C for 60 s. τ_i is 99 μs for the temperature-dependence study in Fig. 32 and 91 μs for time-dependence study in Fig. 33. According to the literature, the attempt dissociation frequency, ν, falls in the range of 1.0×10^{13}-10^{14} s^{-1} and was set to 1.0×10^{14} s^{-1} for the model calculations shown in Figs. 34 and 35 using Eq. (33) [59,135]. The comparison between the experimental data and model calculations is shown in Figs. 34 and 35. Simulations were performed using Eq. (33). Figure 34 shows the case for 1 s dehydrogenation at different temperature, and Fig.

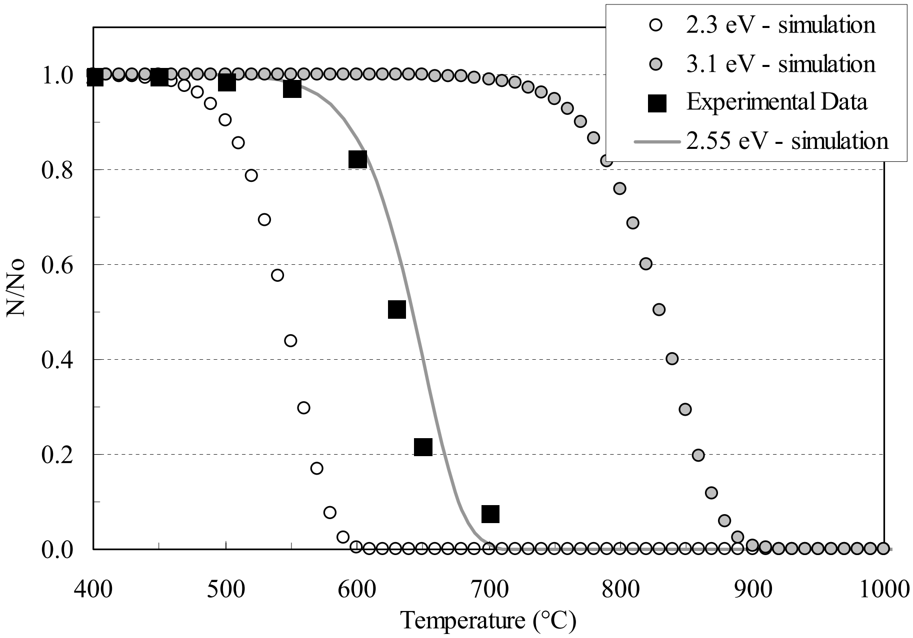

Figure 34: A comparison of simulation and experimental data showing a fraction of passivated defect as a function of annealing temperature for 1 s annealing of a hydrogenated bare EFG Si sample (ν=1.0×10^{14} s^{-1}).

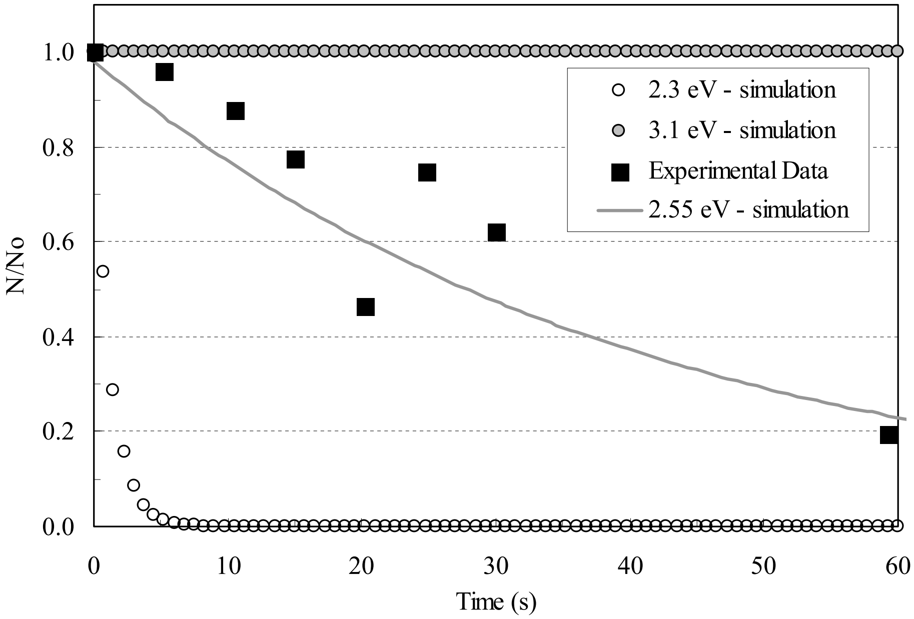

Figure 35: A comparison of simulation and experimental data showing a fraction of passivated defect in a hydrogenated EFG Si sample as a function of annealing time at 550°C (ν=1.0×10^{14} s^{-1}).

35 shows the case of annealing at 550°C for different times. Based on the limited data in the literature, the E_D values fall in the range of 1.5−2.5 eV for hydrogen-impurity complex dissociation, and its value is 3.1 eV for hydrogen-dislocation complex dissociation [59, 136]. Two N/N_O versus temperature curves were first simulated and plotted on Figs. 34 and 35 using Eq. (33) and E_D values of 2.3 eV and 3.1 eV to cover the range of hydrogen dissociation from impurities and dislocations. The measured carrier lifetime data in Figs. 32 and 33 was then used to calculate N/N_O versus temperature according to Eq. (35) and plotted on Figs. 34 and 35 with the simulated curves. Notice that the experimental data points fall within the simulated curves for hydrogen-impurity and hydrogen-dislocation dissociation in both the figures. This supports that the dehydrogenation process involves reactivation of passivated impurities, dislocations, or impurity-decorated dislocations during the annealing process. The model fitted to the experimental data gave an activation energy, E_D, of 2.4 eV for ν of 1.0×10^{13} s^{-1} and 2.55 eV for ν of 1.0×10^{14} s^{-1} in EFG Si.

5.3 Room-Temperature Scanning Photoluminescence Mapping to Study the Hydrogen Passivation and Reactivation of Defects in EFG Silicon

After determining the activation energy for hydrogen-defect dissociation, room-temperature scanning photoluminescence (PL) spectroscopy was performed in an attempt to identify the nature of the passivated defects and to understand the process of hydrogen dissociation from the electrically active defects in EFG Si. The PL spectrum was taken at room-temperature using AlGaAs laser excitation. The two peaks in the PL spectra are shown in Fig. 36: one at 0.8 eV corresponding to the defect band with PL intensity of I_{def} and the other at 1.1 eV corresponding to the band-to-band PL intensity of I_{bb}. It has been shown in [137] and [138] that the defect band peak at 0.8 eV corresponds to impurity-decorated dislocations, which supports the conclusion from the activation energy analysis in previous section. PL mappings were performed on a 50×22 mm^2 EFG Si piece with spatial resolution of 0.5 mm. The EFG Si samples were cleaned and phosphorus diffused, coated with SiN_x in a low-frequency PECVD reactor and hydrogenated in an RTP unit at 750°C for 1 s. The

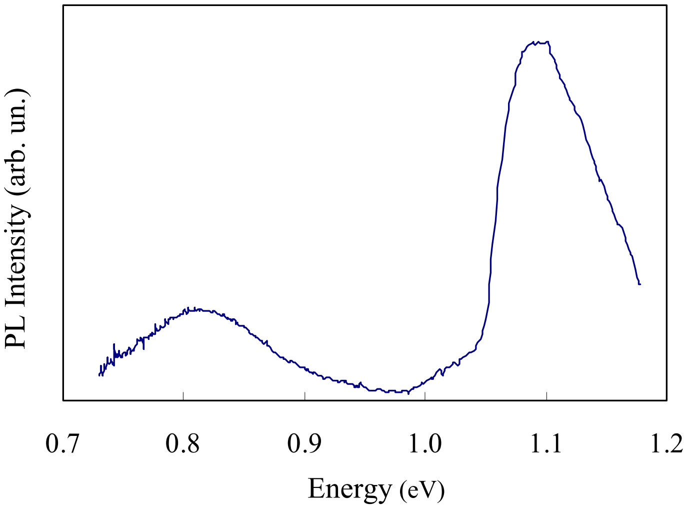

Figure 36: Room-temperature PL spectra on EFG Si after RTP dehydrogenation at 600°C/1 s.

SiN_x AR coating was then removed in 10:1 H_2O:HF solution prior to the PL measurements.

The intensity of both bands, I_{bb} and I_{def}, at a constant generation rate, G, can be expressed in terms of effective minority carrier lifetime (τ_{eff}), radiative band-to-band recombination lifetime (τ_{rad}), and radiative component of Shockley-Read-Hall lifetime (τ_{SRH}). The τ_{eff} is the composite of radiative, non-radiative, and surface recombinations and is generally dominated by non-radiative recombination in Si [137].

$$I_{\text{bb}} = C_1 \times G \times \frac{\tau_{\text{eff}}}{\tau_{\text{rad}}} \tag{36}$$

$$I_{\text{def}} = C_2 \times G \times \frac{\tau_{\text{eff}}}{\tau_{\text{SRH}}} \tag{37}$$

$$\tau_{\text{SRH}} = (N_{\text{def}}\ \nu_{\text{th}}\ \sigma_n)^{-1}, \tag{38}$$

where C_1 and C_2 are the temperature-dependent Si constants, N_{def} is the concentration of radiative defect centers, ν_{th} is the electron thermal velocity, and σ_n is the electron capture cross section of radiative centers [137,138]. Equation (36) shows that the I_{bb} is proportional to the effective minority carrier lifetime, τ_{eff}, since τ_{rad} is a constant for a given resistivity of Si. Thus, PL mapping of the EFG Si wafer will reveal the regions of good lifetime as

Table 8: Average values of PL intensities for I_{bb}, I_{def}, and R-parameter in each annealing step.

	Initial	Hydrogenated	600 °C/1 s dehydrogenated	700 °C/1 s dehydrogenated
I_{bb}	28.81	126.33	112.47	42.80
I_{def}	n.a.*	0.708	0.613	0.339
R-parameter	n.a.*	0.0111	0.0127	0.0237

* PL intensity below detection limit

high I_{bb}. According to Eq. (37), I_{def} is inversely proportional to the radiative component of the Shockley-Read-Hall lifetime. I_{def} is localized in low lifetime regions and generally gives nearly inverse contrast to I_{bb} and effective lifetime maps. The point-by-point ratio of the two PL intensities gives R (R-parameter), which is proportional to the concentration of radiative defects at a given illumination intensity. R is expressed by the following equation:

$$R = I_{\mathrm{def}}/I_{\mathrm{bb}} = \text{const.} \times N_{\mathrm{def}}. \tag{39}$$

R is independent of other recombination channels in the bulk and at the surface.

Table 8 summarizes the two PL intensities and R-parameter after 750°C/1 s hydrogenation and 600°C/1 s and 700°C/1 s dehydrogenation processes. I_{bb}, which is proportional to the effective carrier lifetime, increased from 29 to 126 (arbitrary unit) after 750°C/1 s RTP hydrogenation. The I_{bb} decreased from 126 to 42 after the subsequent 700°C/1 s dehydrogenation step. A substantial reduction in I_{bb} supports rapid dissociation of hydrogen from defect sites at 700°C, which was also observed experimentally in the previous section.

The PL maps of (a) I_{bb}, (b) I_{def}, and (c) point-by-point ratio of I_{bb} [$I_{\mathrm{bb}}(\textit{hydrogenated})$ $/I_{\mathrm{bb}}(\textit{initial})$] for the EFG Si sample are shown in Fig. 37. Figure 38 shows the results of a

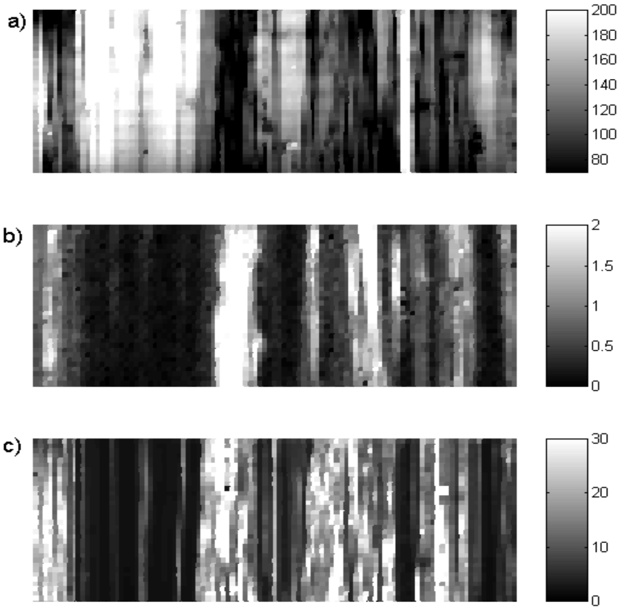

Figure 37: Room-temperature PL mappings of (a) band-to-band (I_{bb}), (b) defect band (I_{def}), and (c) point-by-point ratio of I_{bb}(hydrogenated)/I_{bb}(initial) representing the increase in lifetime. The mapping size is 50×22 mm^2, step=0.5 mm.

line-scan through the above sample at a specific location to assess spatial variation in the reduction in the carrier lifetime [$I_{\mathrm{bb}}(dehydrogenated)/I_{\mathrm{bb}}(hydrogenated)$] after 700°C/1 s dehydrogenation and the radiative defect concentration, R, after 750°C/1 s hydrogenation and 700°C/1 s dehydrogenation. The inverse contrast between I_{bb} and I_{def} can be seen in Fig. 37. It is clear from Figs. 37 and 38 that highly defective regions (low I_{bb} and high R) show much greater reduction in the effective lifetime after the 700°C/1 s dehydrogenation. Figure 38 also shows that in the low effective lifetime region, the impurity-decorated dislocations are the primary carrier recombination center. In addition, the R-parameter [$R(hydrogenated)$] is appreciable in those highly defective regions even after the 750°C/1 s hydrogenation, indicating that all defects are not fully passivated. Finally, the R-parameter increases dramatically in the defective regions after the 700°C/1 s anneal [$R(hydrogenated)$ versus $R(dehydrogenated)$], clearly indicating that significant defect dehydrogenation takes place in the area with high defect density. This is further supported by the increase in average R, which is proportional to the active defect concentration, from 0.0111 to 0.0237

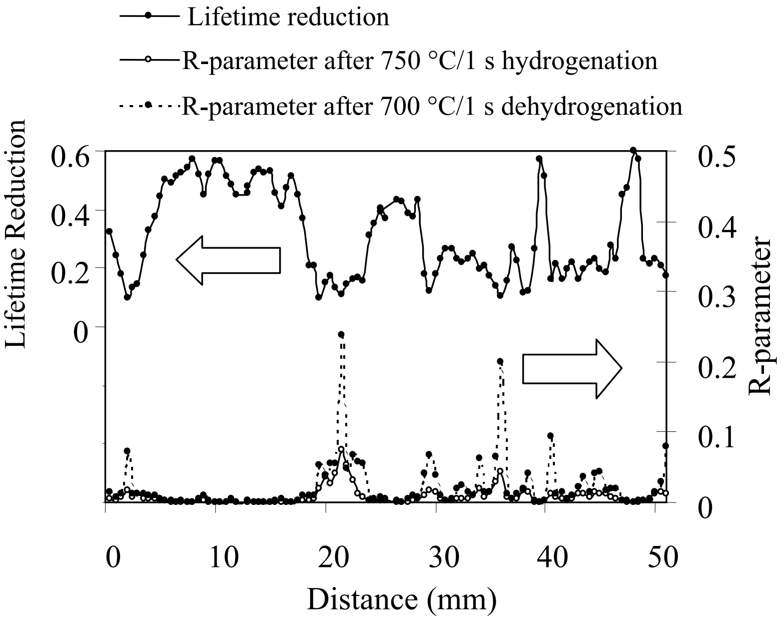

Figure 38: Line scan through a PL map to quantify the loss in carrier lifetime [I_{bb}(hydrogenated)/I_{bb}(dehydrogenated)] and R-parameters ($I_{\mathrm{def}}/I_{\mathrm{bb}}$) changes after hydrogenation and 700°C dehydrogenation.

after the 700°C/1 s dehydrogenation (Table 8). Figure 38 indicates that the reduction in the effective lifetime [$I_{\mathrm{bb}}(dehydrogenated)/I_{\mathrm{bb}}(hydrogenated)$], which is caused by the increase in non-radiative recombination centers, seems to be concurrent with the increase in radiative recombination centers or R. This is also supported by the inverse contrast between I_{bb} and I_{def}. Since I_{bb} increases as τ_{eff} increases [Eq. (36)], and τ_{eff} is dominated by the non-radiative recombination centers in Si, the concentration of non-radiative defects decreases with the increase in I_{bb}. Also, the PL intensity of I_{def} decreases with the increase in I_{bb} or τ_{eff} so τ_{SRH} must increase [Eq. (37)]. The τ_{SRH} represents the radiative component of recombination centers, so the concentration of radiative defects also seems to decrease with the increase in I_{bb}. Thus, dehydrogenation takes place concurrently from both radiative and non-radiative recombination defects, which is supported by the concurrent decrease in I_{bb} and increase in R.

5.4 Conclusions

In this chapter, a model was developed to explain the reason for the optimum firing cycle for defect hydrogenation. The FTIR measurements in SiN_x deposited on FZ Si wafer revealed that the total concentration of bonded hydrogen in SiN_x film decreases as a function of annealing time and temperature, and the rate of release slows down with time at a given temperature. This indicates that the SiN_x film is not an infinite source of hydrogen for defect hydrogenation. Since the supply of hydrogen decreases with time but the thermally-induced dehydrogenation of defects continues at the same rate at a given temperature, the effectiveness of hydrogenation decreases for prolonged firing. The SIMS analysis revealed that the trapped hydrogen at the damaged surface also diffuses into Si bulk or SiN_x layer after a short annealing process in an RTP unit. As a result, the surface concentration of deuterium dropped from 6.0×10^{19} cm^{-3} (as-deposited) to 2.0×10^{18} cm^{-3} (after 750°C/1 s).

A 700°C/1 s anneal in the absence of a hydrogen supply (SiN_x removed) lowered the carrier lifetime of a hydrogenated EFG Si sample from 99 μs to 8 μs, supporting the rapid dissociation of hydrogen-defect complexes during the hydrogenation cycle. Therefore, the optimum hydrogenation temperature and the degree of passivation are dictated by the competition between the supply of hydrogen and dissociation of hydrogen-defect complexes during the hydrogenation cycle. Activation energy for hydrogen-defect dissociation was found to be 2.4–2.6 eV, which falls between the activation energies for the dissociation of hydrogen-impurity and hydrogen-dislocation complexes, suggesting the hydrogenation of impurity-decorated dislocations in the EFG Si. This was also supported by by a defect band observed at 0.8 eV below the conduction band in the PL spectra. Scanning PL spectroscopy clearly showed that defective or low carrier lifetime regions are strongly passivated during the hydrogenation anneal and the same regions are reactivated rapidly during the dehydrogenation anneal. This rapid hydrogenation is the result of the competition between injection of hydrogen atoms from SiN_x film and dissociation from hydrogenated defects.

CHAPTER VI

FABRICATION AND ANALYSIS OF RECORD HIGH-EFFICIENCY STRING RIBBON SILICON SOLAR CELLS

String Ribbon Si is a promising candidate to achieve low-cost and high-efficiency Si solar cells. However, because of the low-cost crystal growth method and high thermal stresses during the material growth, String Ribbon Si not only has a high density of structural defects, such as dislocations, twins, and grain boundaries, but also relatively high concentrations of transition metal impurities that act as carrier recombination centers [29], as discussed in Chapter II. These defects lead to very low as-grown carrier lifetime in the range of 1–5 μs. Therefore, it is necessary to enhance the minority carrier lifetime during the solar cell fabrication in order to achieve high-efficiency solar cells. Impurity gettering during P diffusion, Al-doped back surface field (Al-BSF) formation, and defect hydrogenation from the PECVD SiN_x anti-reflection (AR) layer during contact firing are frequently used in both laboratory and industry with varying degree of success for carrier lifetime enhancement [139].

In spite of very low as-grown carrier lifetime, conversion efficiencies of ribbon Si solar cells are approaching or exceeding 15% in production and 18% in laboratory [122]. Figure 39 shows the efficiency progress of laboratory-scale ribbon cells on EFG Si and String Ribbon Si [35,39,103,105,119,140–146], including the results achieved in this study. Recently, Hahn and Geiger [103] reported 16.7% EFG and 17.7% String Ribbon Si solar cells (both 4 cm^2) using a combination of photolithography-defined front grid contact, thin thermal oxidation for front surface passivation, impurity gettering by annealing of evaporated Al, $\mathrm{ZnS/MgF_2}$ double-layer AR (DLAR) coating, and microwave-induced remote hydrogen plasma for bulk defect passivation. Later, 18.2% EFG and 17.9% String Ribbon Si solar cells were reported

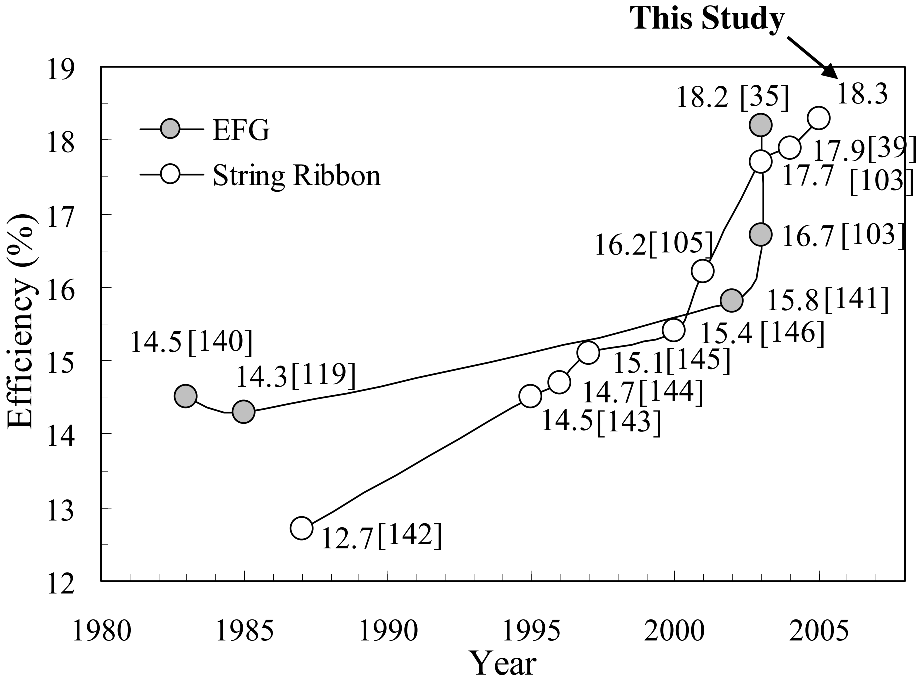

Figure 39: Progress of laboratory-scale ribbon (EFG and String Ribbon) Si solar cells.

by Rohatgi et al. [35, 39] using a laboratory process with photolithography-defined front grid contacts and DLAR coating. Hahn et al. [40] also reported high-efficiency (15.4% cell and 16.0% encapsulated) 80 cm^2 String Ribbon Si solar cells using screen-printing technique with a single-layer antireflection (SLAR) coating. Horzel et al. [36] recently reported 16.4% 92 cm^2 EFG Si solar cell using industry-scale processing but with SiN_x/MgF_2 DLAR coating and laser edge isolation process.

In this chapter, the understanding and fabrication technologies developed in Chapters IV and V are integrated to achieve record high-efficiency ribbon Si solar cells using photolithography-defined as well as screen-printed front grid contacts. This chapter describes the fabrication, characterization, and understanding of the high-efficiency ribbon Si solar cells and their future potential.

6.1 Device Fabrication

In this study, 2.0–3.0 Ωcm String Ribbon Si, grown at Evergreen Solar, Inc. (Marlboro, MA), was used. The FZ Si with a resistivity of 2.5 Ωcm was also included for comparison purpose. All the wafers were p-type (B-doped) with a thickness of ~300 μm.

After the initial cleaning process, the wafers were P diffused in a $POCl_3$ furnace at a set temperature of 850°C for 20 min to form an n^+ emitter with a sheet-resistance of 90–100 Ω/sq. A SiN_x SLAR coating with a thickness of 800 Å and a refractive index of 2.0 was deposited in a low-frequency (50 kHz) plasma-enhanced chemical vapor deposition (PECVD) reactor at 425°C. The front grid contact was formed by either photolithography or screen-printing techniques. For photolithography front contact cells, the deposited SiN_x layer was etched down from ~800 Å to ~700 Å to implement an optimized SiN_x/MgF_2 DLAR coating. For screen-printed cells, a commercial Al paste was screen printed on the entire back surface, and a commercial Ag paste was screen printed on the front followed by a contact firing in a rapid thermal processing (RTP) system (AG Associates Heatpulse 610). The temperature ramp-up rate of 75 °C/s and cooling rate of −40°C/s helped in the formation of an Al-BSF and also promoted SiN_x-induced defect hydrogenation. The temperature of the sample during the heat treatment in an RTP system was monitored by thermocouple mounted on the front surface. For photolithography cells, the front metal grid was defined by evaporation of Ti, Pd, and Ag and a lift-off process followed by Ag plating and evaporation of MgF_2 film to form DLAR coating. Several 4 cm^2 solar cells were fabricated on each large-area wafer and isolated by dicing saw prior to testing and analysis.

6.2 Device Characterization and Analysis

6.2.1 Solar cell results

Table 9 shows the average and best solar cell performance parameters obtained in this study. High V_{OC} values were achieved in String Ribbon Si solar cells (average V_{OC} of 613–615 mV and best V_{OC} of >630 mV). These V_{OC} values are among the highest values reported for ribbon Si solar cells so far, indicating that the PECVD SiN_x-induced defect hydrogenation

Table 9: Average and best solar cell performance parameters. (*) denotes the efficiency measured and verified at NREL.

	ID	V_{OC} (mV)	J_{SC} (mA/cm^2)	FF	Eff. (%)	# cells
Avg.	FZ PL	636	37.0	0.790	18.6	11
Best	2-85-1-9-5*	638	37.0	0.793	18.7	
Avg.	SR PL	615	35.6	0.787	17.2	21
Best	SR1-4*	634	36.8	0.782	18.3	
Avg.	FZ SP	634	34.9	0.760	16.8	12
Best	2-85-1-7-3*	635	34.9	0.768	17.0	
Avg.	SR SP	613	33.9	0.766	15.9	52
Best	SR4-1-1-9*	631	34.5	0.771	16.8	

was quite effective in enhancing the average minority carrier lifetime and reducing the inhomogeneity of electrically active defects in String Ribbon Si. This was attributed to the rapid contact firing in the RTP unit. In [144], the highest V_{OC} value of 639 mV was reported on 0.1 Ωcm String Ribbon Si with an efficiency of 14.7%. The conversion efficiency of 18.3% on 4 cm^2 cell achieved in this study with photolithography contact on String Ribbon Si represents the highest ribbon cell efficiency reported in the literature to date (Fig. 39). This efficiency value was nearly comparable to the 4 cm^2 planar cells (18.7%) fabricated on high-quality monocrystalline FZ simultaneously. In the case of the cells with screen-printed contacts, the best efficiency on String Ribbon Si was 16.8%, which is also comparable to the untextured, screen-printed FZ Si cells (17.0%). Several 4 cm^2 cells were fabricated on large-area String Ribbon Si to study the impact of material inhomogeneity on the solar cell performance. Figure 40 shows the distribution of cell efficiencies on the wafers that contain the 18.3% photolithography and 16.8% screen-printed cells, and Fig. 41

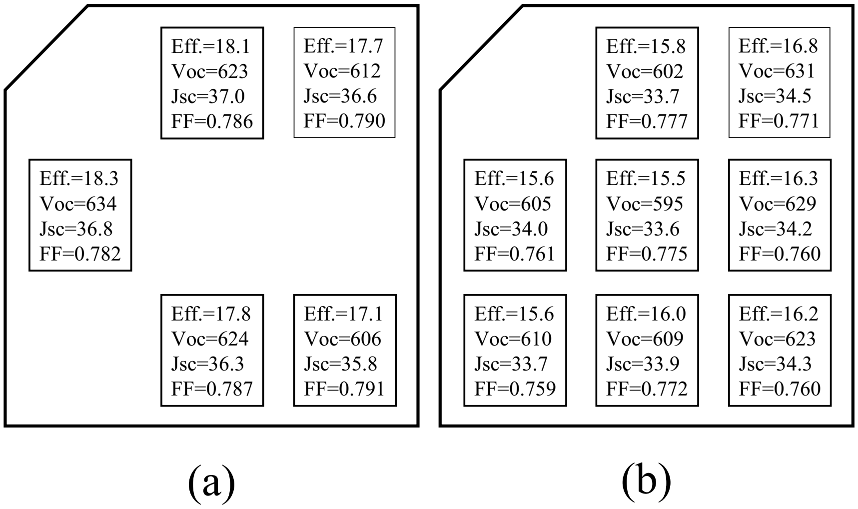

Figure 40: Distribution of cell efficiency on String Ribbon Si fabricated by (a) photolithography and (b) screen-printed front contacts. Cell size is 4 cm^2. Units are % in efficiency, mV in V_{OC}, and mA/cm^2 in J_{SC}.

shows the $I - V$ curves of record high-efficiency 18.3% String Ribbon Si cell fabricated with photolithography-defined front contacts as well as 16.8% screen-printed contacts. Those efficiencies were measured and confirmed at National Renewable Energy Laboratory (Golden, CO). Figure 42 shows the histogram of cell efficiency distribution for both photolithography and screen-printed cells fabricated on several different wafers in this study. Out of the 21 String Ribbon cells with photolithography contacts, 9 cells had an efficiency above 17%, 5 cells over 17.5%, and 2 cells over 18.0%. Out of the 52 screen-printed cells, 30 cells were in the range of 15.5–16.0%, 13 cells exhibited over 16.0% efficiency and 2 cells over 16.5%.

In addition to these record high-efficiency String Ribbon Si cells, the fabrication technologies developed in Chapters IV and V have resulted in very high-efficiency 4 cm^2 EFG Si cells. The EFG Si wafers were provided from SCHOTT Solar, Inc. (Billerica, MA) and have a resistivity of 3–4 Ωcm and a thickness of ~300 μm. Figure 43 illustrates the $I - V$ curves of high-efficiency EFG Si cells fabricated with photolithography-defined (18.2%) and screen-printed (16.6%) front contacts. The 18.2% and 16.6% cells were independently tested

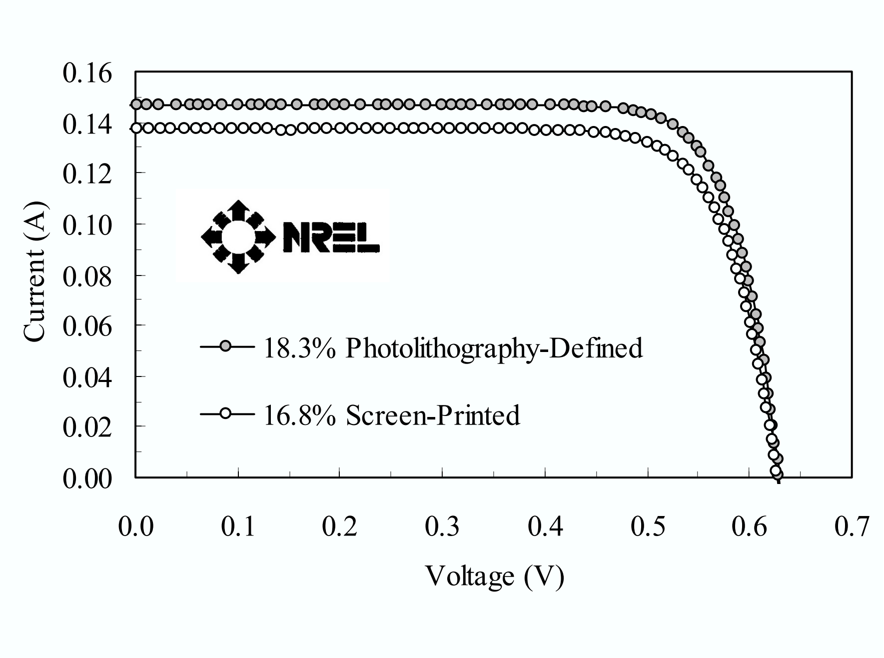

Figure 41: $I - V$ curves of record high-efficiency String Ribbon Si cells fabricated with photolithography (18.3%) and screen-printed (16.8%) contacts. Both cells were tested and confirmed by National Renewable Energy Laboratory.

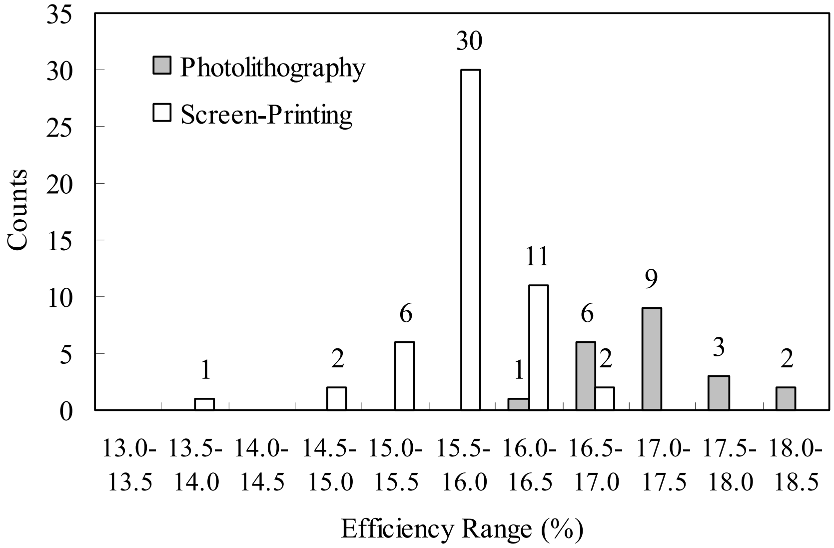

Figure 42: Histogram of solar cell efficiencies fabricated by photolithography and screen-printing front contacts.

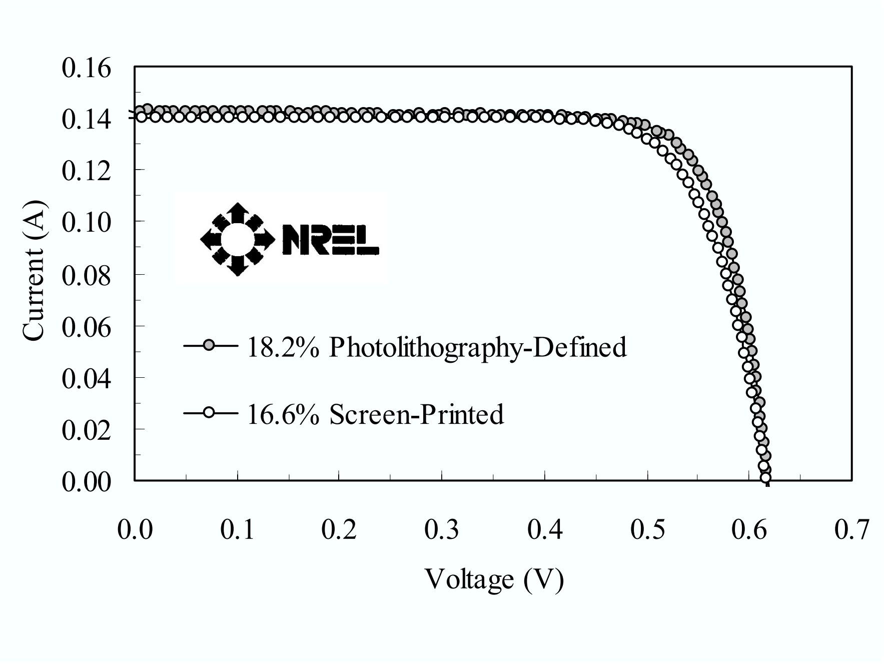

Figure 43: $I - V$ curves of high-efficiency EFG Si cells fabricated with photolithography (18.2%) and screen-printed (16.6%) contacts. Both cells were tested and confirmed by National Renewable Energy Laboratory.

at National Renewable Energy Laboratory and had V_{OC} of 624 mV and 620 mV, J_{SC} of 36.8 mA/cm^2 and 35.2 mA/cm^2, FF of 0.792 and 0.760, respectively. These high-efficiency (>18%) EFG Si cells, combined with String Ribbon Si cells, have provided a proof of the understanding and fabrication technologies developed in Chapters IV and V.

6.2.2 Carrier lifetime measurements using quasi-steady-state photoconductance technique

The key to achieving such high ribbon Si cell efficiencies was hydrogen passivation of defects during cell processing. In order to assess the effectiveness of SiN$_x$-induced defect hydrogenation on average lifetime enhancement, the carrier lifetime measurements were performed by quasi-steady-state photoconductance (QSSPC) technique on several locations at an injection level of 1.0×10^{15} cm^{-3} [20] on as-grown, P diffused, and fully processed String Ribbon Si wafers. Iodine/methanol solution [15] was used for surface passivation during the lifetime measurements. Figure 44 shows the results of average carrier lifetime measurements. The P diffusion gettering process enhanced the carrier lifetime from 2 μs (as-grown) to 8 μs.

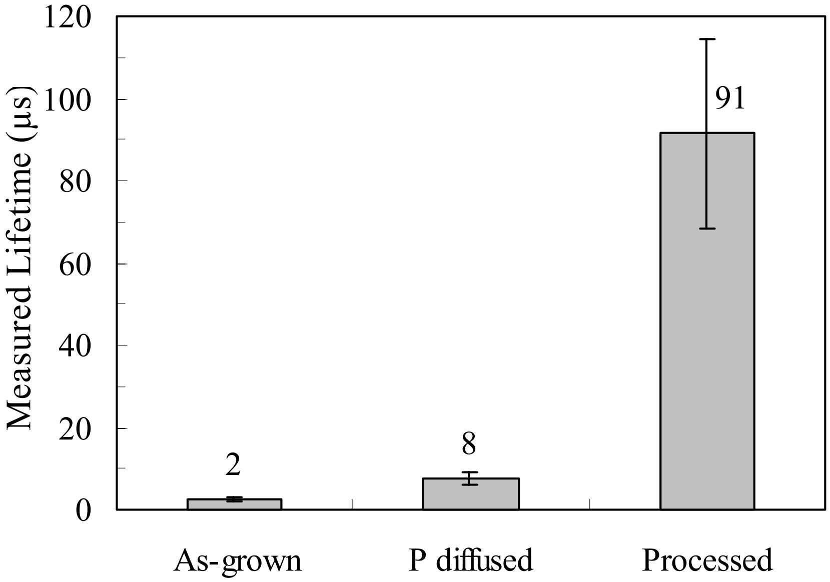

Figure 44: Average lifetime in 2.0–3.0 Ωcm String Ribbon Si after each process step. Measurements were performed on several wafers and points (5 wafers and total 40 points) to account for the inhomogeneous material quality. QSSPC technique was used at an injection level of 1.0×10^{15} cm^{-3}. Error bar in the graph represents the standard deviation.

The defect hydrogenation through PECVD SiN_x firing resulted in the lifetime enhancement from 8 μs to 91 μs in String Ribbon Si. Since the material quality of String Ribbon Si is quite inhomogeneous from wafer to wafer and within a wafer, the lifetime measurements were performed at 40 different locations on five String Ribbon Si wafers. It is important to perform the lifetime measurements at several different locations for establishing lifetime variation because the QSSPC technique itself measures an area-average lifetime over 3.7 cm diameter region [21].

6.2.3 Light beam-induced current scans and internal quantum efficiency measurements

Table 9 in the previous section showed that the best and average cell efficiencies for String Ribbon cells were 18.3% and 17.2% with photolithography contacts and 16.8% and 15.9% with screen-printed contacts, respectively. This gap between the best and average efficiencies is attributed to non-uniform distribution of active defects, even after the very effective defect hydrogenation, which raised the average carrier lifetime from 8 μs to 91 μs. In order to support that the electrically active defects are responsible for this efficiency gap, light beam-induced current (LBIC) scans were performed on selected String Ribbon Si solar cells using PVScan 5000 system [147] equipped with 980 nm laser to reveal the spatial non-uniformity in photoresponse over the entire device area. Figure 45 shows the LBIC scans of 18.3% (SR1-4) and 17.1% (SR1-3) String Ribbon solar cells. Note that these two cells were selected from the same wafer. The LBIC maps in Fig. 45 reveal that the 18.3% cell is relatively free of any localized active defects, which is reflected in the uniform current collection across the device. However, the 17.1% cell showed the presence of active defects over a considerable portion of the device. The impact of active defects on cell parameters can also be seen with the Suns-V_{OC} measurements [148]. The Suns-V_{OC} measurements in Table 10 showed that the 17.1% cell has much higher reverse saturation current density J_{o1} and junction leakage current density J_{o2} compared to the 18.3% nearly defect-free cell. This indicates that the defects in the 17.1% cell introduced the carrier recombination activity both in the bulk and depletion regions.

In an attempt to extract the effective minority carrier diffusion length (L_{eff}), the internal

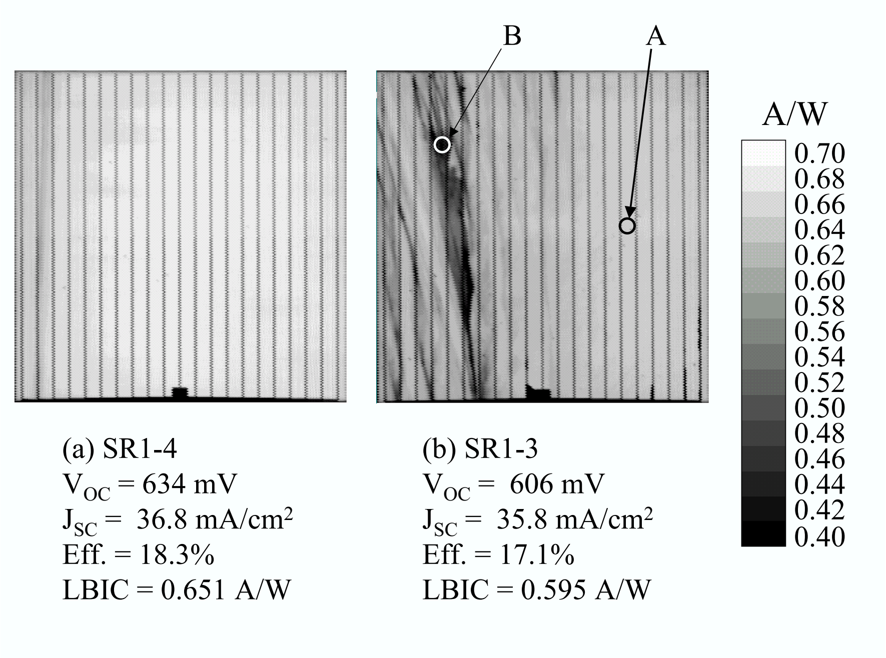

Figure 45: LBIC maps of (a) 18.3% (SR1-4) and (b) 17.1% (SR1-3) String Ribbon Si cells. PVScan 5000 system with 980 nm laser was used.

Table 10: Suns-V_{OC} measurements on selected solar cells. The second-diode ideality factor (n_2) was assumed to be 2.0.

ID	J_{o1} (pA/cm^2)	J_{o2} (nA/cm^2)	V_{OC} from J_{o1} (mV)	Measured V_{OC} (mV)
2-85-1-9-5 (FZ PL)	0.60	35.6	642	638
SR1-4 (SR PL)	0.95	38.5	631	634
SR1-3 (SR PL)	2.31	51.9	607	606
2-85-1-7-3 (FZ SP)	0.76	38.8	637	635
SR4-1-1-9 (SR SP)	0.87	34.8	632	631

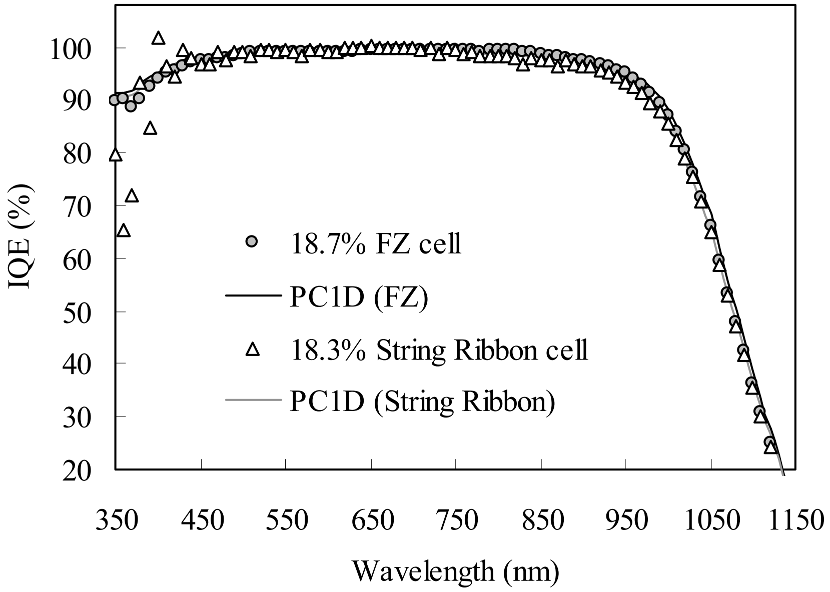

Figure 46: IQE response of 2.5 Ωcm FZ and 2.0-3.0 Ωcm String Ribbon Si cells. Simulated IQE response, corresponding to L_{eff} value of 1590 and 1060 μm, was obtained by PC1D.

quantum efficiency (IQE) measurements were performed on the 18.3% efficient homogeneous String Ribbon cell and the 18.7% FZ Si cell. The measured IQE response was fitted to the simulated IQE response using PC1D program [149]. The L_{eff} value in any region of a solar cell can be extracted by matching the measured and simulated local area IQE response in the long-wavelength range (700–920 nm for a 300 μm thick cells) using the PC1D simulation program [150]. Figure 46 shows the match between measured and simulated IQE response for the FZ and String Ribbon Si cells. The effective front surface recombination velocity (FSRV) was also determined by matching the measured and simulated short-wavelength IQE response [151]. The bulk carrier lifetime of 250 μs was used, which corresponds to the highest measured lifetime value using QSSPC technique. Base contact (or series resistance) and internal conductor (or shunt resistance) values were obtained from $I-V$ measurements. Table 11 shows the key input parameters used in PC1D simulations.

Matching of the simulated IQE with the experimental data gave an L_{eff} value of 1590 μm for the 18.7% FZ Si cell and 1060 μm for the 18.3% String Ribbon cell. The L_{eff} is

Table 11: PC1D inputs for FZ and String Ribbon Si solar cells.

Device Parameter	Input (FZ)	Input (String Ribbon)
Base resistivity (Ωcm)	2.5	2.0
Thickness (μm)	300	300
FSRV (cm/s)	40,000	40,000
Grid coverage (%)	3.5	3.5
Front surface coating	SiN_x/MgF_2 DLAR 70 nm, index = 2.00; 98 nm, index = 1.38	SiN_x/MgF_2 DLAR 70 nm, index = 2.00; 98 nm, index = 1.38
Rear internal reflectance	65%, diffuse	65%, diffuse
Front doping	Spreading resistance measurement	Spreading resistance measurement
Base contact (Series resistance)	0.3 Ω (0.3 $Ωcm^2$)	0.4 Ω (0.4 $Ωcm^2$)
Internal conductor (Shunt resistance)	4.35×10^{-6} S (230,000 $Ωcm^2$)	1.75×10^{-5} S (57,000$Ωcm^2$)
J_{o2} (A/cm^2)	3.56×10^{-8}	3.85×10^{-8}
Bulk lifetime (μs)	1000	250
BSRV (cm/s)	200	225

Table 12: Solar cell performance parameters using PC1D simulations with carrier lifetime of 2 μs for photolithography and screen-printed contacts.

	Voc (mV)	Jsc (mA/cm^2)	FF	Eff. (%)
PL	570	31.1	0.784	13.9
SP	570	29.7	0.774	13.1

given by the following equation [152].

$$L_{\text{eff}} = L_b \left(\frac{1 + \frac{SL_b}{D_n} \tanh \frac{W}{L_b}}{\frac{SL_b}{D_n} + \tanh \frac{W}{L_b}} \right), \tag{40}$$

where S represents the back surface recombination velocity (BSRV), L_b ($= \sqrt{D_n \tau_b}$) is the bulk minority carrier diffusion length, τ_b is the bulk carrier lifetime, and W is the cell thickness. According to Eq. (40), L_{eff} is primarily a composite of bulk and surface recombination for a given resistivity and thickness.

6.2.4 Effect of defect hydrogenation on cell performance

In order to quantify the effect of the optimized defect hydrogenation process on String Ribbon Si cell performance, PC1D simulations were performed using the input parameters shown in Table 11 with a bulk lifetime of 2 μs, which corresponds to the as-grown lifetime in String Ribbon Si (Fig. 44). Table 12 shows the results of PC1D simulations with lifetime of 2 μs for photolithography and screen-printed contacts. If we did not succeed the lifetime enhancement during the cell processing, the efficiency would have resulted in only 13.9% for photolithography and 13.1% for screen-printed contacts. These values are 3.7–4.4% lower than what we have achieved on record high-efficiency cells (18.3% and 16.8%). The PC1D

Table 13: Measured and simulated characteristics on FZ and String Ribbon Si cells using the input parameters listed in Table 11.

Material		V_{OC} (mV)	J_{SC} (mA/cm^2)	FF	Eff. (%)
FZ	Measured	638	37.0	0.793	18.7
	Simulated	636	37.0	0.791	18.6
String Ribbon	Measured	634	36.8	0.782	18.3
	Simulated	632	36.8	0.783	18.2

simulations indicate a successful implementation of the impurity gettering during the P diffusion and defect hydrogenation during the contact firing.

6.2.5 Analysis of performance limiting factors in 18.3% String Ribbon Si cell

The previous section showed that the best 4 cm^2 solar cell performance on String Ribbon Si can approach that of the untextured FZ Si cells. This indicates that the performance of well-passivated String Ribbon cell is not limited by the minority carrier lifetime since FZ Si has a much higher carrier lifetime ($\geq$500 μs). In order to identify the performance limiting factors in these high-efficiency String Ribbon cells and explore how to improve the efficiency further, device simulations were performed using PC1D. First, a good match was obtained between the measured and simulated best String Ribbon Si cell with photolithography contacts with an efficiency of 18.2% and a V_{OC} of 632 mV (Table 13). Next, the carrier lifetime was increased from 250 μs to 500 μs in PC1D, which showed an increase of only 0.1% in absolute efficiency with the doubling in carrier lifetime. This suggests that further lifetime enhancement in good regions of String Ribbon Si will not produce a significant improvement in cell performance. This is not surprising because when the bulk quality becomes high enough, $L_b \gg W$, the carrier recombination at the front and/or rear surface becomes more important. Therefore, the FSRV was decreased in PC1D simulation from 40,000 cm/s to 35,000 cm/s [153], keeping the carrier lifetime fixed at 250 μs. However, no appreciable improvement was observed due to this FSRV reduction. This means that the bulk component of saturation current density J_{ob} or BSRV is limiting the efficiency. Next, the BSRV was reduced from 225 cm/s to 100 cm/s, which gave an improvement of 0.2% in absolute cell efficiency, with a V_{OC} rising to 638 mV. The BSRV of 100 cm/s can be achieved by employing the appropriate rear surface passivation scheme, such as dielectric passivation. Recently, very low surface recombination velocity (less than 100 cm/s) was demonstrated on p-type, 1.5 Ωcm monocrystalline Si by applying the deposition of amorphous Si for rear surface passivation [154]. The dielectric rear surface passivation scheme can also provide a significant improvement in the reflection (90–95% as opposed to 60–65% for Al-BSF) from rear surface [155]. PC1D simulations showed that a combination of improved BSRV to 100 cm/s and BSR to 90% can drive the planar String Ribbon Si cell efficiency with photolithography contacts to 19.0% with a V_{OC} of 638 mV, J_{SC} of 38.1 mA/cm^2, and FF of 0.782 on 2.0 Ωcm material (Table 14). Finally, successful implementation of surface texturing can push the cell efficiency closer to 20%.

6.3 Conclusions

In this chapter, String Ribbon Si solar cells with efficiencies as high as 18.3% and 16.8% (both 4 cm^2) were achieved with photolithography-defined and screen-printed front grid contacts, respectively, using an optimized defect hydrogenation process for carrier lifetime enhancement. In addition, 18.2% and 16.6% EFG Si cells were achieved using the identical process sequence. The 18.3% String Ribbon Si cell is the highest ribbon Si cell efficiency reported in the literature to date. In this study, the area-average carrier lifetime increased from 2–3 μs to >90 μs due to a combination of P diffusion-induced impurity gettering and low-frequency PECVD SiN$_x$-induced defect hydrogenation in String Ribbon Si. It was also found through LBIC analysis that the gap between the best and an average efficiency is

Table 14: Analysis of performance limiting factors on 18.3% String Ribbon Si cell.

Parameter	V_{OC} (mV)	Efficiency (%)
Current simulated cell	632	18.2
Lifetime 250 → 500 μs	634	18.3
FSRV 40,000 → 35,000 cm/s	633	18.2
BSRV 225 → 100 cm/s	638	18.4
BSRV 100 cm/s BSR 90%	638	19.0

primarily attributed to the presence of electrically active defects within the cell area, even after the very effective defect hydrogenation, which raised the average carrier lifetime from 8 μs to >90 μs. The presence of inhomogeneously distributed active defects lowered the solar cell performance significantly by enhancing the carrier recombination in both bulk and depletion regions. Detailed characterization and analysis revealed that the efficiency of String Ribbon Si cells with photolithography contacts can be improved to 19% by developing the high-quality rear surface passivation scheme that can lower the BSRV from 225 cm/s to 100 cm/s and increase the BSR from 65% to 90%.

CHAPTER VII

UNDERSTANDING OF THE EFFECT OF MATERIAL INHOMOGENEITY ON STRING RIBBON SILICON SOLAR CELL PERFORMANCE

In the previous chapter, the record high-efficiency ribbon Si cells were successfully fabricated through understanding and development of process technologies, and it was found that the presence of active defects showed a detrimental effect on cell performance by analyzing and comparing the high-efficiency and average cells using LBIC scans. However, the inhomogeneously distributed electrically active defects are frequently found to be present in the mc-Si materials, even after effective P diffusion gettering and the SiN_x-induced hydrogen passivation of defects. Therefore, understanding and assessing the impact of the inhomogeneous distribution of defects on solar cell performance has become an area of active investigation. For example, Sopori [156] made an attempt to quantify the influence of material inhomogeneities on solar cell performance by developing a methodology and technique to extract an effective minority carrier diffusion length (L_{eff}) from the lateral and vertical distribution of defects to assess their impact on open-circuit voltage (V_{OC}). Mijnarends *et al.* [157] performed numerical simulations to investigate the effect of lateral variations in material quality on solar cell characteristics and found that the wider distribution of diffusion length is detrimental to cell performance. In [158], a practical investigation was performed by fabricating multiple mini solar cells (0.9×0.9 mm^2) to examine V_{OC} across the mc-Si wafer. A strong correlation between local V_{OC} and minority carrier diffusion length was confirmed in these mini solar cells. It was concluded that a narrow distribution of diffusion length is desirable. Bell *et al.* [159] concluded that material inhomogeneities can significantly limit the voltage output, and grains with the low carrier lifetime determine the V_{OC} of mc-Si cells. Warta *et al.* [160] pointed out the limitations of the one-dimensional simulation tools for assessing or predicting the performance of a mc-Si solar cell with a defective crystal structure. A diode network model was proposed and applied to compare the simulated and measured mc-Si solar cell performance. Nagel *et al.* [161] used the diode network model developed in [160] to simulate the solar cell performance parameters on the basis of lifetime mapping on commercial cast material, neglecting the surface recombination and metal contact effects. In [162], the diode network model was also used to demonstrate that a 20% defective region can lead to a 30 mV reduction in V_{OC}. Donolato [163] applied the Voronoi network model to mc-Si with columnar grains and showed that the grains with low carrier lifetime are responsible for the reduction in V_{OC}. Isenberg *et al.* showed by two-dimensional DESSIS simulations that the network model is not applicable if the lateral size of defective structures is smaller than the thickness or diffusion length in good regions.

In this chapter, an effort is made to improve the experimental and theoretical understanding of the impact of spatial distribution of defect inhomogeneities on fully processed high-performance screen-printed ribbon mc-Si solar cells. Since ribbon Si materials generally have an as-grown carrier lifetime below 5 μs, an attempt is made to enhance the gettering and passivation techniques to raise the average carrier lifetime above 90 μs in order to increase the sensitivity and the impact of low diffusion length regions (bad regions). Several 4 cm^2 screen-printed String Ribbon Si solar cells are fabricated and a simple methodology is developed to approximately determine the loss in V_{OC} in these cells resulting from a small fraction of bad region mixed with a large fraction of good region. Model calculations are performed by developing and using simple and approximate analytical expressions to assess the impact of recombination intensity and area fraction of bad regions on V_{OC}. Model calculations are compared with the experimental data to demonstrate that loss in V_{OC} resulting from material inhomogeneity can be predicted with reasonable accuracy by dividing the cell into two regions (best and worst) and using this simple analytical model.

7.1 Experiment

In this study, 300 μm thick, p-type 3–4 Ωcm String Ribbon Si material from Evergreen Solar, Inc. (Marlboro, MA) was used. After the initial cleaning process, the wafers were P diffused in a $POCl_3$ furnace to form 40–50 Ω/sq n^+ emitters. A SiN_x anti-reflection coating with a thickness of 800 Å and a refractive index of 2.0 was deposited in a low-frequency plasma-enhanced chemical vapor deposition (PECVD) reactor. A commercial Al paste was then screen printed on the entire back surface and an Ag grid was screen printed on the front, followed by an anneal in a rapid thermal processing (RTP) system to (i) form an Al-doped back surface field (Al-BSF) on the rear surface, (ii) form a screen-printed Ag ohmic contact on the front surface, and (iii) promote the SiN_x-induced hydrogen passivation of defects. Several 4 cm^2 solar cells were fabricated on each wafer and isolated using a dicing saw, followed by a forming gas anneal at 400 °C for 10 min. The solar cell parameters were extracted by illuminated and dark current-voltage ($I - V$) measurements. The light beam-induced current (LBIC) scans were performed on selected solar cells to map the spatial non-uniformity of photoresponsivity using the PVScan 5000 system [147] equipped with a 980 nm laser. Several regions on each solar cell were then selected to perform local light-biased internal quantum efficiency (IQE) measurements to quantify the difference in material quality in those regions in terms of L_{eff}, which includes bulk and surface effects.

7.2 Results and Discussion

7.2.1 Light beam-induced current scans and internal quantum efficiency measurements

The LBIC scan was performed on each cell to detect the material inhomogeneity in terms of the recombination intensity of electrically active defects. LBIC measures the short-circuit current generated at each spot on the cell. Photoresponse is expressed as Amperes/Watt (A/W). Since several 4 cm^2 solar cells were fabricated on each large-area String Ribbon Si wafer, we selected the wafer containing cells with high, moderate, and low V_{OC} to conduct our study to evaluate the impact of inhomogeneously distributed electrically active defects on V_{OC}. Figure 47 shows the LBIC maps of three String Ribbon Si solar cells on the same wafer with high, moderate, and low V_{OC}. These cells were selected because they also showed maximum contrast between defective and defect-free regions. Table 15 shows the electrical performance parameters of these three String Ribbon Si solar cells. The LBIC maps in Fig. 47 show that cell 1 has relatively uniform current collection over the entire cell area,

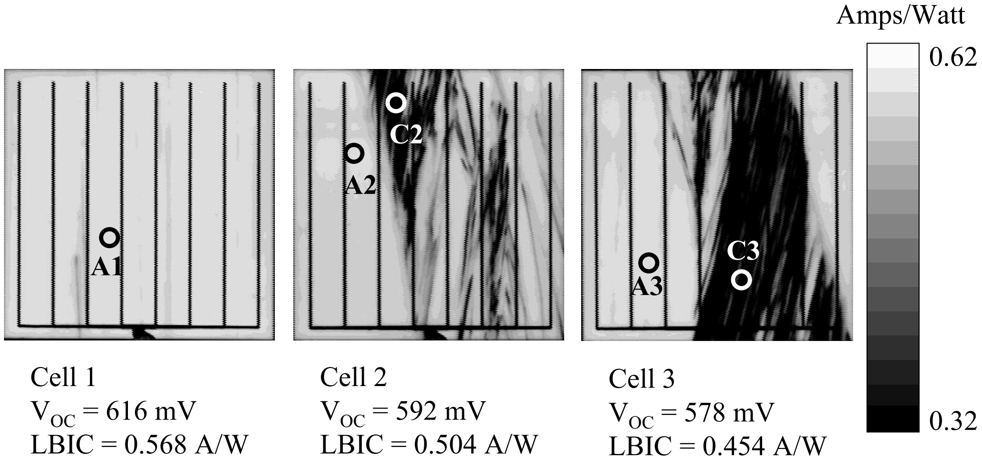

Figure 47: LBIC scans of String Ribbon Si solar cells. High, moderate, and low V_{OC} cells are shown in left, center, and right sides, respectively.

compared to the other two, with little or no detectable bad regions. This is also reflected in the high area-averaged LBIC response of 0.568 A/W along with a high V_{OC} of 616 mV and a cell efficiency of 15.9%. Cells 2 and 3 had a much lower V_{OC} of 592 and 578 mV with cell efficiencies of 15.0% and 14.1% and corresponding area-averaged LBIC response of 0.504 and 0.454 A/W, respectively (Table 15). After the illuminated $I - V$ measurements and LBIC scans, light-biased IQE measurements [164] were taken in selected areas of these String Ribbon Si solar cells, indicated by the circles in Fig. 47. Circles drawn are for visual aid and larger than the actual spot size (~1 mm in diameter) used for the IQE measurements. IQE represents the number of electrons collected per incident photon under short-circuit condition. This is measured as a function of wavelength. The circled regions A1, A2, and A3 on cells 1, 2, and 3, respectively, were selected based on the LBIC maps because they had the highest and nearly equal LBIC responses. These represent the best regions on the three cells. On the other hand, regions C2 and C3 on cells 2 and 3, respectively, gave the

Table 15: Measured String Ribbon Si solar cell parameters and LBIC responses

Cell ID	V_{OC} (mV)	J_{SC} (mA/cm^2)	FF	Eff. (%)	LBIC (A/W)
1	616	33.5	0.773	15.9	0.568
2	592	32.7	0.774	15.0	0.504
3	578	31.4	0.778	14.1	0.454

lowest LBIC response, indicating that these regions are the most defective regions on the cell. Figure 48 shows the light-biased IQE response of all five regions (A1, A2, A3, C2, and C3). As expected, regions C2 and C3 showed a significant degradation in the IQE response in the long-wavelength range (>650 nm) relative to regions A1, A2, and A3. The IQE response in the long-wavelength range is indicative of the combined effect of carrier lifetime and back surface recombination velocity (BSRV) for 300 μm thick Si cells [165]. Consistent with the LBIC response, there was no appreciable difference in the IQE response of regions A1, A2, and A3 in the long-wavelength range, supporting the fact that the best regions on the three solar cells (1, 2, and 3) are nearly identical, despite the significant difference in V_{OC} and defect inhomogeneity.

7.2.2 Extraction of effective diffusion length L_{eff} from the IQE response

V_{OC} is a strong function of recombination in the emitter, base, and at the surfaces. According to theory, the V_{OC} can be expressed as follows [5]:

$$V_{\mathrm{OC}} = \frac{kT}{q} \cdot \ln\Big(\frac{J_{\mathrm{SC}}}{J_{\mathrm{oe}} + J_{\mathrm{ob}}} + 1\Big), \tag{41}$$

where k is the Boltzmann constant, T is the temperature, J_{SC} is the short-circuit current density, J_{ob} is the base components of saturation current density, and J_{oe} is the emitter

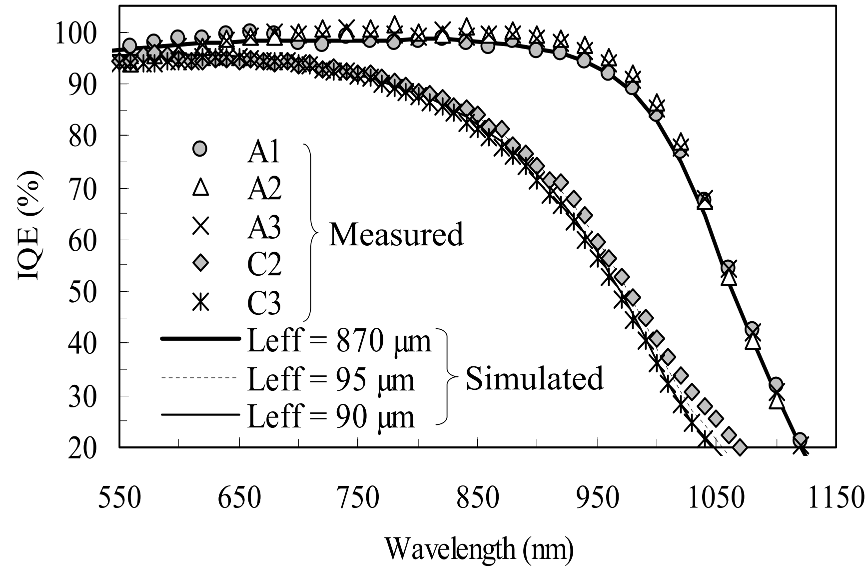

Figure 48: Light-biased IQE response of selected regions (A1, A2, A3, C2, and C3) in String Ribbon Si solar cells and simulated (PC1D) IQE response corresponding to L_{eff} values of 870 μs, 95 μm, and 90 μm.

component of saturation current density. Since the three solar cells were selected from the same wafer, they should have identical emitters, and their J_{oe}, which is a function of emitter doping profile and surface recombination velocity, can be assumed to be identical. Thus, the J_{ob}, which is a function of carrier lifetime and BSRV, must account for the majority of the difference in V_{OC}. The J_{ob} is expressed as follows [152]:

$$J_{\text{ob}} = \frac{qn_i^2 D_n}{N_B L_{\text{eff}}}, \tag{42}$$

where q is the electron charge, n_i is the intrinsic carrier concentration, D_n is the diffusion coefficient of electron, and N_B is the background doping concentration. The effective minority carrier diffusion length, L_{eff}, is defined as [152]:

$$L_{\text{eff}} = L_b \left(\frac{1 + \frac{SL_b}{D_n} \tanh \frac{W}{L_b}}{\frac{SL_b}{D_n} + \tanh \frac{W}{L_b}} \right), \tag{43}$$

where S represents the BSRV, L_b $(= \sqrt{D_n \tau_b})$ is the bulk minority carrier diffusion length, τ_b is the bulk carrier lifetime, and W is the cell thickness. According to Eq. (43), L_{eff} is primarily a function of bulk and surface recombination for the fixed resistivity and thickness.

The L_{eff} value in any region of a solar cell can be extracted by matching the measured and simulated local area IQE response in the long-wavelength range (700−920 nm for 300 μm thick cells) using the PC1D simulation program [150]. This was done by determining and/or using the realistic inputs for the PC1D simulations. For example, front surface recombination velocity (FSRV) was extracted from the measured IQE response in the short-wavelength range [151]. Front doping was determined by the spreading resistance measurement. Base contact (or series resistance) and internal conductor (or shunt resistance) values were obtained from illuminated $I-V$ measurements. The internal diode or junction leakage current (J_{o2}) value was extracted from the dark $I-V$ measurement, assuming the second-diode ideality factor of 2.0. Uniform distribution of D_n was assumed during the L_{eff} extraction using PC1D. The IQE response in long-wavelength range represents the correct value of L_{eff}, which is composed of L_b and BSRV, regardless of the D_n and τ_b values. Figure 48 also shows the match between the measured and simulated IQE response from all five regions, resulting in an L_{eff} of ∼870 μm for regions A1, A2, and A3, ∼95 μm for region C2, and ∼90 μm for region C3. This was done by fixing the BSRV at 250 cm/s and varying the L_b (or τ_b) in PC1D until a good match in the long-wavelength range was achieved. BSRV and L_b were then used to obtain L_{eff} from Eq. (43). Note that these BSRV and L_b values do not necessarily represent the true BSRV and L_b values, but they still give the correct value of L_{eff}. This is because the L_{eff} is a function of both L_b (or τ_b) and BSRV [Eq. (43)]. This was validated by choosing different values of BSRV and performing the same procedure on IQE. As expected, different combinations of L_b and BSRV led to the same L_{eff} value.

The L_{eff} value of 870 μm in region A1, in conjunction with the PC1D inputs in Table 16, was used to obtain the simulated solar cell $I-V$ parameters, which agreed very well with the measured parameters of cell 1 (Table 17), which was nearly uniform. However, as expected, there was a significant difference between the measured solar cell parameters of the defective or low-quality solar cell 3 (Table 17) and the simulated cell parameters when a L_{eff} of 870 μm was used for the entire cell. Table 17 shows that there is a difference of 37 mV in V_{OC}. This difference is largely attributed to the existence of electrically active

Table 16: PC1D input parameters for String Ribbon Si solar cell simulation.

Device Parameter	**Input**
Base resistivity	3.0 Ωcm
Thickness	300 μm
FSRV	150,000 cm/s
Broadband reflectance	6.0%
Front surface coating	78 nm, index = 2.0
Rear internal reflectance	55%, diffuse
Front doping	Spreading resistance measurement
Base contact (Series resistance)	0.75 Ω (0.75 Ωcm^2)
Internal conductor (Shunt resistance)	5.0x10^{-5} S (2.0x10^4 Ωcm^2)
J_{o2}	2.6x10^{-8} A

defects. This demonstrates that the presence of active defects can significantly lower the V_{OC}. This is because the cell from the good and bad regions of a device act in parallel and the lower V_{OC} associated with the bad region pulls down the V_{OC} of the good regions and the entire cell.

The next section shows the development of a simple analytical model to calculate the loss in V_{OC} from the area fraction and recombination intensity of the electrically active defects. The simulated results are then compared with the experimental data in Table 17. Cell 1, which does not have defect inhomogeneity, agrees well with the simulated cell with L_{eff} of 870 μm. However, cell 3, which has significant defect inhomogeneity, is far below the simulated results. Following section deals with the development of an analytical model to explain the difference between cells 1 and 3.

Table 17: Measured and simulated solar cell parameters on String Ribbon Si using an extracted L_{eff} of 870 μm.

Cell ID	V_{OC} (mV)	J_{SC} (mA/cm^2)	Eff. (%)
Simulated	615	33.6	15.9
1	616	33.5	15.9
3	578	31.4	14.1

7.3 Theoretical and Experimental Assessment of Impact of Electrically Active Defects on Solar Cell Performance

7.3.1 Development of the analytical model to assess the loss in V_{OC} resulting from inhomogeneity

The non-uniform distribution of defects, such as grain boundaries, impurities, and dislocations, is common in mc-Si materials. Many of these defects act as localized carrier recombination centers resulting in spatial variation in L_{eff}.

The first step was to develop a simple and approximate analytical model for the quantitative assessment of the effect of distributed L_{eff} on V_{OC}. A mc-Si solar cell is essentially composed of a number of small solar cells (good and bad regions) in parallel, operating at a constant potential across the junction as a result of the electrical connection through grid, emitter, and substrate [21]. The total cell current, I, can be expressed as the summation of currents from local area cells:

$$I = I_1 + I_2 + \cdots + I_i. \tag{44}$$

Assuming the two-diode model and neglecting the series and shunt resistances, Eq. (44)

can be expressed as:

$$\begin{aligned}I_{\mathrm{o1}}\Big[\exp\Big(\frac{qV}{kT}\Big)-1\Big]+I_{\mathrm{o2}}\Big[\exp\Big(\frac{qV}{n_2kT}\Big)-1\Big] &= \\ I_{\mathrm{o1,1}}\Big[\exp\Big(\frac{qV}{kT}\Big)-1\Big] &+ I_{\mathrm{o2,1}}\Big[\exp\Big(\frac{qV}{n_2kT}\Big)-1\Big] \\ +I_{\mathrm{o1,2}}\Big[\exp\Big(\frac{qV}{kT}\Big)-1\Big] &+ I_{\mathrm{o2,2}}\Big[\exp\Big(\frac{qV}{n_2kT}\Big)-1\Big] \\ +\cdots+I_{\mathrm{o1,i}}\Big[\exp\Big(\frac{qV}{kT}\Big)-1\Big] &+ I_{\mathrm{o2,i}}\Big[\exp\Big(\frac{qV}{n_2kT}\Big)-1\Big],\end{aligned} \tag{45}$$

where V is the junction potential, I_{o1} and I_{o2} are the dark saturation current and the junction leakage current, respectively, and n_2 is the second diode ideality factor [166]. Since the I_{o2} component generally has a much smaller contribution to total current at V_{OC} compared to I_{o1} component, Eq. (45) can be approximated as:

$$I_{\mathrm{o1}} = I_{\mathrm{o1,1}} + I_{\mathrm{o1,2}} + \cdots + I_{\mathrm{o1,i}}, \tag{46}$$

$$I_{\mathrm{oe}} + I_{\mathrm{ob}} = (I_{\mathrm{oe,1}} + I_{\mathrm{ob,1}}) + (I_{\mathrm{oe,2}} + I_{\mathrm{ob,2}}) + \cdots + (I_{\mathrm{oe,i}} + I_{\mathrm{ob,i}}), \tag{47}$$

where I_{oe} and I_{ob} are the emitter and base component of the saturation current, respectively.

Due to the high quality of the solar cell emitters used in this work and the same emitter quality for good and bad regions, any variation in $I_{\mathrm{o1,i}}$ can be attributed to the variation in $I_{\mathrm{ob,i}}$. Thus, the emitter contributions to the variation in saturation currents $I_{\mathrm{o1,i}}$ can be neglected compared to the base layer contributions $I_{\mathrm{ob,i}}$. Equation (47) can therefore be approximated to

$$I_{\mathrm{ob}} = I_{\mathrm{ob,1}} + I_{\mathrm{ob,2}} + \cdots + I_{\mathrm{ob,i}}, \tag{48}$$

$$a \cdot J_{\mathrm{ob,avg}} = a_1 \cdot J_{\mathrm{ob,1}} + a_2 \cdot J_{\mathrm{ob,2}} + \cdots + a_i \cdot J_{\mathrm{ob,i}}, \tag{49}$$

$$J_{\mathrm{ob,avg}} = A_1 \cdot J_{\mathrm{ob,1}} + A_2 \cdot J_{\mathrm{ob,2}} + \cdots + A_i \cdot J_{\mathrm{ob,i}}, \tag{50}$$

where $J_{\mathrm{ob,avg}}$ is the area-weighted average of J_{ob}, a is the actual area, and A_i is the area fraction (a_i/a) of each region. Since J_{ob} is inversely proportional to the L_{eff} [Eq. (42)], Eq. (50) can be written as:

$$L_{\mathrm{eu}}^{-1} = A_1 \cdot L_{\mathrm{eff,1}}^{-1} + A_2 \cdot L_{\mathrm{eff,2}}^{-1} + \cdots + A_i \cdot L_{\mathrm{eff,i}}^{-1}. \tag{51}$$

The area-weighted average or effective uniform value of L_{eff} (L_{eu}) can now be expressed as:

$$L_{\text{eu}}^{-1} = \sum_{i=1}^{n}(L_{\text{eff,i}}^{-1} \times A_i). \tag{52}$$

The area-weighted average or effective J_{ob} ($J_{\text{ob,eff}}$) can now be determined by Eq. (42) using the L_{eu}. Finally, the $J_{\text{ob,eff}}$ can be used as follows to obtain the V_{OC}.

$$\begin{aligned} V_{\text{OC}} &= \frac{kT}{q}\ln\Big(\frac{J_{\text{SC}}}{J_{\text{o}}}+1\Big) \\ &= \frac{kT}{q}\ln\Big(\frac{J_{\text{SC}}}{J_{\text{ob,eff}}+J_{\text{oe}}}+1\Big) \\ &\simeq \frac{kT}{q}\ln\Big(\frac{J_{\text{SC}}}{J_{\text{ob,eff}}}+1\Big), \end{aligned} \tag{53}$$

where

$$J_{\text{ob,eff}} = \frac{qn_i^2 D_n}{N_B L_{\text{eu}}}. \tag{54}$$

Note that Eq. (53) ignores the effect of J_{oe}, which is the case for these relatively low V_{OC} (<620 mV) solar cells where base quality dominates the V_{OC}. To support this assumption, J_{oe} was measured on high-resistivity (500−1000 Ωcm) n-type FZ Si using a photoconductance decay technique after double-sided P diffusion, SiN_x deposition, and firing in an RTP unit without the metallization. The measured J_{oe} of 187 fA/cm^2, without metallization, corresponds to a V_{OC} of 671 mV (assuming J_{SC} of 33.5 mA/cm^2), which is much higher than the measured V_{OC} of these cells. The presence of a front grid is expected to lower the emitter-limited value of V_{OC} somewhat, but it will still be much higher than the actual V_{OC} of these cells.

The loss in V_{OC} can now be calculated using the following analytical expression:

$$\begin{aligned} \Delta V_{\text{OC}} &= V_{\text{OC(defect-free)}} - V_{\text{OC(defective)}} \\ &= \frac{kT}{q}\Big[\ln\Big(\frac{J_{\text{SC,high}}}{J_{\text{ob,high}}}+1\Big) - \ln\Big(\frac{J_{\text{SC,avg}}}{J_{\text{ob,eff}}}+1\Big)\Big] \\ &\simeq \frac{kT}{q}\Big[\ln\Big(\frac{J_{\text{SC,high}}}{J_{\text{ob,high}}}\Big) - \ln\Big(\frac{J_{\text{SC,avg}}}{J_{\text{ob,eff}}}\Big)\Big] \\ &= \frac{kT}{q}\ln\Big(\frac{J_{\text{SC,high}}}{J_{\text{SC,avg}}}\cdot\frac{J_{\text{ob,eff}}}{J_{\text{ob,high}}}\Big) \\ &= \frac{kT}{q}\ln\Big(\frac{J_{\text{SC,high}}}{J_{\text{SC,avg}}}\cdot\frac{L_{\text{eff,high}}}{L_{\text{eu}}}\Big), \end{aligned} \tag{55}$$

where $V_{\mathrm{OC(defect\text{-}free)}}$ corresponds to the V_{OC} value in the absence of localized bad regions with uniformly distributed high L_{eff} value ($L_{\mathrm{eff,high}}$=870 μm in this study). $V_{\mathrm{OC(defective)}}$ corresponds to L_{eu} and includes the combined effect of bad regions. The $J_{\mathrm{SC,high}}$ and $J_{\mathrm{SC,avg}}$ values, corresponding to $L_{\mathrm{eff,high}}$ and L_{eu} were obtained from PC1D simulations by fixing the BSRV to the same value (250 cm/s) and adjusting the carrier lifetime to obtain the desired L_{eff} for PC1D simulation. Note that the choice of BSRV does not alter the PC1D output or J_{SC} significantly as long as the L_{eff} is the same.

7.3.2 Model calculations to assess the loss in V_{OC} of a cell with two regions of different recombination intensity

Model calculations were performed using Eqs. (52), (54), and (55) to quantify the impact of inhomogeneous material quality on the V_{OC} of a cell by first dividing it into two regions (good and bad). The $L_{\mathrm{eff,high}}$ for the good region was fixed at 870 μm ($L_{\mathrm{eff}} \simeq 3$ times cell thickness W), the $L_{\mathrm{eff,low}}$ for the bad region was varied, and recombination intensity of the bad region was defined as $R = 1 - L_{\mathrm{eff,low}}/L_{\mathrm{eff,high}}$. This R value represents the recombination activity in the bad region, and it increases with the decrease in $L_{\mathrm{eff,low}}$. The $L_{\mathrm{eff,low}}$ values of 44, 87, 174, and 435 μm were selected for model calculation, corresponding to recombination intensities of 0.95, 0.90, 0.80, and 0.50, respectively. To generate model curves, the area fraction of the bad region was varied from 0 to 50% for each recombination intensity and Eqs. (52), (54), and (55) were used in sequence to calculate L_{eu}, $J_{\mathrm{ob,eff}}$, and ΔV_{OC}. $J_{\mathrm{SC,high}}$ and $J_{\mathrm{SC,avg}}$ were calculated from PC1D using $L_{\mathrm{eff,high}}$ and L_{eu} as inputs. All other inputs (Table 16) were kept the same. Figure 49 shows the results of analytical model calculations. It shows that 10% of the defective area with a recombination intensity of 0.95 can reduce V_{OC} by 28 mV of a device that is capable of producing V_{OC} of 623 mV, which was obtained from Eqs. (53) and (54) using L_{eu} of 870 μm and J_{SC} of 33.5 mA/cm^2. Figure 49 also shows that we need to get below a 5% area fraction with a recombination intensity of 0.50 to avoid any appreciable loss in V_{OC}. To determine the error associated with neglecting J_{oe}, the V_{OC} values were also calculated with J_{oe} of 187 fA/cm^2, which is typical for a SiN$_x$ passivated 40–50 Ω/sq emitter for screen-printed contacts, using the

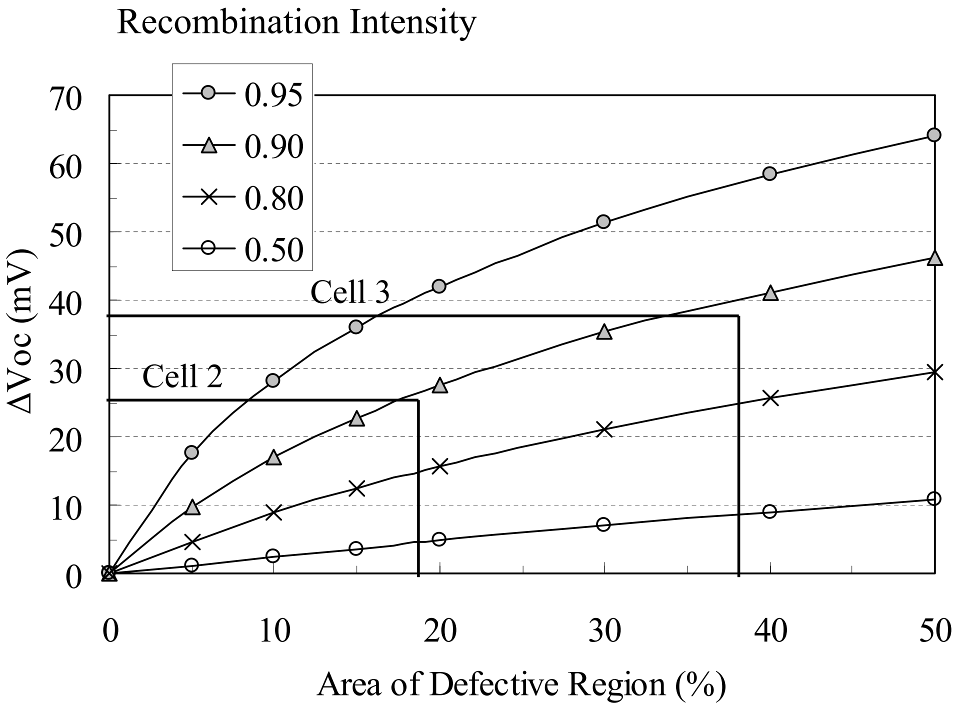

Figure 49: Calculated loss in V_{OC} as a function of defective region with different L_{eff} ratio or recombination intensity. Cell was divided into two regions (high and low L_{eff}s).

following equation:

$$\Delta V_{\text{OC}} = \frac{kT}{q}\Big[\ln\Big(\frac{J_{\text{SC,high}}}{J_{\text{ob,high}} + J_{\text{oe}}} + 1\Big) - \ln\Big(\frac{J_{\text{SC,avg}}}{J_{\text{ob,eff}} + J_{\text{oe}}} + 1\Big)\Big]. \tag{56}$$

The error was found to be ±3 mV in this model calculation.

7.3.3 Model calculations to assess the loss in V_{OC} of a cell with three regions of different recombination intensity

To estimate the error associated with dividing the cell into just two regions, rather than multiple regions, model calculations were performed to include a third region, referred to as the moderate region. In this calculation, the area fractions of all three regions (good, moderate, and bad) were varied. Each curve was obtained by fixing the area fraction of the bad region first and then varying the area fraction of the moderate region from 0% to 100%. The L_{eff} of the good and bad regions were kept at 870 μm and 95 μm. The L_{eff} in the moderate region was fixed at 400 μm and calculations were performed using Eqs. (52),

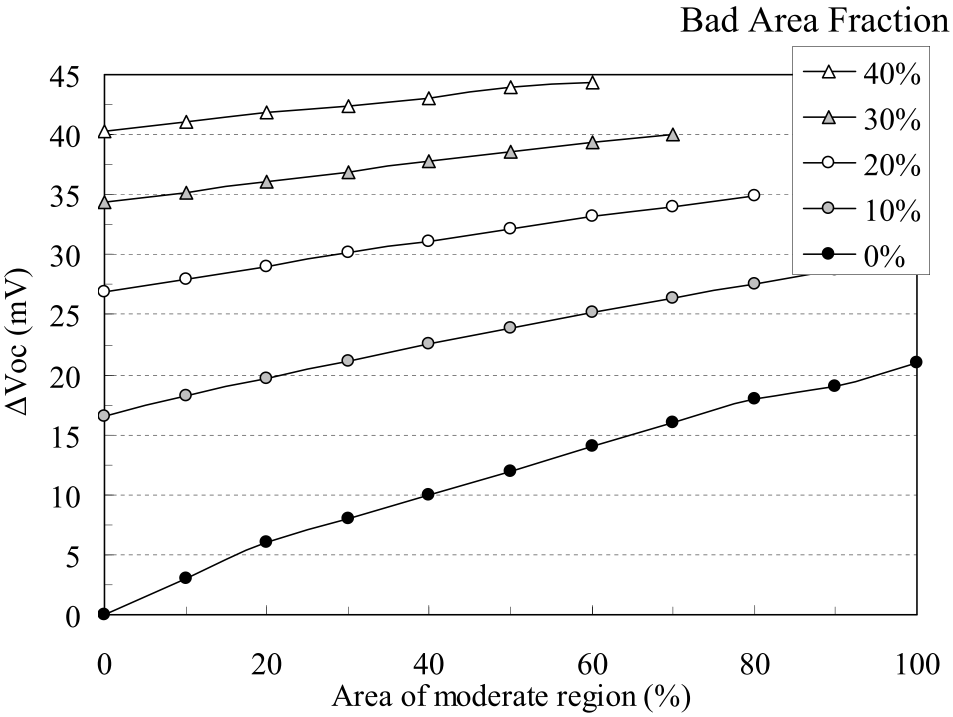

Figure 50: Calculated loss in V_{OC} for each area fraction of defective regions as a function of moderate region.

(54), and (55) in sequence to obtain L_{eu}, $J_{\mathrm{ob,avg}}$, and ΔV_{OC}. The modeling results in Fig. 50 reveal that the bad region has the biggest influence on the loss in V_{OC} (17 mV) even when its area fraction is 10%. This is because, as the moderate area fraction increases from 0% to 50%, for the 10% bad area fraction, the loss in V_{OC} increases from 17 mV to only 24 mV. Figure 50 also shows that if the bad area fraction approaches or exceeds 40%, then it essentially dominates the loss in V_{OC}, which reaches $\sim$40 mV in this example. Thus, an approximate analysis using the best and the worst regions can give a reasonable idea of the loss in V_{OC} resulting from the inhomogeneous distribution of electrically active defects. One can choose more than two or three regions for better accuracy using the same methodology. For a more exact analysis, point-by-point LBIC and IQE maps are needed over the entire cell area to calculate L_{eu} and $J_{\mathrm{ob,eff}}$.

7.3.4 Application of the analytical model to defective cells

An analytical model and approach developed in the previous sections were applied to the two defective cells 2 and 3 in Fig. 47. A statistical analysis of LBIC maps in Fig. 47 was used to assess the area fraction of defective regions. The LBIC output gives a map or range of spectral responses in A/W, which was divided into 16 equal size bins. Figure 51 shows the resulting histograms of the LBIC response for the three cells. Next, each cell was divided into two regions: good region with a spectral response ranging from 0.48 to 0.62 A/W and bad region with a spectral response ranging from 0.32 to 0.46 A/W, i.e, first 8 bins correspond to the bad region and the last 8 bins correspond to the good region. The area fraction of the two regions was determined by

$$A_i = \frac{\sum_{i=1}^{N} B_i}{\sum_{i=1}^{K} B_i}, \tag{57}$$

where B_i is the count in the i^{th} bin, N is the number of bins (=8) in that region (e.g., 0.48–0.62 A/W for good region 1 and 0.32–0.46 A/W for bad region 2), and K is the total number of bins (=16 in this study). This analysis gave the area fractions of 0.02, 0.19, and 0.38 associated with the bad regions for cells 1, 2, and 3, respectively. Note that the grid coverage (6% of cell area) was removed from the histogram in Fig. 51 since there is no carrier generation below the grid. It is important to note that the same procedure can be used to divide the LBIC output into multiple regions instead of just two by assigning different number of bins to each region out of the total of 16.

Recall that the light-biased IQE response in Fig. 48 showed a significant degradation in the long-wavelength IQE response of regions C2 and C3, relative to regions A2 and A3, and the measured and simulated IQE match gave L_{eff} values of 95 μm and 90 μm for regions C2 and C3, respectively, as opposed to 870 μm for regions A2 and A3. According to Eq. (42), this results in significantly higher J_{ob} values of 10^{-12} to 10^{-13} A/cm^2 in regions C2 and C3 relative to the good regions A2 and A3 where J_{ob} of $\sim 10^{-14}$ A/cm^2 is obtained.

Using Eq. (52) and a $L_{\text{eff,high}}$ of 870 μm and $L_{\text{eff,low}}$ of 95 μm with an area fraction of 81% and 19% for the good and bad regions for cell 2 gives a L_{eu} value of 342 μm. Using the L_{eff} values of 870 and 342 μm along with the PC1D inputs in Table 16, J_{SC} values of 33.6

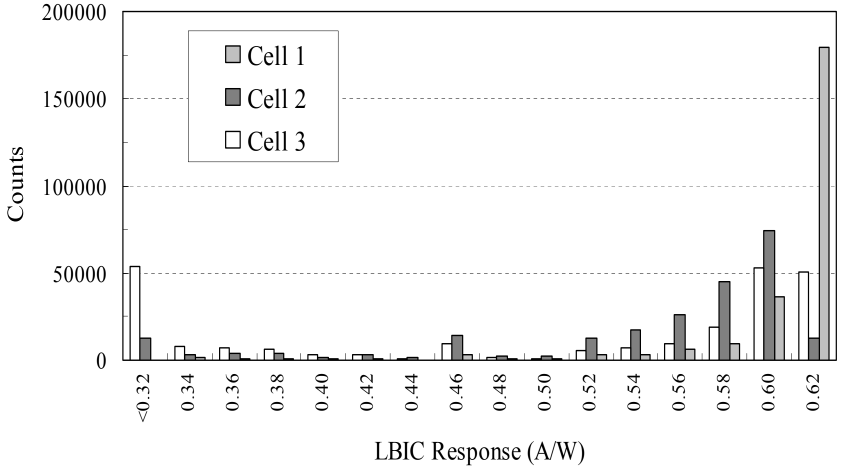

Figure 51: Histograms of LBIC response shown in Fig. 47. Maximum LBIC response was 0.62 A/W for all three cells.

mA/cm^2 ($J_{\mathrm{SC,high}}$) and 32.6 mA/cm^2 ($J_{\mathrm{SC,avg}}$) are obtained from the PC1D simulations. Note that these J_{SC} values are in good agreement with the measured values of 33.5 mA/cm^2 and 32.7 mA/cm^2 for cell 1 and 2, respectively (Table 15). Finally, using these J_{SC} and L_{eff} values in Eq. (55) gives a ΔV_{OC} of 25 mV, which is in good agreement with the measured V_{OC} difference of 24 mV between cell 1 and 2 (Table 15).

Cell 3 was also analyzed using the same methodology shown in Fig. 52. A $L_{\mathrm{eff,high}}$ of 870 μm and $L_{\mathrm{eff,low}}$ of 90 μm with a good and bad area fraction of 62% and 38% for cell 3 gave a L_{eu} value of 203 μm, which resulted in a $J_{\mathrm{SC,avg}}$ value of 31.6 mA/cm^2 from the PC1D simulation. Note that this J_{SC} value is also in good agreement with the measured value of 31.4 mA/cm^2 for cell 3 (Table 15). Equation (55) gave a ΔV_{OC} of 39 mV, which is again in good agreement with the measured V_{OC} difference of 38 mV between cells 1 and 3 (Table 15). Cells 2 and 3 are mapped in Fig. 49 to show the agreement between cell data and model calculations. Even though the model and the procedure outlined above are valid for multiple-region analysis, a simple two-region analytical model gave a fairly good idea of the loss in V_{OC} resulting from the material inhomogeneity in these high-performance

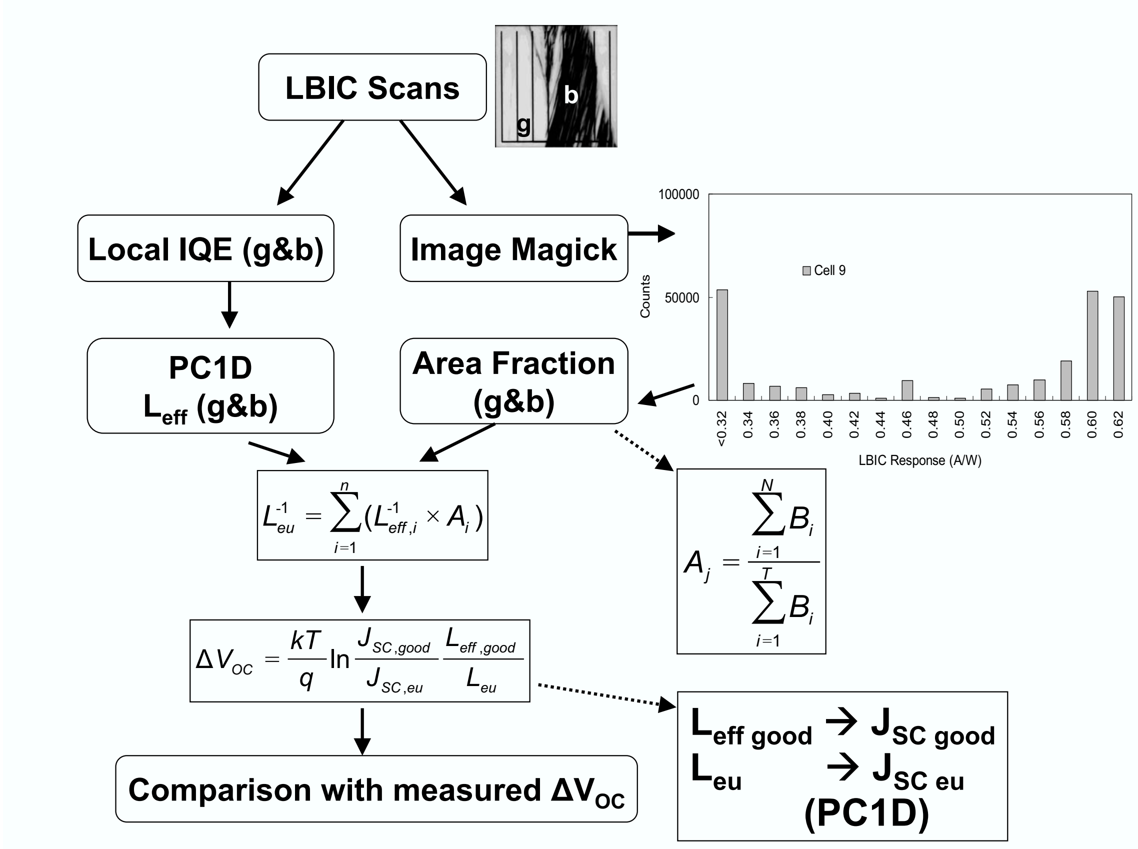

Figure 52: Methodology developed in this model.

screen-printed mc-Si solar cells.

7.3.5 Analysis of the record high-efficiency and average String Ribbon Si cells using an analytical model

In the previous chapter, a record high-efficiency (18.3%) ribbon Si cell was achieved using photolithography-defined front contact formation technique. In spite of the best String Ribbon Si cell efficiency of 18.3%, the average efficiency was only 17.2%, which was 1.1% and 1.4% lower in absolute efficiency compared to the best String Ribbon and FZ Si cells, respectively. This gap in efficiency is mainly attributed to the presence of electrically active defects in certain region as shown in the following discussion.

The LBIC maps in Fig. 45 revealed that this effect reduced the String Ribbon cell efficiency from 18.3% to 17.1% along with a 28 mV loss in V_{OC} and 1.0 mA/cm^2 loss in J_{SC}. In order to understand this phenomenon, the IQE measurements were performed on

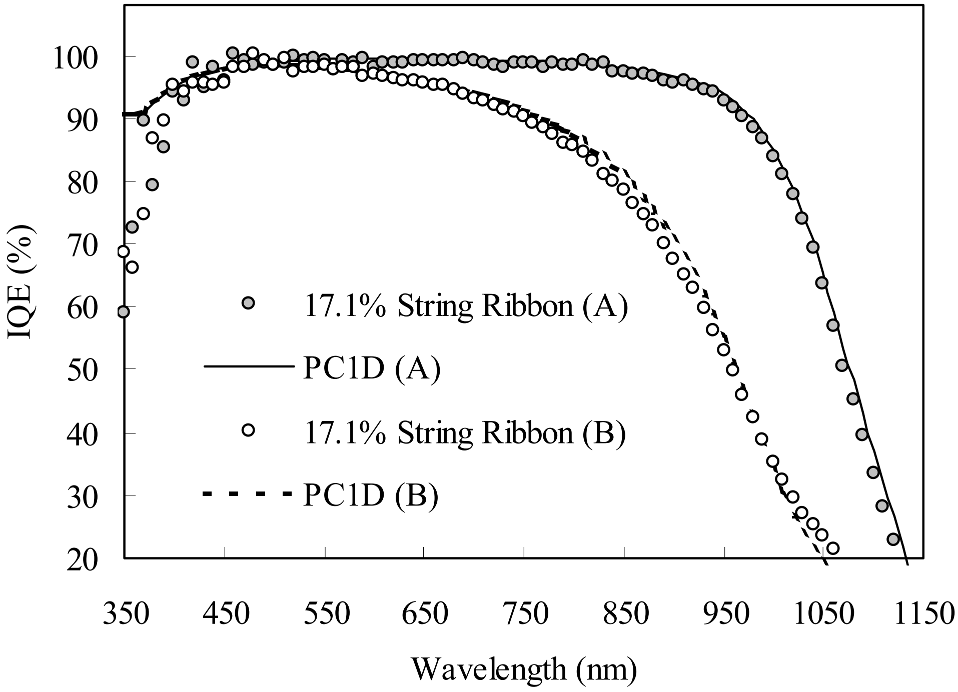

Figure 53: IQE response of 17.1% String Ribbon Si cell (SR1-3) in high (A) and low (B) LBIC response regions. Simulated IQE response, corresponding to L_{eff} value of 1060 and 85 μm, was obtained by PC1D.

high (A) and low (B) LBIC response regions of the 17.1% cell [Fig. 45(b)]. Figure 53 shows the match between the measured and simulated IQE response in those two regions, which gave a significantly lower L_{eff} value of $\sim$85 μm in the defective region (B) compared to 1060 μm in the high LBIC response region.

Next, we applied our simple analytical model (Fig. 52) to quantify the effect of low L_{eff} region on V_{OC}.

In order to extract the area fraction, A_i, the LBIC response in Fig. 45(b) was divided into two regions: good region corresponding to photoresponse in the range of 0.56–0.70 A/W and bad region with photoresponse in the range of 0.40–0.54 A/W. The area fraction of good and bad regions was found to be 85% and 15%, respectively. Using the L_{eff} values of 1060 μm and 85 μm for the good and bad regions, respectively, an L_{eu} value of 389 μm was obtained using an Eq. (52).

The $J_{\mathrm{SC,high}}$ of 36.8 mA/cm^2 (Table 13) and the $J_{\mathrm{SC,avg}}$ of 35.7 mA/cm^2 were determined by the PC1D using L_{eff} of 1060 μm and L_{eu} of 389 μm (BSRV = 225 cm/s and $\tau_b = 35$ μs). Note that $J_{\mathrm{SC,avg}}$ value of 35.7 mA/cm^2 is in good agreement with measured J_{SC} of 35.8 mA/cm^2 in the 17.1% cell. Finally, Eq. (55) gave the loss in V_{OC} of 27 mV because of the defect inhomogeneity, which is in good agreement with the measured V_{OC} loss of 28 mV (Table 10).

The fact that 15% electrically active region reduced the V_{OC} by 28 mV and the cell efficiency by 1.2% in absolute, reiterates the difficultly and challenge in obtaining such high efficiencies on large area production cells on multicrystalline Si materials. More research is needed to understand the exact source and nature of these defective regions, along with the development of the improved material growth and cost-effective defect passivation techniques that can mitigate the influence of inhomogeneously distributed electrically active defects.

7.4 Conclusions

The effect of electrically active defects on V_{OC} was quantified and evaluated through a simple and approximate analytical model. Model calculations were performed to reveal the relationship between the area fraction, recombination intensity of defective region, and the loss in V_{OC}. In this study, three String Ribbon Si solar cells were used to test this model and understand the impact of defect inhomogeneity. A two-region analysis using the model developed in this study gave a reasonable estimate of the loss in V_{OC} resulting from defect inhomogeneity. LBIC and IQE measurements were used to estimate the area fraction and recombination intensity of the defective regions. Model calculations showed that a cell with a 38% area fraction of bad region with a recombination intensity of 0.90 can reduce the V_{OC} by 39 mV. This agreed well with the experimental data for cell 3, which showed a loss in V_{OC} of 38 mV. There was also a good agreement between the experimental data and model calculations, which showed that a 19% area fraction of bad region with a recombination intensity of 0.89 can reduce the V_{OC} by 25 mV. Model calculations revealed that in order to keep the loss in V_{OC} below 5 mV in high-performance devices, the area fraction of the defective region should be below 20% with a recombination intensity of 0.50 or lower. These results show the usefulness of the analytical model and methodology developed in this study in quantitative assessment of the impact of inhomogeneously distributed active defects on mc-Si solar cell performance. Further research is needed to reduce the area fraction and recombination intensity of these defective regions by improving the material growth and defect passivation techniques.

CHAPTER VIII

APPLICATION OF AN ANALYTICAL MODEL TO DETERMINE THE IMPACT OF MATERIAL INHOMOGENEITY ON SMALL- AND LARGE-AREA MULTICRYSTALLINE SILICON SOLAR CELL PERFORMANCE

Despite their attractiveness described in Chap. II, multicrystalline Si (mc-Si) solar cells usually exhibit lower cell performance compared to cells fabricated on FZ and Cz Si [101,167], as discussed in Chap. III. This is partly because of their low as-grown material quality. Most mc-Si materials contain a high concentration of metallic impurities and structural defects, which act as carrier recombination centers [4]. The minority carrier lifetime enhancement in EFG and String Ribbon Si has been attempted by many research groups using P diffusion-induced impurity gettering, PECVD SiN_x-induced defect hydrogenation [125], and microwave-induced remote hydrogen plasma passivation [23]. An area-average lifetime (τ_{avg}) approaching 100 μs has been achieved after cell processing in Chaps. IV and V. Bailey *et al.* [12] performed an impurity gettering experiment using a $POCl_3$ source at 950°C for 120 min on FZ, Cz, and edge-defined film-fed grown (EFG) Si and found that low diffusion length regions in the as-grown EFG Si are highly resistant to diffusion length improvement by P diffusion-induced impurity gettering. Similar results have been reported by other researchers in the literature [48,168,169]. Jastrzebski *et al.* [168] found that impurity gettering by P diffusion significantly improves the minority carrier diffusion length and reduces Fe and Cr concentrations in the good region, but has no effect on diffusion length in the highly defective region. It was suggested in [168] that the carrier recombination centers controlling lifetime in the defective regions are most likely introduced by crystallographic defects, which were formed during the crystal growth process. Macdonald *et al.* [53] performed a

$POCl_3$ gettering at 900°C for 180 min on the cast mc-Si materials from different ingots and locations and found that the largest increase in minority carrier lifetime after P gettering was observed in samples with low dislocation densities and high concentrations of mobile impurities. Sopori *et al.* [49] concluded that the effectiveness of any gettering process for improving large-area mc-Si cell performance is limited by how well it can getter impurities from heavily dislocated regions. Bell *et al.* [159] reported that material inhomogeneities can significantly limit the voltage output because the grains with the low carrier diffusion length determine the V_{OC} of mc-Si cells. This is because the bad regions act in parallel with good regions and can lower the V_{OC} [170]. Therefore, a wide spread in diffusion length within the cell area can be detrimental to device performance [157]. Recently, Geiger *et al.* [23] used a spatially resolved lifetime mapping technique to show a substantial scatter in carrier lifetime (<2 μs to >300 μs) within 5×5 cm^2 EFG and String Ribbon Si wafers after cell processing.

Since defects or material inhomogeneity is an integral part of mc-Si, it is important to assess its impact on cell performance. In this chapter, an attempt is made to quantify the effect of material inhomogeneity on cell performance, including cast, EFG, and String Ribbon Si cells, using an analytical model developed in the previous chapter. In addition, an approach to high-efficiency (>17%) ribbon Si cells is established by model calculations in the presence of the material inhomogeneity.

8.1 Device Modeling and Analysis

8.1.1 Application and validation of the inhomogeneity model

To verify the accuracy and acceptability of an analytical model developed in the previous chapter, several String Ribbon Si solar cells (resistivity of 3.0 Ωcm, cell area of 4.0 cm^2, and thickness of 300 μm) were analyzed using light beam-induced current (LBIC) scans and local internal quantum efficiency (IQE) measurements. A PVScan 5000 system [147], equipped with a 980 nm laser, was used for LBIC analysis. The LBIC scans of String Ribbon Si solar cells (SR1–SR6) along with the cell data are shown in Fig. 54. The LBIC scans reveal that cell SR1 has nearly uniform current collection over the active area compared

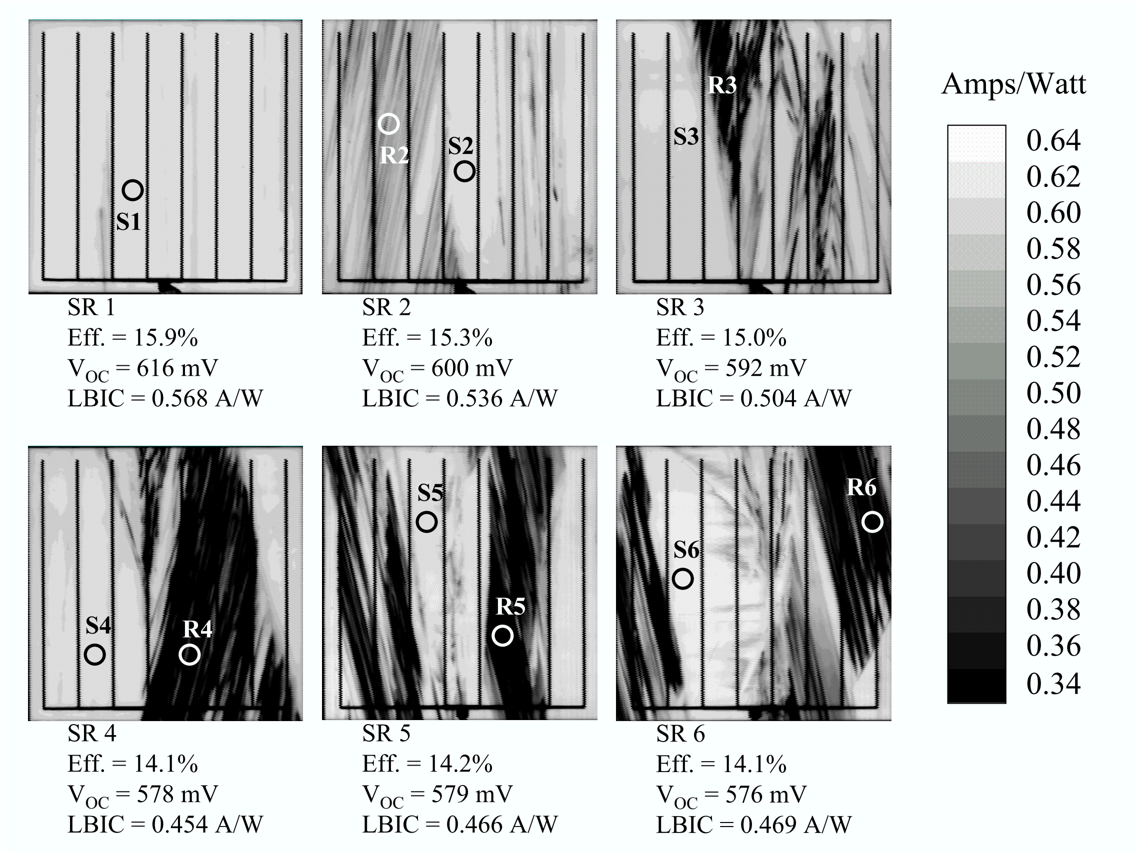

SR 1
Eff. = 15.9%
V_{OC} = 616 mV
LBIC = 0.568 A/W

SR 2
Eff. = 15.3%
V_{OC} = 600 mV
LBIC = 0.536 A/W

SR 3
Eff. = 15.0%
V_{OC} = 592 mV
LBIC = 0.504 A/W

SR 4
Eff. = 14.1%
V_{OC} = 578 mV
LBIC = 0.454 A/W

SR 5
Eff. = 14.2%
V_{OC} = 579 mV
LBIC = 0.466 A/W

SR 6
Eff. = 14.1%
V_{OC} = 576 mV
LBIC = 0.469 A/W

Figure 54: LBIC scans of 4 cm^2 String Ribbon Si solar cells.

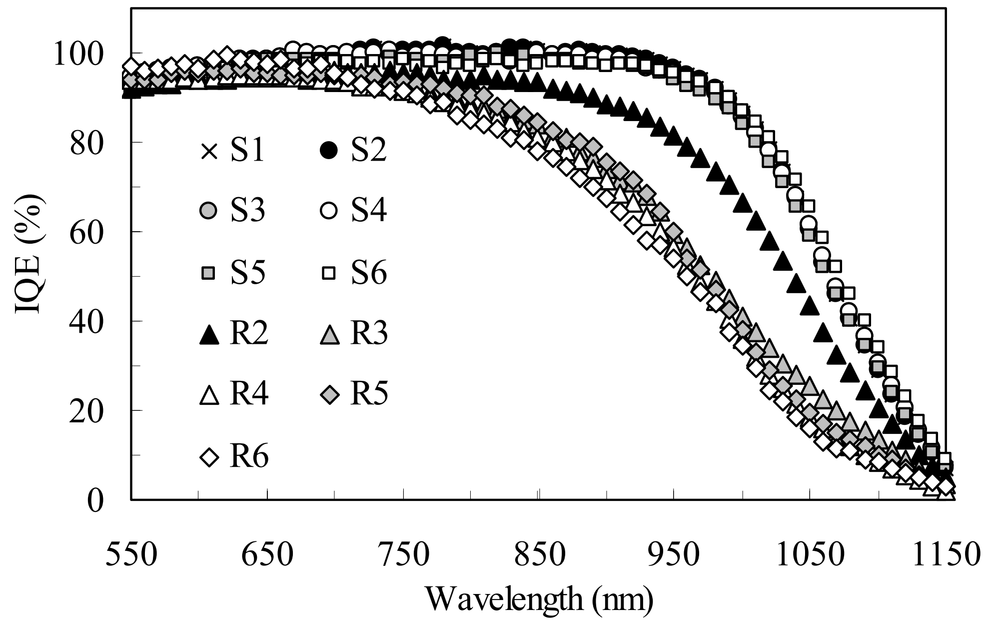

Figure 55: Measured IQE response on String Ribbon Si solar cells.

to the other cells. This is reflected in the higher cell performance of SR1 (616 mV in V_{OC} and 15.9% in efficiency) as well as the higher average LBIC response of 0.568 A/W. The IQE measurements were performed on selected regions (S1-S6 and R2-R6 in Fig. 54) on these cells to extract the effective diffusion length, shown in Fig. 55. Based on the LBIC scans, the best (S1-S6) and the worst (R2-R6) regions were selected for the analysis. The measured IQE response was matched in the long-wavelength range (700–1000 nm) with a simulated response using PC1D by fixing the BSRV (250 cm/s) and varying the bulk carrier lifetime. This gave lifetimes of 150 μs in the good regions (S1-S6) and 2–20 μs in the bad regions (R2-R6). According to Eq. (43), this corresponds to an L_{eff} of $\sim$870 μm for the good regions S1-S6, and 90 μm for region R2, 92 μm for region R3, 79 μm for region R4, 95 μm for region R5, and 282 μm for region R6. It is important to note in this analysis that the BSRV and lifetime values do not necessarily have to be exact, but they should give the correct value of L_{eff}. The area fraction of each region was determined by LBIC maps (Fig. 54). The LBIC output, which gives the map of spectral response (A/W), was divided into

Table 18: Summary of model calculations for loss in V_{OC}.

ID	Fraction B (%)	τ_B (µs)	L_{eu} (µm)	τ_{eu} (µs)	τ_{avg} (µs)	ΔV_{OC} (mV) (measured)	ΔV_{OC} (mV) (modeled)
SR2	20	20	615	73	124	16	9
SR3	19	2.9	342	27	122	24	25
SR4	38	2.6	203	11.6	94	38	38
SR5	40	2.7	199	11.3	91	37	40
SR6	40	2.0	174	9.0	91	40	44
HEM2	12	3.0	437	44	154	14	17
EFG2	15	2.0	355	29	150	30	26

two regions (0.50–0.64 A/W range for the good region and 0.34–0.48 A/W range for the bad region). An image processing program was used to obtain the bad region area fraction of 0.38, 0.40, 0.40, 0.19, and 0.20 for cells SR2, SR3, SR4, SR5, and SR6, respectively. Equation (52) was then used to extract the effective uniform diffusion length (L_{eu}) of 203 μm, 199 μm, 174 μm, 342 μm, and 615 μm using the $L_{\mathrm{eff,high}}$ of 870 μm in combination with $L_{\mathrm{eff,low}}$ of 90 μm, 92 μm, 79 μm, 95 μm, and 282 μm and bad region area fraction of 38%, 40%, 40%, 19%, and 20% for cells SR2, SR3, SR4, SR5, and SR6, respectively. Finally, Eq. (55) was applied to obtain ΔV_{OC} (material inhomogeneity-induced loss in V_{OC}) of 38 mV, 40 mV, 44 mV, 19 mV, and 9 mV for each cell. Table 18 shows that these ΔV_{OC} values calculated from the defect inhomogeneity model are in good agreement with measured loss in V_{OC} of 38 mV, 37 mV, 40 mV, 20 mV, and 16 mV for cells SR2, SR3, SR4, SR5, and SR6, respectively, compared to the cell SR1.

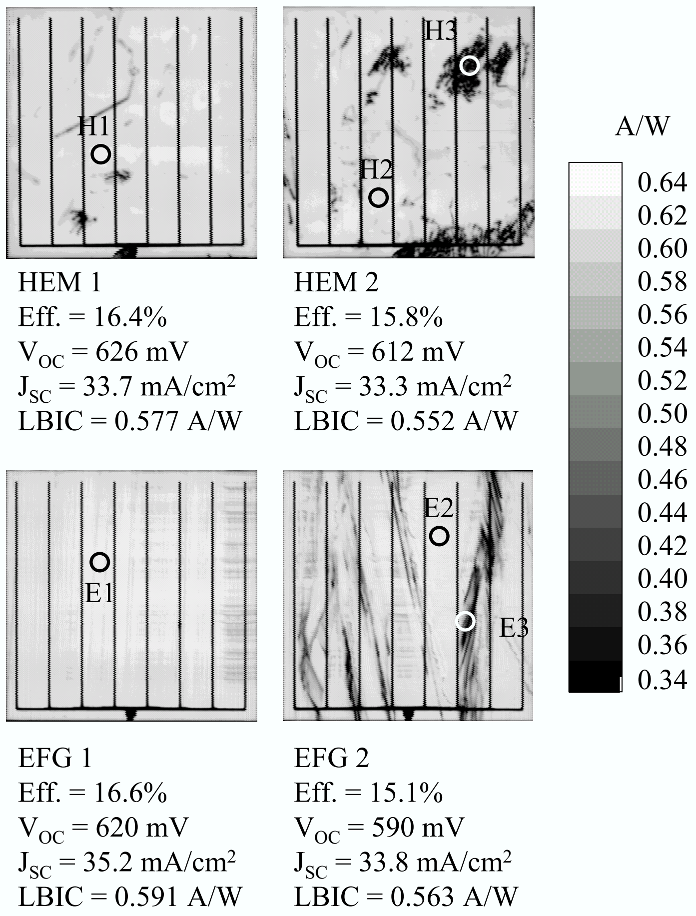

Figure 56: LBIC scans of 4 cm^2 HEM and EFG Si solar cells.

To further test the validity of the above analytical model on other inhomogeneous materials, additional cells fabricated on 1.6 Ωcm cast mc-Si grown by the heat exchanger method (HEM) and 3.0 Ωcm EFG Si were also characterized by the above methodology to assess the loss in V_{OC} using Eqs. (43), (52), and (55). The LBIC scans of the two HEM mc-Si (HEM1 and HEM2) and two EFG Si (EFG1 and EFG2) solar cells, along with the measured difference in V_{OC} and cell data, are shown in Fig. 56. Note that these 4.0 cm^2 cells were selected from the same wafer for each material. Next, the analytical model for inhomogeneity was applied to calculate the loss in V_{OC} on these cells. Again, LBIC scans reveal that HEM1 and EFG1 have a relatively uniform current collection compared to HEM2 and EFG2. The

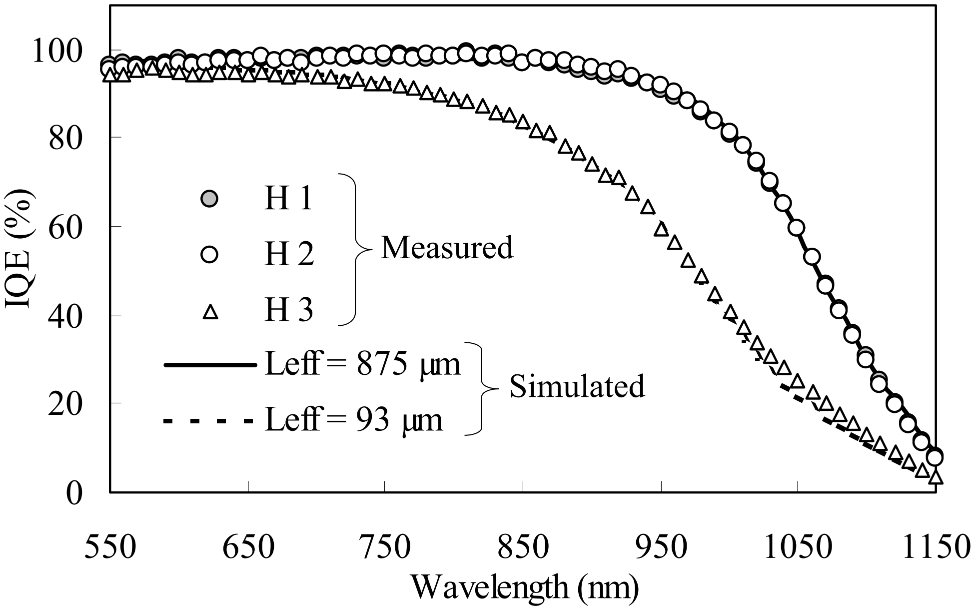

Figure 57: Measured and simulated IQE response on HEM mc-Si solar cells.

local IQE measurements were performed on selected regions H1-H3 on HEM cells and E1-E3 on EFG Si cells, Fig. 56, to extract the effective diffusion length. Figure 57 shows the measured and simulated IQE response from regions H1-H3, which gave an effective diffusion length of 875 μm ($L_{\text{eff,high}}$) for good regions (H1 and H2) and 93 μm ($L_{\text{eff,low}}$) for the bad region (H3). The same image processing, which divides the LBIC response into two regions (0.50–0.64 A/W range for the good region and 0.34–0.48 A/W range for the bad region), gave the bad region area fraction of 0.12 for HEM2 (Fig. 56). Equation (52) then gave L_{eu} of 437 μm, and finally ΔV_{OC} was found to be 17 mV using Eq. (55), which agreed with the measured ΔV_{OC} of 14 mV.

The measured and simulated IQE response for the EFG Si cell are shown in Fig. 58, which gave effective diffusion lengths of 928 μm and 79 μm for good (E1 and E2) and bad (E3) regions, respectively. The area fraction of the bad region was found to be 15% on EFG2 from the LBIC map and image processing. The combination of diffusion length and area fraction gave an L_{eu} of 355 μm using Eq. (52). Finally, the ΔV_{OC} was calculated to

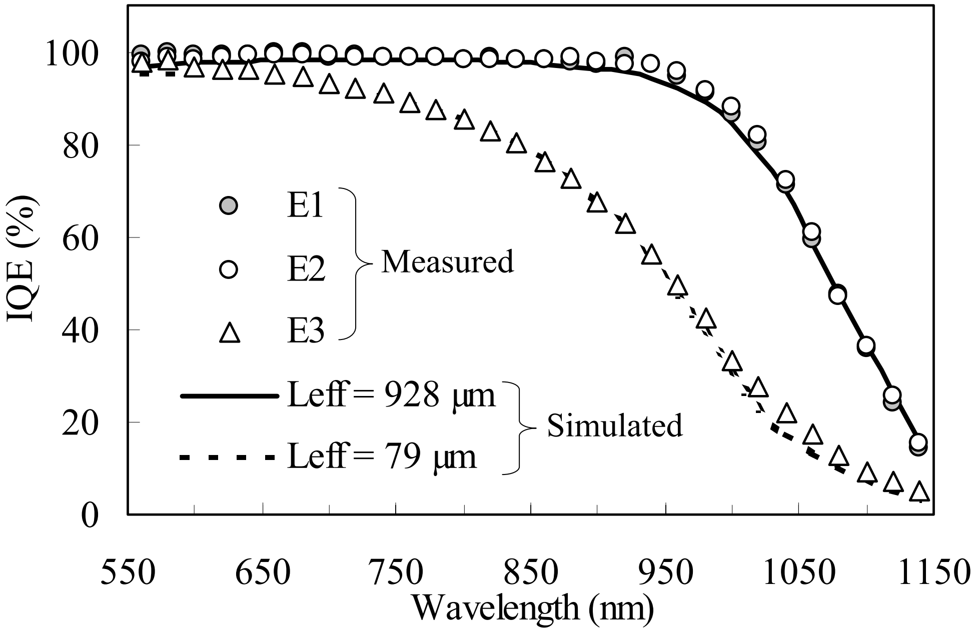

Figure 58: Measured and simulated IQE response on EFG Si solar cells.

be 26 mV using Eq. (55), which agreed well with the measured ΔV_{OC} value of 30 mV. The cells analyzed by the above two-region model are summarized in Table 18, which shows a reasonable agreement between measured and calculated loss in V_{OC} resulting from material inhomogeneity.

The cells analyzed above had a τ_{avg} of 91–154 μs (Table 18), which was determined by averaging the carrier lifetimes in good (A) and bad (B) regions within the cell, as shown below.

$$\begin{aligned}\tau_{\mathrm{avg}} &= \sum_{i=1}^{n} (\tau_i \times A_i), \\ &= \tau_A \cdot A_A + \tau_B \cdot A_B, \end{aligned} \tag{58}$$

where τ_i is the carrier lifetime in region i, and A_i is the area fraction of region i. The PC1D simulations were performed to quantify the effect of carrier lifetime on cell efficiency using the input parameters in Table 16. The PC1D simulations in Fig. 59 indicate that if the bulk lifetime is in excess of 90 μs, the cell efficiency should be over 15.7%. However,

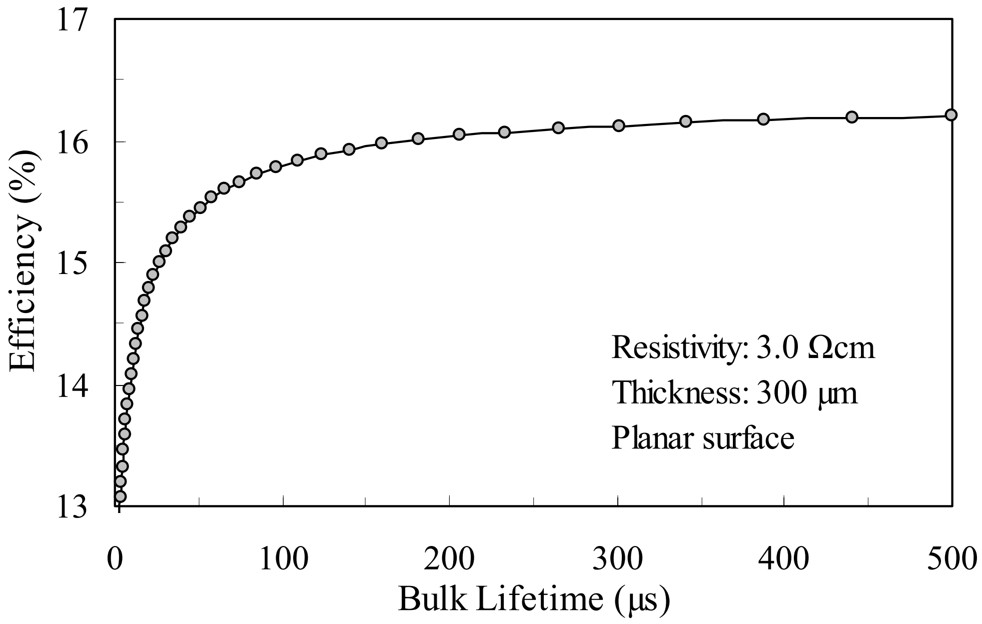

Figure 59: PC1D simulations of cell efficiency as a function of bulk carrier lifetime.

cells SR2–SR6 did not exhibit such a high performance. The difference in the simulated and measured cell efficiencies is attributed to the material inhomogeneity in the mc-Si solar cells. The good and bad regions in a mc-Si cell are connected in parallel; therefore, the V_{OC} in the good region is pulled down by the V_{OC} in the bad region.

In this section, an effort is made to transform the inhomogeneous mc-Si cell into a homogeneous cell of equivalent performance with an effective uniform diffusion length or a uniform bulk lifetime. Equation (52) is used to obtain the L_{eu}, which is the sum of the ratio of area fraction and diffusion length (A/L_{eff}). Then, the extracted L_{eu} is used in place of L_{eff} in Eq. (43), in conjunction with BSRV of 250 cm/s (in our cells), to obtain the effective uniform bulk diffusion length (L_{bu}). Finally, the uniform bulk carrier lifetime (τ_{bu}) is calculated from the equation $L_{\mathrm{bu}} = \sqrt{D_n \tau_{\mathrm{bu}}}$. The procedure for extracting τ_{bu} from the area fraction and carrier lifetime in the good and bad regions is outlined in Fig. 60. The τ_{bu} represents the lifetime of a hypothetical homogeneous cell, which will produce V_{OC} and performance equivalent to the inhomogeneous mc-Si cell. Thus, this model transforms the

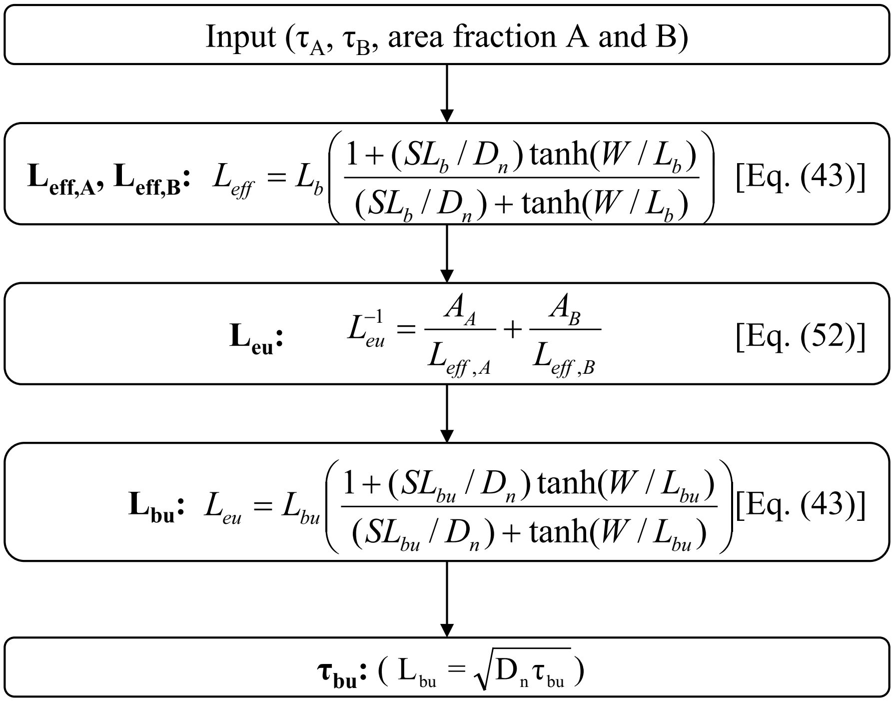

Figure 60: Procedure to obtain τ_{bu} from τ_A, τ_B, area fraction of regions A and B.

inhomogeneously distributed carrier lifetime into an effective homogeneous lifetime value, which is easy to relate to and understand.

Based on the methodology described above, the τ_{bu} was calculated for HEM, EFG, and String Ribbon mc-Si cells. Most noteworthy, this analysis revealed that the τ_{bu} values are much lower than τ_{avg} values in those cells (Table 18). For example, String Ribbon Si cell SR6 had a τ_{avg} of 91 μs, but its τ_{bu} was only 9 μs. To demonstrate that the τ_{bu} truly represents the performance of inhomogeneous mc-Si cells, the loss in V_{OC} was calculated using Eq. (55) by maintaining the τ_{avg} of 100 μs. Model calculations were performed again by dividing the cell into two regions, A and B. The area fraction of region B was varied from 0% to 50%, and the lifetime in region B (τ_B) was also varied from 1.0 μs to 10 μs. The lifetime in region A (τ_A) was adjusted each time to keep the τ_{avg} of 100 μs based on the area fraction of the region B and τ_B. Recall that the combination of area fraction and lifetimes in good and bad regions gives the L_{eu} using Eq. (52), the L_{eu} gives the ΔV_{OC} using Eqs. (43) and (55), and finally L_{eu} and BSRV give the value of L_{bu} and τ_{bu} (Fig. 60). Figure

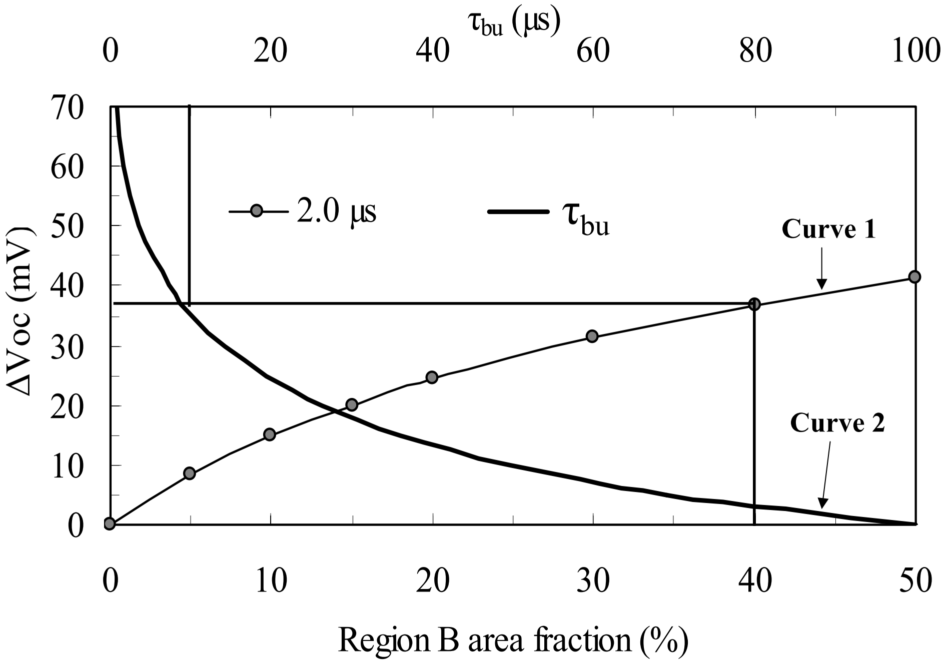

Figure 61: Relationship between τ_B, area fraction, ΔV_{OC}, and τ_{bu}. The cell SR6 ($\tau_{\mathrm{bu}} = 9\ \mu$s, $\Delta V_{\mathrm{OC}} = 40$ mV, $\tau_B = 2.0\ \mu$s, and $A_B = 40\%$) is also shown in the figure.

61 shows two curves; the first curve shows the calculated ΔV_{OC} as a function of the area fraction of bad region B for a fixed τ_B of 2.0 μs and τ_{avg} of 100 μs, and the second curve shows the ΔV_{OC} as a function of τ_{bu} calculated from L_{eu} and BSRV. The experimental data for cell SR6 (area fraction of region B $\simeq$ 40%, τ_B=2.0μs, and ΔV_{OC}=40 mV), which has a τ_{avg} close to 100 μs, is also plotted on this figure, which shows good agreement between the measured and modeled ΔV_{OC} of ~40 mV, curve 1. Curve 2 shows that a ΔV_{OC} of 40 mV corresponds to a τ_{bu} value of 9 μs. Thus, a cell with a 40% bad region with τ_B of 2 μs and τ_{avg} of 100 μs behaves similarly to a homogeneous cell with τ_{bu} of 9 μs, which is about an order of magnitude lower than the average lifetime of 90–100 μs. In this calculation, the τ_{avg} and the base resistivity were assumed to be 100 μs and 3.0 Ωcm, respectively. It can be concluded that the τ_{bu} determines the behavior of the cell more accurately than the τ_{avg}. Figure 61 can be used to determine the τ_B for any value of A_B in a cell with τ_{avg} of 100 μs and τ_B of 2.0 μs. Such curves can be generated for any combination of τ_{avg} and τ_B using

Table 19: Cell performance of large-area EFG Si cells used in this study.

ID	Voc (mV)	Jsc (mA/cm^2)	FF	Eff. (%)
A	603	32.1	0.754	14.6
B	568	29.2	0.766	12.7
C	567	28.8	0.759	12.4

the above methodology.

8.1.2 Inhomogeneity-induced loss in open-circuit voltage of large-area EFG Si cells

The analysis in the previous section was performed on several small-area cells fabricated on large-area wafers. In this section, we applied the analytical model to large-area industry-type EFG Si cells. The cell data of the three 100 cm^2 EFG Si cells used in this investigation is shown in Table 19. Cell A had a high V_{OC} value (>600 mV), and the other two cells (B and C) had much lower V_{OC} (<570 mV). The LBIC scans along with the measured $I-V$ characteristics of these EFG cells are shown in Fig. 62. The IQE measurements were performed on several selected locations, shown in Fig. 62. Note that the best and the worst regions were selected for the IQE measurements. The measured IQE response in the long-wavelength region was matched with the simulated IQE response (Fig. 63) using PC1D to extract the L_{eff} values at each of these locations (Fig. 63). It was found that the best regions had an L_{eff} of 975 μm (τ_b = 200 μs and BSRV = 250 cm/s), and the worst regions had an L_{eff} of 90 μm (τ_b = 2.6 μs and BSRV = 250 cm/s) from the match between measured and simulated long-wavelength IQE response. The area fractions of good and bad regions were found to be 90% and 10% for cell A, 64% and 36% for cell B, and 48% and 52% for cell

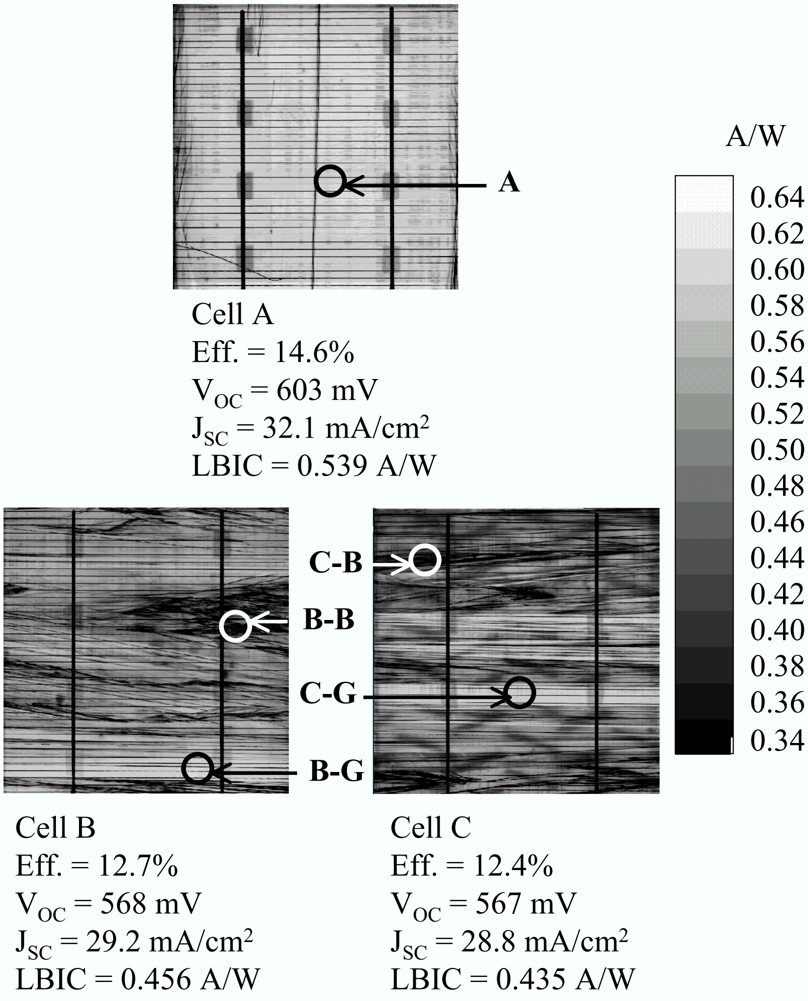

Figure 62: LBIC scans of 100 cm^2 EFG solar cells.

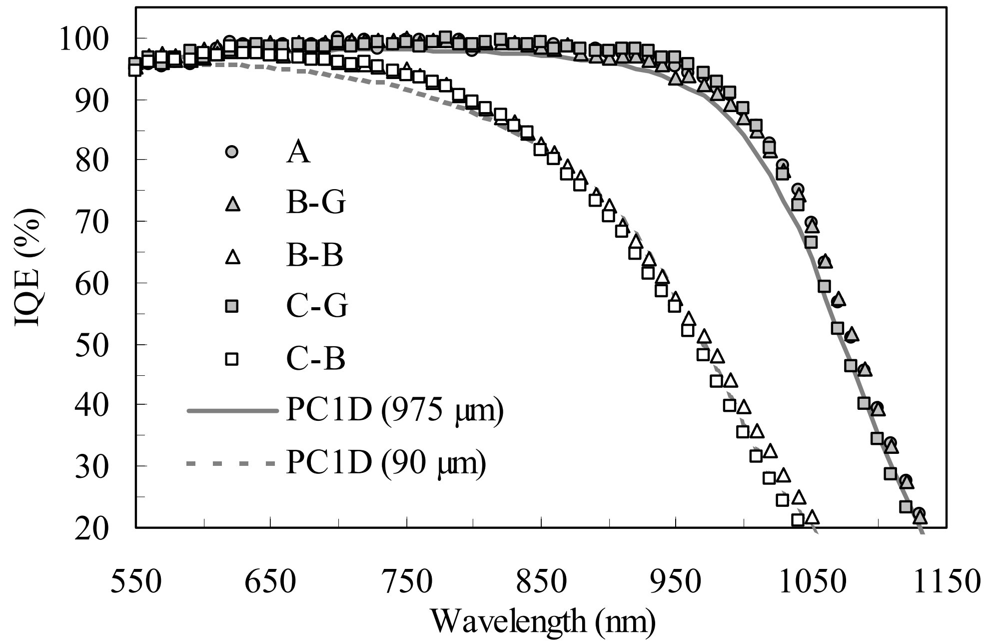

Figure 63: Measured and simulated IQE response in specified locations in Fig. 62.

C, respectively, using the image processing software and dividing the LBIC response into two regions of eight bins each (good: 0.50-0.64 A/W and bad: 0.34-0.48 A/W). The model calculations were performed using these values to assess the loss in V_{OC}, and the results are summarized in Table 20. Since cell A had the lowest fraction of bad region (Fig. 62), cell A was used as a reference cell. The calculated and measured losses in V_{OC} were 39 mV and 35 mV for cell B and 47 mV and 36 mV for cell C, respectively, using the two-region analysis. Since the local IQE measurements were performed only at the two extreme regions (best and worst) within a cell in this study, the distribution of diffusion length between these two extreme regions was ignored during the model calculations. The previous section showed that this worked well for small-area cells. However, large-area cells often contain a wider distribution of diffusion length over the cell area, which may introduce some error in the two-region analysis. In order to investigate the error associated with the wide spread of diffusion length, the model calculations were performed again by dividing the LBIC response on large-area cells into multiple regions. The L_{eff} value for each region was obtained by

Table 20: Calculated and measured loss in V_{OC} for large-area EFG Si cells.

ID	**2-region ΔV_{OC} (mV)**	**4-region ΔV_{OC} (mV)**	**8-region ΔV_{OC} (mV)**	**16-region ΔV_{OC} (mV)**	**Measured ΔV_{OC} (mV)**
B	39	33	31	30	35
C	47	37	34	33	36

linear extrapolation between the measured best and worst L_{eff} values. This is illustrated in Fig. 64 and avoided the need for additional IQE measurements. The summary of model calculations using multiple regions (two-, four-, eight-, and 16-region) is also shown in Table 20. Recall that LBIC response is first divided into 16 bins. For two-region analysis, each region (good and bad) contains eight bins and in 16-region analysis, each bin corresponds to one region. Area fraction for each region was determined by Eq. (57), and L_{eff} for each region can be determined by linear approximation of L_{eff} from LBIC response (Fig. 64). After that, the L_{eu} and ΔV_{OC} can be calculated from Eqs. (52) and (55). Notice that for cell B, the calculated loss in V_{OC} was 39 mV using the two-region analysis. However, the ΔV_{OC} was found to be 33 mV, 31 mV, and 30 mV using four-, eight-, and 16-region analysis, respectively. For cell C, the ΔV_{OC} was 47 mV, 37 mV, 34 mV, and 33 mV using two-, four-, eight-, and 16-region analysis. The ΔV_{OC} value becomes saturated as we include more regions into the calculations. The measured ΔV_{OC} was 35 mV and 36 mV for the cells B and C compared to cell A. However, the 16-region analysis, which is expected to

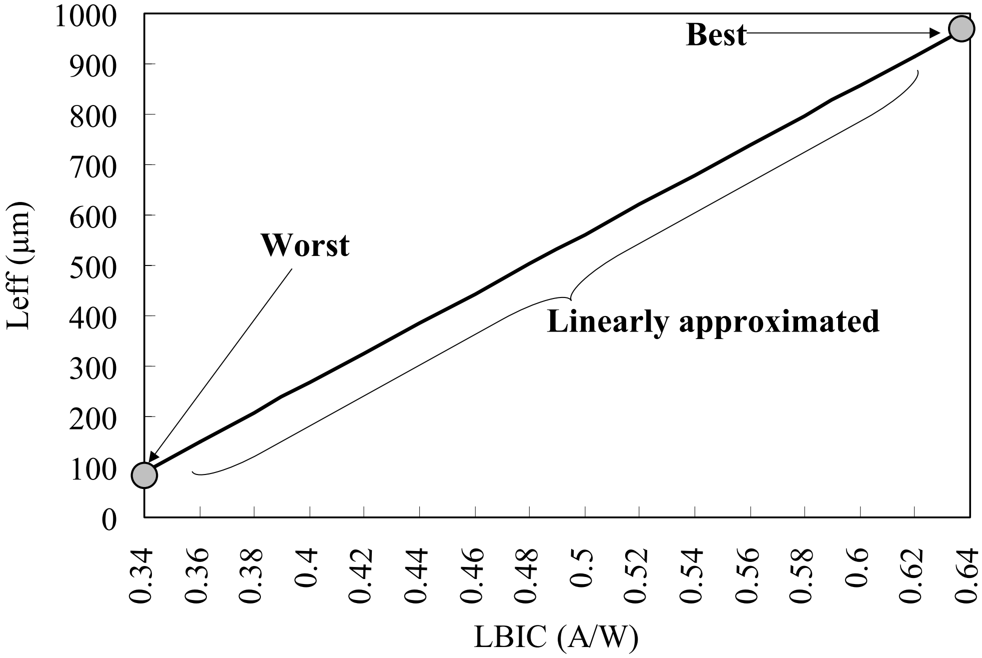

Figure 64: Linear approximation of L_{eff} in μm from LBIC response in A/W. The best and worst points of LBIC response are indicated in the plot.

be the most accurate analysis in this study, gave a ΔV_{OC} of 30 mV and 33 mV for cells B and C, respectively. The small gap between the measured and calculated loss in V_{OC}, even after the 16-region analysis, could be because of the assumption that the reference cell A is completely uniform over the cell area or the error associated with the linear approximation of L_{eff} for each region. Thus, the simple inhomogeneity model using four- or eight-region gives a fairly good idea of the loss in V_{OC} of large-area cells resulting from the distributed defects. Schindler and Warta [171] have also demonstrated the multiple-region analysis for device characterization using a combination of the diode-network model and diffusion length mapping technique.

8.2 Guidelines for Achieving High-Efficiency Ribbon Silicon Solar Cells

8.2.1 Variations in ΔV_{OC} values as a function of material and device parameters

In the previous section, the analytical model, which can take the material inhomogeneity into consideration, was successfully applied to large-area industry-type EFG Si cells to calculate the loss in V_{OC} resulting from the material inhomogeneity. In this section, model calculations are performed by varying key material and device parameters to quantify the impact of each parameter on ΔV_{OC}. According to Eqs. (52) and (55), the ΔV_{OC} is a function of basic material parameters, such as base doping or resistivity, cell thickness, and carrier lifetime in good and bad regions. Therefore, a baseline curve of ΔV_{OC} versus area fraction of the bad region was first established using Eqs. (52) and (55) in conjunction with material and device parameters shown in Table 21. This calculation was done with two-region analysis. Next, ΔV_{OC} was calculated by varying one parameter at a time (base resistivity, cell thickness, τ_B, and τ_{avg}). The results of the sensitivity analysis are shown in Fig. 65 [(a) base resistivity, (b) cell thickness, (c) τ_B, and (d) τ_{avg}]. Figure 65(a) reveal that the base resistivity in the range of 1.3 to 5.0 Ωcm has no appreciable effect on ΔV_{OC}. The cell thickness in the range of 100 to 300 Ωcm also has no significant impact on improving the ΔV_{OC}. However, Fig. 65(c) shows that ΔV_{OC} is a strong function of the carrier lifetime in the bad region (τ_B). For example, if the area fraction of the bad region is 30%, ΔV_{OC}

Table 21: Material and device baseline parameters for model calculations.

Parameter	**Value**
Base resistivity	3.0 Ωcm
Cell thickness	300 µm
Lifetime in bad region (τ_B)	2.0 µs
Area-average lifetime (τ_{avg})	100 µs

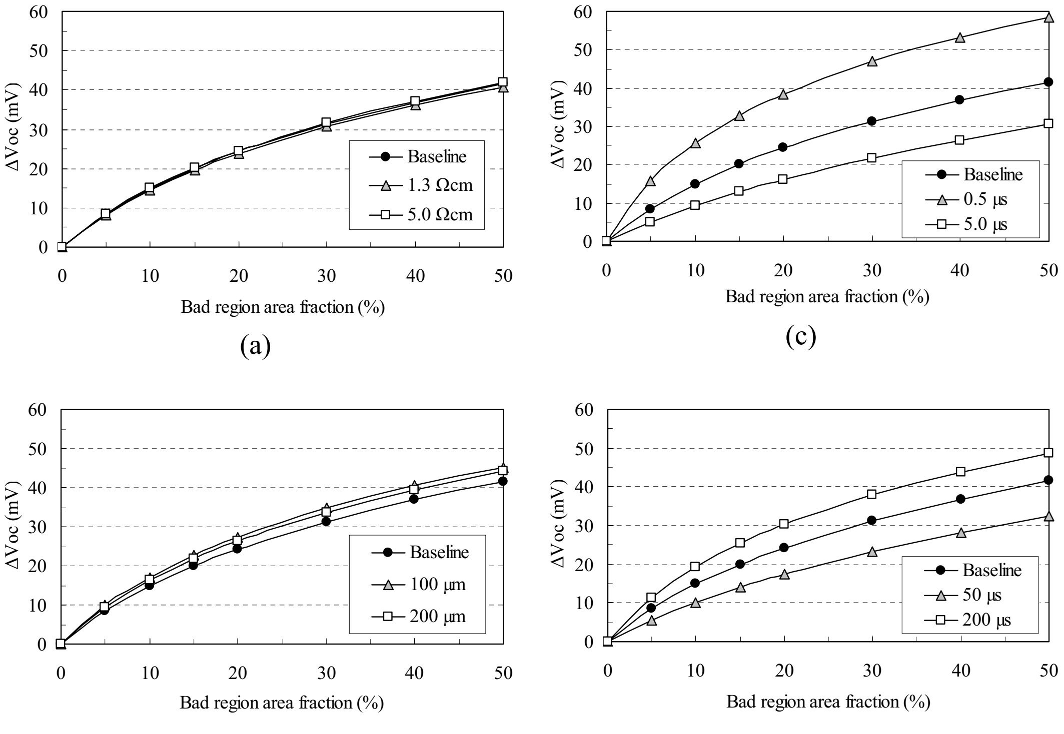

(a) (c)

(b) (d)

Figure 65: Model calculations for ΔV_{OC} as a function of (a) base resistivity, (b) cell thickness, (c) τ_B, and (d) τ_{avg}.

can be improved by 10 mV by increasing the τ_B from 2 to 5 μs. However, if τ_B decreases from 2 to 0.5 μs, the ΔV_{OC} increases by 18 mV. Figure 65(d) shows that if τ_{avg} is improved from 100 to 200 μs, the ΔV_{OC} increases by 8 mV for a 30% of bad region area fraction with τ_B of 2 μs. On the other hand, if τ_{avg} decreased to 50 μs, the ΔV_{OC}s decreases by $\sim$10 mV because the V_{OC} of the good region decreases.

This section dealt with the effect of material and device parameters on ΔV_{OC}. Next section deals with the effect of device design and high-quality surface passivation scheme (BSRV) on V_{OC} in the presence of defects.

8.2.2 Effect of improving carrier lifetime in the good region and BSRV in the presence of defects

It has been shown in the literature [11,172] that the decoration of structural defects by metal impurities significantly enhances carrier recombination activity, and removing metal impurities from such defective regions is extremely difficult. On the other hand, regions without decorated defects can be improved appreciably by effective gettering and passivation.

In the previous sections, we investigated the impact of the bad regions (τ_B and area fraction of region B), by fixing the τ_{avg} at 100 μs. A combination of the defect inhomogeneity model and PC1D device simulations is used in this section to assess the impact of improving the carrier lifetime in the good region A (τ_A) on the cell performance in the presence of defects. This is done by fixing the thickness (300 μm), BSRV (250 cm/s), τ_B (2 μs), and area fraction of bad region B (20%). Note that in this analysis, the τ_{avg} is not fixed at 100 μs. In this study, the V_{OC} was calculated as a function of τ_A in the range of 100 to 500 μs using Eqs. (59) and (60). First, L_{eff} in regions A and B was obtained from Eq. (43) using τ_A, τ_B, and BSRV values. Then, the L_{eu} value in Eq. (59) was obtained from Eq. (52) using the area fractions of the good and bad regions and the corresponding L_{eff} values. The J_{ob} value was then calculated using in Eq. (59), and finally the V_{OC} was calculated using Eq. (60), neglecting the emitter component of saturation current density, J_{oe}.

$$J_{\mathrm{ob}} = \frac{qn_i^2 D_n}{N_B L_{\mathrm{eu}}}, \tag{59}$$

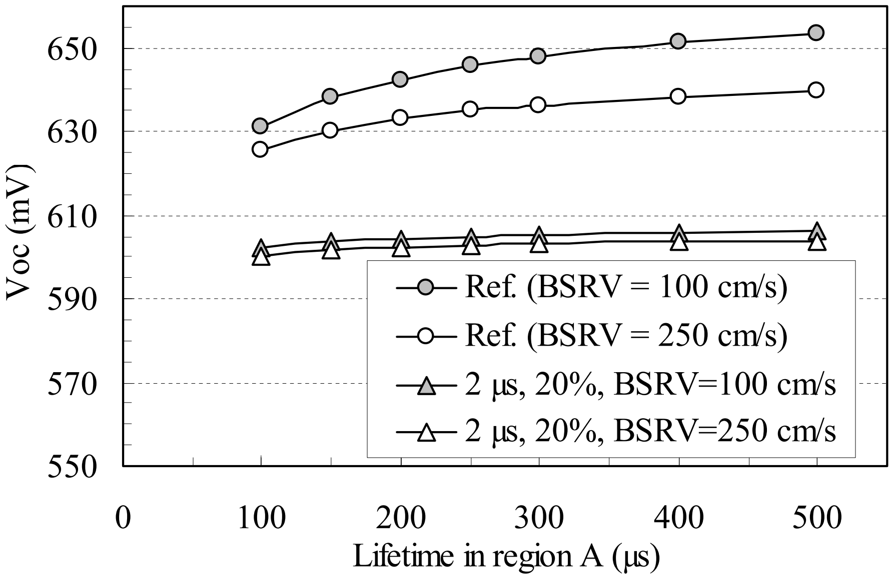

Figure 66: Model calculations of V_{OC} as a function of carrier lifetime in region A (τ_A). Device thickness is 300 μm.

and

$$\begin{aligned} V_{\mathrm{OC}} &= \frac{kT}{q}\ln\Big(\frac{J_{\mathrm{SC}}}{J_{\mathrm{oe}}+J_{\mathrm{ob}}}+1\Big) \\ &\simeq \frac{kT}{q}\ln\Big(\frac{J_{\mathrm{SC}}}{J_{\mathrm{ob}}}+1\Big), \end{aligned} \tag{60}$$

where q is the electron charge, n_i is the intrinsic carrier concentration, D_n is the diffusion coefficient of electron, and N_B is the background doping concentration [152].

The results of model calculations are summarized in Fig. 66. The reference curve (BSRV = 250 cm/s) in Fig. 66 indicates the V_{OC} values for a uniform material without any bad region (area fraction of region B is 0%, $A_B = 0$). Model calculations reveal that an appreciable improvement in V_{OC} ($\sim$14 mV) can be observed when A_B is zero and τ_A is raised from 100 to 500 μs. However, if defects are present with τ_B of 2 μs and bad region area fraction of 20%, the V_{OC} will increase only by 4 mV if τ_A is increased from 100 to 500 μs with a BSRV of 250 cm/s. If the BSRV is improved from 250 to 100 cm/s, a much higher increase in V_{OC} of 23 mV can be observed upon increasing τ_A from 100 to 500 μs in the presence of defect inhomogeneity, however, When τ_B is 2 μs with area fraction of region B of 20%, the increase in V_{OC} is limited to only 4 mV. These results show that the full potential of a high-quality rear surface passivation scheme cannot be realized in the presence of defects. Thus, unless we take care of the real bad regions, improving the good region or BSRV will not have much impact on device performance.

The next section provides guidelines for achieving 17% planar mc-Si solar cells in the presence of the defective regions within the cell.

8.2.3 Design of 17%-efficient planar ribbon mc-Si cells in the presence of defects

The quality of mc-Si material depends on many factors, such as silicon feedstock, crystal growth technique, and growth speed. It is not easy to eliminate the effect of material inhomogeneity by improving material growth and cell process technologies. Therefore, in this section, an approach to high-efficiency (>17%) mc-Si solar cells is outlined in the presence of electrically active defects. This section shows what level of defect and process engineering is necessary to achieve >17% mc-Si cells. This is done by combining the inhomogeneity model with PC1D simulations.

The model used in this section assumes two regions (good and bad) with the τ_{avg} fixed at 100 μs. The base resistivity of 3.0 Ωcm and a thickness of 300 μm are used in the simulations. The initial input parameters used for model calculations in PC1D are shown in Table 22, which represent the current status of ribbon Si solar cells. The input value for carrier lifetime (τ_{bu}) in PC1D was determined by the combination of the area fraction (A_A and A_B) and lifetime in each region (τ_A and τ_B) using Eqs. (43) and (52). The area fraction of region B and its lifetime τ_B were varied from 0 to 50% and 1.0 to 30 μs, respectively. Note that τ_A was varied each time in order to keep the τ_{avg} at 100 μs. The results of PC1D simulations are shown in Fig. 67(a) in the form of a contour plot. The simulations reveal that even if the area fraction of the bad region is reduced to less than 10% and the lifetime in the bad region is improved to greater than 5 μs, the achievable cell efficiency is limited to only 15.5% using the current cell design.

Table 22: Initial input parameters used for device modeling in PC1D.

Parameter	**Value**
Base resistivity	3.0 Ωcm
Thickness	300 µm
FSRV	150,000 cm/s
BSRV	250 cm/s
Grid coverage	6.0%
Front AR coating	78 nm, index = 2.0
Rear internal reflectance (BSR)	55%, diffuse
Front doping profile	45 Ω/sq, Spreading resistance measurement
Base contact (Series resistance)	0.75 Ω (0.75 Ωcm^2)
Internal conductor (Shunt resistance)	5.0x10^{-5} S (2.0x10^4 Ωcm^2)
J_{o2}	2.6x10^{-8} A
Second diode ideality factor	2.0
Area fraction of regions A and B	Variable
Lifetime in regions A (τ_A) and B (τ_B)	Variable
Area-average lifetime (τ_{avg})	100 µs

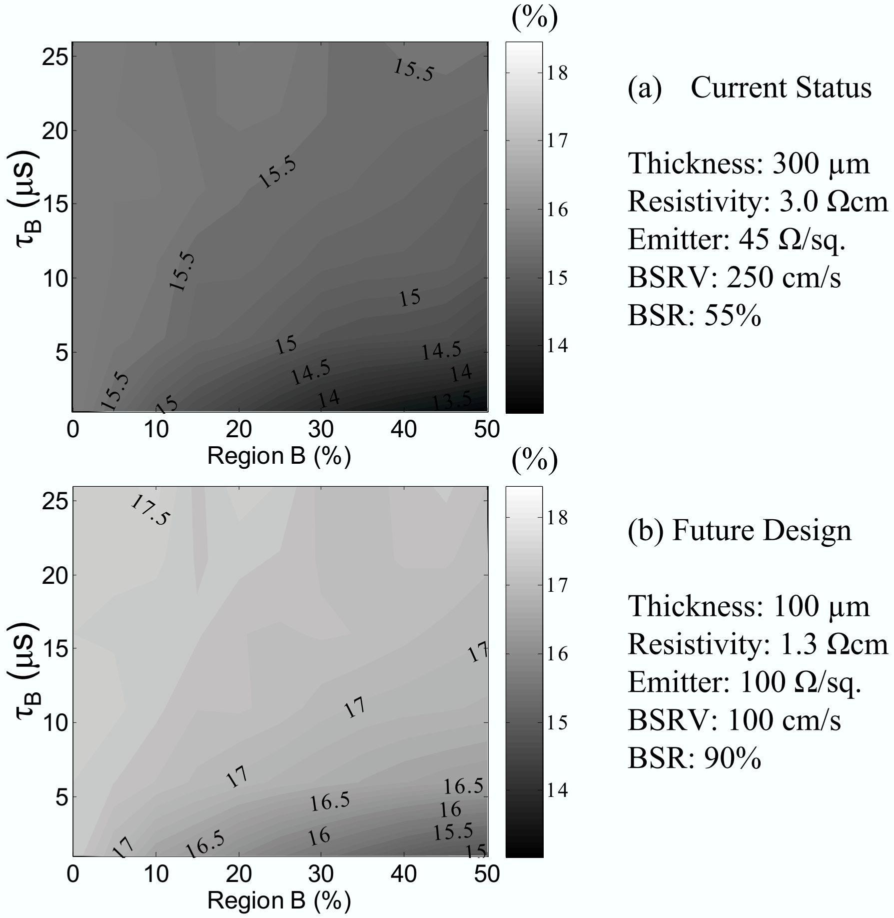

(a) Current Status

Thickness: 300 μm
Resistivity: 3.0 Ωcm
Emitter: 45 Ω/sq.
BSRV: 250 cm/s
BSR: 55%

(b) Future Design

Thickness: 100 μm
Resistivity: 1.3 Ωcm
Emitter: 100 Ω/sq.
BSRV: 100 cm/s
BSR: 90%

Figure 67: Contour plot of (a) current and (b) future ribbon Si solar cell efficiencies as a function of area fraction of region B and τ_B.

To enhance the cell efficiency further, some advanced design features need to be introduced along with the improvement in material quality. In these simulations, we investigated the impact of (i) base resistivity and thickness, (ii) emitter sheet resistance, and (iii) rear surface passivation and rear reflection on cell efficiency in the presence of defects.

PC1D simulations were performed again to estimate the possible cell efficiencies on defective Si materials using these variables and design features. Improved material and device design parameters used in the simulations shown in Fig. 67(b) include 1.3 Ωcm resistivity, 100 μm thickness, 100 Ω/sq. emitter, 100 cm/s BSRV, and 90% back surface reflection. The simulations reveal that with the above design modifications, if the area fraction of the bad region is reduced to less than 10% and the lifetime in the bad region is improved to greater than 5 μs, cell efficiency can be increased to greater than 17.0% on defective materials even with no surface texturing. A successful implementation of surface texturing can raise this efficiency close to 18%.

8.3 Conclusions

An analytical model was developed in this study to understand the impact of highly defective (low diffusion length) regions on mc-Si solar cell performance. This model gives a reasonable estimate of the loss in V_{OC} resulting from material inhomogeneity in mc-Si cells. Model calculations showed that even if the τ_{avg} is 100 μs, the V_{OC} value can vary substantially, depending on the recombination intensity and area fraction of the defective regions.

The analytical model for defect inhomogeneity was applied to large-area EFG Si cells, which contain a wide spread of diffusion lengths over the cell area. The difference between calculated and measured loss in V_{OC} becomes smaller when multiple-region analysis, instead of two-region analysis, is performed on large-area devices.

Model calculations were extended to predict the mc-Si cell performance in the presence of defective regions. It was found that the impact of improving the lifetime in good regions or rear surface passivation is very limited in the presence of defects, even if the lifetime in good regions is improved from 100 to 500 μs and BSRV is reduced from 250 to 100 cm/s. In order to realize the full potential of high-quality surface passivation and high carrier lifetime, the area fraction and recombination intensity of the bad region must be reduced. Model calculations revealed that if the area fraction of the bad region is reduced to less than 10% and the lifetime in the bad region is improved to greater than 5 μs, a planar cell efficiency of 17.0% can be achieved by applying advanced design features, such as high sheet resistance emitters and effective rear surface passivation. Further research is needed to reduce the recombination intensity and the area fraction of bad regions. This can be accomplished by a combination of improving the material growth techniques and developing a novel defect passivation scheme to deactivate the lifetime-limiting defects.

CHAPTER IX

ATTEMPTS TO MINIMIZE AREA FRACTION AND RECOMBINATION INTENSITY OF LOW DIFFUSION LENGTH REGIONS BY HIGH-TEMPERATURE THERMAL CYCLES AND DOUBLE-SIDED PECVD SILICON NITRIDE-INDUCED DEFECT HYDROGENATION

As discussed in Chap. II, the low-cost ribbon Si materials contain metal impurities and structural defects, which lead to a very low as-grown carrier lifetime of 1–5 μs. These lifetimes are not enough to produce high-efficiency cells. Therefore, in Chap. IV, it has been demonstrated that the PECVD SiN$_x$-induced defect hydrogenation can enhance the carrier lifetime from 1–5 μs to $\sim$100 μs. The implementation of an optimized PECVD SiN$_x$-induced defect hydrogenation in an RTP unit has been shown in Chapter V to produce very high-efficiency 4 cm^2 ribbon Si solar cells (18.2% on EFG and 18.3% on String Ribbon Si) using photolithography-defined front grid contacts. However, it was found in Chap. VI that the inhomogeneously distributed unpassivated active defects can lower the cell performance significantly. A simple analytical model was developed in Chapter VII in order to assess the impact of active defects on cell performance as a function of the carrier recombination intensity and area fraction of bad regions. In Chaps. VII and VIII, the analytical model was developed and applied to several small-area (4 cm^2) and large-area (100 cm^2) mc-Si cells to verify the accuracy of the model and used further to establish the guidelines for achieving high-efficiency cells in the presence of active defects.

It was found in Chap. VIII through the model calculations that the key to achieving high-efficiency cells on defective mc-Si materials is to improve the material quality or carrier lifetime in defective regions. An effort is made in this chapter to improve the material homogeneity through the systematic investigation of intense impurity gettering in a conventional tube furnace and single- and double-sided PECVD SiN_x-induced defect hydrogenation by a combination of cell fabrication and room-temperature scanning photoluminescence (PL) technique.

9.1 Effect of P Diffusion-Induced Impurity Gettering

The P diffusion-induced impurity gettering technique has been studied extensively and implemented to improve the material quality [48,49]. In the crystalline Si solar cell fabrication process, the purpose of P diffusion is not only to form the n^+ emitter but also enhance simultaneously the minority carrier diffusion length by removing the impurities in the bulk Si by a well-known gettering effect.

Although the P diffusion gettering has been implemented successfully in the PV industry, it has also been reported in the literature that the effectiveness of P diffusion gettering is quite poor in regions of high dislocation density [12, 53]. It was found in [12] that low diffusion length regions in EFG Si are highly resistant to diffusion length improvement by P gettering. The experimental results in [12] suggested that some of the structural defects in EFG Si become decorated with precipitated metallic impurities during the crystal growth that enhance carrier recombination. Clusters of precipitated metal impurities are highly stable and cannot be gettered by a standard diffusion techniques. There is a need to improve the understanding of the effect of defect clusters on mc-Si solar cells and develop technologies to mitigate their effect.

In this experiment, the effect of P diffusion-induced gettering process is revisited by comparing cells fabricated with standard diffusion process with those fabricated with additional intense gettering process. The standard and intense gettering processes used in this study is shown in Fig. 68. In order to ensure the crystallographic properties, large-area EFG Si wafers (p-type, 300 μm, 3.0 Ωcm) were first cut into two pieces, as shown in Fig. 69. Cells 1-3 (set A) were subject to standard process, and cells 4-6 (set B) were fabricated with the intense gettering process. After the initial surface cleaning, samples in set B received an

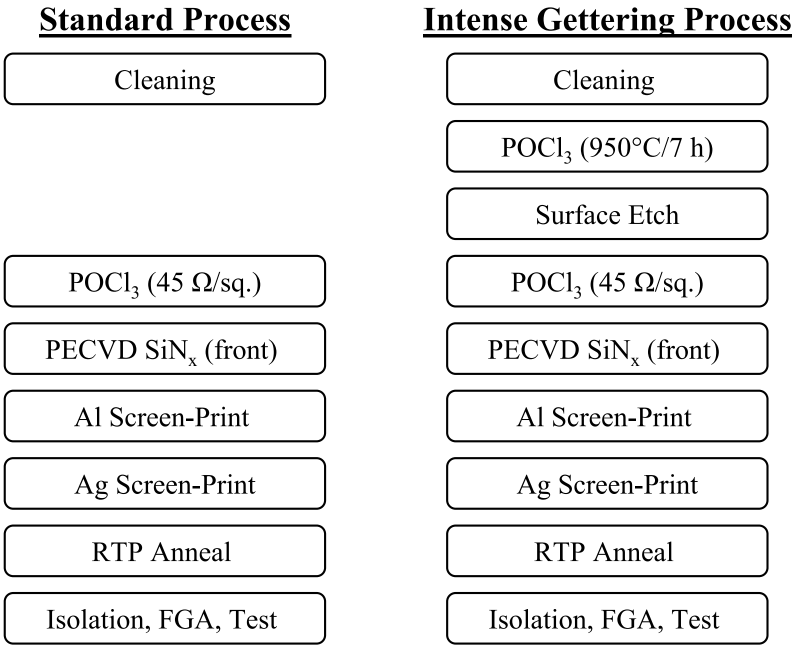

Figure 68: Process sequence for standard and intense gettering processes.

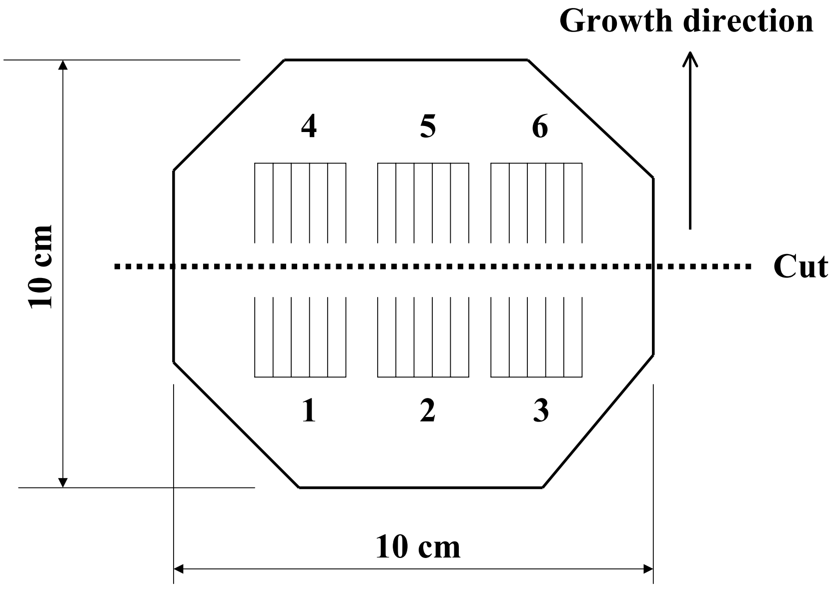

Figure 69: Cell configuration used in this study.

Table 23: Average cell results of standard (A) and intense gettering (B) processes.

Process	V_{OC} (mV)	J_{SC} (mA/cm^2)	FF	Eff. (%)	# of cells
Standard (A)	597	32.6	0.775	15.1	11
Gettered (B)	597	32.1	0.772	14.8	11

additional intense gettering process in a $POCl_3$ furnace at 950°C for 7.0 h, which resulted in a sheet resistance of 1–2 Ω/sq. After this prolonged P pregettering, the diffused regions were etched off, and the standard P diffusion process was performed at 875°C to form 40–50 Ω/sq n^+ emitters. The SiN_x layers were deposited in a low-frequency PECVD reactor. Commercial Al and Ag pastes were then screen printed on the rear and front, respectively, and fired in an RTP unit to form Al-BSF and Ag front grid contacts. Cells were finally isolated into 2×2 cm^2 and annealed in a forming gas at 400°C for 10 min. The cell results are summarized in Table 23, and the distribution of cell efficiencies is shown in Fig. 70. The solar cell parameters were extracted by illuminated and shaded $I - V$ measurements. It was found that there is no appreciable difference in the cell efficiency between sample set A and B, indicating that intense pregettering process did not provide any additional help in removing or deactivating the impurities present in the bulk.

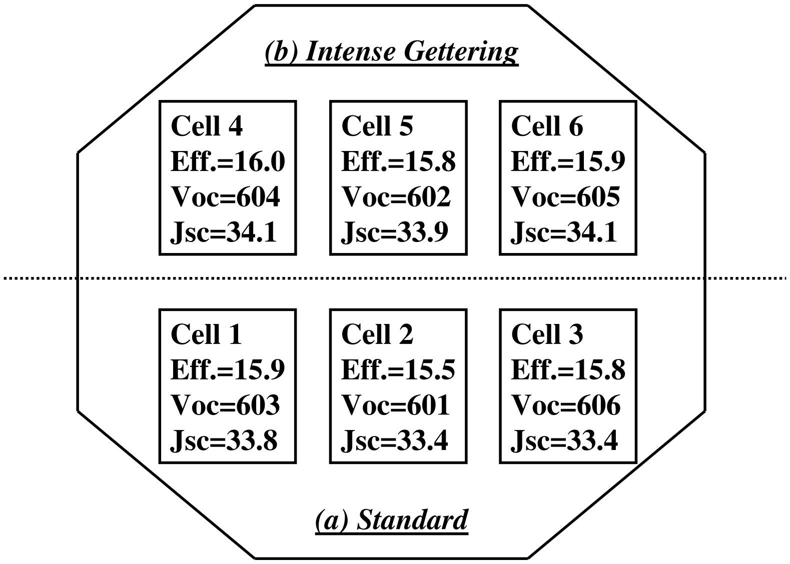

Figure 70: Cell efficiency distribution of standard (A) and intense gettering (B) processes.

9.2 Effect of Intense PECVD SiN$_x$-Induced Defect Hydrogenation

Since intense P diffusion gettering did not help mitigation of impurity-decorated defects, attempt was made to passivate them by more intese hydrogenation step. Large-area (10×10 cm^2) EFG Si wafers were first cut into two pieces to ensure the identical crystallographic properties, as shown in Fig. 69.

After the initial cleaning process, the samples were P diffused in a POCl$_3$ furnace to form 40–50 Ω/sq n$^+$ emitters. Sample set C (Cells 1–3) was processed using the standard fabrication sequence with single-side hydrogenation, and sample set D (Cells 4–6) was processed with double-sided hydrogenation process. A SiN$_x$ antireflection coating with a thickness of 800 Å and a refractive index of 2.0 was deposited on the front of samples in set C and on the both sides of samples in set D. The set D was then annealed in an RTP unit at 750°C to inject hydrogen from both sides for additional defect passivation. The initial SiN$_x$ layers were removed in a 10:1 H$_2$O:HF solution and a new SiN$_x$ layer was deposited on the front. Samples in sets C and D received a screen-printing of commercial Al paste on the rear and

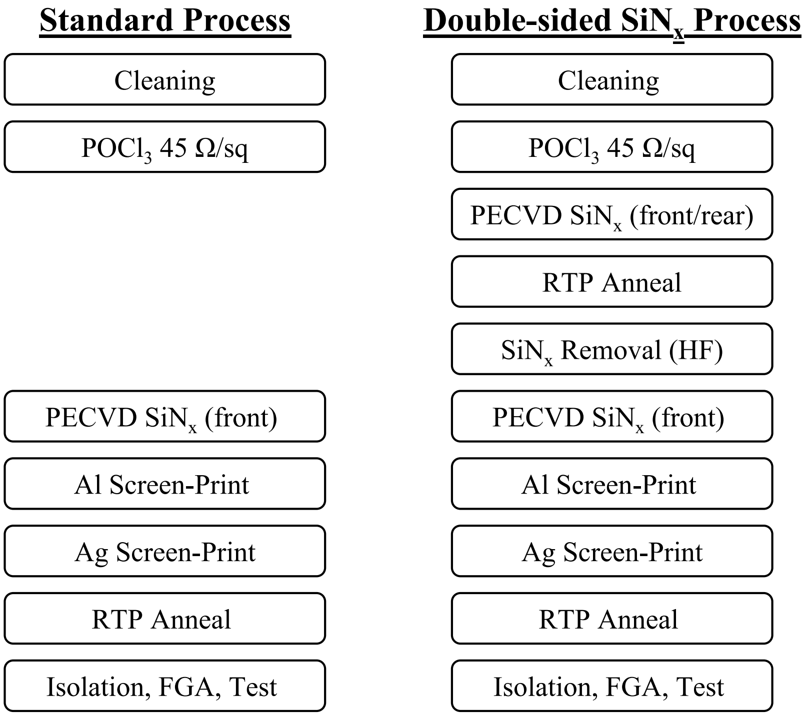

Figure 71: Process sequence for standard and intense hydrogenation processes.

Ag paste on the front, followed by contact firing in an RTP unit to form Al-BSF and Ag grid contacts. Cells were finally isolated (2×2 cm^2) and forming gas annealed at 400°C for 10 min. Process sequences for sets C and D are shown in Fig. 71.

The average solar cell performance parameters are summarized in Table 24, and the distribution of cell efficiencies is shown in Fig. 72. Surprisingly, there was no appreciable difference in the cell performance between the two sets, indicating that the additional double-sided hydrogenation process was also unable to deactivate the remaining impurity-decorated defects. This indicates that the nearly full effectiveness of defect hydrogenation process was achieved with the standard SiN$_x$ film deposited on the front only, and no appreciable enhancement is observed by injecting additional hydrogen from the rear side.

In order to support the effectiveness of PECVD SiN$_x$-induced defect hydrogenation, scanning photoluminescence (PL) measurements were performed on EFG Si materials subjected to single- and double-side hydrogenation. The PL spectrum was taken at room

Table 24: Average cell results of standard (C) and intense hydrogenation (D) processes.

Process	V_{OC} (mV)	J_{SC} (mA/cm^2)	FF	Eff. (%)	# of cells
Standard (C)	594	32.8	0.765	14.9	15
Intense SiN_x (D)	596	33.0	0.762	15.0	15

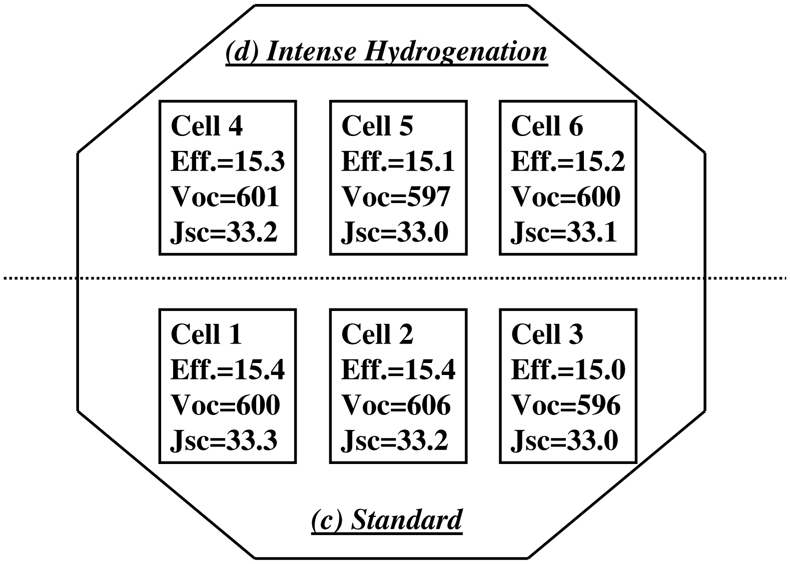

Figure 72: Cell efficiency distribution of standard (C) and intense hydrogenation (D) processes.

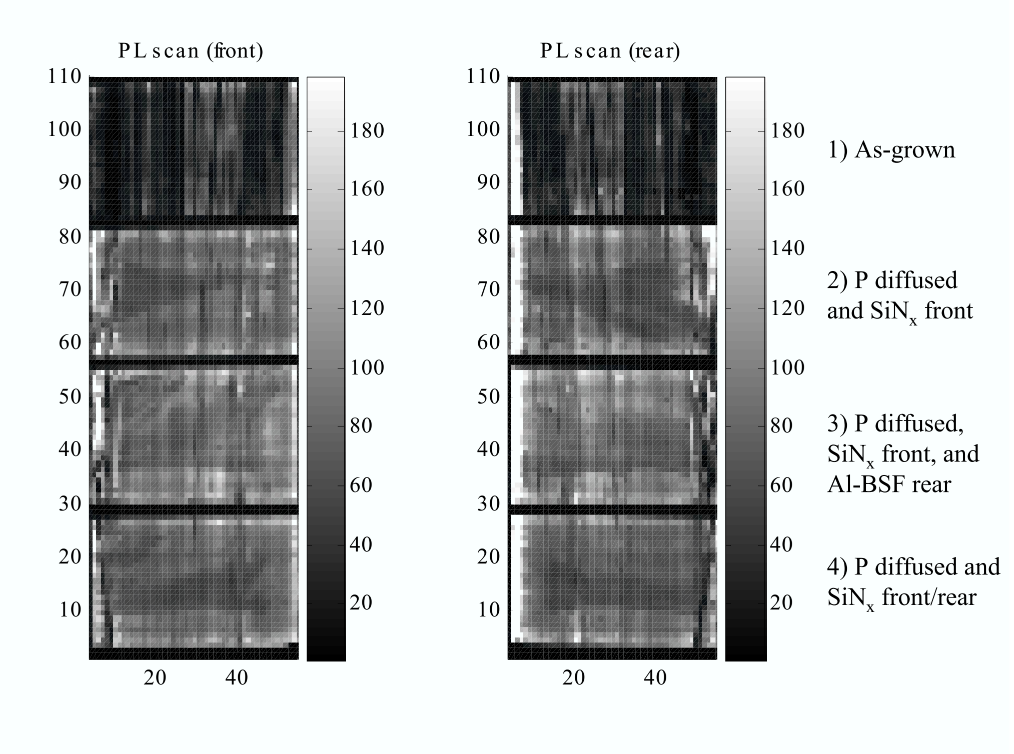

Figure 73: Front and rear PL scans (I_{bb}) of four EFG Si samples: 1) unprocessed or as-grown, 2) P diffused and PECVD SiN$_x$ on the front, 3) P diffused, PECVD SiN$_x$ on the front and Al-BSF on the rear, and 4) P diffused and PECVD SiN$_x$ on the front and rear.

temperature using AlGaAs laser with a wavelength of 800 nm. For details of PL measurements, see [137] and [173]. Four small samples (5.0×2.5 cm^2) were cut from the same EFG wafer and prepared as follows: 1) unprocessed or as-grown, 2) P diffused and PECVD SiN$_x$ on the front, 3) P diffused, PECVD SiN$_x$ on the front and screen-printed Al on the rear, and 4) P diffused and PECVD SiN$_x$ on the front and rear. The P diffusion and SiN$_x$ deposition conditions were kept same as described in previous section. Samples #2, 3, and 4 were annealed in an RTP unit at 750°C for hydrogenation. After the thermal treatment, Al and SiN$_x$ layers were removed in 2:1:1 H_2O:H_2O_2:HCl and 10:1 H_2O:HF solutions, respectively, and Al-BSF and P-doped n$^+$ layers were etched in 15:5:2 HNO_3:CH_3COOH:HF solution. The maps of PL intensity (band-to-band, I_{bb}, which is proportional to effective lifetime [137]) are shown in Fig. 73. The PL measurements were performed from the front as well as the rear side of the EFG samples to quantify the effect of defect passivation on

Table 25: Average values of PL intensities for I_{bb} in each process step.

PL scan (I_{bb})	**As-grown**	**P-diffused +SiN$_x$ front**	**P-diffused+SiN$_x$ front+Al-BSF rear**	**P-diffused +SiN$_x$ front/rear**
Front	27	**77**	88	75
Rear	36	84	91	78

bulk Si. The average values of PL intensity (I_{bb}) after each process step are summarized in Table 25.

Figure 73 and Table 25 reveal that the combination of PECVD SiN$_x$ on the front and Al-BSF on the rear produced maximum enhancement in PL response or carrier lifetime. In addition, there was no appreciable difference in the average PL response for single- and double-sided hydrogenation. It is important to note that majority of the improvement came from single-sided hydrogenation and Al-BSF. PL results are consistent with the cell results, which also showed no appreciable difference between the single- and double-sided hydrogenation (Table 24). This suggests that all the passivatable defects are passivated by hydrogen injected from the single-sided SiN$_x$ film. Therefore, an additional injection of hydrogen from rear side does not play a role since the remaining defects are not affected by hydrogen. More research is needed to eliminate unpassivatable defects or enhance the effectiveness of SiN$_x$-induced defect hydrogenation in order to achieve a homogeneous distribution of carrier lifetime over the entire cell area and high-efficiency ribbon Si cells.

CHAPTER X

GUIDELINES FOR FUTURE WORK

10.1 Surface Texturing for Effective Light Trapping

Another way to improve the cell efficiency is to apply a surface texturing for effective light trapping. PC1D device simulations were performed to quantify the effect of surface texturing on cell performance. The results of simulations are shown in Fig. 74. The random pyramid surface texturing was used in these simulations. The PC1D simulations revealed that the successful implementation of surface texturing can bring an efficiency enhancement of ∼1.0% in absolute. This means that the record high-efficiency String Ribbon Si cells with screen-printed contacts (16.8%) achieved in Chap. III can reach an efficiency of 17.8%, as shown in Fig. 74. However, surface texturing on ribbon Si materials has not been fully successful because of the presence of structural defects, such as twins and grain boundaries. Hahn *et al.* [174] tried to apply an acidic etch for surface texturing ($H_2SO_4/HF/HNO_3$) on Strign Ribbon Si materials, shown in Fig. 75. It was reported in [174] that no appreciable effect was observed on cell efficiency. This could be due to the preferential etching of weakly bonded silicon sites (twins and grain boundaries). Figure 75 clearly shows the preferential etch of twinned regions. New texturing techniques need to be developed to reduce the reflection and increase the ribbon Si cell performance. In addition, a combination of high-quality rear surface passivation (BSRV = 100 cm/s and BSR = 90%) and surface texturing can bring the cell efficiency close to 18% with screen-printing technology.

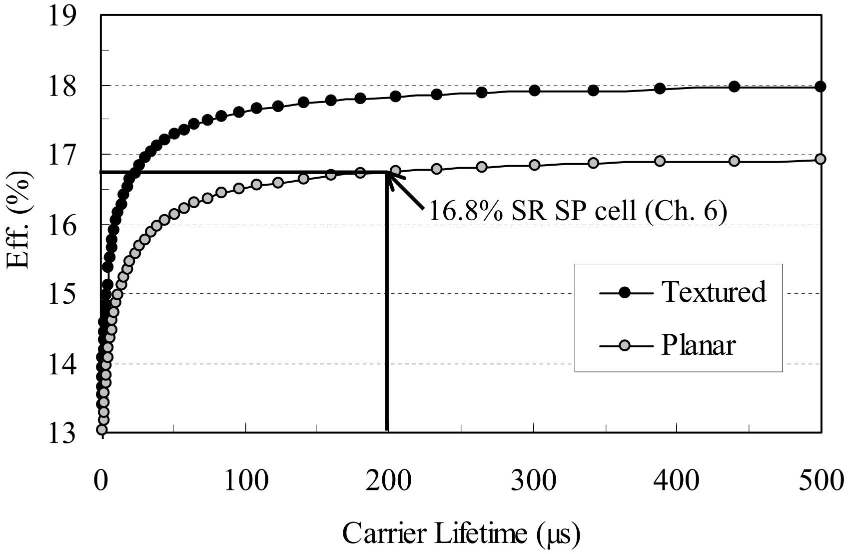

Figure 74: Results of PC1D simulations with and without surface texturing as a function of carrier lifetime.

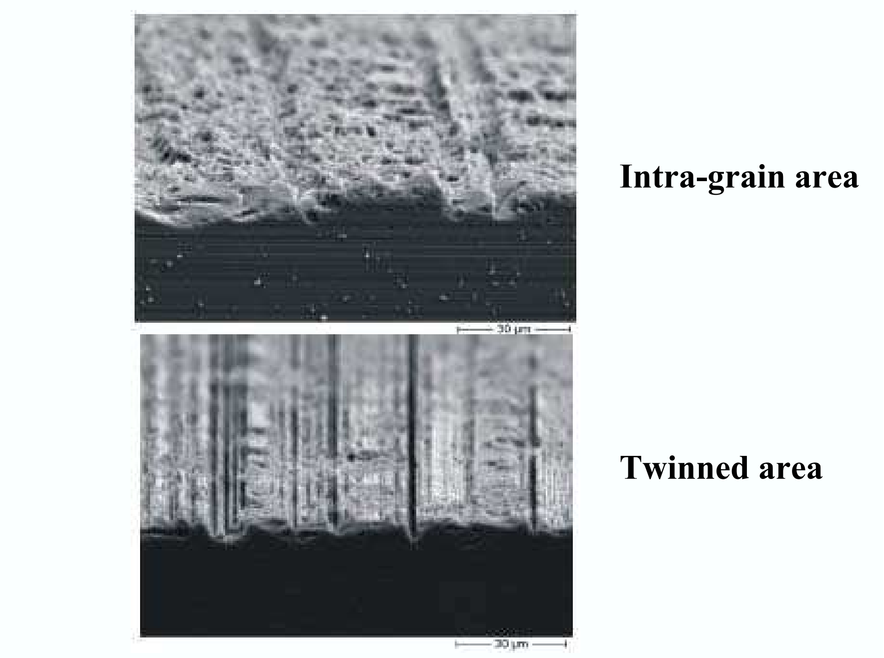

Figure 75: Surface texturing using an acidic etch (H_2SO_4/HF/HNO_3) solution on String Ribbon Si.

APPENDIX A

DETAILED PROCESS SEQUENCE: SCREEN-PRINTED CONTACTS

A.1 Initial Wafer Cleaning

- DI rinse – 5 min
- H_2O:HF 10:1 dip – 1 min
- DI rinse – 5 min
- H_2O:H_2O_2:H_2SO_4: 2:1:1 dip – 5 min
- DI rinse – 5 min
- H_2O:HF 10:1 dip – 1 min
- DI rinse – 5 min
- H_2O:H_2O_2:HCl: 2:1:1 dip – 5 min
- DI rinse – 5 min
- H_2O:HF 10:1 dip – 1 min
- DI rinse – 5 min
- N_2 dry

A.2 $POCl_3$ Diffusion

- Wafer loading
- Diffusion temperature and time setting – 875°C for 40–50 Ω/sq. and 850°C for 90–100 Ωsq., deposition for 20 min and drive-in for 12 min

- Run the process
- Wafer unloading
- Phosphosilicate glass removal in H_2O:HF 10:1 – 1 min
- DI rinse – 5 min
- N_2 dry

A.3 Low-Frequency PECVD SiN_x Deposition

- Wafer loading
- Temperature stabilization at 425°C – 15–20 min
- Gas leak check
- Surface pretreatment – NH_3 gas flow rate: 1000 sccm, plasma power: 250 W, ambient pressure: 1.5 torr for 2 min
- Purge – N_2 gas flow rate: 1000 sccm for 2 min
- Deposition – NH_3 gas flow rate: 3000 sccm, Si_3H_4 gas flow rate: 300 sccm, plasma power 150 W, ambient pressure: 2.0 torr for 3.5 min (750–800 Å, $n \simeq 2.0$)
- Purge – N_2 gas flow rate: 1000 sccm for >4 min
- Wafer unloading

A.4 Al and Ag Screen-Printing

- Belt-dryer temperature and speed setting – 200°C and 2.0 ipm
- Screen and paste selection – Al screen with 200 mesh, Ferro FX53-038 Al conductor paste
- Printer setting – Snap-off distance: 50 mils
- Dummy printing – Adjust squeegee pressure

- Printing
- Dry in a belt
- Clean-up Al screen and printer using IPA
- Screen and paste selection – Ag screen (SD2×2-75-8 for 40–50 Ω/sq. emitter and SD2×2-75-10 for 90–100 Ω/sq. emitter), Ferro CN33-455 Ag conductor paste
- Printer setting – Snap-off distance: 50 mils
- Dummy printing – Adjust squeegee pressure
- Printing
- Dry in a belt
- Clean-up Ag screen and printer using IPA

A.5 Al and Ag Burn-Out Process

- RTC LA-310 belt furnace, recipe name: 425burnout.rcp
- Belt temperature and speed setting – zone 1: 425°C, zone 2: 425°C, zone 3: 425°C, belt speed: 25 ipm
- Temperature stabilization – 15–20 min
- Wafer loading
- Wafer unloading

A.6 Contact Firing in RTP System

- AG Associates HeatPulse-610, recipe name: EFGFCNT.rcp
- RTP warm-up process – Recipe name: WARM-UP.rcp
- Firing temperature and time setting – Peak temperature: 770°C, peak holding time: 1 s, temperature ramp-up rate: 75°C/s, cooling rate: –40°C

- Dummy run – Repeat the recipe three times
- Run

A.7 Cell Isolation

- Check dicing system, dicing wheel, cooling water, and vacuum system
- Wheel setting – Height: 8.5 mils from the chuck
- Dummy cut
- Isolation into 2×2 cm^2 cells
- Surface cleaning using water and alphawipe

A.8 Forming Gas Anneal

- Check gas pressure
- Wafer loading
- Anneal – 400°C for 10 min
- Wafer unloading

APPENDIX B

DETAILED PROCESS SEQUENCE: PHOTOLITHOGRAPHY-DEFINED CONTACTS

B.1 Initial Wafer Cleaning

Same as A.1

B.2 $POCl_3$ Diffusion

Same as A.2

B.3 Low-Frequency PECVD SiN_x Deposition

Same as A.3 (thin down to 650–680 Å in a BOE solution for SiN_x/MgF_2 DLAR)

B.4 Al Screen-Printing

Same as A.4

B.5 Al Burn-Out and Firing

Same as A.5 and A.6

B.6 Rear Al Protection

- Coating of photoresist (SPR220) for rear Al protection – 3000 rpm for 30 s
- Baking – 90°C for 20 min

B.7 Front PR Coating

- HMDS – 3000 rpm for 20 s
- Layer ♯1, Microposit 1818 PR – 3000 rpm for 30 s

- Layer ♯2, Microposit 1818 PR – 3000 rpm for 30 s
- Baking – 90°C for 20 min
- Exposure – 12.5 mW/cm^2, $\lambda = 405$ nm, for 30 s
- Develop – Shipley 351:H_2O 1:3 for 40–60 s
- DI rinse – 5 min
- Optical inspection
- BOE (6:1) etch – >40 s
- DI rinse – 5 min
- Baking – 125°C for 30 min
- BOE (6:1) etch – >50 min
- DI rinse – 5 min

B.8 CVC E-Beam Metal Evaporation

- Wafer loading
- Vacuum step
- Ti evaporation – 600 Å
- Pd evaporation – 600 Å
- Ag evaporation – 400 Å
- Vent
- Wafer unloading

B.9 Lift-Off and PR Removal

- Ultra-sonic bath – 60–120 min
- Dip in Aceton ♯1, Aceton ♯2, Methanol, and IPA – 40 s each
- DI rinse – 5 min
- N_2 dry

B.10 Ag Electro-Plating

- Preparation of Ag plating solution – Cyanide in H_2O
- Dip wafers in the solution, make sure an electrical connection, and turn-on the illumination – 5–10 min
- DI rinse – 3 min
- Optical inspection

B.11 Cell Isolation

Same as A.7

B.12 Forming Gas Anneal

Same as A.8

APPENDIX C

SAMPLE PREPARATION FOR CARRIER LIFETIME MEASUREMENTS

C.1 Al Removal

- Preparation of Al etch solution – H_2O:H_2O_2:HCl 2:1:1 or Al etchant
- Dipping wafers into the solution – >4 h
- DI rinse – 5 min
- Al removal using alphawipe and IPA

C.2 Ag Removal

- Preparation of Ag etch solution – HNO_3:H_2O 1:1
- Dipping wafers into the solution – 15 s
- DI rinse – 5 min
- Ag removal using alphawipe and IPA

C.3 PECVD SiN_x Removal

- Preparation of etch solution – H_2O:HF 10:1
- Dipping wafers into the solution – 10 min
- DI rinse – 5 min

C.4 Al-BSF and n^+ Emitter Removal

- Preparation of silicon etch solution – HNO_3:CH_3COOH:HF 15:5:2
- Dipping wafers into the solution – >8 min

- DI rinse – 5 min
- N_2 dry

C.5 Iodine/Methanol Surface Passivation Solution

- Preparation of iodine/methanol solution – Iodine: 70 mg, Methanol: 250 ml

REFERENCES

[1] P. D. Maycock, “23rd annual data collection,” *PV News*, vol. 27, no. 4, pp. 6–10, 2007.

[2] Energy Information Administration, Available on-line: http://www.eia.doe.gov/emeu/iea/Notes, accessed 10/2006.

[3] D. Margadonna and F. Ferrazza, “The status of crystalline Si modules,” *Renewable Energy*, vol. 15, pp. 83–88, 1998.

[4] R. O. Bell and J. P. Kalejs, “Growth of silicon sheets for photovoltaic applications,” *J. Mater. Res.*, vol. 13, pp. 2732–2739, 1998.

[5] M. A. Green, *Solar Cells.* University of New South Wales, 1986.

[6] R. J. Stirn, “Junction characteristics of silicon solar cells,” in *Proc. 9th IEEE Photovoltaic Specialists Conf.*, 1972, pp. 72–82.

[7] H. J. Hovel, “The effect of depletion region recombination currents on the efficiencies of Si and GaAs solar cells,” in *Proc. 10th IEEE Photovoltaic Specialists Conf.*, 1973, pp. 34–39.

[8] D. K. Schroder, “Carrier lifetimes in silicon,” *IEEE Trans. Electron Devices*, vol. ED-44, pp. 160–170, 1997.

[9] S. K. Pang and A. Rohatgi, “A new methodology for separating shockley-read-hall lifetime and auger recombination coefficients from the photoconductivity decay technique,” *J. Appl. Phys.*, vol. 74, pp. 5554–5560, 1993.

[10] W. M. Bullis and H. R. Huff, “Interpretation of carrier recombination lifetime and diffusion length measurements in silicon,” *J. Electrochem. Soc.*, vol. 143, pp. 1399–1405, 1996.

[11] V. Kveder, M. Kittler, and W. Schroter, “Recombination activity of contaminated dislocations in silicon: A model describing electron-beam-induced current contrast behavior,” *Phys. Rev. B*, vol. 63, p. 115208, 2001.

[12] J. Bailey, S. A. McHugo, H. Hieslmair, and E. R. Weber, “Efficiency-limiting defects in silicon solar cell material,” *J. Electron. Mater.*, vol. 25, pp. 1417–1421, 1996.

[13] D. K. Schroder, *Semiconductor Material and Device Characterization.* John Wiley & Sons, Inc., 1990.

[14] R. A. Sinton, *User Manual: WCT-100 Photoconductance Tool.* Sinton Consulting, Inc., 2000.

[15] H. M’saad, J. Michel, A. Reddy, and L. C. Kimerling, “Monitoring and optimization of silicon surface quality,” *J. Electrochem. Soc.*, vol. 142, pp. 2833–2835, 1995.

[16] H. Nagel, C. Berge, and A. G. Aberle, "Generalized analysis of quasi-steady-state and quasi-transient measurements of carrier lifetimes in semiconductors," *J. Appl. Phys.*, vol. 86, pp. 6218–6221, 1999.

[17] R. A. Sinton and A. Cuevas, "Contactless determination of current-voltage characteristics and minority carrier lifetimes in semoconductors from quasi-steady-state photoconductance data," *Appl. Phys. Lett.*, vol. 69, pp. 2510–2512, 1996.

[18] R. A. Sinton, A. Cuevas, and M. Stuckings, "Quasi-steady-state photoconductance, a new method for solar cell material and device characterization," in *Proc. 25th IEEE Photovoltaic Specialists Conf.*, 1996, pp. 457–460.

[19] A. Cuevas and D. Macdonald, "Measuring and interpreting the lifetime of silicon wafers," *Sol. Energy*, vol. 76, pp. 255–262, 2004.

[20] D. Macdonald and A. Cuevas, "Trapping of minority carriers in multicrystalline silicon," *Appl. Phys. Lett.*, vol. 74, pp. 1710–1712, 1999.

[21] R. Sinton, "Predicting multi-crystalline solar cell efficiency from lifetime measured during cell fabrication," in *Proc. 3rd World Conf. Photovoltaic Energy Conversion*, 2003, pp. 1028–1031.

[22] R. A. Sinton, 2005, private communication.

[23] P. Geiger, G. Kragler, G. Hahn, and P. Fath, "Spatially resolved investigations of lifetime enhancement in vertically grown, multicrystalline silicon ribbons," *Sol. Energy Mater. Sol. Cells*, vol. 85, pp. 559–572, 2005.

[24] G. Emanuel, W. Wolke, and R. Preu, "Lifetime improvements of multicrystalline silicon analysed by spatially resolved lifetime measurements," in *Proc. 3rd World Conf. Photovoltaic Energy Conversion*, 2003, pp. 1100–1103.

[25] J. Henze, P. Pohl, C. Schmiga, M. Dhamrin, T. Saitoh, I. Yamaga, and J. Schmidt, "Millisecond area-averaged lifetimes in gallium-doped multicrystalline silicon," in *Proc. 20th Euro. Photovoltaic Solar Energy Conf.*, 2005, pp. 769–772.

[26] P. Geiger, G. Krangler, G. Hahn, and E. Bucher, "Spacially resolved lifetime investigation of Al- and P-gettering combinations with remote hydrogen plasma passivation in EFG ribbon silicon," in *Proc. 17th Euro. Photovoltaic Solar Energy Conf.*, 2001, pp. 1715–1718.

[27] D. H. Macdonald, "Recmobination and trapping in multicrystalline silicon solar cells," Ph.D. dissertation, Australian National University, 2001.

[28] P. D. Maycock, "PV news annual market survey results," *PV News*, vol. 24, no. 4, pp. 1–5, 2005.

[29] J. P. Kalejs, "Silicon ribbons and foils – state of the art," *Sol. Energy Mater. Sol. Cells*, vol. 72, pp. 139–153, 2002.

[30] H. E. LaBelle, "Melt growth of single crystal sapphire ribbons for use as substrates," *Am. Ceram. Soc. Bull.*, vol. 51, p. 427, 1972.

[31] T. F. Ciszek, "Melt growth of crystalline silicon tubes by a capillary action shaping technique," *Phys. Status Solidi A*, vol. 32, pp. 521–527, 1975.

[32] W. Schmidt, B. Woesten, and J. P. Kalejs, "Manufacturing technology for ribbon silicon (EFG) wafers and solar cells," *Prog. Photovolt: Res. Appl.*, vol. 10, pp. 129–140, 2002.

[33] Schott Solar, Inc., Available on-line: http://www.us.schott.com/english/index.html, accessed 11/2006.

[34] GT Solar Technologies, Inc., Available on-line: http://www.gtsolar.com/, accessed 12/2006.

[35] A. Rohatgi, D. S. Kim, K. Nakayashiki, V. Yelundur, , and B. Rounsaville, "High-efficiency solar cells on edge-defined film-fed grown (18.2%) and String Ribbon (17.8%) Si by rapid thermal processing," *Appl. Phys. Lett.*, vol. 84, pp. 145–147, 2004.

[36] J. Horzel, A. Seidl, and W. Schmidt, "Experimental results on the way towards thin EFG Si solar cells in production," in *Proc. 20th Euro. Photovoltaic Solar Energy Conf.*, 2005, pp. 1289–1292.

[37] J. P. Kalejs, W. Schmidt, I. Schwirtlich, and W. Hoffmann, "Challenges for EFG ribbon technology on the path to large scale manufacturing," in *Proc. 31st IEEE Photovoltaic Specialists Conf.*, 2005, pp. 1301–1304.

[38] Evergreen Solar, Inc., Available on-line: http://www.evergreensolar.com/, accessed 12/2006.

[39] A. Rohatgi, D. S. Kim, V. Yelundur, K. Nakayashiki, A. Upadhyaya, M. Hihali, and V. Meemongkolkiat, "Record-high-efficiency solar cells on multicrystalline materials through understanding and implementation of RTP-enhanced SiN_x-induced defect hydrogenation," in *Tech. Digests 14th Int. Photovoltaic Science Engineering Conf.*, 2004, pp. 635–638.

[40] G. Hahn and A. M. Gabor, "16% efficiency on encapsulated large area screen printed string ribbon cell," in *Proc. 3rd World Conf. Photovoltaic Energy Conversion*, 2003, pp. 1289–1292.

[41] R. L. Wallace, D. Harvey, A. Anselmo, and J. I. Hanoka, "A high-yield, low-cost solar cell process utilizing String Ribbon silicon dual ribobn growth," in *Proc. 31st IEEE Photovoltaic Specialists Conf.*, 2005, pp. 1139–1140.

[42] G. Hahn and A. Schonecker, "New crystalline silicon ribbon materials for photovoltaics," *J. Phys.: Condens. Matter*, vol. 16, pp. R1615–R1648, 2004.

[43] A. Burgers, A. Gutjahr, L. Laas, A. Schronecker, S. Seren, and G. Hahn, "Near 13% efficiency shunt free solar cells on RGS wafers," in *Proc. 4th World Conf. Photovoltaic Energy Conversion*, 2006.

[44] D. C. Senft, "Opportunities in photovoltaics for space power generation," in *Proc. 31st IEEE Photovoltaic Specialists Conf.*, 2005, pp. 536–541.

[45] R. G. Seidensticker, “Dendritic web silicon for solar cell application,” *J. Cryst. Growth*, vol. 39, pp. 17–22, 1977.

[46] S. Narasimha, G. Crotty, A. Rohatgi, and D. L. Meier, “Back surface field effects in the 17.3% efficient n-type dendritic web silicon solar cells,” *Solid-State Electron.*, vol. 42, pp. 1631–1640, 1998.

[47] J. R. Davis, A. Rohatgi, R. H. Hopkins, P. D. Blais, P. Rai-Choudhury, J. R. Mccormick, and H. C. Mollenkopf, “Impurities in silicon solar cells,” *IEEE Trans. Electron Devices*, vol. ED-27, pp. 677–687, 1980.

[48] S. A. McHugo, H. Hieslmair, and E. R. Weber, “Gettering of metallic impurities in photovoltaic silicon,” *Appl. Phys. A*, vol. 64, pp. 127–137, 1997.

[49] B. L. Sopori, L. Jastrzebski, and T. Tan, “A comparison of gettering in single- and multicrystalline silicon for solar cells,” in *Proc. 25th IEEE Photovoltaic Specialists Conf.*, 1996, pp. 625–628.

[50] A. Rohatgi, J. R. Davis, R. H. Hopkins, P. Rai-Choudhury, P. G. Mcmullin, and J. R. Mccormick, “Effect of titanium, copper, and iron on silicon solar cells,” *Solid-State Electron.*, vol. 23, pp. 415–422, 1980.

[51] C. S. Chen and D. K. Schroder, “Kinetics of gettering in silicon,” *J. Appl. Phys.*, vol. 71, pp. 5858–5864, 1992.

[52] J. S. Kang and D. K. Schroder, “Gettering in silicon,” *J. Appl. Phys.*, vol. 65, pp. 2974–2985, 1989.

[53] D. Macdonald, A. Cuevas, and F. Ferrazza, “Response to phosphorus gettering of difference regions of cast multicrystalline silicon ingots,” *Solid-State Electron.*, vol. 43, pp. 571–581, 1999.

[54] S. M. Joshi, U. M. Gosele, and T. Y. Tan, “Improvement of minority carrier diffusion length in Si by Al gettering,” *J. Appl. Phys.*, vol. 77, pp. 3858–3863, 1995.

[55] ——, “Extended high temperature Al gettering for improvement and homogenization of minority carrier diffusion lengths in multicrystalline Si,” *Sol. Energy Mater. Sol. Cells*, vol. 70, pp. 231–238, 2001.

[56] S. Narasimha, A. Rohatgi, and A. W. Weeber, “An optimized rapid aluminum back surface field technique for silicon solar cells,” *IEEE Trans. Electron Devices*, vol. 46, pp. 1363–1370, 1999.

[57] C. T. Sah, J. Y.-C. Sun, and J. J.-T. Tzou, “Deactivation of the boron acceptor in silicon by hydrogen,” *Appl. Phys. Lett.*, vol. 42, pp. 204–206, 1983.

[58] N. M. Johnson, C. Herring, and D. J. Chadi, “Interstitial hydrogen and neutralization of shallow-donor impurities in single-crystal silicon,” *Phys. Rev. Lett.*, vol. 56, pp. 769–772, 1986.

[59] S. J. Pearton, J. W. Corbett, and T. S. Shi, “Hydrogen in crystalline semiconductors,” *Appl. Phys. A*, vol. 43, pp. 153–195, 1987.

[60] J. I. Pankove, P. J. Zanzucchi, and C. W. Magee, “Hydrogen localization near boron in silicon,” *Appl. Phys. Lett.*, vol. 46, pp. 421–423, 1985.

[61] N. M. Johnson, “Mechanism for hydrogen compensation of shallow-acceptor impurities in single-crystal silicon,” *Phys. Rev. B*, vol. 31, pp. 5525–5528, 1985.

[62] K. Bergman, M. Stavola, S. J. Pearton, and J. Lopata, “Donor-hydrogen complexes in passivated silicon,” *Phys. Rev. B*, vol. 37, pp. 2770–2773, 1988.

[63] S. J. Uftring, M. Stavola, P. M. Williams, and G. D. Watkins, “Microscopic structure and multiple charge states of a PtH_2 complex in Si,” *Phys. Rev. B*, vol. 51, pp. 9612–9621, 1995.

[64] M. Stavola, W. Tang, F. Jiang, V. Yelundur, A. Rohatgi, G. Hahn, and J. Kalejs, “Introduction of H into Si as characterized by IR spectroscopy,” in *Proc. 14th NREL Workshop on Crystalline Silicon Solar Cell: Processes and Modules*, 2003, pp. 134–142.

[65] F. Jiang, M. Stavola, A. Rohatgi, D. Kim, J. Holt, H. Atwater, and J. Kalejs, “Hydrogenation of Si from SiN_x(H) films: Characterization of H introduced into the Si,” *Appl. Phys. Lett.*, vol. 83, pp. 931–933, 2003.

[66] V. Yelundur, A. Rohatgi, J. I. Hanoka, and R. Reedy, “Beneficial impact of low frequency PECVD SiN_x:H-induced hydrogenation in high-efficiency String Ribbon silicon solar cells,” in *Proc. 19th Euro. Photovoltaic Solar Energy Conf.*, 2004, pp. 951–954.

[67] N. M. Johnson, D. K. Biegelsen, and M. D. Moyer, “Deuterium passivation of grain boundary dangling bonds in silicon thin films,” *Appl. Phys. Lett.*, vol. 40, pp. 882–884, 1982.

[68] J. I. Hanoka, C. H. Seager, D. J. Sharp, and J. K. G. Paritz, “Hydrogen passivation of defects in silicon ribbon grown by the edge-defined film-fed growth process,” *Appl. Phys. Lett.*, vol. 42, pp. 618–620, 1983.

[69] C. Dube, J. I. Hanoka, and D. B. Sandstrom, “Hydrogen diffusion along passivation grain boundaries in silicon ribbon,” *Appl. Phys. Lett.*, vol. 44, pp. 425–427, 1984.

[70] A. van Wieringen and N. Warmoltz, “On the permeation of hydrogen and helium in single crystal silicon and germanium at elevated temperatures,” *Physica*, vol. 22, pp. 849–865, 1956.

[71] T. Zundel and J. Weber, “Trap-limited diffusion in boron-doped silicon,” *Phys. Rev. B*, vol. 46, pp. 2071–2077, 1992.

[72] Y. Kamiura, M. Yoneta, and F. Hashimoto, “Hydrogen diffusivities below room temperature in silicon evaluated from the photoinduced dissociation of hydrogen-carbon complexes,” *Appl. Phys. Lett.*, vol. 59, pp. 3165–3167, 1991.

[73] R. C. Newman, J. H. Tucker, A. R. Brown, and S. A. McQuaid, “Hydrogen diffusion and the catalysis of enhanced oxygen diffusion in silicon at temperature below 500C,” *J. Appl. Phys.*, vol. 70, pp. 3061–3070, 1991.

[74] B. L. Sopori, K. Jones, and X. J. Deng, "Observation of enhanced hydrogen diffusion in solar cell silicon," *Appl. Phys. Lett.*, vol. 61, pp. 2560–2562, 1992.

[75] P. Doshi and A. Rohatgi, "18% efficient silicon photovoltaic devices by rapid thermal diffusion and oxidation," *IEEE Trans. Electron Devices*, vol. ED-45, pp. 1710–1717, 1998.

[76] A. Usami, M. Ando, M. Tsunekane, and T. Wada, "Shallow-junction formation on silicon by rapid thermal diffusion of impurities from a spin-on source," *IEEE Trans. Electron Devices*, vol. ED-39, pp. 105–110, 1992.

[77] J. Jeong, A. Rohatgi, V. Yelundur, A. Ebong, M. D. Rosenblum, and J. P. Kalejs, "Enhanced silicon solar cell performance by rapid thermal firing of screen-printed metals," *IEEE Trans. Electron Devices*, vol. ED-48, pp. 2836–2841, 2001.

[78] V. Yelundur, A. Rohatgi, J. Jeong, and J. I. Hanoka, "Improved String Ribbon silicon solar cell performance by rapid thermal firing of screen-printed contacts," *IEEE Trans. Electron Devices*, vol. ED-49, pp. 1405–1410, 2002.

[79] S. Seren, G. Hahn, A. Gutjahr, A. R. Burgers, and A. Schonecker, "Ribbon growth on substrate - a roadmap to higher efficiencies," in *Proc. 21st Euro. Photovoltaic Solar Energy Conf.*, 2006, pp. 668–674.

[80] R. A. Sherif, R. R. King, N. H. Karam, and D. R. Lillington, "The path to 1GW of conventrator photovoltaics using multijunction solar cells," in *Proc. 31st IEEE Photovoltaic Specialists Conf.*, 2005, pp. 17–22.

[81] M. Gratzel, "Dye-sensitized solar cells," *J. Photochem. Photobio. C*, vol. 4, pp. 145–153, 2003.

[82] L. C.-K. Liau and H. Chang, "Effect of the thermal stability on dye-sensitized TiO_2 solar cells," in *Proc. 3rd World Conf. Photovoltaic Energy Conversion*, 2003, pp. 236–239.

[83] Konarka Technologies, Inc., Available on-line: http://www.konarka.com/, accessed 12/2006.

[84] Peccell Technologies, Inc., Available on-line: http://www.peccell.com/, accessed 12/2006.

[85] K. Kawano, R. Pacios, D. Poplavskyy, J. Nelson, D. C. Bradley, and J. R. Durrant, "Degradation of organic solar cells due to air exposure," *Sol. Energy Mater. Sol. Cells*, vol. 90, pp. 3520–3530, 2006.

[86] J. M. Kroon, S. C. Veenstra, L. H. Slooff, W. J. H. Verhees, M. M. Koetse, J. Sweelseen, H. F. M. Schoo, W. J. E. Beek, M. M. Wienk, R. A. J. Janssen, X. Yang, J. Loos, V. D. Michailetchi, P. W. M. Blom, J. Knol, and J. C. Hummelen, "Polymer based photovoltaics: novel concepts, materials and state-of-the-art efficiencies," in *Proc. 20th Euro. Photovoltaic Solar Energy Conf.*, 2005, pp. 14–19.

[87] D. Sarti and R. Einhaus, "Silicon feedstock for the multi-crystalline photovoltaic industry," *Sol. Energy Mater. Sol. Cells*, vol. 72, pp. 27–40, 2002.

[88] D. M. Chapin, C. S. Fuller, and G. L. Pearson, "A new silicon p-n junction photocell for converting solar radiation into electrical power," *J. Appl. Phys.*, vol. 25, pp. 676–677, 1954.

[89] J. Lindmayer and J. Allison, "An improved silicon solar cell - the violet cell," in *Proc. 9th IEEE Photovoltaic Specialists Conf.*, 1972, pp. 83–84.

[90] M. A. Green, "Silicon solar cells: Evolution, high-efficiency design and efficiency enhancements," *Semicond. Sci. Technol.*, vol. 8, pp. 1–12, 1993.

[91] J. Haynos, J. Allison, R. Arndt, and A. Meulenberg, "The COMSAT non-reflective cell: A second generation improved cell," in *Proc. Int. Conf. Photovoltaic Power Generation*, 1974, pp. 25–27.

[92] J. Mandelkorn and J. H. Lamneck, "Simplified fabrication of back surface electric field silicon cells and novel characteristics of such cells," in *Proc. 9th IEEE Photovoltaic Specialists Conf.*, 1972, pp. 66–71.

[93] M. A. Green, A. W. Blakers, J. Shi, E. M. Keller, and S. R. Wenham, "19.1% efficient silicon solar cell," *Appl. Phys. Lett.*, vol. 44, pp. 1163–1164, 1984.

[94] A. W. Blakers and M. A. Green, "20% efficiency silicon solar cell," *Appl. Phys. Lett.*, vol. 48, pp. 215–217, 1986.

[95] R. R. King, R. A. Sinton, and R. M. Swanson, "Front and back surface fields for point-contact solar cells," in *Proc. 20th IEEE Photovoltaic Specialists Conf.*, 1988, pp. 538–544.

[96] ——, "Doped surfaces in one sun, point-contact solar cells," *Appl. Phys. Lett.*, vol. 54, pp. 1460–1462, 1989.

[97] A. W. Blakers, A. Wang, A. M. Milne, J. Zhao, and M. A. Green, "22.8% efficient silicon solar cell," *Appl. Phys. Lett.*, vol. 55, pp. 1363–1365, 1988.

[98] J. Zhao, A. Wang, and M. A. Green, "24.5% efficiency silicon PERT cells on MCz substrates and 24.7% efficiency PERL cells on FZ substrates," *Prog. Photovolt: Res. Appl.*, vol. 12, pp. 471–474, 1999.

[99] A. Rohatgi, S. Narasimha, S. Kamra, P. Doshi, C. P. Khattak, K. Emery, and H. Field, "Record high 18.6% efficient solar cell on HEM multicrystalline material," in *Proc. 25th IEEE Photovoltaic Specialists Conf.*, 1996, pp. 741–744.

[100] J. Zhao, A. Wang, M. A. Green, and F. Ferrazza, "19.8% efficient 'honeycomb' textured multicrystalline and 24.4% monocrystalline silicon solar cells," *Appl. Phys. Lett.*, vol. 73, pp. 1991–1993, 1998.

[101] O. Schultz, S. W. Glunz, and G. P. Willeke, "Multicrystalline silicon solar cells exceeding 20% efficiency," *Prog. Photovolt: Res. Appl.*, vol. 12, pp. 553–558, 2004.

[102] P. Sana, A. Rohatgi, J. P. Kalejs, and R. O. Bell, "Gettering and hydrogen passivation of edge-defined film-fed grown multicrystalline silicon solar cells by Al diffusion and forming gas anneal," *Appl. Phys. Lett*, vol. 64, pp. 97–99, 1994.

[103] G. Hahn and P. Geiger, "Record efficiencies for EFG and String Ribbon solar cells," *Prog. Photovolt: Res. Appl.*, vol. 11, pp. 341–346, 2003.

[104] A. Rohatgi, S. Narasimha, S. Kamra, and C. P. Khattak, "Fabrication and analysis of record high 18.2% efficient solar cells on multicrystalline silicon material," *IEEE Electron Device Lett.*, vol. EDL-17, pp. 401–403, 1996.

[105] J. I. Hanoka, "An overview of silicon ribbon growth technology," *Sol. Energy Mater. Sol. Cells*, vol. 65, pp. 231–237, 2001.

[106] M. Taguchi, H. Sakata, Y. Yoshimine, E. Maruyama, A. Terakawa, M. Tanaka, and S. Kiyama, "An approach for the higher efficiency in the HIT cells," in *Proc. 31st IEEE Photovoltaic Specialists Conf.*, 2005, pp. 866–871.

[107] P. D. Maycock, "World cell production grows 40% in 2006," *PV News*, vol. 26, no. 3, pp. 6–8, 2007.

[108] M. P. Mulligan, D. H. Rose, M. J. Cudzinovic, D. M. DeCeuster, K. R. McIntosh, D. D. Smith, and R. M. Swanson, "Manufacture of solar cells with 21% efficiency," in *Proc. 19th Euro. Photovoltaic Solar Energy Conf.*, 2005, pp. 866–871.

[109] K. Shirasawa, N. Matsushima, T. Sakamoto, Y. Inomata, S. Fujii, M. Tsuchida, K. Niira, and K. Fukui, "Over 17% high efficiency multicrystalline silicon solar cell process for large scale production," in *Proc. 19th Euro. Photovoltaic Solar Energy Conf.*, 2004, pp. 616–619.

[110] M. McCann, B. Raabe, W. Jooss, R. Kopecek, and P. Fath, "18.1% efficiency for a large area, multicrystalline silicon solar cell," in *Proc. 4th World Conf. Photovoltaic Energy Conversion*, 2006, pp. 894–899.

[111] C. J. J. Tool, G. Coletti, F. J. Granek, J. Hoomstra, M. Koppes, E. J. Kossen, H. C. Rieffe, I. G. Romijn, and A. W. Weeber, "17% mc-si cell efficiency using full in-line processing with improved texturing and screen-printed contacts on high-ohmic emitters," in *Proc. 20th Euro. Photovoltaic Solar Energy Conf.*, 2005, pp. 578–583.

[112] G. Agostinelli, P. Choulat, H. F. W. Dekkers, Y. Ma, and G. Beaucarne, "Silicon solar cells on ultra-thin substrates for large scale production," in *Proc. 21st Euro. Photovoltaic Solar Energy Conf.*, 2006, pp. 601–604.

[113] S. Arimoto, M. Nakatani, Y. Nishimoto, H. Horikawa, M. Hayashi, H. Namizaki, and K. Namba, "Simplified mass-production process for 16% efficiency multi-crystalline Si solar cells," in *Proc. 28th IEEE Photovoltaic Specialists Conf.*, 2000, pp. 188–191.

[114] W. Jooss, M. McCann, P. Fath, S. Roberts, and T. M. Bruton, "Buried contact solar cells on multicrystalline silicon with optimized bulk and surface passivation," in *Proc. 3rd World Conf. Photovoltaic Energy Conversion*, 2003, pp. 959–962.

[115] F. Duerinckx, P. Choulat, G. Beaucarne, R. J. S. Young, M. Ross, and J. A. Raby, "Improved screen printing process for very thin multicrystalline silicon solar cells," in *Proc. 19th Euro. Photovoltaic Solar Energy Conf.*, 2004, pp. 443–446.

[116] A. W. Weeber, A. R. Burgers, M. J. A. A. Goris, M. Koppes, E. J. Kossen, H. C. Rieffe, W. J. Soppe, C. J. J. Tool, and J. H. Bultman, "16% mc-Si cell efficiencies using industrial in-line processing," in *Proc. 19th Euro. Photovoltaic Solar Energy Conf.*, 2004, pp. 532–535.

[117] T. Sakamoto, N. Kobamoto, T. Sakano, K. okada, N. Nakatani, Y. Miura, H. Hashigami, H. Oowada, K. fukui, and K. Shirasawa, "Mass production technology for multicrystalline silicon solar cells," in *Renewable Energy, Makuhari*, 2006.

[118] Mitsubishi Electric, Press release, Available on-line: http://www.mitsubishielectric.co.jp/news/2007/0531-a.htm, May 2007.

[119] K. V. Ravi, R. C. Gonsiorawski, and A. R. Chaudhuri, "Progress in EFG technology for low cost photovoltaics," in *Proc. 18th IEEE Photovoltaic Specialists Conf.*, 1985, pp. 1222–1225.

[120] M. J. Kardauskas, M. D. Rosenblum, B. H. Mackintosh, and J. P. Kalejs, "The coming of age of a new PV wafer technology - some aspects of EFG polycrystalline silicon sheet manufacture," in *Proc. 25th IEEE Photovoltaic Specialists Conf.*, 1996, pp. 383–388.

[121] B. R. Bathey, J. P. Kalejs, M. D. Rosenblum, M. J. Kardauskas, R. M. Giancola, and J. Cao, "R&D toward a 15+% efficiency solar cell manufacturing line for EFG silicon wafers," in *Proc. 28th IEEE Photovoltaic Specialists Conf.*, 2000, pp. 194–197.

[122] A. Metz, S. Bagus, J. Horzel, J. D. Moschner, P. Roth, B. Schum, A. Seidl, J. P. Kalejs, W. Schumidt, I. Schwirtlich, and W. Hoffmann, "Towards 16% efficient EFG ribbon silicon solar cells," in *Proc. 19th Euro. Photovoltaic Solar Energy Conf.*, 2004, pp. 1064–1069.

[123] G. Hahn, A. Hauser, and A. M. Gabor, "14% efficient large area screen printed String Ribbon solar cells," in *Proc. 17th Euro. Photovoltaic Solar Energy Conf.*, 2001, pp. 1719–1722.

[124] G. Hahn, A. Hauser, A. M. Gabor, and M. C. Cretella, "15% efficient large area screen printed String Ribbon solar cells," in *Proc. 29th IEEE Photovoltaic Specialists Conf.*, 2002, pp. 182–185.

[125] A. Rohatgi, V. Yelundur, J. Jeong, A. Ebong, M. D. Rosenblum, and J. I. Hanoka, "Fundamental understanding and implementation of Al-enhanced PECVD SiN_x hydrogenation in silicon ribbons," *Sol. Energy Mater. Sol. Cells*, vol. 74, pp. 117–126, 2002.

[126] A. Ebong, P. Doshi, S. Narasimha, A. Rohatgi, J. Wang, and M. A. El-Sayed, "The effect of low and high temperature anneals on the hydrogen content and passivation of Si surface coated with SiO_2 and sin films," *J. Electrochem. Soc.*, vol. 146, pp. 1921–1924, 1999.

[127] W. A. Lanford and M. J. Rand, "The hydrogen content of plasma-deposited silicon nitride," *J. Appl. Phys.*, vol. 49, pp. 2473–2477, 1978.

[128] M. Maeda and M. Itsumi, "Thermal dissociation process of hydrogen atoms in plasma-enhanced chemical vapor deposited silicon nitride films," *J. Appl. Phys.*, vol. 84, pp. 5243–5247, 1998.

[129] F. L. Martinez, I. Martil, G. Gonzalez-Diaz, B. Selle, and I. Sieber, "Influence of rapid thermal annealing processes on the properties of SiN_x:H films deposited by the electron cyclotron resonance method," *J. Non-Cryst. Solids*, vol. 227-230, pp. 523–527, 1998.

[130] G. V. Gadiyak, V. G. Gadiyak, M. L. Kosinove, and E. G. Salman, "Model and computer simulations resutls of defect transformation and decomposition of SiN_x:H films during high temperature treatment," *Thin Solid Films*, vol. 335, pp. 19–26, 1998.

[131] C. Boehme and G. Lucovsky, "Dissociation reactions of hydrogen in remote plasma-enhanced chemical-vapor-deposition silicon nitride," *J. Vac. Sci. Technol. A*, vol. 19, pp. 2622–2628, 2001.

[132] P. Atkins, *Physical Chemistry, 5th ed.* Freeman, 1994.

[133] S. J. Pearton, 2004, private communication.

[134] W. L. Hansen, E. E. Haller, and P. L. Luke, "Hydrogen concentration and distribution in high-purity germanium crystals," *IEEE Trans. Nucl. Sci.*, vol. NS-29, pp. 738–744, 1982.

[135] S. J. Pearton, W. C. Dautremont-Smith, J. Chevallier, C. W. Tu, and K. D. Cummings, "Hydrogenation of shallow-donor levels in GaAs," *J. Appl. Phys.*, vol. 59, pp. 2812–2817, 1986.

[136] H. J. Moller, *Semiconductors for Solar Cells.* Artech House, 1993.

[137] S. Ostapenko, I. Tarasov, J. P. Kalejs, C. Haessler, and E. U. Reisner, "Defect monitoring using scanning photoluminescence spectroscopy in multicrystalline silicon wafers," *Semicond. Sci. Technol.*, vol. 15, pp. 840–848, 2000.

[138] I. Tarasov, S. Ostapenko, W. Seifert, M. Kittler, and J. P. Kalejs, "Defect diagnostics in multicrystalline silicon using scanning techniques," *Physica B*, vol. 308–301, pp. 1133–1136, 2001.

[139] F. Duerinckx and J. Szlufcik, "Defect passivation of industrial multicrystalline solar cells based on PECVD silicon nitride," *Sol. Energy Mater. Sol. Cells*, vol. 72, pp. 231–246, 2002.

[140] J. I. Hanoka, C. H. Seager, D. J. Sharp, and J. K. G. Panitz, "Hydrogen passivation of defects in silicon ribbon grown by the edge-defined film-fed growth process," *Appl. Phys. Lett.*, vol. 42, pp. 618–620, 1984.

[141] J. W. Jeong, Y. H. Cho, A. Rohatgi, M. D. Rosenblum, B. R. Bathey, and J. P. Kalejs, "Rapid thermal processing to enhance PECVD SiN-induced hydrongenation in high-efficiency EFG Si solar cells," in *Proc. 29th IEEE Photovoltaic Specialists Conf.*, 2002, pp. 250–253.

[142] E. M. Sachs, D. Ely, and J. Serby, "Edge stabilized ribbon ESR growth of silicon for low cost photovoltaics," *J. Cryst. Growth*, vol. 82, pp. 117–121, 1987.

[143] D. S. Ruby, W. L. Wilbanks, C. B. Fleddermann, and J. I. Hanoka, "The effect of hydrogen-plasma and PECVD-nitride deposition on bulk and surface passivation in String Ribbon Si solar cells," in *Proc. 13th Euro. Photovoltaic Solar Energy Conf.*, 1995, pp. 1412–1414.

[144] R. L. Wallace, J. I. Hanoka, A. Rohatgi, and G. Crotty, "Thin silicon String Ribbon," *Sol. Energy Mater. Sol. Cells*, vol. 48, pp. 179–186, 1997.

[145] R. L. Wallace, J. I. Hanoka, S. Narasimha, S. Kamra, and A. Rohatgi, "Thin silicon String Ribbon for high efficiency polycrystalline solar cells," in *Proc. 26th IEEE Photovoltaic Specialists Conf.*, 1997, pp. 99–102.

[146] C. C. Striemer, F. Shi, P. M. Fauchet, and S. P. Duttaqupta, "Porous silicon texturing of polysilicon substrates," in *Proc. 28th IEEE Photovoltaic Specialists Conf.*, 2000, pp. 932–935.

[147] K. F. Carr, N. Carison, P. Weitzmann, B. L. Sopori, C. Marshall, and L. Allen, "Characterization of silicon solar cells and substrates with the PVScan 5000," in *Proc. AIP Conf. 13th NREL Photovoltaic Program Rev.*, 1996, pp. 553–557.

[148] R. A. Sinton and A. Cuevas, "A quasi-steady-state open-circuit voltage method for solar cell characterization," in *Proc. 16th Euro. Photovoltaic Solar Energy Conf.*, 2000, pp. 1152–1155.

[149] D. A. Clugston and P. A. Basore, "PC1D version 5: 32-bit solar cell modeling on personal computers," in *Proc. 26th IEEE Photovoltaic Specialists Conf.*, 1997, pp. 207–210.

[150] V. Meemongkolkiat, M. Hilali, K. Nakayashiki, and A. Rohatgi, "Process and material dependence of Al-BSF in crystalline Si solar cells," in *Tech. Digests 14th Int. Photovoltaic Science Engineering Conf.*, 2004, pp. 401–402.

[151] M. M. Hilali, A. Rohatgi, and S. Asher, "Development of screen-printed silicon solar cells with high fill factors on 100 Ω/sq. emitters," *IEEE Trans. Electron Devices*, vol. ED-51, pp. 948–955, 2004.

[152] P. A. Basore, "Extended spectral analysis of internal quantum efficiency," in *Proc. 23rd IEEE Photovoltaic Specialists Conf.*, 1993, pp. 147–152.

[153] M. M. Hilali, K. Nakayashiki, A. Ebong, and A. Rohatgi, "Investigation of high-efficiency screen-printed textured Si solar cells with high sheet-resistance emitters," in *Proc. 31st IEEE Photovoltaic Specialists Conf.*, 2005, pp. 1185–1188.

[154] M. Schaper, J. Schmidt, H. Plagwitz, and R. Brendel, "20.1%-efficient crystalline silicon solar cell with amorphous silicon rear-surface passivation," *Prog. Photovolt: Res. Appl.*, vol. 13, pp. 381–386, 2005.

[155] O. Schultz, M. Hofmann, S. W. Glunz, and G. P. Willeke, "Silicon oxide/silicon nitride stack system for 20% efficient silicon solar cells," in *Proc. 31st IEEE Photovoltaic Specialists Conf.*, 2005, pp. 872–876.

[156] B. L. Sopori, "Inhomogeneities in silicon solar cells and their influence on cell performance - an experimental study," in *Proc. 14th IEEE Photovoltaic Specialists Conf.*, 1980, pp. 606–611.

[157] P. E. Mijnarends, G. J. M. Janssen, and W. C. Sinke, "The effect of material inhomogeneities on the characteristics of semicrystalline silicon solar cells: the second diode," *Sol. Energy Mater. Sol. Cells*, vol. 33, pp. 345–360, 1994.

[158] R. Baldner, H. Lautenschlager, C. Schetter, R. Schindler, and W. Warta, "Open circuit voltage losses in multicrystalline silicon: an investigation by mini solar cells," in *Proc. 25th IEEE Photovoltaic Specialists Conf.*, 1996, pp. 641–644.

[159] R. O. Bell, M. Prince, F. V. Wald, W. Schmidt, and K. D. Rasch, "A comparison of the behavior of solar silicon material in different production processes," *Sol. Energy Mater. Sol. Cells*, vol. 41/42, pp. 71–86, 1996.

[160] W. Warta, J. Sutter, B. F. Wagner, and R. Schindler, "Impact of diffusion length distributions on the performance of mc-silicon solar cells," in *Proc. 2nd World Conf. Photovoltaic Energy Conversion*, 1998, pp. 1650–1653.

[161] H. Nagel, A. G. Aberle, and S. Narayanan, "Method for the evaluation of the influence of gettering and bulk passivation on non-uniform block-cast multicrystalline si solar cells," *Diffus. Defect Data B, Solid State Phenom.*, vol. 67/68, pp. 503–508, 1999.

[162] B. L. Sopori, W. Chen, J. Gee, and K. Jones, "On the performance limiting behavior of defect clusters in commertial silicon solar cells," in *Proc. 2nd World Conf. Photovoltaic Energy Conversion*, 1998, pp. 152–155.

[163] C. Donolato, "Voronoi network modelling of multicrystalline silicon solar cells," *Semicond. Sci. Technol.*, vol. 15, pp. 15–23, 2000.

[164] J. Metzdorf, "Calibration of solar cells. I. The differential spectral responsivity method," *Appl. Opt.*, vol. 26, pp. 1701–1708, 1987.

[165] V. Meemongkolkiat, M. Hilali, and A. Rohatgi, "Investigation of RTP and belt fired screen printed Al-BSF on textured and planar back surfaces of silicon solar cells," in *Proc. 3rd World Conf. Photovoltaic Energy Conversion*, 2003, pp. 1467–1470.

[166] S. M. Sze, *Semiconductor Devices: Physics and Technology.* John Wiley & Sons, 1985.

[167] G. Agostinelli, P. Choulat, H. F. W. Dekkers, S. DeWolf, and G. Beaucarne, "Screen printed large area crystalline silicon solar cells on thin substrates," in *Proc. 20th Euro. Photovoltaic Solar Energy Conf.*, 2005, pp. 647–650.

[168] L. Jastrzebski, W. Henley, D. Schielein, and J. Lagowski, "Improvement of diffusion length in polycrystalline photovoltaic silicon by phosphorus and chlorine gettering," *J. Electrochem. Soc.*, vol. 142, pp. 3869–3872, 1995.

[169] C. T. Ho, G. Moeller, and J. D. Mathias, "Effect of heat treatment on the bulk diffusion length of EFG ribbon silicon," *Solid-State Electron.*, vol. 26, pp. 247–250, 1983.

[170] T. Buonassisi, A. M. Lorenz, and G. J. Tarnowski, “Nature, impact, and remediation of the principal lifetime-limiting defects in String Ribbon material,” in *Proc. 21st Euro. Photovoltaic Solar Energy Conf.*, 2006, pp. 1505–1507.

[171] R. Schindler and W. Warta, “Improvements and limits of the open circuit voltage of mc-silicon solar cells,” *Phys. Stat. Sol.*, vol. 222, pp. 389–404, 2000.

[172] S. A. McHugo, “Release of metal impurities from structural defects in polycrystalline silicon,” *Appl. Phys. Lett.*, vol. 71, pp. 1984–1986, 1997.

[173] K. Nakayashiki, A. Rohatgi, S. Ostapenko, and I. Tarasov, “Minority carrier lifetime enhancement in edge-defined film-fed grown Si through rapid thermal processing-assisted reduction of hydrogen-defect dissociation,” *J. Appl. Phys.*, vol. 97, pp. 024 504/1–8, 2005.

[174] G. Hahn, I. Melnyk, C. Dube, and A. M. Gabor, “Development of a chemical surface texture for String Ribbon silicon solar cells,” in *Proc. 20th Euro. Photovoltaic Solar Energy Conf.*, 2005, pp. 1438–1441.

PUBLICATIONS

Patent Disclosure

[1] A. Rohatgi, J.-W. Jeong, **K. Nakayashiki**, V. Yelundur, D.S. Kim, and M. Hilali, "Silicon solar cells and methods of fabrication," USPTO ♯20050189015.

[2] A. Rohatgi, D.S. Kim, **K. Nakayashiki**, and B. Rounsaville, "Boron diffusion in silicon devices," USPTO ♯20060183307.

Journal Papers

[1] A. Rohatgi, D.S. Kim, **K. Nakayashiki**, V. Yelundur, and B. Rounsaville, "High-efficiency solar cells on edge-defined film-fed grown (18.2%) and string ribbon (17.8%) Si by rapid thermal processing," *Appl. Phys. Lett.*, vol. 84, pp. 145–147, 2004.

[2] A. Rohatgi, M.M. Hilali, and **K. Nakayashiki**, "High-efficiency screen-printed solar cell on edge-defined film-fed grown ribbon Si through optimized rapid belt co-firing of contacts and high-sheet-resistance emitter," *Appl. Phys. Lett.*, vol. 84, pp. 3409–3411, 2004.

[3] I. Tarasov, S. Ostapenko, **K. Nakayashiki**, and A. Rohatgi, "Defect passivation in multicrystalline Si for solar cells," *Appl. Phys. Lett.*, vol. 85, pp. 4346–4348, 2004.

[4] **K. Nakayashiki**, A. Rohatgi, S. Ostapenko, and I. Tarasov, "Minority carrier lifetime enhancement in edge-defined film-fed grown Si through rapid thermal processing-assisted reduction of hydrogen-defect dissociation," *J. Appl. Phys.*, vol. 97, pp. 024504/1–8, 2005.

[5] **K. Nakayashiki**, V. Meemongkolkiat, and A. Rohatgi, "High efficiency screen-printed EFG Si solar cells through rapid thermal processing-induced bulk lifetime enhancement," *Prog. Photovolt: Res. Appl.*, vol. 13, pp. 17–25, 2005.

[6] **K. Nakayashiki**, V. Meemongkolkiat, and A. Rohatgi, "Effect of material inhomogeneity on the open-circuit voltage of String Ribbon Si solar cells," *IEEE Trans. Electron Devices*, vol. ED-52, pp. 2243–2249, 2005.

[7] M.M. Hilali, **K. Nakayashiki**, C. Khadilkar, R.C. Reedy, A. Rohatgi, A. Shaikh, S. Kim, and S. Sridharan, "Effect of Ag particle size in thick-film Ag paste on the electrical and physical properties of screen-printed contacts and silicon solar cells," *J. Electrochem. Soc.*, vol. 153, pp. A5–A11, 2006.

[8] V. Meemongkolkiat, **K. Nakayashiki**, D.S. Kim, R. Kopecek, and A. Rohatgi, "Factors limiting the formation of uniform and thick Al-back surface field and its potential," *J. Electrochem. Soc.*, vol. 153, pp. G53–G58, 2006.

[9] V. Meemongkolkiat, **K. Nakayashiki**, A. Rohatgi, G. Crabtree, J. Nickerson and T.L. Jester, "Resistivity and lifetime variation along the commercially grown Ga- and B-doped Czochralski Si ingots and its effect on light-induced degradation and performance of solar cells," *Prog. Photovolt: Res. Appl.*, vol. 14, pp. 125–134, 2006.

[10] M.M. Hilali, **K. Nakayashiki**, A. Ebong, and A. Rohatgi, "High-efficiency (19%) screen-printed textured cells on low-resistivity float-zone silicon with high sheet-resistance emitters," *Prog. Photovolt: Res. Appl.*, vol. 14, pp. 135–144, 2006.

[11] D.S. Kim, V. Yelundur, **K. Nakayashiki**, B. Rounsaville, V. Meemongkolkiat, A.M. Gabor, and A. Rohatgi, "Ribbon Si solar cells with efficiencies over 18% by hydrogenation of defects," *Sol. Energy Mater. Sol. Cells*, vol. 90, pp. 1227–1240, 2006

[12] **K. Nakayashiki**, B. Rounsaville, V. Yelundur, D.S. Kim, A. Rohatgi, R. Clark-Phelps, and J.I. Hanoka, "Fabrication and analysis of high-efficiency String Ribbon Si solar cells," *Solid-State Electron.*, vol. 50, pp. 1406–1412, 2006.

[13] S. Kleekajai, F. Jiang, M. Stavola, V. Yelundur, **K. Nakayashiki**, A. Rohatgi, G. Hahn, S. Seren, and J. Kalejs, "Concentration and penetration depth of H introduced into crystalline Si by hydrogenation methods used to fabricate solar cells," *J. Appl. Phys.*, vol. 100, pp. 093517/1-7, 2006.

[14] **K. Nakayashiki**, V. Meemongkolkiat, and A. Rohatgi, "Assessment of the impact of electrically active defects on multicrystalline Si solar cell performance," submitted for publication in *Sol. Energy Mater. Sol. Cells*, 2007.

Conference Proceedings and Technical Digests

[1] B. Damiani, **K. Nakayashiki**, D.S. Kim, V. Yelundur, S. Ostapenko, I. Tarasov, and A. Rohatgi, "Light induced degradation in promising multi-crystalline Si materials for solar cell fabrication," *3rd World Conf. Photovoltaic Energy Conversion*, Osaka, 2003, pp. 927–930.

[2] **K. Nakayashiki**, D.S. Kim, A. Rohatgi, and B.R. Bathey, "Understanding of RTP-assisted reduction of hydrogen dissociation from defects in EFG Si," *14th Int. Photovoltaic Science Engineering Conf.*, Bangkok, Thailand, 2004, pp. 643–644. (***Conference Best Paper Award***)

[3] V. Meemongkolkiat, M. Hilali, **K. Nakayashiki**, and A. Rohatgi, "Process and material dependence of Al-BSF in crystalline Si solar cells," *14th Int. Photovoltaic Science Engineering Conf.*, Bangkok, Thailand, 2004, pp. 401–402. (***Conference Best Paper Award***)

[4] A. Rohatgi, D.S. Kim, V. Yelundur, **K. Nakayashiki**, A. Upadhyaya, M. Hilali, and V. Meemongkolkiat, "Record high efficiency solar cells on multicrystalline materials through understanding and implementation," *14th Int. Photovoltaic Science Engineering Conf.*, Bangkok, Thailand, 2004, pp. 635–638. (***Invited Paper***)

[5] **K. Nakayashiki**, A. Rohatgi, I. Tarasov, S. Ostapenko, L. Gedvilas, B. Keyes, B.R. Bathey, and J.P. Kalejs, "Investigation of spatially non-uniform defect passivation in EFG Si by scanning photoluminescence technique," *31st IEEE Photovoltaic Specialists Conf.*, Lake Buena Vista, Florida, 2005, pp. 1265–1268.

[6] V. Yelundur, **K. Nakayashiki**, M. Hilali, and A. Rohatgi, "Implementation of a homogeneous high-sheet-resistance emitter in multicrystalline Si solar cells," *31st IEEE Photovoltaic Specialists Conf.*, Lake Buena Vista, Florida, 2005, pp. 959–962.

[7] V. Meemongkolkiat, **K. Nakayashiki**, A. Rohatgi, G. Crabtree, J. Nickerson, and T.L. Jester, "The effect of the variation in resistivity and lifetime on the solar cells performance along the commercially grown Ga- and B-doped Czochralski ingots," *31st IEEE Photovoltaic Specialists Conf.*, Lake Buena Vista, Florida, 2005, pp. 1115–1118. (***Conference Best Poster Award***)

[8] M.M. Hilali, **K. Nakayashiki**, and A. Rohatgi, "Investigation of high-efficiency screen-printed textured Si solar cells with high sheet-resistance emitters," *31st IEEE Photovoltaic Specialists Conf.*, Lake Buena Vista, Florida, 2005, pp. 1185–1188.

[9] V. Meemongkolkiat, **K. Nakayashiki**, D.S. Kim, S. Kim, A. Shaikh, and A. Rohatgi, "Investigation of screen-printing Al paste for local back surface field formation," *4th World Conf. Photovoltaic Energy Conversion*, Waikoloa, Hawaii, 2006, pp. 1338-1341.

[10] D.S. Kim, A. Das, **K. Nakayashiki**, B. Rounsaville, V. Meemongkolkiat, and A. Rohatgi, "Silicon solar cells with boron back surface field formed by using boric acid," *22nd Euro. Photovoltaic Solar Energy Conf.*, Milan, Italy, 2007.

[11] A. Ebong, **K. Nakayashiki**, V. Upadhyaya, A. Rohatgi, B.R. Bathey, M.D. Rosenblum, J. Salami, and A. Shaikh, "Screen-printed solar cells on less than 200 μm thick EFG sheet silicon," *22nd Euro. Photovoltaic Solar Energy Conf.*, Milan, Italy, 2007.

Workshop Proceedings and Extended Abstracts

[1] **K. Nakayashiki**, A. Upadhyaya, M. Hilali, A. Rohatgi, J.P. Kalejs, B. Bathey, and K. Matthei, "Record high efficiency screen-printed belt co-fired cells on EFG Si ribbon (16.1%) and HEM mc-Si (16.9%)," *13th NREL Workshop Crystalline Si Solar Cell Materials and Processes*, Vail, Colorado, 2003, pp. 215–218.

[2] D.S. Kim, **K. Nakayashiki**, V. Yelundur, B. Rounsaville, A. Rohatgi, A.M. Gabor, B.R. Bathey, and J.P. Kalejs, "Record high efficiency solar cells on EFG (18.2%) and String Ribbon (17.8%) Si by rapid thermal processing," *13th NREL Workshop Crystalline Si Solar Cell Materials and Processes*, Vail, Colorado, 2003, pp. 219–223.

[3] V. Meemongkolkiat, **K. Nakayashiki**, D.S. Kim, and A. Rohatgi, "Factors that limit the formation of an uniform and thick screen-printed Al back surface field," *14th NREL Workshop Crystalline Si Solar Cell Materials and Processes*, Winter Park, Colorado, 2004, pp. 259–262.

[4] V. Meemongkolkiat, **K. Nakayashiki**, B.C. Rounsaville, and A. Rohatgi, "Effect of oxygen on the quality of Al-BSF in Si cells," *15th NREL Workshop Crystalline Si Solar Cell Materials and Processes*, Vail, Colorado, 2005, pp. 249–252.

[5] B.C. Rounsaville, **K. Nakayashiki**, V. Yelundur, D.S. Kim, A. Rohatgi, R. Clark-Phelps, and J.I. Hanoka, "Over 18% efficiency solar cells on String Ribbon Si material

by rapid thermal processing," *15th NREL Workshop Crystalline Si Solar Cell Materials and Processes*, Vail, Colorado, 2005.

[6] A. Rohatgi, M. Hilali, A. Ristow, A. Upadhyaya, **K. Nakayashiki**, V. Yelundur, and A. Ebong, "Opportunities and challenges in crystalline Si photovoltaics," *13th Int. Workshop The Physics Semiconductor Devices*, New Delhi, India, 2005, pp. 20–28. (***Invited Paper***)

[7] A. Rohatgi, V. Yelundur, **K. Nakayashiki**, and A. Ebong, "Development of hydrogen bulk defect passivation and screen-printed contacts on high sheet resistance emitters for low-cost high-efficiency silicon solar cells," *DOE Solar Energy Technologies Program Review Meeting*, Denver, Colorado, 2005.

[8] A. Rohatgi, M.Hilali, A. Ristow, V. Meemongkolkiat, A. Upadhyaya, **K. Nakayashiki**, V. Yelundur, and A. Ebong, "Future direction of cost effective crystalline silicon photovoltaics," *2nd Workshop Future Direction Photovoltaics*, Tokyo, 2006, pp. 25–32. (***Invited Paper***)

[9] **K. Nakayashiki**, V. Yelundur, A. Rohatgi, S. Ostapenko, B.R. Bathey, and M.D. Rosenblum, "Effect of single- and double-side PECVD SiN$_x$-induced defect hydrogenation in EFG Si," *16th NREL Workshop Crystalline Si Solar Cell Materials and Processes*, Denver, Colorado, 2006, pp. 219–222.

[10] A. Rohatgi, **K. Nakayashiki**, and V. Yelundur, "Impact of the inhomogeneous distribution of electrically active defects on multicrystalline silicon solar cell performance," *DOE Solar Energy Technologies Program Review Meeting*, Denver, Colorado, 2007.

[11] A. Ebong, **K. Nakayashiki**, V. Upadhyaya, and A. Rohatgi, "Large area (100 cm^2) EFG silicon solar cells with screen-printed contacts)," *17th NREL Workshop Crystalline Si Solar Cell Materials and Processes*, Vail, Colorado, 2007, pp. 271–274.

[12] S. Ramanathan, **K. Nakayashiki**, V. Yelundur, A. Rohatgi, C. Dube, and J.I. Hanoka, "Fabrication and analysis of high-efficiency textured String Ribbon silicon solar cells," *17th NREL Workshop on Crystalline Silicon Solar Cell Materials and Processes*, Vail, Colorado, 2007, pp. 281–285.

[13] S. Kleekajai, C. Peng, M. Stavola, V. Yelundur, **K. Nakayashiki**, A. Rohatgi, and J. Kalejs, "Introduction of H into Si from a SiN$_x$ coating: Role of the SiN$_x$ density and the Si/SiN$_x$ interface," *17th NREL Workshop on Crystalline Silicon Solar Cell Materials and Processes*, Vail, Colorado, 2007, pp. 122–129.